Geodätisch-geophysikalische Arbeiten in der Schweiz

(Fortsetzung der Publikationsreihe
«Astronomisch-geodätische Arbeiten in der Schweiz»)

herausgegeben von der

Schweizerischen Geodätischen Kommission
(Organ der Akademie der Naturwissenschaften Schweiz)

Sechsundsiebzigster Band
Volume 76

High-resolution GPS tomography in view of hydrological hazard assessment

Simon Lutz

2009

Adresse der Schweizerischen Geodätischen Kommission:

Institut für Geodäsie und Photogrammetrie
ETH Zürich
Schafmattstrasse 34
CH-8093 Zürich, Switzerland

Internet: http://www.sgc.ethz.ch

ISBN 978-3-908440-20-8

Redaktion des 76. Bandes:
Dr. S. Lutz, J. Müller-Gantenbein, Prof. Dr. A. Geiger
Druck: Print-Atelier ADAG, Zürich

VORWORT

Das Hauptziel des vorliegenden Projektes bestand darin, die Machbarkeit der GPS Tomographie in einem lokal begrenzten Gebiet nachzuweisen und zu untersuchen, ob und in welchem Masse zeitnahe vierdimensionale Modelle des Wasserdampfes hochaufgelöst bestimmt werden können. Die Verfahren sollten nicht nur für permanente GPS Stationen eingesetzt, sondern auch in Messkampagnen mit nicht-permanenten Messnetzen erprobt und getestet werden. Herr Simon Lutz hat die Arbeiten mit hervorragendern Einsatz ausgeführt.

Wichtig für den Qualitätsvergleich sind GPS-unabhängige Datensätze. Herr Lutz benutzte dazu die Bodenstationen des automatischen Meteo-Netzes ANETZ, welches durch den Schweizerischen Wetterdienst MeteoSchweiz unterhalten wird. Hinzu kamen Ballonsondierungen der MeteoSchweiz in Payerne, aber auch eigene in den Kampagnen gestartete Sonden. Die von Herrn Lutz durchgeführte Optimierung der Verteilung der Messstationen war wichtig, um bestmögliche Resultate und eine mit den Meteomodellen vergleichbare räumliche Resolution zu erhalten.

Die durchgeführten Untersuchungen basierten auf zwei Messkampagnen, die im Kanton Wallis durchgeführt worden waren. Unabhängige Daten lieferte das numerische Wettervorhersagemodell von MeteoSchweiz. Ein ausführlicher Vergleich der aus COSMO-7 invertierten zenitalen Laufzeitverzögerungen mit den integralen Schätzmethoden ergab zufriedenstellende Übereinstimmungen. Aufgrund einer systematischen Analyse aller erhobenen vertikalen Profile wurde eine Übereinstimmung der tomographischen Lösung in der Grössenordnung von 10 ppm nachgewiesen.

Am Schluss untersuchte Herr Lutz die wichtige Frage, ob und mit welcher Qualität eine „Near real-time“ Prozessierung möglich ist. Sie ist durch das Fehlen von hochpräzisen Bahndaten limitiert. Man ist stattdessen auf sogenannte „ultra-rapid orbits“ angewiesen. Eine weitere Alternative, die es zu untersuchen galt, lieferten die auf den Trägerwellen aufmodulierten Bahndaten. Herr Lutz konnte aufzeigen, dass die Benutzung von „ultra-rapid orbits“ zufriedenstellende Resultate lieferte und damit ein wichtiger Fortschritt in Richtung Quasi-Echtzeit-Analyse erfolgen kann.

Herr Lutz hat komplizierte geodätisch-atmosphärenphysikalische Zusammenhänge bearbeitet und in realen Feldkampagnen erfolgreich erprobt. Die erreichte Auflösung der Refraktivitätsverteilung in einem lokalen, nicht-permanenten GPS-Stationsnetz kann als hervorragend bezeichnet werden.

Herrn Lutz gebührt grosse Anerkennung. Mit dem vorliegenden Bericht öffnet er den Weg für ein wissenschaftlich wie auch praktisch wichtiges Gebiet der Satellitengeodäsie. Nationale und internationale Bemühungen, den Wasserdampf zeitlich und räumlich hochaufgelöst bestimmen zu können, belegen die grosse Bedeutung der Resultate. Die Schweizerische Geodätische Kommission gratuliert Herrn Lutz zu seiner grundlegenden Arbeit. Damit konnte ein wichtiger Beitrag zur schweizerischen Geodäsie geleistet werden. Herr Lutz hat dieses Projekt mit beispiellosem Einsatz erfolgreich bearbeitet und auch international grosse Anerkennung gefunden.

Der Schweizerischen Akademie für Naturwissenschaften danken wir für die Übernahme der Druckkosten.

Prof. Dr. Hans-Gert Kahle
Institut für Geodäsie und Photogrammetrie
ETH Zürich

Prof. Dr. Alain Geiger
ETH Zürich
Präsident der SGK

PREFACE

L'objectif principal de ce projet était de démontrer la faisabilité de la tomographie GPS dans une région locale et limitée ainsi que d'étudier jusqu'à quel degré un modèle de vapeur d'eau troposphérique 4D peut être estimé en quasi temps réel. Les méthodes développées ne devaient pas se limiter aux stations GPS permanentes, mais devaient également être testées et appliquées sur des réseaux de type non permanents, réalisés lors de campagnes de mesures. Simon Lutz a réalisé ce travail avec un enthousiasme et avec un engagement particulièrement remarquable.

Afin de valider la qualité des résultats, des données indépendantes des observations GPS sont indispensables. Pour ce faire, Simon Lutz a utilisé le réseau des stations météorologiques automatiques ANETZ régies par MétéoSuisse, le service météorologique national. De plus, il a disposé de données provenant des ballons sondes de MétéoSuisse lancés depuis la station de Payerne, ainsi que de ses propres sondes, engagées lors de ses propres campagnes. Afin d'obtenir les meilleurs résultats ainsi qu'une résolution spatiale comparable à celle des modèles météorologiques, l'optimisation de la distribution des stations de mesures réalisé par Simon Lutz fût très importante.

Les études se sont basées sur deux campagnes de mesures qui se sont déroulées dans le canton du Valais. Les données indépendantes ont été tirées du modèle de prédiction météorologique de MétéoSuisse COSMO-7. Des comparaisons détaillées entre les délais zénithaux issus de l'inversion de COSMO-7 avec ceux de ses propres résultats donnent des concordances satisfaisantes. Sur la base d'analyses systématiques de tous les profils verticaux, il a démontré que les résultats de la tomographie coïncident dans un ordre de grandeur de 10 ppm.

Finalement, Simon Lutz a étudié une question importante. Elle est de savoir avec quelle qualité un traitement en proche temps réel est réalisable. Ce traitement n'est pas simple et est limité par la disponibilité des données d'orbites de satellites précis. Dès lors, nous sommes contraints d'utiliser les orbites ultra rapides „ultra-rapid orbits". Une autre alternative, qui a été étudiée, est donnée par les orbites diffusées par modulation des ondes porteuses. Simon Lutz a pu démontrer que l'utilisation des orbites ultra rapides donne des résultats satisfaisants et a ainsi réalisé une avance importante en direction d'analyses en quasi temps réel.

Simon Lutz a combiné des relations géodésiques et atmosphériques complexes et a ensuite appliqué les approches théoriques de la tomographie GPS à des campagnes réelles. La résolution des champs de réfractivité obtenus dans un réseau de stations GPS local non permanent est remarquable.

Simon Lutz mérite une grande reconnaissance. Avec ce rapport, il ouvre la voie scientifique et pratique d'un domaine important de la géodésie satellitaire. Les efforts internationaux pour estimer la vapeur d'eau avec une haute résolution spatio-temporelle témoignent de l'importance des résultats. La commission géodésique suisse félicite Simon Lutz pour son travail fondamental. Il a ainsi apporté une contribution importante à la commission géodésique suisse. Simon Lutz a travaillé pour ce projet avec un engagement sans précédent et a également reçu une reconnaissance internationale.

Nous remercions l'académie des sciences naturelles pour la prise en charge des frais d'impression.

Prof. Dr. Hans-Gert Kahle
Institut de Géodésie et Photogrammétrie
ETH Zürich

Prof. Dr. Alain Geiger
ETH Zürich
Président de la CGS

FOREWORD

The main goal of this project was to prove the feasibility of GPS tomography in a locally limited region and to investigate to which degree near real-time 4D models of tropospheric water vapor can be determined. The method developed should not only be tested and applied for permanent GPS but also for non-permanent campaign-type networks. Simon Lutz has performed the work with great enthusiasm and persistence.

For assessing the quality of the results achieved, data sets are necessary which are independent from GPS observations. Simon Lutz used ground stations of the Meteo Network ANETZ, which is being maintained by the national weather service of Switzerland, MeteoSwiss. In addition balloon soundings of MeteoSwiss launched at Payerne have been utilized. The opimization for the distribution of the stations was important to achieve best possible results and to establish the same resolution as is given in numerical weather prediction models.

The studies performed were based on two measuring campaigns, which had been conducted in the canton of Valais, Switzerland. Independent data sets were provided by the numerical weather prediction model of MeteoSwiss, COSMO-7. A detailed comparison of zenithal path delays based on inversions of COSMO-7 with his own results yielded satisfying accordance. Based on a systematic analysis for all vertical profiles an agreement of the order of 10 ppm was verified.

Finally Simon Lutz explored the important question to what extent „near real-time“ processing would be possible. This task is difficult because of the limited availability of precise orbits. Instead „ultra-rapid orbits“ have to be used. Another alternative are the orbital data modulated on the carrier waves. Simon Lutz was able to prove, that „ultra-rapid orbits“ furnished satisfactory results. With this conclusion an important contribution towards near real-time processing could be achieved.

It is confirmed that Simon Lutz has accomplished to merge complicated geodetic-atmospheric interrelationships and that he has successfully applied the theoretical approach of GPS tomography in actual campaigns. The resolution achieved for the distribution of refractivity can be considered extremely promising, given the local extent of the non-permanent GPS network.

With this report he contributes significantly to satellite geodetic applications which are both scientifically and practically of high importance. National and international efforts to determine tropospheric water vapor at high spatio-temporal resolution account for the importance of the work accomplished. The Swiss Geodetic Commission congratulates Simon Lutz on his widely recognized contribution to Swiss Geodetic Science. He has pursued this project successfully with persistent, painstaking endeavor and has gained wide international recognition.

We are grateful to the Swiss National Science Foundation for funding the research project and to the Swiss Academy of Sciences for financing the printing costs.

Prof. Dr. Hans-Gert Kahle
Institute of Geodesy and Photogrammetry
ETH Zurich

Prof. Dr. A. Geiger
ETH Zurich
President of SGC

Abstract

In the last few years, the use of propagation delays of GNSS radio signals due to the atmospheric effect has gained considerable importance as a valuable contribution to numerical weather forecasting. GPS-based tomography is a dedicated method to resolve the temporal variation and spatial distribution of the most important constituent of the atmosphere, the tropospheric water vapor. The four-dimensional tomographic approach, however, has not yet been completely established. Investigations on the small-scale high-resolution configuration will now help to determine and model water vapor distribution and variation over local, mountainous catchment areas. Especially, the development towards near real-time analysis with a high update rate of less than one hour will reveal the potential in the field of short and medium range forecasts.

Three main objectives were defined for this research project: The first objective was the study of the feasibility of GPS tomography in a small-scale and Alpine area. Furthermore, the processing of campaign-type measurements had to be considered specifically. The second aim was the determination of the four-dimensional distribution of atmospheric water vapor over a local region using GPS tomography in view of hydrological hazard assessment. Thirdly, aspects of real-time determination had to be investigated. In this context, it had to be accounted for that, instead of precise GNSS satellite orbits, predicted ones like broadcast ephemerides or ultra-rapid orbits had to be used. Also, it had to be addressed that the processing time is a critical issue in real-time computation. As a consequence, the parameters of the complete GPS processing were refined and adapted to near real-time applications. Furthermore, new algorithms in the tomographic software were to be designed and evaluated.

The tomographic software package AWATOS (Atmospheric Water Vapor Tomography Software), developed at the Geodesy and Geodynamics Laboratory, ETH Zurich, was used for the assimilation of double-differenced GPS observations and interpolated meteorological data sets. The spatial distribution of water vapor can be determined by least-squares inversion with a high temporal resolution.

The work was carried out in five steps: Simulations helped to design an optimal GPS network for the tomographic purpose. Based on these findings, two dedicated field campaigns were performed to study the feasibility of the method for a non-permanent densification network in an Alpine region in Switzerland. Secondly, GPS derived zenith total delays (ZTD) as well as double-differenced residuals were estimated using a high performance and high accuracy postprocessing software package (Bernese GPS Software Version 5.0). The results were validated by comparison with independent methods. With the software package COMEDIE, meteorological data was collocated and interpolated for the separation of the total delays into a wet and a dry part. In the third step, this set of data was processed with the GPS tomography software package AWATOS to obtain spatially and temporally highly-resolved wet refractivity fields. An automatic generation of tomographic voxel models was

developed in the forth step. This tool allows high flexibility in tomographic processing and forms a fundamental part of an adaptive method of choosing voxel models at a particular spatial resolution. In the fifth step, the aspects of near real-time processing was investigated.

Measurements from a solar spectrometer and data from the current numerical weather model COSMO-7 of MeteoSwiss were available for comparison purposes. During the campaigns, radiosondes were launched to measure vertical profiles of the tropospheric meteorological components in situ and to validate the tomographic results.

The success of the tomographic method was revealed by the statistical analyses. The wet refractivity profiles from the GPS tomography software package AWATOS in the high-resolution mode match the profiles derived from corresponding radiosonde measurements within 10 ppm (refractivity units). The AWATOS profiles represent the characteristics of the different tropospheric layers in most cases with high significance.

The accuracy of GPS tomography in near real-time was assessed based on dedicated case studies with real-time orbits. The error budget of the near real-time calculations was compared to the best postprocessing solutions available. Due to large variations in the time series of the Up component of the GPS coordinate estimation, the broadcast ephemerides are not recommended for GPS meteorological applications. But ultra-rapid orbits, which are also available in real-time, yield satisfying results regarding tropospheric parameter estimation (ZTD) and the high-resolution GPS tomographic analysis.

Zusammenfassung

In den letzten Jahren hat die Analyse der durch den troposphärischen Wasserdampf verursachten Laufzeitverzögerung der Satellitensignale (z.B. des globalen Positionierungssystems GPS) stark an Bedeutung für die numerische Wettervorhersage zugenommen. GPS-Tomographie ist eine verheissungsvolle Methode, um die räumliche Verteilung des Wasserdampfs, des in Bezug auf Wetter und Klima wichtigen Bestandteils der Atmosphäre, mit fast beliebiger zeitlicher Auflösung zu bestimmen. Die vierdimensionale Anwendung der GPS-Tomographie wurde jedoch noch nicht abschliessend entwickelt. Nun soll die Untersuchung einer kleinräumigen und hochaufgelösten Konfiguration dazu beitragen, die Verteilung des Wasserdampfs über einem eng begrenzten, gebirgigen Gebiet zu modellieren und zu bestimmen. Insbesondere werden die Fortschritte im Bereich einer Echtzeit-Auswertung und einer hohen Wiederholbarkeitsrate von weniger als einer Stunde das Potential der Methode für die kurz- und mittelfristige Wetterprognose aufzeigen.

Für diese Arbeit wurden drei Hauptziele formuliert: das erste Ziel bestand darin, die Machbarkeit der GPS-Tomographie in einem kleinrämigen, alpinen Gebiet und die Möglichkeiten und Grenzen von Kampagnen-basierten Messungen nachzuweisen. Im Hinblick auf die Erkennung von hydrologischen Gefahren sollte als zweites Ziel die lokale vierdimensionale Verteilung des atmosphärischen Wasserdampfs mit Hilfe der GPS-Tomographie bestimmt werden. Drittens sollten die Aspekte der Quasi-Echtzeit-Analyse untersucht werden. Dabei ist zu bedenken, dass für die GPS-Prozessierung keine hochgenauen Orbits, sondern die in Echtzeit verfügbaren "broadcast" Ephemeriden oder "ultra-rapid" Orbits verwendet werden, die auf Vorausberechnungen basieren. Die Berechnungszeit ist ebenfalls ein wichtiges Kriterium, das in die Überlegungen zur Echtzeitanalyse einfliessen muss. Die Parameter der GPS-Prozessierung mussten daher verfeinert und an die Anforderungen der Quasi-Echtzeit-Analyse angepasst werden. Es galt ausserdem, neue Algorithmen in der GPS-Tomographie zu entwerfen und zu evaluieren.

Das GPS-Tomographie-Software-Paket AWATOS (Atmospheric Water Vapor Tomography Software), entwickelt am Institut für Geodäsie und Geodynamik der ETH Zürich, assimiliert GPS-Doppeldifferenz-Beobachtungen und interpolierte Daten von Wetterstationen in ein drei-dimensionales Gittermodell. Mit Hilfe der Ausgleichsrechnung nach der Methode der kleinsten Quadrate lässt sich die räumliche Verteilung des Wasserdampfs mit einer hohen zeitlichen Auflösung bestimmen.

Die vorliegende Studie war in fünf Arbeitsschritte unterteilt: Für tomographische Zwecke konnte mittels Simulationen ein optimales GPS-Netzwerk der Bodenstationen in einem alpinen Projektgebiet bestimmt werden. Auf der Grundlage dieser Analysen wurden in einem ersten Schritt zwei Feldkampagnen durchgeführt, um die Qualität der Methode der GPS-Tomographie für ein nicht-permanentes Verdichtungsnetz in einem lokal begrenzten Raum in den Schweizer Alpen zu untersuchen. Im zweiten Schritt wurden mit der leistungsstarken, aktuellen Bernese GPS Software Version 5.0 sowohl die Troposphärenparameter ZTD (totale Laufzeitverzögerun-

gen in Zenithrichtung) als auch die Residuen der Doppeldifferenz-Beobachtungen berechnet. Die Resultate wurden mit unabhängigen Methoden validiert. Mit Hilfe des Software-Pakets COMEDIE wurden die meteorologischen Daten mittels eines Kollokations-Ansatzes auf die GPS-Stationskoordinaten interpoliert, um die totale Laufzeitverzögerung in einen feuchten und trockenen Anteil aufzugliedern. Im dritten Schritt wurde der gesamte Datensatz in der GPS-Tomographie-Software AWATOS prozessiert, um räumlich und zeitlich hoch aufgelöste Feuchtrefraktivitätsfelder zu erzeugen. Der vierte Schritt untersuchte unterschiedliche hochauflösende Konfigurationen. Dazu wurde ein Programm entwickelt, welches automatisch tomographische Voxelmodelle (das ist die dreidimensionale Diskretisierung der Atmosphäre) entwickelt. Dies gestattet eine hohe Flexibilität in der tomographischen Auswertung. Zudem ist es grundlegend wichtig für eine adaptive Methode, um räumlich unterschiedlich aufgelöste Modelle zu generieren und evaluieren. Im fünften und letzten Schritt wurden die wichtigsten Aspekte der Echtzeit-Analyse erarbeitet.

Zu Vergleichszwecken standen die Messdaten eines geodätischen Solarspektrometers und Analysedaten des aktuellen numerischen Wettermodels COSMO-7 der MeteoSchweiz zur Verfügung. Zur Validierung der Resultate wurden Ballonsondierungen während beider Kampagnen durchgeführt, mit denen Vertikalprofile der meteorologischen Parameter der Troposphähre in situ gemessen wurden.

Der Erfolg der tomographischen Methode zeigt sich in den statistischen Analysen. Die mit Hilfe der Tomographiesoftware AWATOS in hoch-aufgelöster Konfiguration erzeugten Feuchtrefraktivitäts-Profile stimmen in der Grössenordnung von 10 ppm (Einheit der Refraktivität) mit denen überein, die aus den betreffenden Radiosondenmessungen errechnet wurden. Überwiegend deutlich zeigen sich in den AWATOS-Profilen die Chakateristika der verschiedenen Schichten der Troposphäre.

Die Genauigkeit der GPS-Tomographie in der Quasi-Echtzeit-Analyse wurde auf Grundlage mehrerer Fallstudien mit Echtzeit-Bahndaten untersucht. Die Zusammenstellung der Fehler der Quasi-Echtzeit-Rechnungen wurde mit den best möglichen Lösungen (d.h. hochgenaue Bahndaten) verglichen. Die direkt durch die Satelliten übermittelten "broadcast" Ephemeriden sind für GPS-basierte meteorologische Anwendungen nicht zu empfehlen, da die Zeitreihen der Vertikalkomponente der Koordinatenschätzungen grosse Unterschiede aufweisen. Hingegen zeigen sogenannte "ultra-rapid" Orbits, die auch für Echtzeit-Auswertungen zur Verfügung stehen, hierbei wie im Hinblick auf die Qualität der Schätzung des troposphärischen Parameters und die tomographische Analyse zufriedenstellende Resultate.

Contents

Abbreviations

AGNES	Automated GPS Network for Switzerland (operated and maintained by swisstopo)
AMSL	Above mean sea level
ANETZ	Automated Meteorological Monitoring Network of Switzerland (operated and maintained by MeteoSwiss)
AWATOS	Atmospheric Water Vapor Tomography Software
COMEDIE	Collocation of Meteorological Data for Interpolation and Estimation of Tropospheric Path Delays
COITROPA	Collocation and Interpolation of Tropospheric Path Delays
COSMO	Consortium for Small-Scale Modeling
EUREF	European Reference Frame
GEMOSS	Geodetic Mobile Solar Spectrometer
GNSS	Global Navigation Satellite Systems
GPS	Global Positioning System
IERS	International Earth Rotation and Reference Systems Service
IGS	International GNSS Service
IPCC	Intergovernmental Panel on Climate Change
ITRF	International Terrestrial Reference Frame
MJD	Modified Julian Date
PBL	Planetary Boundary Layer
UTC	Coordinated Universal Time
WMO	World Meteorological Organization
ZPD	Zenith Path Delay, further distinction between ZDD for Zenith Dry Delay, ZWD for Zenith Wet Delay and ZTD for Zenith Total Delay

Mathematical symbols and expressions

e	Euler's number
π	Pi, the ratio of a circle's circumference to its diameter
$\overrightarrow{x}, \overrightarrow{y}, \overrightarrow{z}$	Column or row vectors
$\mathbf{A}, \mathbf{B}, \mathbf{C}$	More-dimensional matrices
rms	Root mean square, also known as the quadratic mean error $\operatorname{rms}(x_1, x_2, ..., x_n) = \sqrt{\frac{1}{n} \cdot \sum_{i=1}^{n} x_i^2}$
σ	Sample standard deviation $\sigma(x_1, x_2, ..., x_n) = \sqrt{\frac{1}{n-1} \cdot \sum_{i=1}^{n} \left(x_i - \frac{1}{n} \cdot \sum_{i=1}^{n} x_i \right)^2}$
$\frac{\partial f}{\partial y}$	Partial derivative of function f with respect to y

Chapter 1

Introduction

1.1 Trends in GPS meteorology

Water vapor plays an essential role in the dynamics and thermodynamics of atmospheric storm systems and the hydrological cycle on local, regional and global scales (see e.g. Grebner, 1996). It is a key climate variable (see e.g. Salstein et al., 1983; Shine and Sinha, 1991; Elliott, 1995; Oltmans and Hofmann, 1995; Schneider et al., 1999). Water vapor is a precursor of precipitation and a very significant fraction of the energy released to the atmosphere comes from latent heat via water vapor (see e.g. Pugnaghi et al., 2002). In the lower troposphere, condensation of water vapor into precipitation provides latent heat, which dominates the structure of the tropospheric diabatic heating.

Water vapor is also the most important gaseous source of infrared but also visible and ultraviolet light opacity in the atmosphere (see e.g. Johns, 1965; Liou, 1980), accounting for about 60 % of the natural greenhouse effect for clear skies (Kiehl and Trenberth, 1997). It provides a large positive feedback in model projections of climate change. This effect was investigated and confirmed in several studies and publications (see e.g. Rind et al., 1991; Genio, 1994; Hall and Manabe, 1999; Schneider et al., 1999; Soden et al., 2002; Philipona et al., 2005; Solomon et al., 2007). It is difficult to resolve the atmospheric water vapor distribution because of its characteristics of fast variation in spatial and temporal scales. Hence, improved monitoring of atmospheric water vapor will lead to more accurate forecasts of precipitation and severe weather and to a better understanding of global climate and climatic change (see also e.g. Norquist and Chang, 1994).

Yuan et al. (1993); Rocken et al. (1995); Davis et al. (1996); Duan et al. (1996); Elgered et al. (1997); Borbás (1998); Gradinarsky et al. (2002) and others successfully tested the hypothesis that the Global Positioning System (GPS) can be used to detect long and short-term global and regional airmass changes by estimating integrated precipitable water vapor. Atmospherically induced propagation path delays and unmodeled multipath are major contributors to GPS measurement error. Propagation delays of the GPS code and phase signals caused by the neutral atmosphere (i.e. the troposphere) are, nowadays, probably the ultimate accuracy-limiting factor for geodetic applications of GPS (e.g. tectonics and sea-level changes, see also Johansson, 1998; Tsuda et al., 1998; Dach et al., 2007). Water vapor is the largest source of variable atmospheric delay (see e.g. Emardson and Jarlemark, 1999; Gregorius and Blewitt, 1999; de Haan, 2006). Changes in the distribution of water vapor, therefore also in the available potential energy, are associated with clouds, convection, storms and weather fronts. In addition, variations resulting from orographic, frontal, coastal and seasonal gradients may be present (see e.g. Solheim

et al., 1999). Especially, their differential effects with respect to the GPS receiver sites may become important for very precise applications (see e.g. Tranquilla and Al-Rizzo, 1993).

Over the past few years, the potential of GPS for determining the four-dimensional refractivity field of the troposphere has been investigated (see e.g. Ware et al., 2000; Bengtsson et al., 2003). It has been shown that ground-based GPS receivers provide valuable information of integrated precipitable water vapor. This is achieved by estimating the time-varying zenith wet delay, which is retrieved by stochastic filtering of raw GPS observations (see e.g. Tralli and Lichten, 1990; Bevis et al., 1992; Rocken et al., 1995; Coster et al., 1996; Davis and Elgered, 1998; Tregoning et al., 1998; Wolfe and Gutman, 2000; Stoew and Elgered, 2004). Several feasibility studies have demonstrated the usefulness of the method. Furthermore, near-real time applications of zenith total and wet delay estimation have been investigated (see e.g. Rocken et al., 1997b; Kruse et al., 1999; Flores et al., 2000a; Ge et al., 2000; Dick et al., 2001; Douša, 2004; Foster et al., 2005). Stoew and Elgered (2004) and others concluded that GPS data provides information to better predict extreme weather conditions, such as thunderstorms, lightning, night-time fog or intense precipitation and flooding.

In the meantime, meteorological institutes all over the world successfully assimilate GPS zenith path delays or integrated precipitable water vapor data into numerical weather prediction models: E.g. the National Center for Atmospheric Research and the NOAA Forecast Systems Laboratory, Boulder, USA (Kuo et al., 1993; Ha et al., 2003; Gutman et al., 2004; Smith et al., 2004, 2007), and the Department of Meteorology, Florida State University (de Pondeca and Zou, 2001a; Peng and Zou, 2004), further the University of Nottingham together with the Meteorological Office in the UK (Baker et al., 2001; Higgins, 2001; Jerrett and Nash, 2001), MeteoSwiss in Switzerland (Brockmann et al., 2001; Guerova, 2003a; Guerova et al., 2006), the German Weather Service (DWD) (Köpken, 2001) and the GFZ, Potsdam, in collaboration with the DWD (Reigber et al., 2002; Gendt et al., 2004; Grzeschik et al., 2006) as well as the Instituto Nacional de Meteorologia together with the Institute of Space Studies of Catalonia in Spain (Cucurull et al., 2000, 2004).

More recent studies assimilating also GPS slant water vapor were carried out at the Japan Meteorological Agency (Nakamura et al., 2004; Seko et al., 2004a) as well as at the Danish Meteorological Institute (Vedel and Sattler, 2002; Vedel et al., 2004), at the Finnish Meteorological Institute (Eresmaa et al., 2006), at the French Meteorological Office (Poli et al., 2006, 2007), in Italy (Pacione et al., 2001a; Faccani et al., 2005) and the Shanghai Meteorological Center and the State Key Laboratory of Severe Weather in China with collaborative partner universities (Ding et al., 2007; Zhang et al., 2007). Elgered (2001); Haase et al. (2001a); van der Marel and The COST-716 Team (2004); Elgered et al. (2005) summarize similar works within the frame of COST Action 716 of the European Community. There is also research done in order to assimilate data from the numerical weather models into the GPS processing (see e.g. Marshall et al., 2001; Pany et al., 2001; Cucurull et al., 2002a and also Sec. 2.4.3, pp. 26, in terms of advanced mapping functions for GPS path delays).

Beyond integrated precipitable water vapor, entire profiles and the vertical stratification are of even greater benefit for the improvement of meteorological models and

forecasting tools. Therefore, tomographic methods were investigated to resolve for a spatial and temporal distribution of the precipitable water vapor in the atmosphere using not only the zenith wet delay but also the slant-path or line-of-sight wet delay (see e.g. Rocken et al., 1993; Ware et al., 1997; Seko et al., 2000; Braun et al., 2003; Cao et al., 2006; Mao et al., 2007).

MacDonald et al. (2002) have carried out an extensive study on the diagnosis of three-dimensional water vapor using slant observations from a GPS network. Within the study, a hypothetical network of ground-based GPS receivers has been simulated. The study points out that it may be feasible to determine the three-dimensional water vapor field at high temporal and spatial resolutions with much higher accuracy than currently known. A significant improvement in predicting precipitation and severe weather should thus be possible. Moreover, GPS tomography, in principle, is expected to show hitherto unpredictable small-scale behavior of the water vapor content (see e.g. Bi et al., 2006; Fadil and Sari, 2006).

1.2 Research review of atmospheric water vapor profiling

Tomography has developed from a medical diagnostics tool, commonly denoted as computer tomography, to become an imaging technique for various applications including geodesy and geophysical investigations of solar-terrestrial processes (see e.g. Hofmann-Wellenhof et al., 2001; Pryse, 2003). Referring to ionospheric tomography, the line integral of electron density, the so-called TEC (Total Electron Content), is measured over a large number of ray paths traversing the ionosphere. This part of the atmosphere extends in various layers from about 50 km to 1000 km above the mean surface of the earth. Those measurements are inverted to produce an image of electron density in ionosphere maps (see e.g. Kunitsyn and Tereshchenko, 2003). Rius et al. (1997); Ruffini et al. (1998a) successfully improved the technique of ionospheric stochastic GPS tomography and applied the method to calibrate radar altimeters (see also Flores, 1999).

In recent years, communication and global navigation satellite systems (such as GPS) have been exploited via space-based radio occultation or limb sounding methods to obtain profiles of atmospheric parameters: refractivity, dry and wet temperature, pressure field and specific humidity in the earth's neutral atmosphere. Furthermore, horizontal wind speed and information on the gravity waves propagating through the atmosphere and mesosphere and the electron density in the ionosphere can be detected and investigated on a global scale. First theoretical and practical studies were carried out at the Jet Propulsion Laboratory JPL, Pasadena (Yunck et al., 1988; Melbourne et al., 1994; Kursinski et al., 1995, 2000; Poli et al., 2003; de la Torre Juárez and Nilsson, 2003). The University Corporation for Atmospheric Research, Boulder, Colorado, and partner organizations investigated preliminary results (Yuan et al., 1993; Ware et al., 1996; Sokolovskiy, 2001). They intend also to assimilate this data into numerical weather prediction models (see e.g. Zou et al., 1995; Kuo et al., 2000; Poli et al., 2002; Gorbunov and Kornblueh, 2003; Healy et al., 2005; Cucurull et al., 2006; Healy and Thépaut, 2006; Huang et al., 2007).

In cooperation with the JPL, the Geoforschungs Zentrum Potsdam GFZ joined the research community (Wickert et al., 2001; Liou et al., 2005; Heise et al., 2006) as well as the Institute for Atmospheric Physics, Moscow, in collaboration with the Max Planck Institute for Meteorology, Hamburg, are focusing on the reconstruction of the most critical, lowest part of the troposphere (see e.g. Gorbunov and Gurvich, 1998; Gorbunov and Kornblueh, 2001). Reigber et al. (2005) gives a critical overview of the successful results and various applications of the GPS occultation technique. The actual constellation allows to generate profiles with a vertical resolution of several hundred meters to a kilometer and an average horizontal spacing of 50 km twice a day. Without additional data interpretation the result suffers from the inherent horizontal averaging because an isotropic ionosphere without gravity waves activity and horizontal gradients does not exist (see e.g. Budden, 1985; Davies and Rush, 1985; Yeh and Raymund, 1991; Belloul and Hauchecorne, 1997; Leitinger et al., 1997; Ahmad and Tyler, 1999; Kunitsyn and Tereshchenko, 2003; Abdullah et al., 2007).

Although the concept of atmospheric profiling via radio occultation is quite simple, attention must be paid to separate the numerous factors that can affect the occulted signal. These include motion of the satellites, clock drifts, relativistic effects, oblateness of the earth, separation of the ionosphere and the neutral atmosphere and contribution of the upper atmosphere, where sensitivity of the GPS signal is weak (see e.g. Hardy et al., 1994; Feng and Herman, 1999; Rieder and Kirchengast, 2001; Hajj et al., 2002; Syndergaard, 2002; Yunck and Hajj, 2005). Furthermore, water vapor limits the accuracy of temperature and refractivity recovery below 5 to 8 km AMSL because of uncertainty in the moisture, multipath and receiver tracking error effects (see e.g. Gorbunov, 2002; Ao et al., 2003; Jensen et al., 2003; Sokolovskiy, 2003; Beyerle et al., 2004; Kuo et al., 2004; Vespe et al., 2004). Theoretical temperature accuracy is better than 0.5 °C at the tropopause, degrading to about 1 °C at 40 km altitude (Ware et al., 1996; Rocken et al., 1997a; Steiner et al., 1999).

The sensitivity of atmospheric refractivity to water vapor pressure, however, means that refractivity profiles can in principle yield information on the atmospheric humidity distribution. For this, independent information on the temperature and pressure distribution from numerical weather prediction models or independent observational data is necessary (Businger et al., 1996; Rieder and Kirchengast, 2001). Foelsche and Kirchengast (2001) successfully combined the radio occultation data with ground-based GPS zenith wet and slant wet delays by a two-dimensional, height-resolving tomographic imaging technique.

Several independent approaches have been pursued in order to determine the three-dimensional structure of the tropospheric water vapor using the ground-based GPS tomographic method: The tomographic software called LOTTOS (Local Tropospheric Tomographic Software) has been developed within a Ph.D. thesis at the Universitat Politècnica de Catalunya (Flores, 1999). Based on the ionospheric stochastic approach (see e.g. Ruffini et al., 1998b; Flores, 1999), the software uses wet slant delays as input. Various simulations and some real-data comparisons have been presented by Flores et al. (1999, 2000b, 2001); Elósegui and Davis (2001). In these studies, the range in site elevations from sea level to 2000 m was an essential factor in resolving the water vapor structure. The University Corporation for Atmospheric Research in Boulder, USA, tested the software with their dense GPS network in the Oklahoma-Kansas area.

The software has been improved within another Ph.D. thesis at the Chalmers University of Technology in Sweden (Gradinarsky, 2002) and compared to a wet refractivity Kalman filter technique using simulated and real data (Gradinarsky and Jarlemark, 2002, 2004). In the case of real data, the tomographic inversion is able to capture the general profile trend, but fails to disclose the details of the profile. This is mainly due to the limits in the network geometry and the noise in the slant delays.

An alternative method has been derived by Nilsson et al. (2004); Nilsson (2005); Nilsson and Gradinarsky (2006). This approach uses raw GPS phase data directly to estimate the water vapor distribution. The method was tested in a number of simulations, in which the impact of network size, the possible horizontal and vertical resolutions, the observation noise and the inclusion of additional global navigation satellite systems were studied. The relative errors in the simulations showed that the method will not retrieve the refractivity accurately in the upper troposphere, where the estimated parameter is very low. This is expected because the method is sensitive to the absolute refractivity through slant wet delays. Nevertheless, the refractivities in the lowest layers are retrieved accurately in all simulations, especially when the wet refractivity distribution differs from the average (Nilsson and Gradinarsky, 2006).

A few tomographic approaches were carried out along with meteorological GPS projects in Japan and China. One of their main goals was to monitor rapid changes of water vapor in order to predict Asian Monsoon and other atmospheric turbulences. The Japanese network consists of up to 1000 GPS receivers, distributed over the entire country. Hirahara (2000) successfully demonstrated the capability of GPS as a water vapor sensor for determining the four-dimensional distribution of refractivity based on one way phase residuals and slant delays. Because the observational equations are usually singular, a damped least-squares method, popular in seismic tomography, was applied. Yet, with a two hour temporal resolution, the tomography has shown a too slow variation of wet refractivity compared to reference observations.

In a case study associated with the quasi-stationary Baiu front, Seko et al. (2000) introduced a so-called moving-cell method to analyze a beta-mesoscale precipitation system. This method of wind-induced moving-cell tomography was further developed by Noguchi et al. (2004); Seko et al. (2004b) for local-scale phenomena down to a temporal resolution of 10 min. They worked on the assumption that the whole grid moves at the speed of the horizontal wind velocity. But this method cannot resolve the effect of vertical wind because wind velocity is complex and unpredictable. Song et al. (2006) showed that GPS tomography can improve the initial water vapor field of short-term weather prediction models and enhances the accuracy of numerical weather forecasts.

A research group in Taiwan investigated a parametrized tomographic approach for a 5 by 5 model with 4 km horizontal resolution and eleven layers with a constant thickness of one kilometer (Liou et al., 2003). They introduced surface meteorological measurements and an assumption of zero refractivity at a reasonable height to constrain the tomographic inversion system. This decreased the errors significantly. Bi et al. (2006) evaluated the tomographic method in a relatively flat area with pure GPS observables compared to a combination with vertical constraints from average radiosonde measurements over three days. The analysis with a voxel model with

less than 16 by 22 km^2 horizontal and 800 m vertical grid resolution and an update rate of 1 hour lead to the best results for the retrieved water vapor density in terms of absolute humidity profiles.

French research groups realized a further approach within the framework of the ESCOMPTE program (Cros et al., 2004; Bock et al., 2002a). ESCOMPTE focuses on the retrieval of water vapor distribution using the high-density GPS network in the region of Marseille, southern France, with a vertical extension between sea level and 700 m height. In their tomographic experiment, Champollion et al. (2005) used the standard atmospheric model for mid-latitude as the vertical constraining condition. Although local peaks in the tropospheric water vapor field at 4000 m altitude could not be resolved, the three-dimensional tomographic results with a vertical resolution of 500 m and an update rate of 30 min agreed very well with radiosondes. Bastin et al. (2005) investigated a Mistral/sea breeze event complementing the GPS tomography analysis of the small-scale vertical and horizontal distribution of water vapor by high-resolution numerical simulations.

The software package AWATOS (Atmospheric Water Vapor Tomography Software) is the basis of the present investigations and will be explained in more detail in Chapter 3, pp. 33f. The software is being developed at ETH Zurich (Kruse, 2001; Troller et al., 2002a; Troller, 2004; Troller et al., 2006a,b) and has been tested with data from a measurement campaign in Hawaii. It is further used to determine 40 humidity profiles over Switzerland with data from the Automated GNSS Network AGNES of swisstopo. Recently, it has even been implemented in an operational routine analyzing AGNES data and observations from the Swiss meteorological network ANETZ of MeteoSwiss (Troller et al., 2007a,b).

In different experiments carried out by Shrestha (2003); Hoyle (2005); Skone and Hoyle (2005), wet refractivity profiles were derived from four-dimensional tomographic water vapor prediction model. They were integrated into zenith wet delays using simulations as well as a regional real-time GPS network in southern California, USA, and in southern Alberta, Canada. The zenith wet delays from both, quiet and stormy days, were compared with independent radiosonde measurements. An accuracy of 0.3–1.2 cm was obtained under the condition of a priori vertical profile information from radiosondes.

Braun and Rocken (2003) explored single-frequency GPS tomography. Combined with Raman lidar[1], the four-dimensional presentation of water vapor density was calculated for a 1 km horizontal and 500 m vertical grid together with a time resolution of 30 min. Despite the constraints of the vertical structure in the tomographic column with Raman lidar, they concluded that it is difficult to assess small-scale tomographic results of water vapor using single-frequency GPS networks.

There are further projects based on simulation studies which contribute to the understanding of the influence of additional satellite systems (e.g. GLONASS, Galileo, Low Earth Orbiter) and the assimilation of the tomographic results into numerical weather prediction models.

[1] LIDAR (Light Detection and Ranging) is an optical remote sensing technology that measures properties of scattered light to find the range and/or other information of a distant target. The prevalent method to determine distance to an object or surface is to use laser pulses.
For further information about Raman lidar see e.g. the website of the NASA Raman Lidar Group at http://ramanlidar.gsfc.nasa.gov.

The approaches mainly differ in using different software packages for the GPS postprocessing (GIPSY-OASIS II, GAMIT or the Bernese GPS Software Version 4.2 and 5.0) or different a priori information to stabilize the tomographic analysis. Most methods use double-difference techniques and retrieve wet refractivity profiles based on continuously operating GPS networks. Only a few studies treat campaign-type measurements to test the feasibility of the method in a specific area. Instead, simulations were carried out to produce synthetic observations for such a case.

1.3 Significance of high-resolution GPS tomography

1.3.1 For the research community

GPS meteorology has gained considerable importance as a valuable contribution to weather forecasting. The tomographic approach, however, has not yet been completely established. Especially the small-scale high resolution configuration has not been treated until now. The development in this domain will help to determine and to model the water vapor content and high resolution distribution over catchment areas. This stands in direct causal relationship with hydrological hazard.

A declared mandate of a trans-disciplinary platform at ETH Zurich, called HazNETH (see the website on http://www.hazneth.ethz.ch), is firstly to develop cross-boundary avenues to explore the causal relation between different processes as well as their combined effects on our natural and social environment. Secondly, it is to develop tools capable of handling phenomena acting at different time and spatial scales. In this context, the determination of the atmospheric refractivity or humidity field with high-resolution GPS tomography stands at the beginning of the hydrological cycle.

The next generation of numerical weather prediction models currently being developed, e.g. at the Federal Office of Meteorology and Climatology, MeteoSwiss, will require a precise analysis of the three-dimensional water vapor distribution. Especially, quantitative precipitation forecasts with an explicit simulation of the convection at the kilometer scale are very sensitive to the humidity field. With the planned use of a rapid update cycle and forecasts frequently repeated, water vapor analysis should be available many times a day. In this regard, GPS tomography will become an important source of data for weather models.

Moreover, an extensive examination of the tropospheric effect in GPS measurements will show further aspects in high-precision GPS processing and positioning, in general. The wet refractivity field determined by high-resolution GPS tomography could further lead to a completely anisotropic modeling of the tropospheric error. The evaluation of the coordinate repeatability and the zenith path delays together with different independent measurement technologies will help to interpret the results of a campaign-type GPS network analysis.

At last, this project forms a part of a continuously developing research object which will benefit of the findings for further improvement of the technique of GPS tomography on a regional and local scale (see also Chapter 10).

1.3.2 For practical applications

The investigations into high-resolution GPS tomography will ultimately contribute to a better predictability of natural hazards related to the hydrological cycle. Due to the apparent climate change, this topic is presently also being discussed in national and international politics. It is combined with a debate about the funding of an optimized system for forecasting meteorological hazards (e.g. the project OWARNA, "Optimierung von Warnung und Alarmierung" of the Swiss Federal Office for Civil Protection and the National Emergency Operations Centre). In this context, the Swiss Federal Office of Meteorology and Climatology, MeteoSwiss, activated an Internet platform for public information distribution (MAP D-PHASE[2], see e.g. Arpagaus, 2007), which gives insight into the weather forecasting processes for general use.

The results of this study will help to define criteria for a measurement network (permanent as well as campaign-type) in order to obtain high-quality GPS tomographic results, which then may be introduced into the forecasting processes of numerical weather models.

1.4 Objectives

In order to assess the impact of ground-based GPS water vapor tomography in meteorological forecasting applications, the results must be available within near real-time and must be produced with an accuracy comparable with the one of existing meteorological measurement techniques and numerical weather prediction models. Three superordinate objectives were to be achieved:

1. The feasibility of GPS tomography in a small-scale and Alpine region has to be assessed. Furthermore, the convenience and limitations of campaign-type measurements for tomographic applications have to be addressed.
2. Investigations have to be carried out to obtain water vapor fields with a comparable spatial and temporal resolution to the current numerical weather model. The results have to be statistically analyzed and validated with independent measurement techniques.
3. The most important aspects in terms of near real-time processing in view of supporting weather forecasting models will be treated. The developed algorithms and the new data will be analyzed and compared with the best possible, high-accuracy and post-processed solutions.

[2] D-PHASE stands for Demonstration of Probabilistic Hydrological and Atmospheric Simulation of flood Events in the Alpine region. MAP D-PHASE aims at demonstrating progress and improved understanding of processes related to heavy orographic precipitation due to the Mesoscale Alpine Program (MAP). As a Forecast Demonstration Project (FDP) of the World Weather Research Program this is being realized in true forecast mode and including all components of an end-to-end forecasting system and with a predefined evaluation protocol.
For actual information on the status of MAP D-PHASE see the website at http://www.map.-meteoswiss.ch.

Based on these problem specifications, the work was divided into five tasks each with an own list of objectives to be attained:

- First of all, two field campaigns have to be carried out in an Alpine region with high potential of hydrological hazard. The network geometry of the GPS stations as well as of the additional meteorological measurement systems have to be simulated and optimized previously to the tomographic analysis and to guarantee the acquisition of high quality observations. Furthermore, independent observations, i.e. weather balloon soundings and solar spectrometry, have to be recorded and prepared for comparison and validation purposes.
- The second step and most important in GPS meteorological studies is the estimation of the tropospheric parameters (tropospheric induced path delays and phase residuals) from GPS observations with high accuracy. Problems in terms of a priori models and corresponding mapping functions have to be addressed. Furthermore, strategies to decorrelate zenith path delays and station heights have to be investigated. The results will be validated by comparing the time series with independent measurement techniques and the current numerical weather model COSMO-7 of MeteoSwiss.
- The third task is the determination of the four-dimensional distribution of tropospheric water vapor using campaign-type GPS tomography in a region with rugged topography. The results will be appraised in view of hydrological purposes. The basic requirements as well as the preparation of the necessary data sets shall be discussed. The accuracy and feasibility of the method will be investigated by systematic comparison and validation with independent data.
- In a forth step, existing algorithms for double-difference GPS tomography will be further developed to meet the requirements of spatial and temporal high resolution. The specifications of the operating and scheduled numerical weather prediction models in Switzerland are used as a guideline. The current weather models are based on a grid with 7 km or 2 km horizontal resolution with more than 40 layers in the spatial domain. Typically, these models have an update rate of one hour. Analyzing selected high-resolution configurations, the convenience and limitations of GPS tomography in view of hydrological hazard assessment in an Alpine region will be assessed.
- The fifth task includes investigations in terms of near real-time applications and the assessment of the potential of forecast characteristics of local high-resolution GPS tomography. The GPS data from two measurement campaigns in the canton of Valais, Switzerland, is processed offline but in near real-time quality. A limiting factor in processing GPS data in near real-time is the availability of precise satellite orbits and clocks. Products available in real-time, e.g., broadcast ephemerides and ultra-rapid orbits with a predicted part of maximum 24 hours provided by the International GNSS Service, are introduced into the GPS data analysis. These results are to be evaluated and compared with the results from processing final products with highest accuracy.

Based on the findings gained during the work, recommendations for future investigations in the domain of high-resolution ground-based water vapor GPS tomography will be collected and formulated in the outlook-chapter at the end.

1.5 Structure

In Chapter 2, basic equations, formulas and additional software packages (for the GPS processing as well as for the processing of meteorological data sets) are described. Chapter 3 explains in detail the procedures within the tomographic software package AWATOS, the assessment of the error budget as well as the simulation and network analysis tools.

Chapter 4 gives an overview of two dedicated field campaigns carried out in the canton of Valais, Switzerland, in July and October 2005. The description of the GPS station networks can be found in Appendix B. Chapter 5 illustrates the preprocessing of all different kind of data sets (GPS observations, ground meteorological measurements and radiosondes) with intermediate results for the further tomographic analysis. The treatment and analysis of the data of the numerical weather model COSMO-7 is explained in Chapter 6.

The principal enhancements of the tomographic software package AWATOS are listed in Chapter 7 with special emphasis on the setup of the analysis study. Chapter 8 summarizes the results. The objectives achieved in this work are concluded in Chapter 9. An outlook for further studies and recommendations for future investigations in GPS tomography is given in Chapter 10.

Chapter 2

Theoretical background of GPS meteorology

In Sec. 2.1 and Sec. 2.2, the treatment of the parameter atmospheric water vapor and its influence on radio waves are described. Moisture derived from refractivity is related more directly to specific rather than to relative humidity because refractivity essentially represents a molecule counter (see e.g. Kursinski and Hajj, 2001). The modeling of the path delays is treated in Sec. 2.3.

Sec. 2.4 presents the basics of the Global Positioning System (GPS) in terms of meteorological applications. At the end of the chapter, in Sec. 2.5, the software package COMEDIE is explained. It will be used for processing meteorological data and for interpolation of tropospheric path delays based on a collocation approach.

2.1 Atmospheric water vapor

Atmospheric water vapor is a precondition of rainfall. The total content of water vapor is limited by its temperature. Within the atmosphere, the temperature of water vapor is equal to the air temperature (see Grebner, 1996).

Humidity, usually measured as non-conservative relative humidity, is converted to the temperature independent value of water vapor pressure. The partial water vapor pressure e_p is reconstructed on the basis of the two meteorological parameters relative humidity H_r and air temperature T using the following empirical formulas (see also Berg, 1948; Beutler et al., 1989b; Richner et al., 1996, 1999; Herschke, 2002; Troller, 2004; Stoew and Elgered, 2005):

$$\begin{aligned} e_p &= \frac{H_r}{100} \cdot e_s(T) \\ &= \frac{H_r}{100} \cdot 6.1078 \cdot 10^{\frac{7.5 \cdot T}{T+237.3}} && \text{(2.1a)} \\ &= \frac{H_r}{100} \cdot e^{-37.2465+0.213166 \cdot (T+273)-0.000256908 \cdot (T+273)^2} && \text{(2.1b)} \end{aligned}$$

Another approximation for the behavior of the partial water vapor pressure in relation to the dew point temperature T_d is the following formula (see also e.g. Berg, 1948; Murray, 1967; Zuev and Komarov, 1987):

$$\begin{aligned} e_p &= e_s(T_d) \\ &= 6.112 \cdot e^{\frac{17.67 \cdot T_d}{T_d+243.5}} && \text{(2.1c)} \end{aligned}$$

e_p partial water vapor pressure in hPa
e_s saturated water vapor pressure in hPa
H_r relative humidity in %
T air temperature in °C
T_d dew point temperature in °C (see also Eq. 2.2)

The surface dew point temperature is a good indicator for integrated atmospheric moisture (see e.g. Smith, 1966; Lowry and Glahn, 1969). It was investigated in the comparison and validation part of this work. Dew point temperature can be approximated by the simple formula:

$$T_d = T - \frac{100 - H_r}{5} \tag{2.2}$$

Eqs. (2.1b) and (2.1c) show the exponential behavior of the parameter water vapor pressure e_p. In practical applications, Eq. (2.1a) was utilized to convert the meteorological measurement data and the data from the numerical weather model into water vapor pressure for further use.

Figs. 2.1(a) and 2.1(b) show an example of a typical temperature and partial water vapor profile measured by a radiosonde launched at the station Susten on a sunny day during the field campaign in October 2005. The altitude of the tropopause, here at about 12 km AMSL, can clearly be identified at the end of the decreasing temperature with an almost constant gradient. After this point, the temperature keeps stable or even increases again. Another important piece of information from the profiles is that the water vapor pressure above 8 km is nearly zero.

The vertical distribution of the atmospheric water vapor pressure between the earth's surface and about 8 km altitude is very variable over the time, whereas, for example, the air pressure (as shown e.g. in Fig. 2.1(c)) is a much more stable quantity and is, therefore, more easily predictable.

2.2 Radio wave refractivity

The propagation of radio waves through the earth's neutral atmosphere and ionosphere are accompanied by random phase and amplitude variations. On the one hand, this has an adverse effect on the performance of communication and navigation systems. On the other hand, it provides a mean of obtaining information about random disturbances in the medium of radio wave propagation (see e.g. Yeh and Liu, 1972; Gossard, 1978; de Munck and Spoelstra, 1992; Kolesnik et al., 2002).

In dry air, refractivity is proportional to air mass in the propagation path and is therefore predictable from atmospheric surface pressure (see e.g. Trenberth and Guillemot, 1994). Furthermore, refractivity can be separated into non-dispersive and dispersive components. The dispersive component depends on molecular resonances in the vicinity of the propagation carrier frequency. Since GPS carrier frequencies are far away from molecular resonances, their influence can be ignored (Solheim et al., 1999). However, refractivity in cloud droplet, rain, snow and haze is due to displacement of charge in the dielectric medium and to scattering. Polar atmospheric

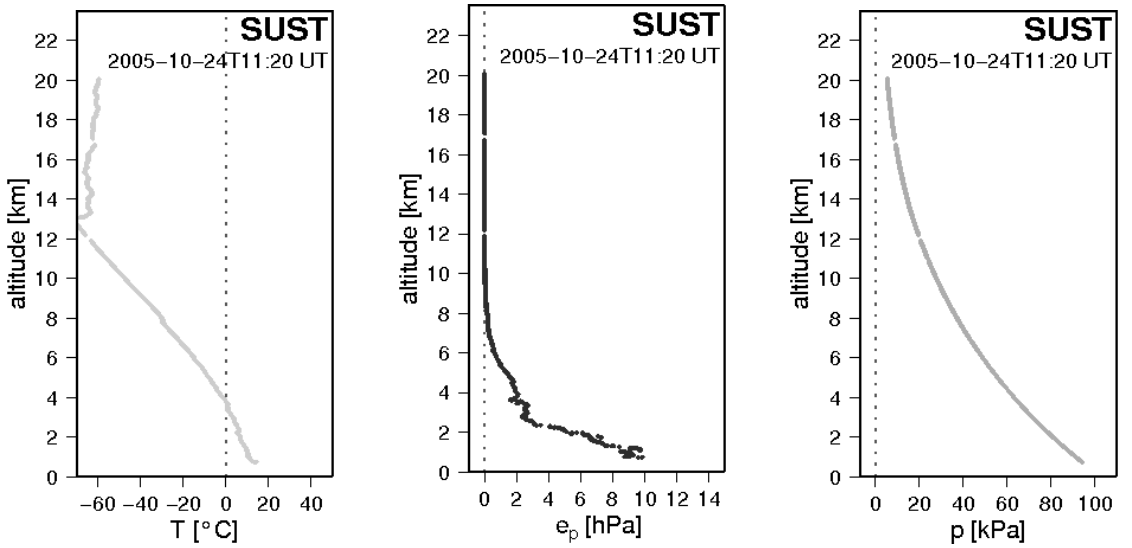

(a) Characteristic air temperature profile measured by a radiosonde.

(b) Typical profile of the vertical trend of partial water vapor pressure on a sunny day.

(c) Profile of the meteorological parameter air pressure in the earth's atmosphere.

Fig. 2.1: Profiles of temperature T, partial water vapor pressure e_p and air pressure p next to the non-permanent GPS station SUST in Susten at 678 m AMSL in the main valley of the canton of Valais, Switzerland. The radiosonde was launched during the measurement campaign in autumn 2005 on October 24, 2005, at 11:20 UT.

gases and hydrometeors contribute to non-dispersive atmospheric refractivity (see e.g. Huang and Wang, 1992).

The characterization of this phenomenon is described in Solheim et al. (1999): In atmospheric gases, the refractivity is due to displacement of the electron cloud of the gaseous constituents and, additionally, to alignment of electrically and magnetically polar molecules with the propagated electric and magnetic fields. Significant electrically polar molecules include water vapor, some oxides of nitrogen and many chlorine and organic compounds. With the exception of water vapor, the partial pressure of significant polar molecules is essentially constant in the atmosphere. The only significant atmospheric molecule with a magnetic moment is oxygen.

The calculation of the total radio wave refractivity N is an important topic of research at least since the first remote sensing measurement systems have been established. Based on a general formula published by Essen and Froome (1951) using the three meteorological parameters air pressure p, air temperature T and partial water vapor pressure e_p (see Eq. 2.3), the empirically determined constants k_1, k_2 and k_3 have been permanently improved (see e.g. Smith and Weintraub, 1953; Tatarskii, 1971; Thayer, 1974; Hill et al., 1982; Hartmann and Leitinger, 1984; Bevis et al., 1994).

$$\begin{aligned} N &= (n-1) \cdot 10^6 \\ &= k_1 \cdot \frac{p_{dry}}{T} \cdot Z_{dry}^{-1} + k_2 \cdot \frac{e_p}{T} \cdot Z_{wet}^{-1} + k_3 \cdot \frac{e_p}{T^2} \cdot Z_{wet}^{-1} \end{aligned} \tag{2.3}$$

N	total radio wave refractivity in ppm
n	refractive index
p_{dry}	partial pressure of all dry gases in hPa ($p_{dry} = p - e_p$)
p	atmospheric pressure in hPa
e_p	partial water vapor pressure in hPa
T	absolute air temperature in K (0 °C = 273.16 K)
k_1, k_2	empirically determined physical constants in $\mathrm{KhPa^{-1}}$
k_3	empirically determined physical constant in $\mathrm{K^2hPa^{-1}}$
Z_{dry}, Z_{wet}	compressibility of dry air and water vapor

The inverses of the compressibility factors Z_{dry} and Z_{wet} are investigated and evaluated by Owens (1967); Spilker (1996). In the following, these factors are set to 1, thus all correction terms are accumulated in the parameters k_1, k_2 and k_3.

The refractive index n of a medium is defined as the ratio of the phase velocity of a wave phenomenon such as light or sound in a reference medium, e.g. in the vacuum, to the phase velocity in the medium itself. The third term in Eq. (2.3) results from the dipole moment of water vapor and is about 20 times larger than the second term (Solheim et al., 1999).

So far, the coefficients for microwave refractivity proposed by Thayer (1974) have been used by many authors, particularly in the field of geodesy. They are based on an extrapolation from optical measurements to the infrared and radio regions. The temperature effects dominate the variations in optical refractive index, while for radio frequencies humidity is more important (see also McBean and Elliott, 1981; Hill et al., 1982). For infinite wavelength, the final form of the weighted mean formula for the non-dispersive radio wave refractivity N for air with 0.0375% (375 ppm) content of carbon dioxide[3] after Rueeger (2002) is:

$$N = N_{total} = \underbrace{77.6890 \cdot \frac{p - e_p}{T}}_{N_{dry}} + \underbrace{71.2952 \cdot \frac{e_p}{T} + 375463 \cdot \frac{e_p}{T^2}}_{N_{wet}} \tag{2.4}$$

The dry component (N_{dry}) is due to the "dry" gases and the induced dipole moment of the water molecules in the atmosphere, whereas the wet component (N_{wet}) is related to the wet or non-hydrostatic part (the permanent dipole moment of the water molecule) of the atmosphere (see also Mendes, 1999; Stoew and Elgered, 2004).

The change in the zenith hydrostatic delay (see Sec. 2.3), caused by the updated value of the CO_2 content in k_1, is only 0.1 mm (Elgered and van der Marel, 2005). The largest uncertainty is in k_3 and is approximately 1 % (after Stoew and Elgered, 2004). Applying the relations in Eq. (2.4) to the observation data of the radiosonde shown in Fig. 2.1, the refractivity profiles in Fig. 2.2 can be generated.

The high correlation of the dry refractivity profile to the pressure data (see Fig. 2.1(c) and Kleijer, 2004) is obvious, whereas the wet refractivity reproduces the water vapor pressure characteristics in those conditions (see also Nilsson, 2005). The total refractivity is strongly dominated by the dry part including the higher

[3] For the global trend of the CO_2 concentration in the atmosphere, see e.g. Sturm et al. (2005); Solomon et al. (2007) and the website at http://www.esrl.noaa.gov/gmd/ccgg.

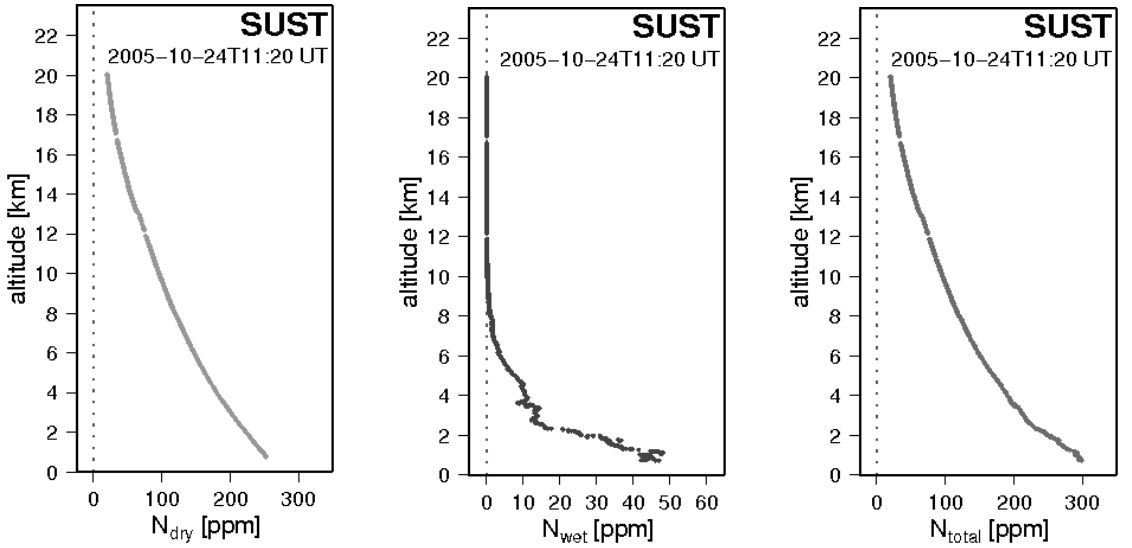

(a) Typical profile of the dry component of the radio wave refractivity.

(b) Wet refractivity profile.

(c) The total refractivity profile is the sum of the dry and the wet refractivity part.

Fig. 2.2: Profiles of dry, wet and total radio wave refractivity converted from balloon sounding observations taken at station SUST (compare to the profiles of the observed meteorological data temperature, humidity and air pressure in Fig. 2.1) according to Eq. (2.4).

frequency variations of the wet part in the lowest troposphere. The altitude of the tropopause can be recognized by a bend in the profiles of the dry and total refractivity at about 13 km.

Regarding the data of the numerical weather model COSMO (see Chapter 6) used for validation and comparison purpose, there is an additional meteorological parameter available (the specific humidity q_v) which is converted into wet refractivity (after Troller, 2004):

$$\begin{aligned} N_{wet}(q_v) &= Q \cdot 10^6 \cdot q_v \cdot \frac{\rho_{dry}}{\rho_{water}} \\ &= Q \cdot 10^6 \cdot q_v \cdot \frac{p}{R_{dry} \cdot T_{virt}} \cdot \frac{1}{\rho_{water}} \end{aligned} \tag{2.5}$$

$N_{wet}(q_v)$	wet component of the radio wave refractivity from q_v in ppm
Q	annual correction model (see Eq. 2.6)
q_v	specific humidity in kgkg^{-1}
ρ_{dry}	mass density of air in kgm^{-3}
ρ_{water}	mass density of water in kgm^{-3} (averaged to 1 000)
p	atmospheric pressure in Pa
R_{dry}	specific gas constant for dry air (287.05 Jkg^{-1}K^{-1})
T_{virt}	virtual temperature $= T \cdot \left(1 + 0.378 \cdot \frac{e_p}{p}\right)$ in °C
T	air temperature in °C
e_p	partial water vapor pressure in Pa

The annual model Q used in Eq. (2.5) is evaluated and published e.g. in Emardson and Derks (2000); Troller (2004); Nilsson (2005). The model is a function depending on the station latitude and the day of year:

$$Q = a_0 + a_1 \cdot \Theta + a_2 \cdot sin\left(2 \cdot \pi \cdot \frac{t_{doy}}{365}\right) + a_3 \cdot cos\left(2 \cdot \pi \cdot \frac{t_{doy}}{365}\right) \tag{2.6}$$

with

$$a_0 = 5.882, \quad a_1 = 0.01113, \quad a_2 = 0.064, \quad a_3 = 0.127$$

Q	annual model
Θ	latitude of the station in degree
t_{doy}	time in day of year

The development of the annual model Q for a station within the project area in the canton of Valais, Switzerland, is shown in Fig. 2.3. It can be concluded that the mean value of Q is about 6.4 for Central Europe with an annual variation of ± 0.1. The higher the stations latitude, the larger the mean value of Q. The annual model is commonly used to convert the non-hydrostatic or wet path delay into integrated precipitable water vapor (see also Emardson and Derks, 2000; Troller, 2004).

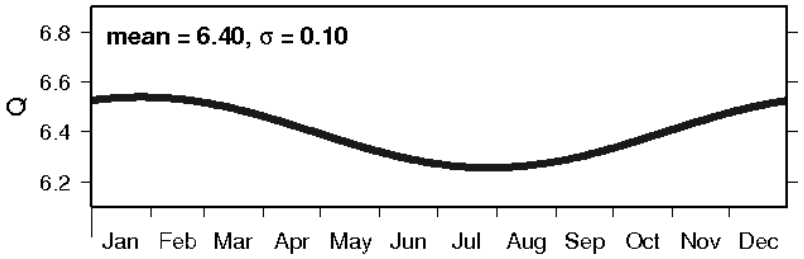

Fig. 2.3: Function of the annual model Q (see Eq. 2.6) for the station at Susten at 46.3 ° North within the project area in the canton of Valais, Switzerland.

The values of $N_{wet}(q_v)$ have only been investigated for comparison purpose with the wet refractivity N_{wet} derived from the relative humidity data of the postprocessed numerical weather prediction model COSMO. The results show a sufficient

agreement which confirms the exclusive use of N_{wet} from partial water vapor pressure (see Eq. 2.4) for the present investigations. Examples of profiles from COSMO are discussed in Sec. 6.4.1, pp. 78f. (see also Doms and Schättler, 2002).

2.3 Refraction and path delay modeling

2.3.1 Definition

Refraction is described by Snell's law, which states that the angle of incidence is related to the angle of refraction (see e.g. Berg, 1948; Brunner, 1992; Kleijer, 2004). Refractive delays of radio waves are induced by the earth's ionosphere and the neutral atmosphere. Refraction in the ionosphere is dispersive, that is, the refractive index is a function of the operating frequency (see e.g. Budden, 1985; Spoelstra, 1992; Klobuchar, 1996). It can be measured and corrected for the first-order ionospheric range and range-rate effects by using dual-frequency receivers (see e.g. King et al., 1987; Brunner and Gu, 1991; Bassiri and Hajj, 1993; Klobuchar, 1996; Hofmann-Wellenhof et al., 2001; Jakowski et al., 2002).

Tropospheric refraction of radio waves is the path delay caused by refractivity of gases, hydrometeors and other particulates, depending on their nonconducting or dielectric constant and on their concentration, as well as on the forward scattering from hydrometeors and other particulates in the neutral (i.e. the non-ionized) part of the earth's atmosphere (see e.g. Solheim et al., 1999; Hofmann-Wellenhof et al., 2001). These delays must be properly characterized to achieve the highest accuracy in surveying and atmospheric sensing using GPS signals.

Unmodeled delays can induce horizontal and vertical errors of several centimeters (see e.g. Solheim et al., 1999). Using microwaves emitted by satellites for positioning purpose, the refractivity induced tropospheric path delay variations cause a positioning error mainly in the height component (see e.g. van Dam et al., 1994; Dodson et al., 1996; Kaniuth et al., 1998; Mendes, 1999; van der Hoeven et al., 2002). For an elevation cutoff angle of 20 ° it is approximately two to three times larger than the path delay error itself (Geiger, 1987; Beutler et al., 1989b; Herschke, 2002; Tregoning and Herring, 2006).

To a first order, the station height bias Δh induced by a relative troposphere error in zenith direction $\Delta\mathrm{ZPD}_{rel}$ with respect to the maximum zenith angle z_{max} of the observation scenario may be computed as (see e.g. Beutler et al., 1989b; Dach et al., 2007):

$$\Delta h \approx \frac{\Delta\mathrm{ZPD}_{rel}}{cos(z_{max})} \tag{2.7}$$

For a relative troposphere bias of only 1 cm and for an elevation cutoff angle of 3 ° Eq. (2.7) leads to an approximated error in the estimated height component of 19 cm. According to Beutler et al. (1989a) the impact of an absolute troposphere error $\Delta\mathrm{ZPD}_{abs}$ on the error of the baseline length Δl with respect to the earth's radius R can be written as:

$$\frac{\Delta l}{l} \approx \frac{\Delta \mathrm{ZPD}_{abs}}{R \cdot cos(z_{max})} \tag{2.8}$$

Eq. (2.8) implies that an absolute troposphere bias of 10 cm induces a scale bias of 0.05 ppm for an elevation cutoff angle of 20 ° and of 0.3 ppm for a cutoff angle of 3 ° (see Beutler et al., 1989a; Janes et al., 1991; Dach et al., 2007).

2.3.2 The Saastamoinen formula

One of the most common models to compute the total tropospheric refraction using the meteorological parameters air pressure, temperature and water vapor pressure from surface measurements is the Saastamoinen formula or refined Saastamoinen model Eq. (2.9) (see Saastamoinen, 1972, 1973c; Geiger, 1987). It is based on the laws associated with an ideal gas.

$$\Delta\rho = \underbrace{10^{-6} \cdot \frac{k_1 \cdot R_d}{g_m}}_{\approx\ 0.002277} \cdot \frac{1}{\cos(z)} \cdot \left[p_1 + e_{p,1} \cdot \left(\frac{1255}{T_1} + 0.05 \right) - B \cdot \tan^2(z) \right] + \delta_R \tag{2.9}$$

$\Delta\rho$	tropospheric refraction or path delay along line of sight in m
z	zenith angle of the satellite in rad
R_d	gas constant of dry air in $\mathrm{Jkg^{-1}K^{-1}}$
g_m	mean gravitational acceleration in $\mathrm{ms^{-2}}$
p_1	atmospheric pressure at start point in hPa
$e_{p,1}$	partial water vapor pressure at start point in hPa
T_1	air temperature at start point in K

B and δ_R are correction terms related to the observer height and the zenith angle z of the satellite (see the tabulated terms in e.g. Saastamoinen, 1973c; Hofmann-Wellenhof et al., 2001; Troller, 2004). The model Eq. (2.9) implicitly contains a zenith dependent mapping function (see Baueršíma, 1983).

The largest atmospheric delay results from dry or "hydrostatic" constituents (gases excluding water vapor). The hydrostatic delay is directly proportional to atmospheric pressure and can be accurately modeled (see e.g. Thayer, 1974; Herring, 1992; Kleijer, 2004). Although the delay caused by the wet portion is relatively small, it cannot be determined accurately from surface measurements of water vapor because surface measurements do not yield good estimates of the columnar water vapor content. This is due primarily to the inhomogeneous distribution of water vapor in the troposphere (Remondi, 1984). After Troller (2004), $\Delta\rho$ may be decomposed into a dry and a wet component (see Eq. 2.13). For the tomographic procedure described in this work, there is no differentiation into hydrostatic and non-hydrostatic, but only into dry and wet path delay.

According to the ideal gas law the total air pressure p can be divided into partial pressures of dry air (p_{dry}) and water vapor pressure (e_p). It can be written:

$$p_{dry} = p - e_p \tag{2.10}$$

Thus, the partial densities of air are expressed as (see e.g. Saastamoinen, 1972, 1973a,b):

$$\rho_{dry} = \frac{p - e_p}{R_{dry} \cdot T} \quad \text{and} \quad \rho_{wet} = \frac{e_p}{R_{wet} \cdot T} \tag{2.11}$$

R_{dry} specific gas constant for dry air (287.05 $\mathrm{Jkg^{-1}K^{-1}}$)
R_{wet} specific gas constant for water vapor (461.50 $\mathrm{Jkg^{-1}K^{-1}}$)

The dry part of the path delay is then obtained by integrating the partial density of dry air along the ray path $(r - r_1)$ between point P and point P_1 considering the vertical distribution of all three meteorological parameters in the atmosphere (see e.g. Fig. 2.1). Eq. (2.12) shows the mathematical formulation of the standard profiles (see Saastamoinen, 1973a,b,c):

$$T = T_1 + \beta \cdot (r - r_1) \tag{2.12a}$$

$$p = p_1 \cdot \left(\frac{T}{T_1}\right)^{-\frac{g}{R_{dry} \cdot \beta}} \tag{2.12b}$$

$$e_p = e_{p,1} \cdot \left(\frac{T}{T_1}\right)^{-\frac{\nu \cdot g}{R_{dry} \cdot \beta}} \tag{2.12c}$$

$(r - r_1)$ line element between point P and P_1
β vertical gradient of temperature (assumed to be constant)
g acceleration due to local gravity
ν numerical coefficient determined from local observations

Considering these standard profiles, the dry delay $\Delta^{dry}\rho$ is calculated and the wet part $\Delta^{wet}\rho$ is the supplement to the total path delay $\Delta\rho$ (see Eq. 2.9 and Saastamoinen, 1973a,b,c; Troller, 2004):

$$\Delta^{dry}\rho = \frac{0.002277}{\cos(z)} \cdot \Big(\underbrace{p_1 - 0.155471 \cdot e_{p,1}}_{\int_{r_1}^{r} \rho_{dry}\, dr} - B \cdot \tan^2(z) \Big) + \delta_R \tag{2.13a}$$

and

$$\Delta^{wet}\rho = \frac{0.002277}{\cos(z)} \cdot \left(\frac{1255}{T_1} + 0.205471 \right) \cdot e_{p,1} \tag{2.13b}$$

Due to the relatively small influence of the parameter $e_{p,1}$ for the dry part, in contrast to the influence on the wet part, the dry delay can be modeled with very high accuracy using only surface meteorological observations. This is realized in the definition of the hydrostatic delay (see e.g. Thayer, 1974; Tregoning and Herring, 2006). If the barometric pressure is known to $\pm 1\,\mathrm{hPa}$, the zenith hydrostatic delay

can be estimated with an accuracy of 2.3 mm or better using the Saastamoinen model (Bevis et al., 1996; Mendes, 1999; Solheim et al., 1999). The zenith non-hydrostatic component is much more difficult to predict from surface meteorological data, and the best models show values of root mean square scatter about the mean of a few centimeters (Mendes, 1999).

Usually, when estimation water vapor with GPS, the parameters temperature and air pressure are assumed to be known from ground measurements in the surroundings of the GPS antenna. This means that any error in the estimated zenith path path delay (i.e. zenith angle $z = 0°$) can be found in the derived precipitable water vapor with its full influence (see e.g. Bevis et al., 1994; Fang et al., 1998; Dach and Dietrich, 2000). A zenith path delay of 1 mm corresponds to about 0.15 mm of precipitable water vapor for mean atmospheric conditions (Dach and Dietrich, 2000).

2.3.3 Integrating tropospheric refractivity

The GPS signal from the satellite to the ground receiver is delayed by the variation of the refraction index due to temperature, pressure and water content. The troposphere is a non-dispersive medium for radio waves up to frequencies of about 10 to 15 GHz (see e.g. LeVine, 1972; Baueršíma, 1983; Mendes, 1999; Klobuchar and Kunches, 2003). Tropospheric refraction is thus identical for both GNSS carriers, f_1 and f_2, and for both phase and code measurements (see Eq. 2.19, p. 25).

The tropospheric slant path delay $\Delta\rho_p^r$ between station p and satellite r is defined by the following integral:

$$\Delta\rho_p^r = \int_p^r (n-1)\ ds = 10^{-6} \cdot \int_p^r N\ ds \tag{2.14}$$

$\Delta\rho_p^r$	slant path delay between station p and satellite r in m
n	location dependent refractive index
N	location dependent tropospheric or total refractivity in ppm

The unit of refractivity (ppm) is equivalent to mm of electrical path delay per km of geometric distance. The integration has to be performed along the actual signal path through the atmosphere. According to Eq. (2.4), it is possible to separate $N(s)$ into a dry and a wet component.

In case of vertical refractivity profiles, as e.g. for the data of the numerical weather model COSMO, the radio soundings, or the resulting profiles from the tomographic analysis, and the integrated path delays in zenith direction (ZDD for the dry, ZWD for the wet and ZTD for the total zenith path delay) can be calculated as the summation along the profile considering the model levels or observation heights. Additionally, an estimated value according to the separated Saastamoinen formula Eq. (2.13) for the top end of the profile in vertical direction is introduced (see also Vedel et al., 2001). It has to be considered that a small but negligible error due to

a non-standard atmospheric behavior at this height will be taken into account.

$$\mathrm{ZDD} = 10^{-6} \cdot \sum_{i=2}^{l} (h_i - h_{i-1}) \cdot \frac{N_{dry,i-1} + N_{dry,i}}{2} + \underbrace{0.002277 \cdot (p_l - 0.155471 \cdot e_{p,l}) + \delta_R}_{\text{see Eq. (2.13a)}} \tag{2.15a}$$

$$\mathrm{ZWD} = 10^{-6} \cdot \sum_{i=2}^{l} (h_i - h_{i-1}) \cdot \frac{N_{wet,i-1} + N_{wet,i}}{2} + \underbrace{0.002277 \cdot \left(\frac{1255}{T_l} + 0.205471 \right) \cdot e_{p,l}}_{\text{see Eq. (2.13b)}} \tag{2.15b}$$

The zenith total delay can be written as

$$\mathrm{ZTD} = \mathrm{ZDD} + \mathrm{ZWD} \tag{2.15c}$$

l	total number of vertical levels of the model
h_i	altitude of level i in m
$N_{dry,i}, N_{wet,i}$	dry and wet refractivity values available for level i in ppm
$p_l, T_l, e_{p,l}$	meteorological parameters at top level l in hPa, K and hPa
δ_R	correction term at top level l according to Eq. (2.9)

The correction term δ_R in Eq. (2.15) is negligible because the zenith angle is 0 °. The additional Saastamoinen term for the zenith dry delay (Eq. 2.15a) at the top end of the COSMO profiles (i.e. 22.5 km) is about 10 cm. The term for the zenith wet delay (Eq. 2.15b) is less than 0.002 mm.

All parameters of the tomographic refractivity profiles are related to layers with specific thickness (i.e. $\Delta h_i \cdot N_i$ in the case of layer i) and not to levels as they are in the data of the numerical weather model COSMO. Furthermore, there is no need for adding the Saastamoinen term to the ZWD integrating the wet refractivity profiles due to the fact that there is supposedly no wet refractivity above the top border of the selected voxel model, e.g above 12.5 km altitude (see also the discussion on voxel model design in Sec. 7.2.1, pp. 93f.).

If the vertically integrated water vapor overlying a receiver is stated in terms of precipitable water (PW), that is, as the length of an equivalent column of liquid water, then this quantity can be related to the ZWD at the receiver by Eq. (2.16a) (see e.g. Hogg et al., 1981; Askne and Nordius, 1987; Bevis et al., 1994; Duan et al., 1996; Davies and Watson, 1998; Guerova, 2003b; Kleijer, 2004):

$$\mathrm{PW} = \Pi \cdot \mathrm{ZWD} \tag{2.16a}$$

with

$$\Pi = \frac{10^6}{\rho \cdot R_v \left(\frac{k_3}{T_m(e_p, T)} + k_2'(k_1, k_2) \right)} \tag{2.16b}$$

PW	integrated precipitable water vapor in m
ZWD	zenith wet delay in m
ρ	density of liquid water in kgm^{-3}
R_v	specific gas constant for water vapor in Jkg^{-1}K^{-1}
$T_m(e_p, T)$	weighted mean temperature of the atmosphere in K
e_p	partial water vapor pressure in hPa
T	air temperature in K
$k_1, k_2, k_2'(k_1, k_2)$	physical constants in KhPa^{-1} (see Eq. 2.3)
k_3	physical constant in K^{2}hPa^{-1} (see Eq. 2.3)

The major uncertainties in Π result from the uncertainties in the mean temperature of the atmosphere T_m and in the physical constants k_1, k_2 and k_3 (see e.g. Bevis et al., 1994; Ross and Rosenfeld, 1997; Liou et al., 2000a). For the rule of thumb, Π can be approximated by the dimensionless value of 6.4^{-1} (see also the annual model in Fig. 2.3 and the related discussion). In this case, a zenith wet delay of 10 cm is equal to 1.56 cm integrated precipitable water vapor.

2.3.4 Path delay interpolation with COITROPA

For comparison purposes, it is useful to collocate time series of zenith path delays and to interpolate them into any location, e.g. for the data of the numerical weather model COSMO with respect to the station coordinates of the nearest GPS site (see Chapter 6). Therefore, the following exponential collocation approach is used with spatial and temporal gradients implemented in the software package COITROPA. This software performs a least-squares four-dimensional collocation adjustment and interpolation of tropospheric path delays. (see also Herschke, 2002; Troller and Brockmann, 2002; Troller, 2004).

GPS estimated zenith path delays or integrated refractivity profiles from e.g. the numerical weather models are introduced in COITROPA along with associated three-dimensional coordinates and time information. A least-squares collocation adjustment and interpolation are carried out with appropriate functional and stochastic models (after Moritz, 1973; Wirth, 1990). Therefore, COITROPA is able to account for rapid temporal variation of the water vapor and the path delays.

The functional model

Due to a collocation approach, the functional model can be chosen as simple as possible, and unmodeled systematic parts will be assigned to the signal (Troller, 2004; Troller et al., 2006b). On condition of an isothermal atmosphere, the air pressure can be modeled using an exponential approach (see also Fig. 2.1(c)).

Since the main part of the total path delay depends directly on the current air pressure, a similar model is used:

$$\mathrm{ZPD}(x,y,z,t) = \Big[\mathrm{ZPD}_0 + a\cdot(x-x_0) + b\cdot(y-y_0) + c\cdot(t-t_0)\Big]\cdot e^{-\frac{z-z_0}{h_s}} \quad (2.17)$$

$\mathrm{ZPD}(x,y,z,t)$	zenith path delay (dry, wet, or total) in m
ZPD_0	zenith path delay at reference point in m
a, b, c	coefficients for the horizontal and temporal gradients
h_s	scaling height in m

The reference coordinates x_0, y_0 and z_0 and the reference time t_0 are calculated as mean value of all measurement points or referring to mean sea level height. Morland and Mätzler (2007) used a similar exponential relationship for the one dimensional case to normalize time series of GPS derived integrated water vapor to $z_0 = 500\,\mathrm{m}$ altitude. The scaling height h_s has to be determined empirically. It is recommended to take the values of the related meteorological components: For the dry and total path delay the most dominant part is the air pressure profile. Water vapor pressure determines mainly the wet path delay.

An example of initial parameters used for the analysis of the COSMO data, discussed in Chapter 6, are shown in Tab. 6.3 on p. 86. The parameters are based on operating experience and the statistical analysis from the meteorological data processing discussed in Sec. 5.3, Tabs. 5.4 and 5.5 on p. 70.

The stochastic model

The stochastic model is defined by a signal and a noise part. The connection is given by a covariance function (see also Höflinger, 1993; Kruse, 2001; Troller et al., 2006b):

$$\Phi_{i,j} = \frac{\sigma_0^2}{1 + \left[(\frac{x_i - x_j}{\Delta x_0})^2 + (\frac{y_i - y_j}{\Delta y_0})^2 + (\frac{z_i - z_j}{\Delta z_0})^2 + (\frac{t_i - t_j}{\Delta t_0})^2\right]} \quad (2.18)$$

$\Phi_{i,j}$	covariance function between point i and point j
σ_0^2	a priori variance of the signal
$\Delta x_0, \Delta y_0, \Delta z_0$	correlation length of the spatial components
Δt_0	correlation length of the time component

To achieve a high quality of the interpolated path delays, it is important to properly choose the correlation lengths and the variances according to the input and output data.

2.4 The Global Positioning System (GPS)

2.4.1 Introduction to GPS

GPS is a dual-use, satellite-based system that provides accurate positioning, navigation and timing information to users worldwide. Originally developed by the

U.S. Department of Defense as a military system, GPS has become a global utility. Private users and public organizations benefit from this system in many different applications, including aviation, road, marine and rail navigation, telecommunications, emergency response, resource exploration, mining and construction (see e.g. Parkinson and Spilker, 1996b). It is even used for managing risks of financial transactions (see e.g. Kaplan and Hegarty, 2006).

The GPS consists of a constellation of satellites that transmit L-band radio signals (see Tab. 2.1) to unlimited numbers of users engaged in navigation, time transfer and relative positioning (for further reading on this topic see e.g. King et al., 1987; Parkinson and Spilker, 1996a,b; Beutler et al., 1999; Hofmann-Wellenhof et al., 2001; Seeber, 2003; Kaplan and Hegarty, 2006). The present full constellation provides global coverage with four to eight satellites simultaneously observable above 15 ° elevation.

	frequency	wave length
f_1	1575.42 MHz	19.05 cm
f_2	1227.60 MHz	24.45 cm

Tab. 2.1: The two main carrier frequencies of the GPS signal.

The signals emitted are delayed by radio wave refractivity (see Sec. 2.2) as they propagate from GPS satellites to ground-based GPS receivers. In the neutral atmosphere, a dry and a wet part of the total path delay can be distinguished. The size of the dry delay is dominated by the air pressure in the atmosphere, whereas the wet delay is nearly proportional to the quantity of atmospheric water vapor integrated along the signal path (see also Eq. 2.13). This characteristic of GPS is used in the field of GPS meteorology. However, if the water vapor has condensed, the attenuation even for dense rainfall has a very small effect on radio waves at frequencies less than 2 GHz (see e.g. Spilker, 1996).

A "stochastic" method minimizes survey errors by fitting atmospheric delays during GPS antenna coordinate determination. The method generally models a spherically layered atmosphere using a mapping function (Niell, 1996) and does not consider horizontal atmospheric gradients. More complex models would require a more sophisticated approach to resolve additional atmospheric parameters (see e.g. de Munck, 1992; Davis et al., 1993; Coster et al., 1997; Ware et al., 1997; Bar-Sever et al., 1998; Elósegui et al., 1999; Emardson and Jarlemark, 1999; Solheim et al., 1999; Niell, 2001; Pany, 2002; Boehm and Schuh, 2004; Boehm et al., 2006b and Abdullah et al., 2007 in terms of ionospheric horizontal gradients).

In opposition to parameter estimation, external correction strategies can be seen as research tools for achieving high accuracy geodetic positioning. External correction relies on the use of independent techniques for the measurements of hydrostatic and wet path delays. In the presence of hydrostatic gradients, numerical weather prediction models might also be used, either for an external correction of hydrostatic path delay or for replacing hydrostatic mapping functions (see also Sec. 2.4.3).

2.4.2 The GPS observation equations

The GPS code and phase observation equations (zero-differences) for both frequencies f_1 and f_2 (after Remondi, 1984; Dach et al., 2007) are as follows:

$$\text{Code:} \quad \begin{cases} P^r_{1,p} = \rho^r_p + c\delta_p - c\delta^r + I^r_p + \Delta\rho^r_p \\ P^r_{2,p} = \rho^r_p + c\delta_p - c\delta^r + \dfrac{f_1^2}{f_2^2} \cdot I^r_p + \Delta\rho^r_p \end{cases} \tag{2.19a}$$

$$\text{Phase:} \quad \begin{cases} L^r_{1,p} = \rho^r_p + c\delta_p - c\delta^r - I^r_p + \Delta\rho^r_p + \lambda_1 n^r_{1,p} \\ L^r_{2,p} = \rho^r_p + c\delta_p - c\delta^r - \dfrac{f_1^2}{f_2^2} \cdot I^r_p + \Delta\rho^r_p + \lambda_2 n^r_{2,p} \end{cases} \tag{2.19b}$$

ρ^r_p	geometric distance between receiver p and satellite r
δ_p	error of the receiver clock
δ^r	error of the satellite clock
$\Delta\rho^r_p$	tropospheric refraction or slant path delay
I^r_p	ionospheric refraction
f	carrier frequency
λ	wave length
n^r_p	unknown integer number of cycles (initial phase ambiguity)

Double-differences are the basic observables in the Bernese GPS Software. Forming double-difference observations (see e.g. Fig. 3.2 on p. 38 for a schematical representation of the configuration), the errors of the receiver and satellite clocks can be eliminated.

$$\text{Code:} \quad \begin{cases} P^{rs}_{1,pq} = \rho^{rs}_{pq} + I^{rs}_{pq} + \Delta\rho^{rs}_{pq} \\ P^{rs}_{2,pq} = \rho^{rs}_{pq} + \dfrac{f_1^2}{f_2^2} \cdot I^{rs}_{pq} + \Delta\rho^{rs}_{pq} \end{cases} \tag{2.20a}$$

$$\text{Phase:} \quad \begin{cases} L^{rs}_{1,pq} = \rho^{rs}_{pq} - I^{rs}_{pq} + \Delta\rho^{rs}_{pq} + \lambda_1 n^{rs}_{1,pq} \\ L^{rs}_{2,pq} = \rho^{rs}_{pq} - \dfrac{f_1^2}{f_2^2} \cdot I^{rs}_{pq} + \Delta\rho^{rs}_{pq} + \lambda_2 n^{rs}_{2,pq} \end{cases} \tag{2.20b}$$

In the case of an ionosphere-free linear combination of the two carrier frequencies f_1 and f_2, the double-difference phase measurements Eq. (2.20b) may be written as:

$$L^{rs}_{3,pq} = \rho^{rs}_{pq} + \frac{1}{f_1^2 - f_2^2} \cdot \left(f_1^2 \lambda_1 n^{rs}_{1,pq} - f_2^2 \lambda_2 n^{rs}_{2,pq} \right) + \Delta\rho^{rs}_{pq} \tag{2.21}$$

In GPS tomography for wet refractivity field determination it is recommended to use the ionosphere-free linear combination of the double-differenced phase measurements (see e.g. Troller, 2004). This combination eliminates the ionosphere error in the first order approximation.

2.4.3 Mapping functions and standard models

Precipitable water or the zenith wet delay (ZWD) can be considered as the average of all slant-path wet delays to all GPS satellites observed from one site over a period of time scaled to zenith (see also Bevis et al., 1994; Braun et al., 2003). Typical ZWD estimations assume that the water vapor field is horizontally homogeneous and temporally unchanging during the time period for which the individual observations are averaged. Thereby, two main lines of approaches were pursued:

- One is to estimate time varying gradient parameters that model the complicated spatial variability of the zenith wet delay (see e.g. Davis et al., 1993; Bar-Sever et al., 1998; Rothacher et al., 1998; Meindl et al., 2004).
  Introducing tropospheric gradient parameter estimation also allows to reduce the elevation cutoff angle for the GPS processing, which improves the repeatability of the station coordinates, especially in the horizontal plane, and smooths the time series of the estimates.
- The second approach is to directly compute the unmodeled delay along the line-of-sight path between a GPS receiver and transmitting satellite.
  This can be achieved e.g. by means of water vapor radiometer data (see e.g. Dodson et al., 1996; Doerflinger et al., 1998; Braun et al., 2003), Raman lidar data (see e.g. Bock et al., 2001; Tarniewicz et al., 2002) or based on meteorological data collocation techniques (see also e.g. Sec. 2.5, pp. 30f.).

High-resolution GPS tomography will potentially contribute to the second approach. Based on fully available four-dimensional wet refractivity fields, slant wet path delays can be estimated at each epoch and for any line-of-sight passing through the voxel model (see e.g. Sec. 3.1.1 on pp. 33). Afterwards, these estimates can be considered in the GPS processing in order to directly correct the observations.

Atmospheric delay as a function of elevation angle can be calculated using mapping functions. Several mapping functions have been developed during the last few years. The slant wet delay $\Delta^{wet}\rho_p^r$ at radio wavelength for elevation angles down to 3 ° can be represented as a sum of the isotropic and non-isotropic terms (Niell, 1996; Ifadis and Savvaidis, 2001; Braun et al., 2003):

$$\Delta^{wet}\rho_p^r = \mathrm{ZWD}_p \cdot m^{wet}(z_p^r) + S_p^r \tag{2.22}$$

$\Delta^{wet}\rho_p^r$	slant wet delay between station p and satellite r
ZWD_p	zenith wet delay for station p
$m^{wet}(z_p^r)$	zenith angle dependent wet mapping function
z_p^r	zenith angle of satellite r related to station p
S_p^r	non-isotropic component of the slant wet delay

The mapping function is defined as the ratio of the electrical path length (also referred to as the delay) through the atmosphere at geometrical zenith angle to the electrical path length in the zenith direction. To a first order all mapping functions may be approximated by a simple mapping function for a plane parallel medium. It is the secant of the zenith angle z (or cosecant of the elevation angle):

$$m(z) \approx m^{dry}(z) \approx m^{wet}(z) \approx \frac{1}{cos(z)} \tag{2.23}$$

At low elevation angles (e.g. down to 3 °), atmospheric curvature and ray bending require more complex mapping functions, especially due to the complex structure of the temperature and humidity field within the planetary boundary layer (see e.g. Hall, 1979; Webb, 1984; Stull, 1999). Another issue are the elevation angle dependent phase errors for a GPS antenna/mount combination, which can produce ZWD errors of greater than 30 mm over a few hour interval for typical GPS satellite coverage (see Niell et al., 2001). The parameters of the mapping function can be based on both geographical and meteorological observations. The coefficients of the Niell wet mapping function $\mathrm{NMF_{wet}}$ (see Eq. 2.24) depend only on the site latitude Θ (see Niell, 1996, and for further reading also Davis et al., 1985; Herring, 1992; Mendes and Langley, 1998; Mendes, 1999; Niell, 2000; Shrestha, 2003; Kleijer, 2004; Troller, 2004; Stoew and Elgered, 2005). When the mapping function is truncated to a finite number of terms (usually three), then the form is:

$$m(z) = \mathrm{NMF_{wet}}(z, \Theta) = \frac{1 + \dfrac{a_{wet}(\Theta)}{1 + \dfrac{b_{wet}(\Theta)}{1 + c_{wet}(\Theta)}}}{cos(z) + \dfrac{a_{wet}(\Theta)}{cos(z) + \dfrac{b_{wet}(\Theta)}{cos(z) + c_{wet}(\Theta)}}} \tag{2.24}$$

The coefficients a, b and c in Eq. (2.24) were developed using radiosonde data over a wide range of latitudes. The values are tabulated e.g. in Niell (1996). For the dry or hydrostatic mapping function these coefficients are not only latitude dependent (tabulated values a_{avg} and a_{amp}) but also time dependent with respect to the day of the year (t_{doy}). The parameter a_{dry} at time t_{doy} from January 0.0 (in UT days) is calculated as:

$$a_{dry}(\Theta, t_{doy}) = a_{avg}(\Theta) - a_{amp}(\Theta) \cdot cos\left(2 \cdot \pi \cdot \frac{t_{doy} - T_0}{365.25}\right) \tag{2.25}$$

The adopted phase T_0 is usually set to January 28 (i.e. $T_0 = 28$). A further correction term $\Delta m(z)$ is added to Eq. (2.24) (with the corresponding coefficients), which is related to the height H of the observing site above mean sea level in km:

$$\Delta m(z) = H \cdot \frac{\mathrm{d}m(z)}{\mathrm{d}h}$$
$$= H \cdot \left(\frac{1}{cos(z)} - \frac{1 + \dfrac{a_{ht}}{1 + \dfrac{b_{ht}}{1 + c_{ht}}}}{cos(z) + \dfrac{a_{ht}}{cos(z) + \dfrac{b_{ht}}{cos(z) + c_{ht}}}} \right) \tag{2.26}$$

with

$$a_{ht} = 2.53 \cdot 10^{-5}, \quad b_{ht} = 5.49 \cdot 10^{-3}, \quad c_{ht} = 1.14 \cdot 10^{-3}$$

The parameters a_{ht}, b_{ht} and c_{ht} were determined by least squares fit to the height corrections at nine elevation angles between 3 and 90 °. Fig. 2.4 gives the annual mode of the dry Niell mapping function ($\mathrm{NMF_{dry}}$) for an elevation angle of 5 ° and a station height of 0.73 km (station Susten). The tabulated parameters for a latitude of 45 ° were chosen (see Niell, 1996).

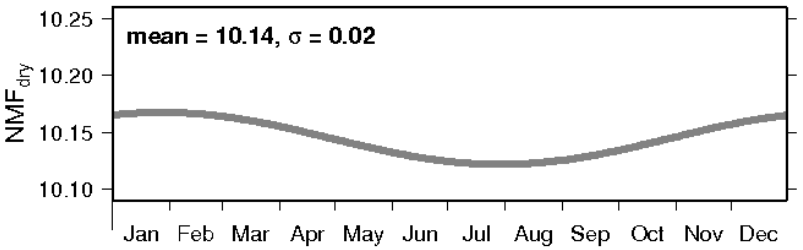

Fig. 2.4: Function of the dry or hydrostatic Niell mapping function at 5 ° elevation angle (see also e.g. Nilsson, 2005). The adopted phase is set to January 28 ($T_0 = 28$).

In the case of a 5 ° elevation angle, the dry mapping function amplifies the zenith dry delay by a factor 10 with respect to the slant path delay (see Fig. 2.4). At 10 °, the impact is about half as large ($\mathrm{NMF}_{dry}(z = 80) \approx 5.6$) and a slant dry delay at 15 ° elevation is accounted for the zenith dry delay estimation by a factor 3.8^{-1}.

However, at low elevation angles, and if hydrostatic gradients are present, mapping functions may not adequately model highly variable delays induced by water vapor (see e.g. Ohtani and Naito, 2000; Bock and Doerflinger, 2001; Guo and Langley, 2003). Rocken et al. (2001) concluded that the most demanding meteorological and geodetic GPS applications should use location- and time-specific "direct" mapping functions rather than parametrized functions, especially if low elevation observations are used. Schueler et al. (2000); Niell (2001); Pany (2002); Boehm (2004); Boehm et al. (2006a,b), for instance, described tropospheric mapping functions (e.g. the Isobaric Mapping Function, the Vienna Mapping Function or the Global Mapping Function) at radio frequencies to very low elevation angles based on data from

numerical weather models. They further investigated their impact on the determination of geodetic parameters compared to traditional mapping functions. Especially, regional height biases and annual errors could have been significantly reduced using the new functions.

Common GPS software packages usually include only a few mapping functions. The Bernese GPS Software Version 5.0 contains the simple $cos(z)$ mapping function and the corresponding a priori model (see e.g. Saastamoinen, 1972 and Eq. 2.9 on p. 18), a modified Hopfield model (Hopfield, 1969, 1971), the dry and wet Niell formula (see e.g. Niell, 1996 and Eq. 2.24 on p. 27) and a few more. The Niell model is implemented as a product of the Saastamoinen zenith delay and the Niell mapping function. For some a priori models, there is also the possibility to use only the dry component (Saastamoinen, Hopfield and Niell). This option is normally chosen when estimating site-specific troposphere parameters. Accordingly, the dry component is computed, the wet component is estimated, and the correct mapping function (dry and wet) may be applied for each component (see Dach et al., 2007). The Global Mapping Function will be implemented in a future version of the Bernese software.

2.4.4 Troposphere modeling in the Bernese GPS Software

The Bernese GPS Software Version 5.0 continues the tradition of its predecessors as a high performance, high accuracy and highly flexible reference GPS/GLONASS (GNSS) postprocessing package (see Dach et al., 2007). Its characteristics are state-of-the-art modeling, detailed control over all relevant processing options, powerful tools for automation, the adherence to up-to-date, internationally adopted standards and the inherent flexibility due to a highly modular design[4].

The tropospheric refraction term $\Delta\rho_p^r$ from Eq. (2.19) can be written according to Rothacher et al. (1998); Meindl et al. (2004); Dach et al. (2007) as:

$$\Delta\rho_p^r(t) = \overbrace{\Delta\rho_{apr,p}(z_p^r)}^{\text{a priori model}} + \overbrace{\Delta\rho_p(t)\cdot m(z_p^r)}^{\text{ZPD}} + \underbrace{\Delta^n\rho_p(t)\cdot\frac{\partial m(z_p^r)}{\partial z}\cdot cosA_p^r + \Delta^e\rho_p(t)\cdot\frac{\partial m(z_p^r)}{\partial z}\cdot sinA_p^r}_{\text{horizontal gradients}} \tag{2.27}$$

$\Delta\rho_p^r(t)$	tropospheric path delay between station p and satellite r in m
t	observation time
z_p^r, A_p^r	zenith, azimuth of satellite r as observed from station p in rad
$\Delta\rho_{apr,p}(z_p^r)$	slant delay according to an a priori model in m
$\Delta\rho_p(t)$	zenith path delay in m
$m(z_p^r)$	respective mapping function for $\Delta\rho_p(t)$
$\Delta^n\rho_p(t)$	horizontal north troposphere gradient parameter in m
$\Delta^e\rho_k(t)$	horizontal east troposphere gradient parameter in m

[4] For further information related to the Bernese GPS Software see the website at http://www.-bernese.unibe.ch

After the parameter estimation, the Bernese GPS Software saves the troposphere data in so-called Bernese troposphere files. These files contain zenith path delays and, optionally, gradient estimates for multiple stations. In addition, information on the a priori model and time resolution used during the creation process is listed (see also Dach et al., 2007).

In the tomographic software package AWATOS (further described in Sec. 3.2), both, the zenith path delay alone and together with the gradient parameters, can be used to retrieve the wet refractivity field in the atmosphere above a specified area. Within AWATOS, the same atmospheric models and mapping functions are used for the data analysis.

The troposphere path delay and the mapping function may depend on the site location and the day of the year due to seasonal variations. The tropospheric delay from the a priori model may be computed while site-specific ZPD and gradient parameters must be estimated during the processing. The Bernese GPS Software Version 5.0 offers several a priori models and corresponding mapping functions to take the tropospheric refraction (Dach et al., 2007) into account.

Tab. 2.2 gives an overview of the tropospheric zenith total delay (ZTD) sensitivity as a function of air pressure, temperature and relative humidity (see also Geiger, 1987; Dach et al., 2007).

p hPa	T °C	H_r %	$\frac{\partial \mathrm{ZTD}}{\partial p}$ mm/hPa	$\frac{\partial \mathrm{ZTD}}{\partial T}$ mm/°C	$\frac{\partial \mathrm{ZTD}}{\partial H_r}$ mm/%
1 000	0	50	2	-3	0.6
1 000	30	50	2	-14	4.0
1 000	0	100	2	-5	0.6
1 000	30	100	2	-27	4.0

Tab. 2.2: Sensitivity analysis of the tropospheric zenith total delay (ZTD) estimation as a function of air pressure p, temperature T and relative humidity H_r (see Dach et al., 2007).

In more humid conditions, the impact on ZTD estimation with respect to an error in the temperature measurement becomes larger than in dry conditions. In general, a heated environment is more sensitive to temperature and humidity data accuracy for path delay estimation. The sensitivity due to an error in the pressure parameter does not depend on temperature and humidity.

2.5 The software package COMEDIE

Pressure, temperature and water vapor pressure are collocated and interpolated by using the software package COMEDIE (see Cocard et al., 1992; Geiger et al., 1995; Kruse, 2001; Troller et al., 2002b). It is applied in order to obtain meteorological parameters at each GPS station for the decomposition of the total path delays into the dry and wet components (see Eq. 2.13) based on a different meteorological

measurement network than the GPS network. COMEDIE is also used to calculate the a priori values of refractivity (see Sec. 3.1.2 and Eq. 2.4 on p. 14) as input for the tomographic analysis.

2.5.1 4-D refractivity field from meteorological data

The software package COMEDIE (Collocation of Meteorological Data for Interpolation and Estimation of tropospheric path delays) allows a four-dimensional modeling of meteorological observations of pressure p, temperature T and water vapor pressure e_p in space and time. It is based on the method of least-squares collocation (see Moritz, 1973; Wirth, 1990; Geiger and Cocard, 1992; Geiger et al., 1996; Herschke, 2002; Troller et al., 2002b).

The main equation of the collocation reads as follows (see also Eckert et al., 1992; Höflinger, 1993; Troller, 2004):

$$\overrightarrow{l} = \mathbf{A} \cdot \overrightarrow{x} + \overrightarrow{s'} + \overrightarrow{n} \tag{2.28}$$

$\overrightarrow{l}$	measurement
$\mathbf{A}$	design matrix
$\overrightarrow{x}$	vector of unknowns
$\overrightarrow{s'}$	signal part of the measurement
$\overrightarrow{n}$	measurement noise

The functional part is represented by the term $\mathbf{A} \cdot \overrightarrow{x}$. The remaining component of the observation $\overrightarrow{l}$ is separated into a signal and a noise part according to a chosen covariance function. Herschke (2002) studied the modeling and extrapolation algorithms of path delays especially for zenith total delays in GPS signals compared with data from the automated meteorological network ANETZ of MeteoSwiss.

As a major result, arbitrarily chosen observation points can be interpolated in the collocated area using the following equations (see also Wirth, 1990; Kruse, 2001):

$$\overrightarrow{t} = \mathbf{A} \cdot \overrightarrow{x} + \overrightarrow{s} \tag{2.29a}$$

$$\overrightarrow{s} = \mathbf{C_{s's'}} \cdot \mathbf{C_{ll}}^{-1} \cdot (\overrightarrow{l} - \mathbf{A} \cdot \overrightarrow{x}) \tag{2.29b}$$

$\overrightarrow{t}$	predicted value at the interpolated point
$\mathbf{A}$	design matrix for the interpolated point
$\overrightarrow{s}$	signal of the interpolated point
$\mathbf{C_{s's'}}$	covariance matrix of the signal
$\mathbf{C_{ll}}$	covariance matrix of the observations

The outcome of Eq. (2.29) is discussed in more detail in Sec. 5.3, pp. 68f., based on the meteorological data processing of the two measurement campaigns (see Chapter 4).

2.5.2 Estimation of tropospheric path delays

The collocated and interpolated four-dimensional refractivity field enables to determine path delays at any desired location within the area of the meteorological data coverage. The dry and wet path delays are then determined by an integration along the desired ray path.

Because of the sparse data availability above the tropopause, the integration with COMEDIE is only accurate up to about 12 km altitude (see also Geiger et al., 1996; Hirter, 1998; Troller, 2004; Troller et al., 2006b).

Chapter 3

Ground-based GPS tomography of the neutral atmosphere

The principle of ground-based GPS tomographic reconstruction was first developed in order to solve the spatial distribution of the electron content in the ionosphere (ionospheric tomography, see e.g. Leitinger, 1994; Ruffini et al., 1998b).

The delay induced by the (neutral) atmosphere in the GPS signals can be estimated with a precision of a few millimeters from simultaneous observations to about a dozen GPS satellites (Elósegui and Davis, 2001). These path delays can then be converted into precipitable water vapor estimates resulting in a continuous, accurate, all-weather and real-time GPS-derived humidity field determination.

3.1 Models, methods and algorithms

3.1.1 The tomographic voxel model

GPS tomography consists of obtaining estimates of the water vapor refractivity field from measurements of integrated water vapor by inverting a discretized form of Eq. (2.14). To account for the temporal variations of the wet refractivity field, one such inversion is performed at each observing epoch or group of epochs during which the refractivity is assumed to remain constant (see also Elósegui and Davis, 2001).

In the tomographic approach, a discretization of the atmosphere with a three-dimensional voxel model is used[5] (see also Flores, 1999). For each voxel, an unknown but constant refractivity N_i is introduced. According to Eq. (2.14), the total slant path delay for one observation $\Delta\rho_p^r = \Delta\rho_j$ between station p and satellite r can then be expressed as a summation over each individual voxel of the voxel model, where the GPS signal passes through (see also Kruse, 2001; Troller, 2004). The observed ray traversing the atmosphere from the emitting satellite to the ground-based receiver is delayed. The amount and distribution of water vapor in the atmosphere influence this delay. A three-dimensional voxel model is introduced with a constant, mean refractivity within each voxel (see Fig. 3.1). The rays are allocated by ray tracing algorithms. The total slant path delay is given by Eq. (3.1).

$$\Delta\rho_p^r = \Delta\rho_j = 10^{-6} \cdot \sum_{i=1}^{k} N_i \cdot \Delta s_{i,j} \tag{3.1}$$

[5] A voxel (a combination of the words volumetric and pixel) is a volume element, representing a value on a regular grid in three-dimensional space.

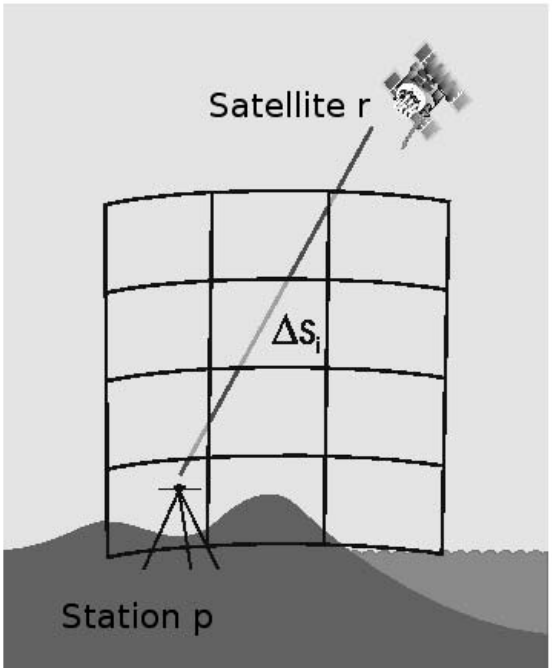

Fig. 3.1: Principle of GPS tomography (Troller, 2004, p. 71).

$\Delta\rho_j$	slant path delay of observation j in m
k	total number of voxels in the voxel model
N_i	unknown tropospheric refractivity in voxel i in ppm
$\Delta s_{i,j}$	length of the ray j in voxel i in m

In matrix notation Eq. (3.1) reads as (see also e.g. Troller, 2004; Nilsson, 2005):

$$\overrightarrow{\Delta\rho} = \mathbf{A} \cdot \overrightarrow{N} \tag{3.2}$$

The refractivity value N_i of each voxel is determined by performing a least-squares adjustment. Flores (1999); Flores et al. (2000c) indicated that the minimal thickness of a tomographic voxel layer should be 350 m. If it is less than this, noise will affect the tomographic solution. Yet, if the horizontal grid size exceeds a certain limit, projections on the ground of all rays end up being in the same cell. Thus all observation equations are linearly correlated with respect to the corresponding voxels. Because the refractivity in one box is imposed to be uniform and unchanging during one update cycle of the analysis, the tomographic inverse problem can hardly be determined without any additional input data (see e.g. Seko et al., 2000; Liou et al., 2003; Bi et al., 2006).

Bender and Raabe (2005, 2007); Bender et al. (2007) investigated the reliability of the information in a given set of GPS signals as a precondition to an optimal tomographic reconstruction. The spatial distribution of the geometric intersection points between different ray paths is used to estimate the information density. Hereby, the voxel model geometry is limited in view of vertical as well as of horizontal resolution. To deal with these restrictions auxiliary information can be introduced in

the tomographic equation system: an a priori model (see Sec. 3.1.2) and inter-voxel constraints (see Sec. 3.1.3).

3.1.2 The a priori model

Most of the previous studies in tropospheric GPS tomography (see Sec. 1.2) have revealed that a priori information is required in the tomographic method in order to accurately retrieve the vertical structure of the atmosphere. For example, Braun and Rocken (2003) used the Raman lidar, Skone and Hoyle (2005) used single radiosondes, Champollion et al. (2005) used the standard atmosphere. Bi et al. (2006) introduced a priori information by applying the average results of all radiosonde profiles over a certain time period as a priori profiles. Another research group in China uses the output of forecasts from numerical weather prediction models as a priori information for the tomographic processing (Song et al., 2006).

Basically, the tomographic a priori model is used to fill selected voxels by externally produced refractivity values with an appropriate weight. These values are treated as pseudo-observations in the final tomographic equation (see Eq. 3.7 on p. 39).

3.1.3 Inter-voxel constraints

As some voxels in the voxel model may not be crossed by any ray due to the irregular distribution of the transmitting satellites in the sky, inter-voxel constraints are introduced as pseudo-observations to strengthen the partly ill-conditioned tomographic inversion system (see also Troller et al., 2006b, 2007a,b). They are calculated basically similarly to the stochastic model of the COITROPA software package (see Eq. 2.18) for the three spatial dimensions. Since the state of the atmosphere is usually continuous, the inter-voxel constraints are due to have a smoothing character in space.

The covariance function between two points in the voxel model can be written as (see Troller, 2004):

$$\Phi_{i,j} = \frac{\sigma_0^2}{1 + \left[(\frac{x_i - x_j}{\Delta x_0})^2 + (\frac{y_i - y_j}{\Delta y_0})^2 + (\frac{z_i - z_j}{\Delta z_0})^2 \right]} \tag{3.3}$$

$\Phi_{i,j}$	covariance function between voxel i and voxel j
σ_0^2	a priori variance of the signal
$\Delta x_0, \Delta y_0, \Delta z_0$	correlation length of the individual components

In the final form of the tomographic equation system of AWATOS (see Eq. 3.7, p. 39), inter-voxel constraints have to be available for each voxel. They are combined in a row vector $\overrightarrow{\Phi_i}$ with the size of the total number of voxels (k) in the voxel model

and added to the design matrix. The elements x of this vector are defined as (see Troller, 2004):

$$\overrightarrow{\Phi_i} \; : \; x = \begin{cases} -1, & \text{if } j = i \\ \dfrac{\Phi_{i,j}}{\Phi_{sum,i}}, & \text{if } j \text{ neighboring to } i \\ 0 & \text{in all other cases} \end{cases} \tag{3.4a}$$

with

$$\Phi_{sum,i} = \sum_{j=1}^{k} \Phi_{i,j} \tag{3.4b}$$

The definition $x = -1$, if $j = i$, accounts for the condition that the scalar product $\overrightarrow{\Phi_i} \cdot \overrightarrow{N}$ must always be 0 for all voxels in the model.

With respect to the temporal continuity of the state of the atmosphere, the a priori model (see Sec. 3.1.2) can be chosen accordingly. Thus, the result of one analysis is the initial condition of the successive run. The weights of the a priori values depend on the temporal resolution of the tomographic processing.

3.1.4 Separation of the total path delay

If one is interested not only in the determination of the total refractivity field but also in the dry or wet part, the zenith total path delays have to be separated accordingly. This is done with respect to the constitutive meteorological condition using Eq. (2.13).

Nowadays, the wet delay or, if available, wet refractivity, is usually assimilated into numerical weather prediction models to obtain additional humidity information combining this data with temperature profiles (see e.g. Norquist and Chang, 1994). This involves only additional errors of the temperature estimates and the uncertainties due to the separation procedure, if starting from total delays or total refractivities. When calculating the humidity from the dry or total refractivity, however, also the errors of the air pressure profile have to be taken into account (see Eq. 2.4). The influence of an error in the temperature profile has a much smaller impact here.

In tropospheric GPS tomography, the phase residuals are processed. Because the models for the dry delays are usually well established and implemented in geodetic GPS processing software, the residuals are mostly affected by the wet part of the atmosphere (see also Sec. 3.2.1 and also e.g. Elósegui and Davis, 2001). Therefore, these residuals are especially suited for water vapor tomography and tropospheric humidity sensing of wet refractivity.

3.2 The software package AWATOS

3.2.1 Double-difference GPS tomography

The Atmospheric Water Vapor Tomography Software Package AWATOS is based on double-differenced GPS observations (see Troller et al., 2002a). Processing double-differences, the remaining errors in the GPS observation equation (see Sec. 2.4.2) are due to ionospheric and tropospheric refraction.

With dual-frequency receivers, the ionospheric refraction can be eliminated, too (see Sec. 2.4.2). No clock correction models have to be applied. It is, therefore, especially well suited for near real-time application in weather prediction and allows sensing the atmospheric structure below the noise level of current satellite and receiver clock errors. The residuals obtained by the GPS postprocessing are reconstructed to slant path delays, thus Eq. (3.1) can be rewritten as:

$$\Delta\rho_{pq}^{rs} = 10^{-6} \cdot \sum_{i=1}^{k} N_i \cdot \Delta s_i{}_{pq}^{rs} \tag{3.5}$$

$\Delta\rho_{pq}^{rs}$	double-differenced path delay in m
k	total number of voxels in the model
N_i	unknown refractivity in voxel i in ppm
$\Delta s_i{}_{pq}^{rs}$	length of all double-difference rays in voxel i in m

Eq. (3.6a) describes the reconstruction of the double-difference ray path delay $\Delta\rho_{pq}^{rs}$ from the four corresponding slant path delays (see also Troller et al., 2002a). In Eq. (3.6b), the connection to the parameters estimated in the GPS preprocessing part is given: double-differenced phase residuals and zenith path delays with corresponding mapping function, see Eq. (2.27).

$$\Delta\rho_{pq}^{rs} = \left(\Delta\rho_q^r - \Delta\rho_p^r\right) - \left(\Delta\rho_q^s - \Delta\rho_p^s\right) \tag{3.6a}$$

$$= \Big[m(z_q^r) \cdot \mathrm{ZPD}_q - m(z_p^r) \cdot \mathrm{ZPD}_p\Big] - \Big[m(z_q^s) \cdot \mathrm{ZPD}_q - m(z_p^s) \cdot \mathrm{ZPD}_p\Big] + v_{pq}^{rs} \tag{3.6b}$$

$\Delta\rho_p^r$	slant path delay between station p and satellite r in m
ZPD_p	zenith path delay at station p in m
$m(z_p^r)$	mapping function for elevation angle z between p and r
v_{pq}^{rs}	double-differenced phase residual (see p. 61f.) in m

The ensemble of all these parameters and functions (tropospheric a priori model and mapping function) has to be imperatively consistent with the GPS preprocessing analysis. In another case, the reconstructed slant path delays would adopt respective biases. Fig. 3.2 shows the graphical representation of this reconstruction and Eq. (2.22), on p. 26, explains the usage of the mapping function.

The mapping function $m(z_p^r)$ has to be chosen according to the kind of delay (dry, wet, or total) being processed. Horizontal tropospheric gradients estimated

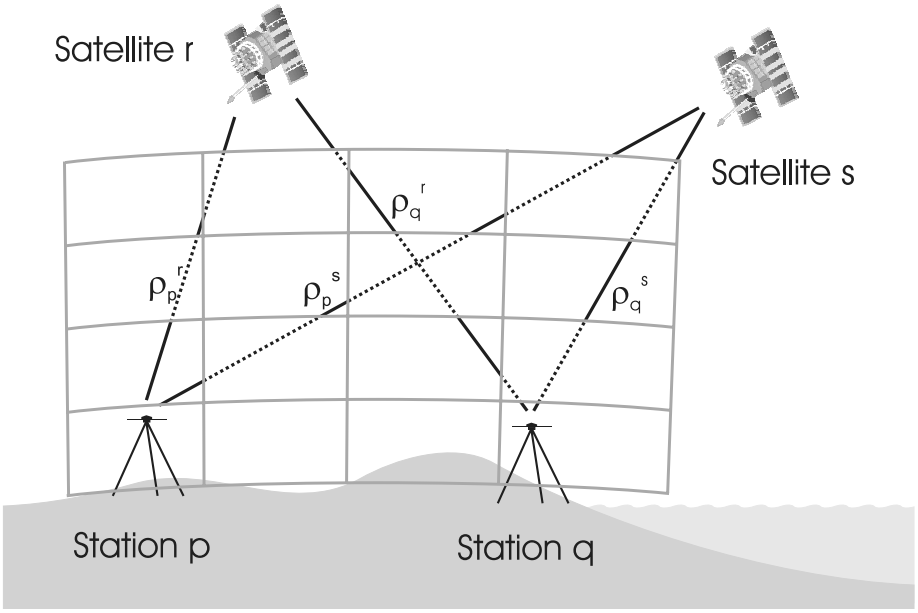

Fig. 3.2: Double-difference GPS tomography implemented in the software package AWATOS (Troller, 2004, p. 75). The reconstructed double-differenced observations (four slant path delays for each receiver baseline) are allocated to the corresponding voxels.

together with the zenith path delays within the GPS processing software have to be taken into account. After an appropriate GPS analysis, the double-differenced phase residuals can be interpreted as being affected only by the wet components of the atmospheric error. Therefore, Eq. (3.6a) may be used for reconstructing mainly the double-differenced wet path delay.

The main advantage of this approach is that satellite and receiver clock biases are already eliminated (Ware et al., 1997). However, the double-difference phase residual contains not only troposphere information but also other not linearly eliminated information such as site and internal multipath, antenna phase center variations and, possibly, unmodeled clock errors and ionosphere information (e.g. higher-order ionosphere effects). Therefore, these effects are then being interpreted as tropospheric effects as well (Troller, 2004).

3.2.2 The tomographic equation system

The tomographic system expressed by Eq. (3.5) is typically under-determined and highly correlated (see e.g. Aparicio and Rius, 2004) because not all individual volume elements are crossed by receiver satellite rays. Thus, spatial smoothing inter-voxel constraints according to Eq. (3.3) are introduced as pseudo-observations. Furthermore, a priori values are calculated according to Sec. 3.1.2.

The final form of the tomographic equation system incorporating the GPS path delays, the a priori refractivity values and the inter-voxel constraints implemented in AWATOS can be written as follows:

$$\begin{pmatrix} \mathbf{A} \\ \overrightarrow{\Phi_i} \end{pmatrix}^{\mathbf{T}} \mathbf{P} \cdot \begin{pmatrix} \Delta\rho_{pq}^{rs} \\ \mathrm{ZTD}_p \\ N_{0,i} \\ 0_i \end{pmatrix} = \begin{pmatrix} \mathbf{A} \\ \overrightarrow{\Phi_i} \end{pmatrix}^{\mathbf{T}} \mathbf{P} \begin{pmatrix} \mathbf{A} \\ \overrightarrow{\Phi_i} \end{pmatrix} \cdot \begin{pmatrix} N_1 \\ N_2 \\ N_3 \\ N_4 \\ N_5 \\ N_6 \\ \cdots \end{pmatrix} \tag{3.7}$$

$\mathbf{A}$	design matrix
$\mathbf{P}$	weight matrix
$\overrightarrow{\Phi_i}$	inter-voxel constraints for voxel i (see Eqs. 3.3 and 3.4)
$\Delta\rho_{pq}^{rs}$	reconstructed double-differenced slant path delays in m
ZTD_p	zenith total delay from GPS processing at station p in m
$N_{0,i}$	a priori information for voxel i in ppm
0_i	inter-voxel constraint added for voxel i
N_i	unknown refractivity in voxel i in ppm

If no inter-voxel constraints are introduced and only a few a priori values are set, the inversion system Eq. (3.7) is under-determined because the double-differenced slant path delays are highly spatially and temporally correlated. To handle with this inconvenience, investigations were done in order to apply a singular value decomposition (see Troller, 2004). For this work, the coefficients of Eq. (3.3) were optimized for the target area and the voxel model in use and inter-voxel constraints were always considered.

The vector of unknowns $\overrightarrow{N}$ has the size of the number of voxels in the voxel model. Therefore, analyzing a voxel model with higher spatial resolution will lead to an enlarged inversion system and, hence, to a longer calculation time.

3.2.3 Ray tracing and the design matrix

The design matrix of the tomographic inversion system Eq. (3.7) can be created applying a ray tracing algorithm. The double-difference slant path delays are allocated to the corresponding voxels (see Fig. 3.2). The path lengths $\Delta s_i{}_{pq}^{rs}$ from Eq. (3.5) are calculated and added to the first section of the design matrix $\mathbf{A}$.

The zenith total delays for each station (ZTD) affect only the voxels in the vertical column above the station itself. According to the generation strategy for the a priori refractivity values, the design matrix $\mathbf{A}$ is further expanded. Such strategies may e.g. be to take only voxels on the earth's surface derived from ground meteorological networks into account, to choose voxels along a balloon sounding path, voxels at the top edge of the model or, in the case of a temporal correlation, the full voxel model from the previous tomographic analysis.

3.2.4 (Pseudo-) Observations and the weight matrix

Besides the double-differenced slant path delays and the zenith total delays, pseudo-observations are derived either from GPS independent measurements (e.g. the

a priori values from meteorological data) or from "artificial" construction algorithms (e.g. inter-voxel constraints). They are introduced to strengthen the tomographic equation system, by adding additional elements to or next to the diagonal of the design matrix $\mathbf{A}$ (see Eq. 3.7). This helps numerical matrix inversion algorithms to solve the tomographic problem. Furthermore, this pseudo-observations are based on considerations about the physical behavior of the atmosphere.

For the least-squares adjustment, a covariance matrix containing the weightings of the observations and pseudo-observations has to be defined as well. The weight matrix $\mathbf{P}$ in Eq. (3.7) contains the inverted variances of all observations and pseudo-observations of the tomographic analysis. The observations include the double-differenced path delays with estimated a priori standard deviations and the zenith total delays with the variances calculated by GPS processing. Usually, weights are set up observation class by observation class, but they may also be set individually.

3.2.5 Error budget

In order to analyze the results of the tomographic inversion, three basic quality indicators are estimated based on Eq. (3.7):

- The condition number of the design matrix $\mathbf{A}$
- The a posteriori standard deviation from $\mathbf{A^T PA}$
- The square root of the diagonal elements of the cofactor matrix $(\mathbf{A^T PA})^{-1}$

The condition number is an indicator for the geometrical configuration of the tomographic system, i.e. the constellation of the GPS receiver network in relation to the GPS satellite constellation for the time of one analysis update as well as the distribution of the additional pseudo-observations.

In terms of analyzing the quality of a specific ground-based GPS network for the tomographic solution of a selected voxel model, the degree of freedom and the a priori variance of each unknown refractivity value can be computed without any observations. This technique was used within the network analysis tool described in the next section.

3.3 Network analysis tool

MacDonald et al. (2002) suggested that if there are approximately 100 observations within one hour per GPS station (i.e. sampling interval of 30 s) and if the retrieved three-dimensional moisture is required with vertical resolution of 500 m, the ground-based GPS station network should be formed with 40 km resolution.

Elósegui and Davis (2001); Bi et al. (2006); Nilsson and Gradinarsky (2006); Bender and Raabe (2007) and others pointed out that the quality of moisture data in a three dimensional distribution retrieved by tomography is related closely to the horizontal and vertical distances between GPS stations. Furthermore, GPS networks with stations located at similar heights are limited in determining the vertical information of the amount of water vapor without additional data being introduced (see

e.g. Elósegui and Davis, 2001). The high-resolution GPS tomography is very sensitive to the number of regional sites and the geometric configuration of the network. In a perfect network, the spacing among neighboring stations should be equal to the horizontal resolution of the voxel model, so that most of the voxels are crossed by signal rays (see e.g. Bi et al., 2006; Ding et al., 2007).

Prior to the dedicated field campaigns for the present work, a network analysis tool was developed to determine a suitable GPS network in the project area for predetermined high-resolution tomographic processing. After the horizontal grid of the three-dimensional voxel model is designed, there should be at least one GPS station in each unit.

At the beginning of the project, a tool for an automatic generation of tomographic voxel models (see Sec. 3.1.1) was developed. This tool allows more flexibility in the tomographic processing. Besides, it is a fundamental part for an adaptive method to choose suitable voxel models according to the predicted resolution. Furthermore, rudimentary simulations allowed to design optimal GPS network configurations for tomographic purposes (see Lutz et al., 2005). Particularly, the behavior of the value of $(\mathbf{A^T P A})^{-1}$ (see also Secs. 3.2.5 and 3.2.2) was investigated and analyzed.

Especially in the case of a mountainous target area, it is essential to find an optimal distribution of the GPS stations according to the expected horizontal and vertical resolution of the tomographic processing. The visibility of the GPS satellites from ground-based antennas is another restrictive issue to take into account. This topic is discussed in more detail in Secs. 4.3.1 and 4.4.1 as well as in Appendix B.

Chapter 4

Outline of the two field campaigns

4.1 Introduction

Two dedicated field campaigns, each lasting seven days, were organized and carried out in the canton of Valais in the southwest of Switzerland (Fig. 4.1) in July and October 2005. The main objective was to capture data to pursue GPS tomography in an area with rough topography. The data will contribute to the development of the tomographic approach toward a high-resolution application in view of hydrological hazard assessment.

In the eastern part of the mountainous canton of Valais (see Fig. 4.2), within an area of approximately 50 km by 50 km, 17 (in July) respectively 23 (in October) ground-based geodetic GPS campaign stations with dual-frequency receivers were mounted for permanent measurement during the time of the two measurement campaigns. Additionally, meteorological systems were installed and operated in the same region next to GPS stations to obtain appropriate a priori ground data for the tomographic processing. Furthermore, weather balloons were prepared and started at selected launch sites for validating the final results.

This chapter gives a short description of the project area (Sec. 4.2) and the data acquisition of both measurement campaigns (Sec. 4.3 and Sec. 4.4) including an overview of the different data sets and some preprocessing considerations.

4.2 The project area in the canton of Valais (Switzerland)

The canton of Valais in the southwest of Switzerland has always been and still is threatened by natural, especially hydrological hazards like heavy rainfall, slumps or even flooding. Several organizations of ETH Zurich therefore decided to accumulate experience in this area to profit from the same general, i.e. geographical conditions. This cooperation contributes to the improvement of methods and tools for integral risk management as a base for sustainable development.[6] Furthermore, a newly established data base, which contains the data of the different projects, is intended to support scientists and decision makers in this area and similar areas in solving interdisciplinary problems and questions.

To keep the extent of the project area organizable and maintainable during the campaigns, a 50 km by 50 km region in the eastern part of the canton of Valais (see

[6] For further information on the research network for natural hazards at ETH Zurich (HazNETH) see http://www.hazneth.ethz.ch.

Fig. 4.1), including a section of the main valley of the Rhone river and four side valleys to the south, was selected as target area. The elevation of the topography varies in this area between 500 m and over 4 000 m AMSL.

The contour map Fig. 4.2 gives an impression of the shape of the terrain in angular view. It is obvious that this area is not predestined for high-quality GPS measurements because of the deep valleys and the obstructed line of sight by the mountain peaks from the satellites to the antennas (see also the satellite visibility in the skyplots for the GPS stations in Appendix B, pp. 183ff.).

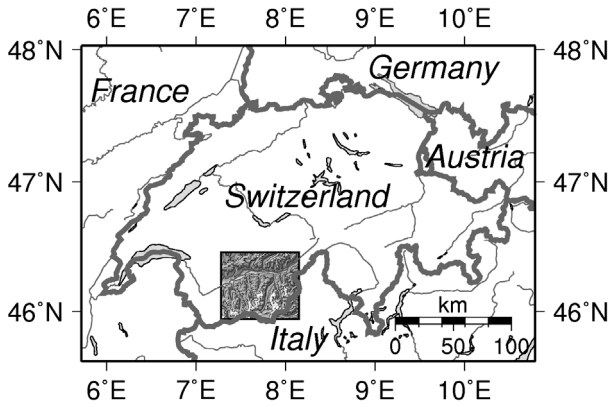

Fig. 4.1: Project area of about 50 km by 50 km in the Swiss Alps in the southwest of Switzerland. This region was selected due to its high degree of exposure to natural, especially hydrological hazards. It is also the target area of other interdisciplinary research projects.

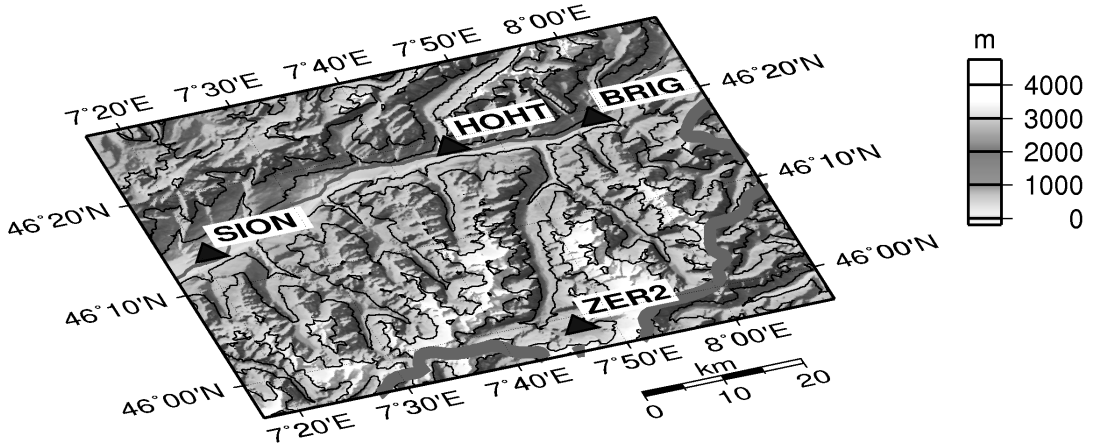

Fig. 4.2: Contour map (equidistance: 1000 m) of the project area in the eastern part of the mountainous canton of Valais. The locations of existing and operating national permanent GPS stations within this area in July 2005 are indicated with dark triangles and labeled with their internal station abbreviation. The stations in Sion (SION at 527 m AMSL), Brig (BRIG at 702 m) and Zermatt (ZER2 at 3119 m) are operated by the company Swissat, Hohtenn (HOHT at 935 m) belongs to swisstopo's automated network AGNES.

In mountainous areas, another limitation of precise GPS vertical measurement lies in the difficulty of estimating tropospheric delay due to high differential elevation and large weather variability (see e.g. Urfer-Henneberger and Turner, 1982; Gurtner et al., 1989; Doerflinger et al., 1998).

4.3 The July 2005 field campaign

The first field campaign to obtain a suitable data set for high-resolution ground-based water vapor GPS tomography took place from 8 to 14 July, 2005. The development of the major meteorological constituents measured at two stations in the project area of the automated network ANETZ of MeteoSwiss is given in the Appendix in Fig. A.2, p. 180.

There was an almost continuous increase of air pressure measured on the surface during the first half of the campaign, recognizable especially in the time series of Evolène in Fig. A.2. The daily fluctuations in the pressure data of Visp were due to the strong up and down wind system in the main valley of the canton of Valais. The water vapor pressure shows no significant pattern. Rainfall occurred at both stations on the second day (July 9, 2005). Some shorter showers of rain were recorded at the station Evolène. The sun was shining every day. The mean daily temperature was rising during the seven days.

4.3.1 GPS network

The existing GPS network of four permanent stations in the project area was supplemented by seventeen non-permanent stations for the time of the campaign. Fig. 4.3 shows the station distribution of the permanent and non-permanent GPS networks in the target region. The hardware configuration used during the campaign is summarized in Appendix B by Tabs. B.1, B.2, B.4 and B.5.

In order to assess the impact of the GPS satellite sky distribution on the error propagation (see e.g. Geiger, 1987; Santerre, 1991) based on visual inspection, the skyplots of the stations in the project area are shown in Fig. **??** and Appendix B, too. Based on these investigations, examinations in terms of changing cutoff elevation angles were tested in the GPS data processing part (see Sec. 5.2) and in the tomographic analysis (see e.g. Sec. 8.1.2, p. 120, for a comparison of results with different cutoff angles).

Although, the main problem with GPS data used in meteorological applications is found to be related to the design of GPS antennas (see e.g. Yang et al., 1999), there were eight different receiver and antenna types operating during the first field campaign. Due to maintenance work (battery change, data download, etc.), the campaign stations did not record permanent observation time series. There are gaps of several minutes to a few hours. The graphical representation of the time span of the data actually usable for the GPS tomography can be found in Fig. 7.7(a) on p. 102.

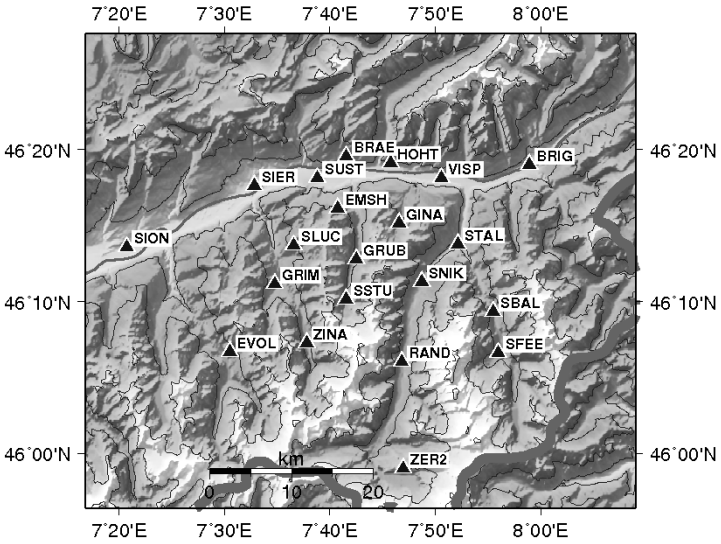

Fig. 4.3: GPS network of the campaign in the eastern part of the Valais in July 2005. Besides the sixteen campaign stations of this project (see Tab. B.1, p. 184), a few others in the local area network are shown: HOHT is part of the permanent network AGNES of swisstopo. BRIG, SION and ZER2 are stations of the Swissat Virtual Reference Stations network. The non-permanent station SIER was temporally mounted and operated by the office Geosat S.A. in Sierre.

4.3.2 Meteorological ground measurement network

There are five stations of the Swiss national automated network ANETZ of MeteoSwiss within the project area. Four of them are next to or near a GPS station: Evolène (EVOL), Sion (SION), Visp (VISP) and Zermatt (ZER2 and since October 2005 also ZER1). These stations are equipped with a dozen different high-quality meteorological sensors.

Data of pressure, temperature and humidity was used for the processing. Furthermore, pressure, temperature and humidity measurements from the local permanent network RESIVAL of the Service for Environmental Protection, state of Valais, were available together with data from the Alpine network IMIS of the Swiss Federal Institute for Snow and Avalanche Research, Davos (only temperature and humidity). Nine additional meteorological measurement systems were mounted next to non-permanent GPS stations to densify the network for the refinement of the data. Fig. 4.4 shows the whole meteorological sensor network within the project area.

4.3.3 Radiosondes

Gutman et al. (2004) concluded that GPS sites, that are close enough to upper-air sites to be within the same air mass most of the time, can be used to quality control radiosonde moisture soundings. Therefore, to capture in situ measurements for validation purpose, radiosondes were launched within the project area during the time of the campaign. The lightweight and low cost Mark II microsondes from the

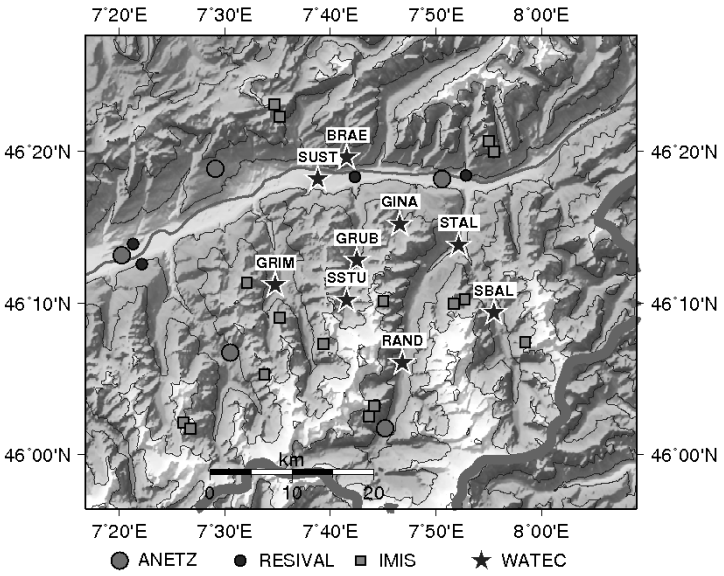

Fig. 4.4: Locations of the meteorological measurement systems during the field campaign in July 2005. Permanently measuring networks for the parameters pressure, temperature and humidity are ANETZ (operated by the Swiss Federal Office of Meteorology and Climatology, MeteoSwiss) and RESIVAL (operated by the Service for Environmental Protection, state of Valais). The network IMIS (from the Swiss Federal Institute for Snow and Avalanche Research, Davos) provides only temperature and humidity data. The WATEC network was specially mounted for the duration of the campaign. The equipment of its stations is given in Tab. 4.1.

Station	Height m	Hardware	Observation types		
			p	T	H_r
BRAE	1508.5	Mechanical thermo-hygrograph		✓	✓
GINA	2003.5	Mechanical thermo-hygrograph		✓	✓
GRIM	1596.5	Mechanical thermo-hygrograph		✓	✓
GRUB	1843.8	Mechanical thermo-hygrograph		✓	✓
RAND	1406.4	C10		✓	✓
SBAL	1482.7	CAPTEC	✓	✓	✓
SSTU	2181.8	David Instruments	✓	✓	✓
STAL	805.1	Sommer	✓	✓	✓
SUST	678.4	HMP 35A		✓	✓

Tab. 4.1: Meteorological equipment of the non-permanent WATEC campaign stations in July 2005. The observation types are air pressure p, air temperature T and relative humidity H_r. All stations measured temperature and the high variable relative humidity. The more conservative parameter air pressure was collected at three stations only, but covering the height range between 800 and 2200 m AMSL.

(a) Mechanical thermo-hygrograph installed nearby the GPS station GRIM (see Figs. 4.3 and 4.4 for the geographical location) protected from direct solar radiation and rainfall.

(b) Weather station of David Instruments (on the right hand side), mounted on the shore of the storage lake of Turtmann next to the GPS station SSTU (Leica System 500) (for the geographical location see Fig. 4.3 and the satellite visibility is given in Fig. 4.6(a)). The GPS antenna is put on a standard wooden tripod.

Fig. 4.5: Mechanical thermo-hygrograph (left panel), registering temperature and relative humidity, and the digital weather station of David Instruments (right panel), sensing temperature, humidity, pressure and wind.

VIZ Meteorological Systems Group of Sippican, Inc., designed for automatic upper air soundings, were utilized to measure pressure, temperature and relative humidity.

The temperature is measured with a thin rod thermistor ranging from –90 °C to +60 °C with an accuracy of ±0.2 °C (rms) and a resolution of 0.1 °C. A carbon element measures relative humidity between 5 and 100 % (within –50 °C and +40 °C) with 2 % rms and a resolution of 1 %. Both sensors exhibit a variation in resistance with the parameter being sensed. A capacitive aneroid provides highly accurate (±0.5 hPa with a resolution of 0.1 hPa), continuous pressure measurement over the entire synoptic range (1080 hPa to 3 hPa).[7] All meteorological parameters are sampled once per second throughout the flight.

Fig. 4.7 shows the preparation of a radiosonde at the non-permanent campaign station SNIK in St. Niklaus in the Mattertal (see Fig. 4.3). During the first field campaign, seventeen radiosondes were launched from seven different locations distributed over the whole project area collocated with GPS sites (see the stations GRUB, RAND, SNIK, SSTU, STAL, SUST and ZINA on the map in Fig. 4.3). This data was later used for validation purpose of the refractivity profiles as well as for the time series of integrated path delays.

[7] All sensors are pre-calibrated at the factory and require no ground baseline check prior to launch. The instrument is powered by a single water-activated battery.
For further information concerning the microsonde's technical specifications see http://www.-sippican.com.

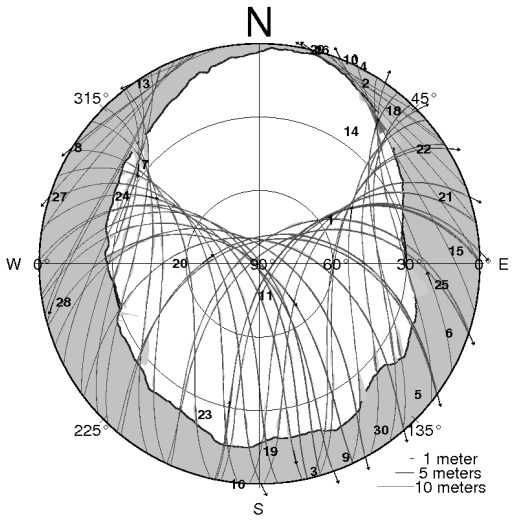

(a) Pseudorange multipath skyplot for station SSTU (Leica 500).

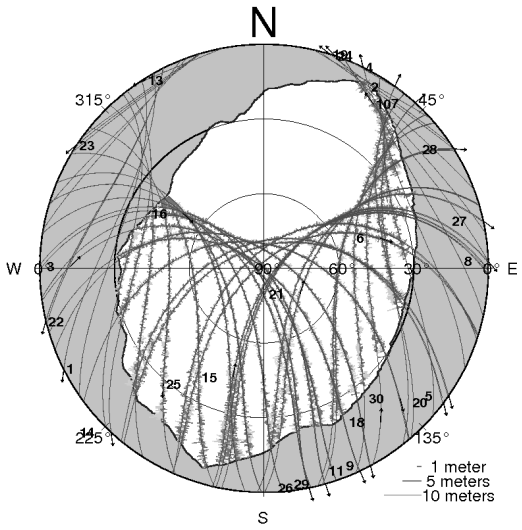

(b) Pseudorange multipath skyplot for station SNIK (Trimble NetRS).

Fig. 4.6: Multipath maps for the carrier frequencies f_1 (dark colored) and f_2 (light colored) observed at stations SSTU and SNIK. The multipath is plotted for every epoch perpendicular to the satellite tracks.

(a) A. Somieski (left) and M. Troller (right) preparing a Mark II microsonde for launch.

(b) Countdown for radiosonde launch next to the wastewater treatment plant in St. Niklaus.

Fig. 4.7: Preparation of a radiosonde launch at the station SNIK in the Mattertal (see map in Fig. 4.3). The skyplot in Fig. 4.6(b) depicts the narrowness of the valley.

4.4 The October 2005 field campaign

The second field campaign took place from 20 to 26 October, 2005. In the Appendix, in Fig. A.3, p. 181, the weather development is characterized by the time series of a few meteorological parameters observed at the ANETZ stations in the project area, Evolène and Visp. After a decrease of air pressure, a sudden increase on the fourth day indicates a slow going cold front passage and the sinking air behind the front. Also, water vapor pressure raised on that day, followed by an almost continuous decrease. The cold front passage was accompanied by heavy rainfall due to convectional uplift mechanisms of the wet air (see e.g. Grebner, 1996 and Fig. 4.8) on October 23, 2005. These showers of rain were measured at both stations. Afterward, especially at Evolène, the relative humidity decreases continuously down to 40 % from the middle until the end of the campaign.

Compared to the time series of July 2005 (see in the Appendix, Fig. A.2 on p. 180), the daily variations of the air pressure parameter at station Visp in the main valley is not very pronounced. The cold front passage dominates the behavior of the measurements at both stations. According to Liou and Huang (2000); Liou et al. (2000b) such extreme weather events will be reflected in the time series of GPS derived wet path delays (see Chapter 8).

Weather fronts move over a fixed point on the earth over a period of one to several hours (see Fig. 4.8). During this time, the integrated refractivity, proportional to the ray path delay, undergoes rapid variation. The cold front nose height is typically between 0.5 and 3.5 km and the dry height between 2 and 6 km. The slope can be 0.3 to 1.5 °, and the fronts pass with 38 to 63 kmh^{-1}. It causes a bias in the estimated station position (see e.g. Gregorius and Blewitt, 1999). Therefore, this campaign data requires careful analysis. However, the results will give new insight in GPS processing during weather front passages.

Analyzing the data of Scanning Multichannel Microwave Radiometers, Katsaros et al. (1989) found that a strong gradient in integrated atmospheric water vapor is a good indicator of surface locations of fronts in mid-latitude cyclones. A second significant indicator of frontal activity is precipitation. Melfi et al. (1989) examined the detailed structure of atmospheric fronts using ground-based Raman lidar moisture observations. The study revealed the importance of moisture measurements for investigating rapidly evolving atmospheric processes such as the movement and structure of fronts. The data clearly showed the presence of an elevated nose within the frontal zone close to the surface. Fluctuations in the lidar measured moisture mixing ratio within the sloping frontal zone were suggested as an indication of either turbulence or the presence of gravity waves (Melfi et al., 1989).

A case presented by de Haan et al. (2004) showed that the amount and temporal changes of water vapor in a convective system can be estimated by GPS, which, together with information on flow, gives insight into the possibility of the occurrence of a weather situation with intense precipitation events. But Huang and van Graas (2007) found a close correlation between large tropospheric spatial decorrelation errors and severe weather conditions, what has to be considered as well.

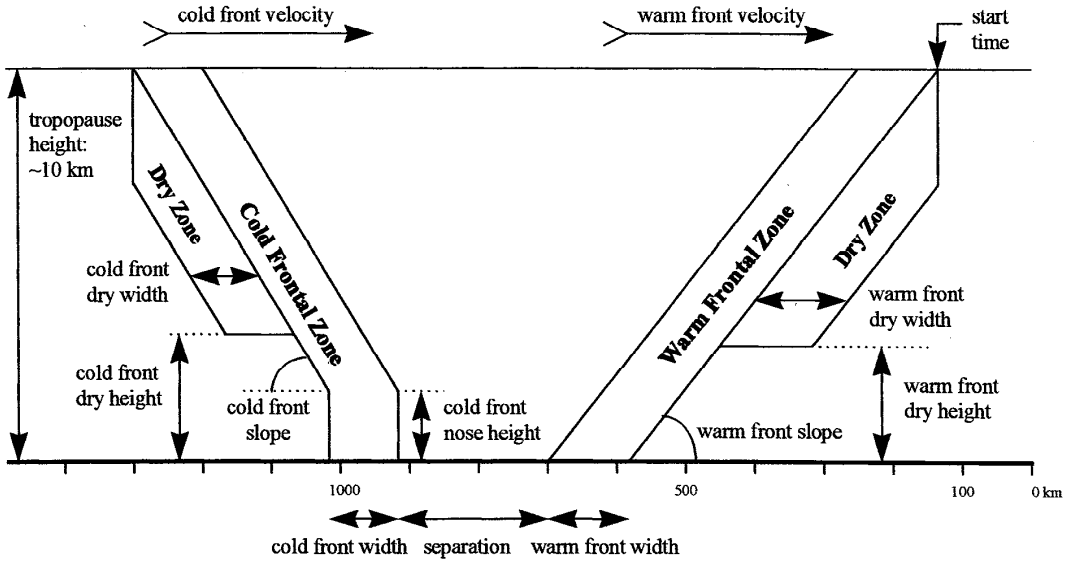

Fig. 4.8: Geometrical model parameters for cold and warm fronts (Gregorius and Blewitt, 1999, p. 15 263). Note that the model is largely idealized and that in this diagram the vertical scale is greatly exaggerated. A horizontal scale bar is shown to visualize the approximate dimensions of typical weather fronts.

4.4.1 GPS Network

In addition to fourteen sites occupied in the campaign in July 2005 by non-permanent GPS systems (see Sec. 4.3.1), eight more permanent stations were operating in October 2005. At the same time, a measurement campaign with nine GPS stations of the Swiss Federal Office of Topography swisstopo took place within the project area concentrated around the village of Turtmann in the main valley (see also Brockmann, 2007). The tabulated summaries of the hardware configuration and GPS equipment in use during the campaign are given in Appendix B in Tabs. B.1, B.2, B.4, B.4 and B.5.

Fig. 4.10 shows two stations of the non-permanent three-dimensional geodetic network Turtmann, which was operated by the Swiss Federal Office of Topography swisstopo during the time of the field campaign in October 2005. In contrast to the tripod installations of the WATEC campaign stations (see the example at the storage lake of Turtmann in Fig. 4.5(b) on p. 48), the GPS antennas of the Turtmann network were mounted on robust pillar-like steel structures.

The influence of different local environmental effects on the observations was studied by means of pseudorange multipath maps. Multipath is calculated from the RINEX observation files with the GPS preprocessing software teqc (see Estey and Meertens, 1999). Figs. 4.11(a) and 4.11(b) show the examples for the two stations BRAE and SUST of the Turtmann network.

Especially at the second frequency f_2 the surroundings of the station at Susten (SUST) is very sensitive to multipath signals in the GPS pseudorange observations. For both stations a slight systematic increase of multipath effects can be recognized at lower elevations. In extreme conditions, this effects can reach up to 10 m for a

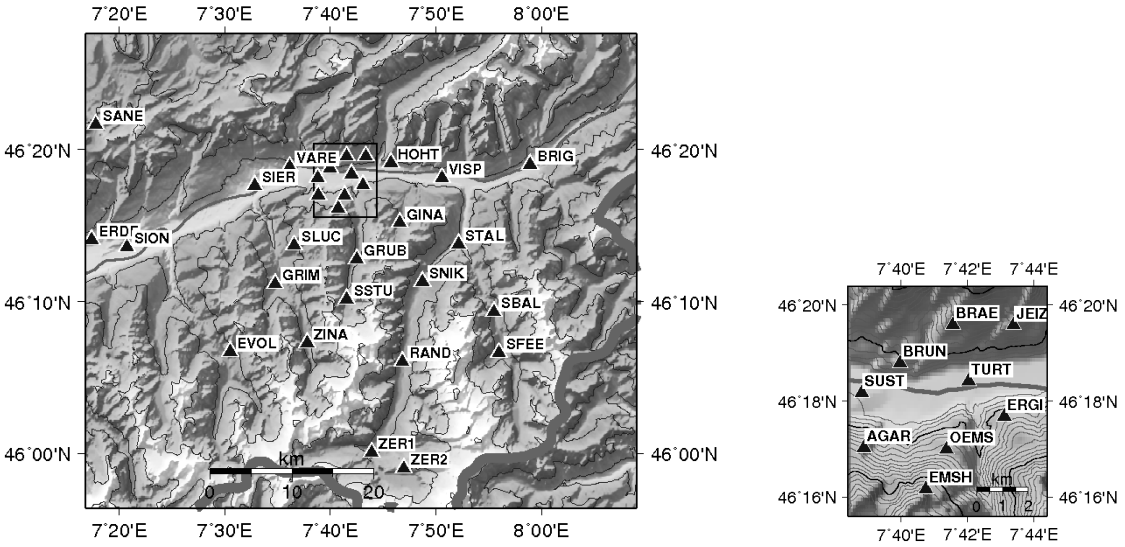

(a) The target area with GPS network for the processing of the campaign in October 2005. The campaign stations of this project are shown with the stations of the TURTMANN network (see Subfig. (b)). BRIG, SION and ZER2 are stations of the permanent network of Swissat, HOHT and ZER1 belong to the AGNES network of swisstopo.

(b) 100 m contour enlargement map of the black rectangle in Subfig. (a) with the locations of the nine GPS station sites of the 3-D network TURTMANN.

Fig. 4.9: GPS network in the project area during the field campaign in October 2005. Compared to the campaign in July, more stations were operated: Four additional permanent stations and all stations of the Turtmann remeasurement campaign (Fig. (b)).

single observation. To avoid an impact of such observations an elevation dependent weighting function will be introduced into the GPS data processing (see Sec. 5.2.3).

The data availability for the stations of the October 2005 campaign after the GPS processing is shown in Fig. 7.7(b) on p. 102. Furthermore, the remaining data after the pre-elimination of unusable baselines according to Sec. 7.2.4, p. 101, is given. Therefore, for a few stations in the project area only zenith path delays are available for GPS tomography without the corresponding double-differenced slant path residuals and the respective geometry.

(a) GPS site at Brantschen (BRAE) at 1509 m AMSL looking to the south-east.

(b) GPS station at Susten (SUST) at 678 m AMSL looking to the north.

Fig. 4.10: Station Brantschen and Susten of the geodetic Turtmann network during the October 2005 campaign. The stations were equipped with Trimble antennas TRM41249.00. The corresponding multipath skyplots are shown in Fig. 4.11.

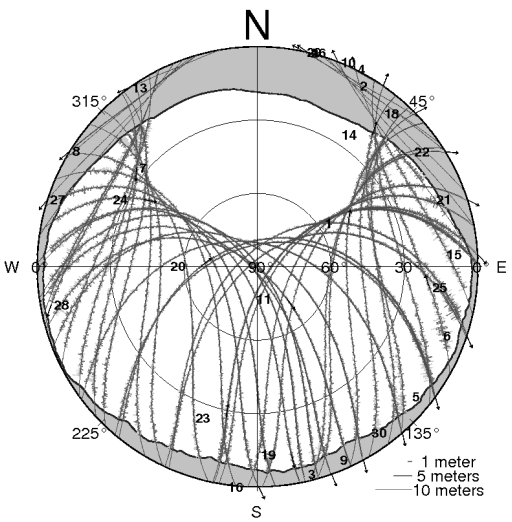

(a) Pseudorange multipath map for station BRAE in October 2005.

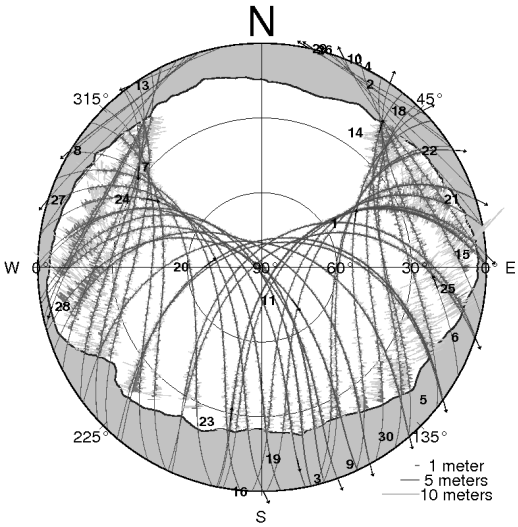

(b) Pseudorange multipath map for station SUST in October 2005.

Fig. 4.11: Multipath maps for the carrier frequencies f_1 (dark colored) and f_2 (light colored) observed at stations BRAE and SUST of the Turtmann network during one day. The multipath is plotted perpendicular to the tracks (curves with corresponding satellite PRN number) for every epoch and satellite.

4.4.2 Meteorological ground measurement network

The networks of permanent meteorological stations were complemented by thirteen non-permanent stations (see Fig. 4.12), four more than in the July 2005 campaign. They were mounted next to GPS receivers and operated for the campaign in October 2005. The main hardware components of these stations (network WATEC) are summarized in Tab. 4.2.

Concerning the permanent stations, the data of the same networks was available as in the July 2005 campaign: The automated meteorological network ANETZ from MeteoSwiss (including the station at Evolène and Visp next to GPS campaign stations), the network RESIVAL of the Service for Environmental Protection, state of Valais, and a selection of stations of the IMIS network of the Swiss Federal Institute for Snow and Avalanche Research SLF, Davos.

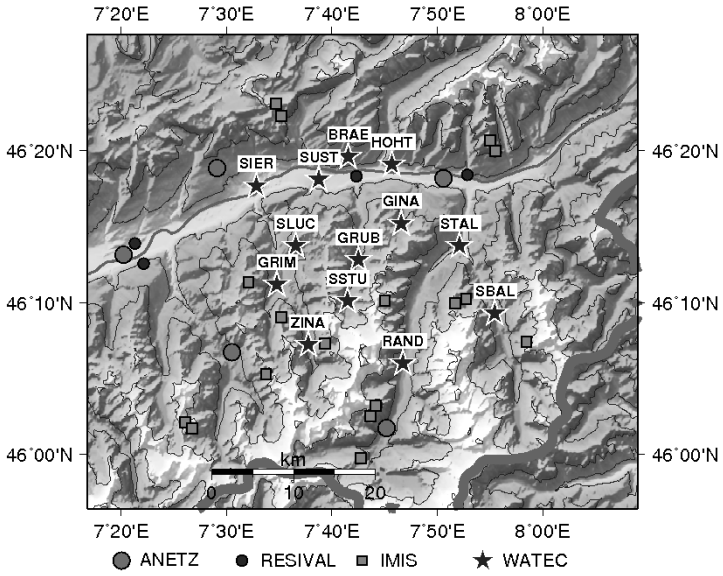

Fig. 4.12: Locations of the meteorological measurement systems during the field campaign in October 2005. The equipment of the non-permanent WATEC stations is given in Tab. 4.2.

4.4.3 Radiosondes

During the second field campaign, 33 radio soundings were carried out from six different launch sites (see the stations GRUB, SNIK, STAL, SUST, VISP and ZINA in Fig. 4.9) within the project area.[8] There was a particularly large number of launches, up to three times a day, at station SUST at 728 m AMSL in the main valley in the northwest of the project area. This was to achieve a high temporal resolution of reference data for this location. After the validation and outlier detection with the COSMO data (see Sec. 6.4.1 on pp. 78f.) a few of the soundings were excluded from further comparison processes.

[8] For further information on the radiosonde type see Sec. 4.3.3.

Station	Height m	Hardware	Observation types p	T	H_r
BRAE	1508.6	Mechanical thermo-hygrograph		✓	✓
GINA	2003.5	Mechanical thermo-hygrograph		✓	✓
GRIM	1596.9	Mechanical thermo-hygrograph		✓	✓
GRUB	1844.2	Mechanical thermo-hygrograph		✓	✓
HOHT	935.0	Sommer	✓	✓	✓
RAND	1406.9	C10		✓	✓
SBAL	1483.1	CAPTEC	✓	✓	✓
SIER	551.2	Mechanical thermo-hygrograph		✓	✓
SLUC	2186.7	Mechanical thermo-hygrograph		✓	✓
SSTU	2182.3	David Instruments	✓	✓	✓
STAL	805.6	HMP 35A		✓	✓
SUST	678.0	Sommer	✓	✓	✓
ZINA	1693.7	CAPTEC	✓	✓	✓

Tab. 4.2: Meteorological equipment of the non-permanent WATEC stations in the October 2005 field campaign. Air temperature T and relative humidity H_r were measured at each station. Some stations distributed over the entire project area provided also air pressure p observations.

4.4.4 Solar Spectrometry for comparison purpose

In the second field campaign, a portable prototype of a solar spectrometer was deployed for the determination of tropospheric water vapor with high precision for comparison purpose. The Geodetic Mobile Solar Spectrometer (GEMOSS) was mounted together with a weather station at the AGNES site HOHT in the main valley in the north of the project area (see Figs. 4.9(a) and 4.12).

GEMOSS is based on high-resolution absorption measurements with a broadband solar spectrometer (see e.g. Johns, 1965). It allows the simultaneous measurement of numerous single vibrational-rotational absorption lines in the wavelength range between 728 nm and 915 nm. The total error in the zenith wet path delay is estimated at the 3 mm level. This represents an excellent accuracy, which allows for a reliable correction of observations for high-precision applications. Further characteristics and principles of this measuring system are described in detail in Sierk et al. (1997); Sierk (2001); Somieski (2005).

(a) The rotating sensors of the Geodetic Mobile Solar Spectrometer GEMOSS are protected by a transparent dome.

(b) Installation of GEMOSS on the terrace of the house. The GPS station HOHT of the AGNES network is mounted on its roof.

Fig. 4.13: The Geodetic Mobile Solar Spectrometer (GEMOSS) mounted at the AGNES site HOHT in the center north of the project area (see Fig. 4.9(a)).

Chapter 5

Data preprocessing

5.1 Introduction

The following data has to be prepared and preprocessed for the GPS tomographic analysis using the software package AWATOS (see Sec. 3.2):

- raw data from the GPS measurements (from the campaign stations as well as from selected national and international permanent networks) (see Sec. 5.2)
- data from the meteorological measurement readings, acquired during the campaigns and from automatic networks (see Sec. 5.3)
- data from the radiosonde launches for validation purposes
- data from the solar spectrometer GEMOSS (operated only during the field campaign in October 2005) for validation and comparison purposes

Additionally, data from the operational numerical local weather model COSMO-7 is preprocessed and prepared for validation and comparison purposes, which is described in Chapter 6. Each class of data named above needs specific treatment. This will be discussed briefly in the following sections. Also, estimated parameters of the data quality from the pre-analysis and comparison studies will be shown. The main differences in the data processing and the preliminary results between the two field campaigns will be highlighted as well.

5.2 GPS data processing

5.2.1 Overview

The GPS processing has to be carried out in order to obtain high-quality tropospheric parameter estimates (ZPD with or without horizontal gradients, see also Sec. 2.4.4), satellite orbits for the ray tracing part in AWATOS (see Sec. 3.2.3) and the double-difference residuals to reconstruct the slant path delays (see Sec. 3.2.1).

Before the GPS data can be introduced into the GPS postprocessing software package, it mainly has to be translated into the receiver independent exchange format RINEX (Gurtner and Estey, 2006) and homogenized. For that purpose, mainly the multi-purpose preprocessing software toolkit teqc (see Estey and Meertens, 1999) from the University NAVSTAR Consortium (UNAVCO) was chosen. It offers trans-

lation, editing and quality check of GNSS data[9]. The Bernese GPS Software Version 5.0 (see Dach et al., 2007) was then used to estimate the station coordinates and to generate path delays and double-differenced residuals, applying standard models analysis strategies (see e.g. Hugentobler et al., 2004).

The GPS observation files of the local campaign network in the canton of Valais were complemented by data from the automated GPS network of Switzerland (AGNES) and the national virtual reference station network of the company Swissat. Especially for the second campaign, stations of the geodetic network TURTMANN from the remeasurement campaign of swisstopo and the newly established permanent GPS network TECVAL of ETH Zurich were taken into account, too. For details regarding the different networks see in Appendix B, pp. 183f. Additionally, data from permanent GPS stations of international organizations (e.g. IGS, EUREF) and from french networks (RGP, REGAL) was introduced to establish a suitable reference frame for accurate and reliable results. The complete GPS network for the first campaign in July 2005 is shown in Fig. 5.2(a) and the one for the campaign in October 2005 in Fig. 5.2(b).

5.2.2 Criteria for fix station selection

By incorporating a few remote global tracking stations and thus some long baselines into the geodetic analysis of a regional GPS network, it is possible to resolve the absolute value of the zenith total delay at each station in the augmented network (see e.g. Duan et al., 1996; Klein Baltink et al., 2002). This approach delivers a pure GPS solution for precipitable water retrieval.

Different criteria can be set up to obtain high-quality results from the GPS processing and for comparable solutions for both campaigns. Based on the selected stations, a geodetic datum definition should be applicable, and an rms error verification can be carried out. Some requirements for meteorological GPS networks are mentioned in Barlag et al. (2005); de Haan (2006). The following conditions have to be considered when selecting the reference stations:

- They have to be the same in the July and October campaigns.
- They have to be stable in terms of coordinate repeatability and with long time series for accurate velocity determination (e.g. fixed stations from the IGS reference frame ITRF2000 for the datum definition of IGS00b). The standard deviation parameters for the three-dimensional spatial components can be obtained by e.g. the time corresponding freely available SINEX files from the combined IGS or EUREF solution.
- They should have run for the duration of both times seven days at least.
- They should span a large area by some long baselines to decorrelate the Up-component from the ZTD estimation (see e.g. Klein Baltink et al., 2002; Stoew and Elgered, 2005; Lawrence et al., 2006).
- The longest baselines should not extend 2000 km (for the ambiguity resolution).

[9] For further information see the website at http://facility.unavco.org.

Fig. 5.1 shows a suitable network of the reference stations used for further processing. The region covered is about 2000 km by 2000 km, with inter-station distances of up to 1000 km.

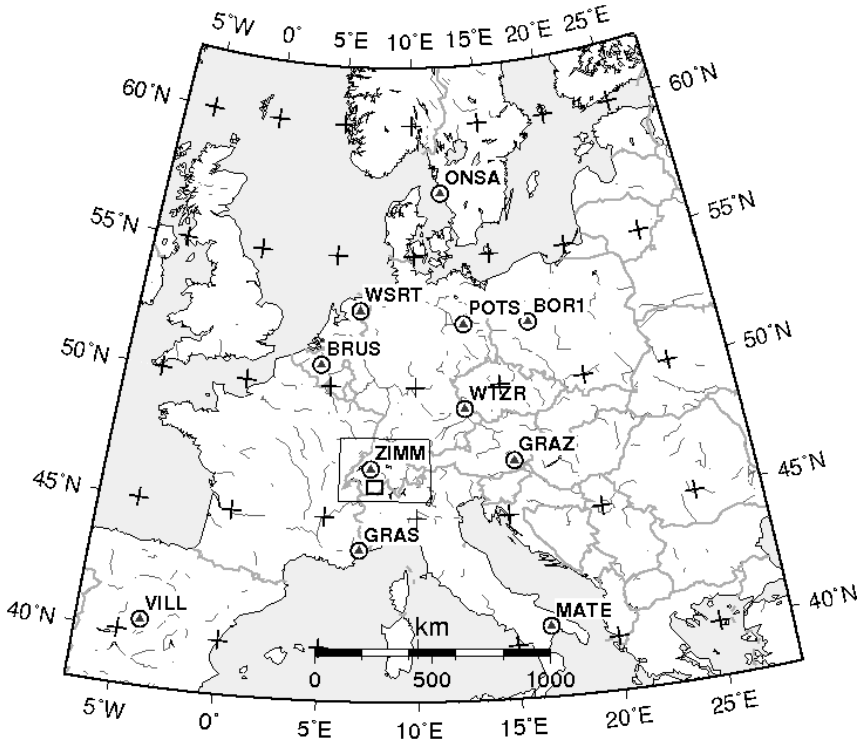

Fig. 5.1: Subset of the fix station network in Europe for the current IGS reference frame definition of IGS00b used for the GPS campaign data processing. The stations are labeled with their official four character abbreviations. The three-dimensional standard deviation for these stations is less than 7 mm. The frame of Figs. 5.2(a) and 5.2(b) is given by the larger black rectangle. The project area is located within the smaller black rectangle in the southwest of Switzerland between 46° and 47° North and 7° to 8° East.

5.2.3 Parameter settings in the Bernese GPS Software

The Bernese GPS Software Version 5.0 has been chosen for the processing of the GPS data due to its flexibility, modular design and state-of-the-art modeling characteristics (see also Sec. 2.4.4, pp. 29f.). Because the double-difference method is the basic observation type, the output can directly be integrated into the tomographic processing with the software package AWATOS (see Sec. 3.2.1).

Despite the Bernese GPS Software Version 5.0 is not designed for real-time parameter estimation, near real-time conditions can be simulated by introducing specific input files. Thus, the sensitivity of AWATOS to these conditions can be assessed. Adapted from the high-quality routine processing for double-difference GPS data analysis, the following processing strategies were chosen to generate the input information for small-scale, high-resolution GPS tomography:

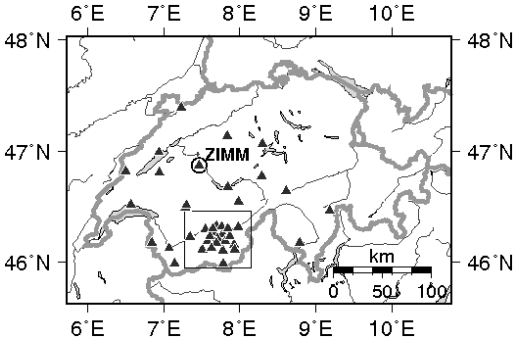

(a) GPS network within Switzerland for the campaign in July 2005. The seventeen high-density GPS campaign stations in the project area in the eastern part of the mountainous canton of Valais are supplemented by stations of the Swiss national permanent networks AGNES and Swissat.

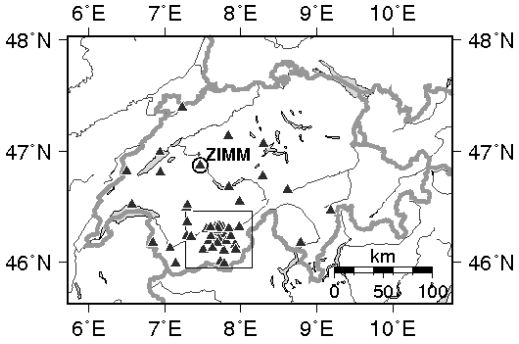

(b) GPS network in October 2005. Especially within the project area itself, there are ten more stations compared to the setup in July 2005 (see Subfig. (a)): The permanent network TECVAL as well as the campaign stations of the three-dimensional geodetic network TURTMANN.

Fig. 5.2: Representation of the Swiss part of the GPS network for the Bernese processing. The GPS network in Switzerland is a combination of the non-permanently installed campaign stations and mainly the national permanent network AGNES of swisstopo and Swissat's GPS network. The location of the IGS reference frame station at Zimmerwald (ZIMM) is labeled and marked with a circle. The black rectangle in Figs. (a) and (b) represents the border of the project area (see also Figs. 4.3 and 4.9(a)).

- Double-differenced ionosphere-free L_{3pq}^{rs} phase observations (see Eq. 2.21)
- Combined IGS orbits (see e.g. Beutler et al., 1995b) from the Crustal Dynamics Data Information System (CDDIS)[10] prepared according to Sec. 5.2.3
- Daily coordinate solution constrained to the IGS00b version of the ITRF2000 reference frame
- Hourly estimation of unconstrained tropospheric ZPD parameters with and without horizontal gradients of different temporal resolution
- A priori model for the ZTD parameters: Dry Niell, mapping function for the remaining part: Wet Niell (see also Sec. 2.4.3) The settings have to be stored for the later reconstruction of the slant path delays within the tomographic processing (see also Sec. 3.2.1, p. 37)
- 3 ° cutoff angle (a few stations were configured to measure only down to 5 ° or 10 ° elevation for memory saving purpose) with elevation dependent weighting ($cos(z)$)
- 30 s data sampling (some campaign stations measured with 1 s, 10 s and 15 s observation interval, the data from the IGS and other permanent networks are usually already pre-sampled to 30 s)

[10] For further information on the CDDIS GNSS data archive, see the website at http://cddis.gsfc.nasa.gov.

- Incorporation of ocean tide loading corrections
- Baseline definition: OBS-MAX (i.e. maximum number of similar observations to two identical satellites from two receivers), no predefined baselines
- IGS elevation-dependent relative type specific antenna phase center variation model (`PHAS_COD.I01`) supplemented by data of the non-IGS antenna types operated during the campaigns
- Normalized phase residuals (see section below), introduced into Eq. (3.6b), p. 37, of the tomographic reconstruction algorithm

Bar-Sever (1996) showed that processing low elevation cutoff angles leads to better results for ZTD estimation compared to water vapor radiometer measurements. This is mainly due to a more realistic determination of the simultaneously estimated geodetic height component of a GPS station. But changing the elevation cutoff angle modifies the systematic biases due to multipath effects, phase center variations of the antenna and a different satellite constellation (see e.g. Geiger, 1987, 1988; Elósegui et al., 1995; Stoew and Elgered, 2004).

Obtaining phase residuals

The residuals correspond to the difference between the adjusted double-difference observations and the raw observations. Therefore, the sum of the actual observation vector plus the residual vector equals the adjusted observation vector. In the Bernese GPS Software, these residuals are called "real" residuals (Dach et al., 2007).

"Normalized" residuals, though, are residuals divided by the square root of the corresponding diagonal element of the co-factor matrix of the residuals (see Eq. 5.1). This cofactor matrix is the difference between the inverse weighting matrix (or covariance matrix) of the actual observations ($\mathbf{P^{-1}}$) and the cofactor matrix of the adjusted observations ($\mathbf{D(y)}$).

$$v_{norm}(i) = \frac{v(i)}{\sqrt{\mathbf{D_{ii}(v)}}} \tag{5.1}$$

with

$$\mathbf{D(v)} = \mathbf{P^{-1}} - \mathbf{D(y)}$$
$$\mathbf{D(y)} = \mathbf{A}\left(\mathbf{A^T P A}\right)^{-1}\mathbf{A^T}$$

$v_{norm}(i)$	normalized residual of observation i
$v(i)$	real residual of observation i
$\mathbf{D(v)}$	cofactor matrix of the residuals
$\mathbf{D_{ii}(v)}$	diagonal element of $\mathbf{D(v)}$ for observation i
$\mathbf{P}$	weighting matrix of the actual observations
$\mathbf{D(y)}$	cofactor matrix of the adjusted observations

Usually, "normalized" residuals are computed for outlier detection. For GPS tomography, it is important to include very low elevation measurements for the ray

tracing (see Sec. 3.2.3, p. 39), but to reduce the impact of errors at these angles due to improper tropospheric models, mapping functions and multipath effects (see also Spilker, 1996). The algorithm for "normalized" residuals is performing such an attenuation.

Considering loading effects

The estimates of the tropospheric zenith path delay and of the station height are highly correlated (see e.g. Elósegui et al., 1998; Rothacher and Beutler, 1998; Rothacher et al., 1998; Dach and Dietrich, 2000; Ohtani and Naito, 2000; Dong et al., 2002; Haefele et al., 2004). On the one hand, low elevation data and long baselines have to be introduced into the processing to decouple height and troposphere parameters. On the other hand, long baselines in double-difference processing are very sensitive to site displacements. In terms of site displacement modeling, the tectonic plate motion, solid earth tides, pole tides and permanent tides (see e.g. Farrell, 1972) are taken into account.

Furthermore, the ocean tidal loading effects (see e.g. Scherneck, 1991, 1993) are calculated using the coefficients from the GOT00.2 model, an update of GOT99.2b (see e.g. Ray, 1999; Allinson et al., 2004; Urschl et al., 2005; Bos and Scherneck, 2007). The ocean loading effect has a periodic influence on station heights with major frequencies in the diurnal and semi-diurnal band and with amplitudes up to several centimeters (Shum et al., 1997; Dach and Dietrich, 2000; Penna and Stewart, 2003).

Without loading corrections, a significant amount of the relative vertical tidal motion of the station would be absorbed in the hourly tropospheric delay estimates (see Dragert et al., 2000). Models for atmospheric loading effects (see e.g. Chapman and Lindzen, 1970; van Dam et al., 1994; Sun et al., 1995), non-tidal ocean loading, post-glacial rebound or varying ground water level effects are not applied within the Bernese GPS Software Version 5.0, because they are rather small (Dach et al., 2007).

Preparation of earth orientation, GNSS orbit and satellite clock information

The ZTD errors caused by orbit uncertainties are correlated both temporally and spatially, meaning that observed rapid changes and differences between nearby GPS sites have a high "common mode rejection" of orbit induced errors (see e.g. Dodson and Baker, 1998; Stoew and Elgered, 2004). This is a critical issue especially in high dense GPS networks like the campaign networks in the project area. By processing also distant stations from the IGS reference frame network and applying the OBS-MAX strategy for baseline generation (see Sec. 5.2.3), this problem can be addressed and sorted out to a great extent.

In order to investigate the possibilities and limitations of near real-time GPS tomography, orbit types with shorter latency but lower accuracy than final products have to be considered and carefully analyzed. Baueršíma (1983) published a rule of thumb for the error Δx in a component of a baseline of length l as a function of an orbit error of size ΔX:

$$\Delta x \approx \frac{l}{d} \cdot \Delta X \approx \frac{l}{2 \cdot 10^7\, m} \cdot \Delta X \tag{5.2}$$

The parameter $d \approx 2 \cdot 10^7\, m$ stands for the approximate distance between the satellite system and the survey area. Assuming an orbit error ΔX of 1 m the error in a component of a baseline of length 100 km would be approximately 5 mm (see also e.g. Kaplan and Hegarty, 2006).

In this section, the processing steps for the preparation of the mandatory earth orientation, GNSS orbit and clock data are discussed (see for detailed information Dach et al., 2007). An algorithm was developed to proceed with the different kinds of orbit products from the International GNSS Service (IGS) (see e.g. Beutler et al., 1999), from final products to real-time broadcast data (see e.g. Hugentobler et al., 2004; Dow et al., 2005 and Tab. C.1 on p. 194 in the Appendix).

IGS products support scientific activities such as improving and extending the International Terrestrial Reference Frame (ITRF) maintained by the International Earth Rotation and Reference Systems Service (IERS), monitoring deformations of the solid Earth and variations in the liquid Earth (sea level, ice sheets, etc.) and in Earth rotation, determining orbits of scientific satellites and monitoring the troposphere and ionosphere. Especially in terms of frequency stability of the satellite clocks, the precise products (final, rapid and ultra-rapid) lead to a significant improvement for further processing compared to the broadcast orbits (see also e.g. McCaskill et al., 1994). The error in the broadcast orbits is amplified by diurnal as well as by annual variations (see e.g. Warren and Raquet, 2003).

The term "broadcast ephemerides" refers collectively to the predicted GPS satellite positions that are contained in the Navigation Message, which is transmitted by each GPS satellite (see e.g. King et al., 1987). Therefore, the broadcast ephemerides are available in real-time, but they have an accuracy of "only" about 1.6 m (see in the Appendix, Tab. C.1 on p. 194). The precise ephemerides, however, have an accuracy of a few centimeters. The final products are available within about two weeks. Latencies for so-called rapid and ultra-rapid products are below one day and three hours, respectively.

The combined IGS ultra-rapid products are issued twice every day with a delay of three hours after the end of the included data interval. They are based on solutions from up to seven different IGS Analysis Centers. The main reason for generating ultra-rapid products are the requirements, both in timeliness and accuracy, for near real-time atmospheric monitoring, e.g. for weather predictions (see also e.g. Kruse et al., 1999; Ge et al., 2000; Gendt et al., 2001; Kruse, 2001; Springer and Hugentobler, 2001; Klein Baltink et al., 2002; Fragner and Weber, 2003; Iwabuchi et al., 2006; Smith et al., 2007).

Each ultra-rapid orbit file covers 48 hours. The first 24 hours are based on actual GPS observations (real orbits), the second 24 hours are extrapolated (predicted orbits). With an accuracy below one decimeter in the predicted part, they are considerably better than broadcast orbits (see Tab. C.1). With this orbit quality, Springer and Hugentobler (2001) demonstrated the possibility of estimating tropospheric zenith path delays with a precision of 7 mm. This corresponds to approximately 1 mm of precipitable water vapor (see also Eq. 2.16). Therefore, the ultra-rapid product can be considered as a valuable contribution to high-precision

near real-time GPS processing and for applications in terms of numerical weather prediction (see e.g. Douša, 2001; Gendt et al., 2004; de Haan, 2006).

The following processing steps were carried out to obtain standardized orbit files for both the GPS data analysis and the GPS tomography (see Sec. 3.2.1 for the slant path delay reconstruction algorithm).

1. Download earth rotation information (erp files) in IERS format and generate Bernese ERP/IEP files with the program POLUPD.
2. Download GPS orbit and clock information (sp3 files, sampled at 15 min) or broadcast ephemerides files (postprocessed with RXNPRE). Then generate Bernese tabular orbit files (TAB) and a priori satellite clock information files (CLK) with the output of step 1 using the program PRETAB (twelve hour interval for second degree polynomials).
3. Generate standard orbit files (STD) and summary files combining the tabular orbit files of step 2 and the earth rotation information files of step 1 using the program ORBGEN.
4. Generate daily precise orbit files (PRE) on the basis of a 30 s interval from the output of the previous steps using the program STDPRE.

The ERP/IEP files, the CLK and the STD files are used in the further processing of the Bernese GPS Software, whereas the PRE files are compiled for the future work in the tomographic software AWATOS. The downloaded files (erp and sp3) are so-called IGS combined products from the GNSS data analysis centers. They are available in different quality: final, rapid and ultra-rapid. In Appendix C, Tab. C.1 on p. 193 gives an overview of the available products[11].

5.2.4 Network solutions

The GPS processing is done by performing a state-of-the-art set up. The final daily solutions for the coordinate estimation were obtained processing all the available orbit types described in Tab. C.1. The quality of the estimated coordinates are characterized by the formal rms error with respect to the reference frame and the mean standard deviation (σ) of each component for the stations within the project area summarizing the seven days of both campaigns. They are listed in Tabs. 5.1 and 5.2.

The data of the project stations, which was used for the double-differenced baseline generation with final orbits, is given in Fig. 7.7(a) for the July campaign and in Fig. 7.7(b) for the October 2005 campaign. Processing broadcast orbits caused insignificantly more data gaps due to outlier rejection.

The results shown in Tabs. 5.1 and 5.2 reveal that processing final or rapid orbits horizontal coordinates with an accuracy of less than 1.8 mm can be achieved. The error in the vertical component does not exceed 7.8 mm. If ultra-rapid products are used, the standard deviation of Northing (N) and Easting (E) rises about 30 % in

[11] Source: http://igscb.jpl.nasa.gov.

Jul 8–14, 2005	stations	mean rms			mean σ		
		N	E	Up	N	E	Up
	#	mm	mm	mm	mm	mm	mm
final orbits	21	0.43	0.33	2.30	1.80	1.48	7.77
rapid orbits	21	0.43	0.33	2.30	1.79	1.42	7.46
ultra-rapid orbits	21	0.44	0.34	2.39	2.30	2.00	9.10
broadcast ephemerides	21	0.67	0.52	3.68	3.75	10.05	16.12

Tab. 5.1: Mean formal rms error and standard deviation (σ) of the daily solutions of the GPS station coordinates within the project area. The data was processed with different orbit types for the duration of the field campaign in July 2005.

Oct 20–26, 2005	stations	mean rms			mean σ		
		N	E	Up	N	E	Up
	#	mm	mm	mm	mm	mm	mm
final orbits	29	0.37	0.28	1.82	1.25	1.17	7.76
rapid orbits	29	0.36	0.28	1.81	1.37	1.17	7.78
ultra-rapid orbits	29	0.40	0.30	1.93	2.28	2.39	7.69
broadcast ephemerides	29	0.53	0.42	2.75	2.18	8.76	12.69

Tab. 5.2: Mean formal rms error and standard deviation (σ) of the daily solutions of the GPS station coordinates within the project area. The data was processed with different orbit types for the duration of the field campaign in October 2005.

the July 2005 campaign and more than 60 % in the October 2005 campaign. The negative impact of the lower orbit accuracies does not affect the Up-component in this order of magnitude. The rms and σ values rise for the broadcast results because they are not postprocessed and reanalyzed (and actually no real IGS products) and the ephemerides have a much lower accuracy. The three-dimensional accuracy of all coordinate estimates of the ground stations degrades significantly for this processing type.

The estimation of the hourly retrieved tropospheric path delays from the GPS observations and its rms error is of particular interest for this study. Bock et al., 2002b found that computing coordinate solutions over 24 hour sessions is a method for smoothing out most of the effects of the short-term variability in tropospheric water vapor. Despite this, only an accuracy of about 7 to 10 mm σ (see Tabs. 5.1 and 5.2) is achieved in the vertical coordinate processing precise products, mainly due to the mismodeling of the tropospheric path delay.

Fig. 5.3 presents time series of ZTD at the non-permanent campaign GPS station SLUC during the field campaign in October 2005 as an example. The GPS system was installed at the mountain station of the funicular railway in St-Luc (for the geographical location see map in Fig. 4.9(a)). The mean value for the seven days of

data and the mean formal rms error were calculated. GPS orbits with three different qualities were processed: final orbits, ultra-rapid orbits and broadcast ephemerides.

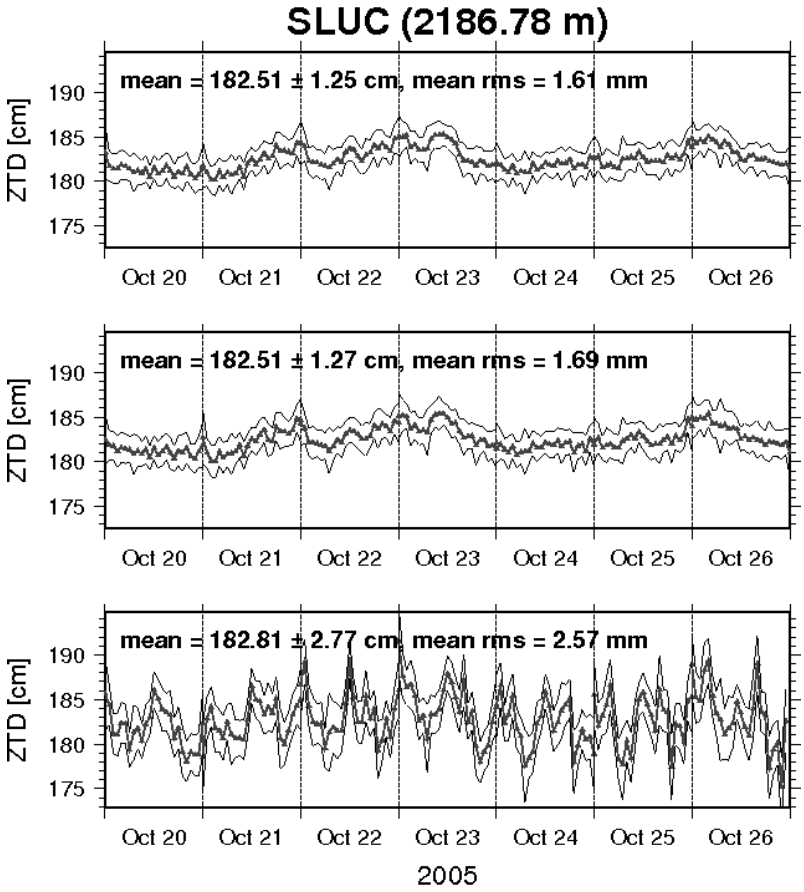

Fig. 5.3: Zenith total delay time series with rms error bar from GPS postprocessing of the station at St-Luc (SLUC) in October 2005. Final orbits (top panel), ultra-rapid orbits (middle panel) and broadcast ephemerides (bottom panel) have been used.

The standard deviation of the daily solution of the Up-component at station SLUC during the seven days of the October 2005 campaign, processed with final orbits, was 5.5 mm, with ultra-rapid orbits 5.8 mm and with broadcast ephemerides almost twice as large (8.6 mm). Depending on the antenna and receiver types of the campaign stations, there was a slight correlation discovered between the trend of the daily coordinates and the ZTD estimations. A positive correlation can be detected at e.g. Fig. 5.4 for the daily Up-component estimation along the cold front passage on October 23 and 24 compared to the hourly ZTD time series in Fig. 5.3. The data derived was recorded from the Leica GPS system mounted at station SLUC. Pacione and Vespe (2003) detected annual and semiannual signatures in the ZTD residuals time series that can be assigned to similar signals found in the GPS coordinate time series. To avoid the dependency of this correlation related to the antenna and receiver types, absolute antenna phase center variation models or multipath stacking maps should be introduced in the GPS processing (see e.g. Iwabuchi et al., 2004; Shoji et al., 2004). This could not have been carried out within this work due to the absence of data required.

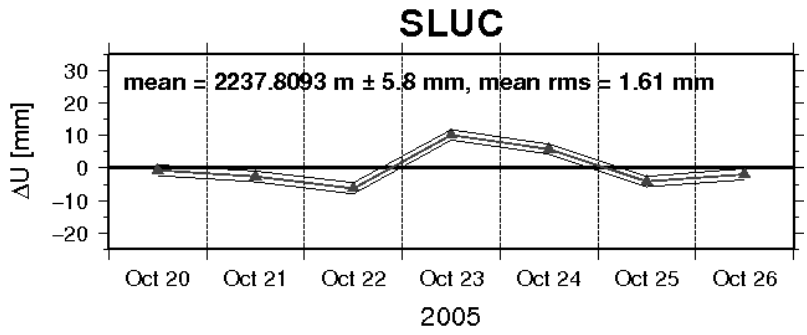

Fig. 5.4: Time series of the daily coordinate estimation (in WGS-84) with rms error bar. The results are obtained from GPS postprocessing of the station SLUC in October 2005. During this campaign, SLUC was equipped with a Leica 1200 System. Ultra-rapid orbits have been used.

The impact of different orbit types on the time series of hourly ZTD are similar to those on the Up-component of the coordinate estimations (see Tabs. 5.1 and 5.2). Only the analysis with broadcast ephemerides yields to unclear and unreasonable results. The ZTD time series shows an evident oscillation with semi-diurnal cycles and an amplitude of almost 3 cm (see also Warren and Raquet, 2003).

Although the specification given by the WMO (see e.g. de Haan, 2006) on ZTD accuracies for GPS meteorology is achieved (order of 10 to 15 mm), based on these results, processing broadcast ephemerides is not recommended because this leave erroneous patterns in the time series.

5.2.5 Section summary

The examination of the GPS data preprocessing for both field campaigns shows the following three major results in terms of different IGS data inclusion:

- Final and rapid orbits lead to a very similar outcome regarding the quality of the parameter estimations (coordinates, path delays and rms errors). The north component of all stations in the project are has a mean standard deviation of less than 1.8 mm, the east component varies within 1.5 mm and the Up-component is determined better than ±7.8 mm.
- Ultra-rapid orbits with accuracies half as good (see Tab. C.1 on p. 194) also show negligible formal rms values. Yet, the coordinate repeatability (σ) reveals a slightly reduced quality of the results with respect to those obtained with final or rapid orbits. The Up-component degrades about 17 % whereas the horizontal components are up to 60 % worse than the results with final or rapid orbits.
- Rocken et al. (1995) and others concluded in their studies that broadcast orbits do not have sufficient accuracy to retrieve tropospheric zenith path delays. This could be reconfirmed by the analysis of the preprocessed data.
  When processing with broadcast ephemerides, the parameters in the Up-direction as well as in horizontal plane are difficult to estimate. Variations

in the repeatability occur with the size of the double magnitude compared to ultra-rapid orbit and clock data processing. Especially, the repeatability of the Up-component, which is correlated with the estimated zenith total delay parameters, reaches more than 1 cm with regard to both campaigns. Furthermore, there are large variations in the ZTD time series introduced by systematic and random noise.

For near real-time applications with GPS meteorological objectives it is therefore recommended to use ultra-rapid precise orbital products for the parameter estimation in the GPS processing.

5.3 Meteorological data processing

The pressure, temperature and humidity measurements from the meteorological systems mounted and operated in the project area during the field campaigns (Sec. 4.3.2 and Sec. 4.4.2) were supplemented by a selection of additional data:

- from the national network ANETZ (Fig. 5.5), operated by MeteoSwiss,
- the regional network IMIS (Interkantonales Mess- und Informationssystem), operated by the Swiss Federal Institute for Snow and Avalanche Research, Davos (data of temperature and humidity for every 30 min), and
- some international radiosonde launch sites (Fig. 5.6).

The automatic monitoring network (ANETZ) is the most comprehensive monitoring network of MeteoSwiss. The first stations were put into service in the late 1970s. The majority of the ANETZ stations has been replacing conventional stations. The automatic monitoring network covers all regions and altitudes of Switzerland. In the case of ANETZ stations, all instrumental measurements are carried out automatically every 10 min and transmitted to the main computer in Zürich.

Weather parameters are recorded at certain stations by the observers between three to eight times a day. After checks and any necessary corrections, the hourly, daily, weekly, monthly and annual values are calculated from the data recorded every 10 min.[12] Furthermore, data from the local permanent network RESIVAL could be used. For the geographical location of the ANETZ, IMIS and RESIVAL networks during the two field campaigns see Fig. 4.4 on p. 47, and Fig. 4.12 on p. 54.

Data from official radiosondes of the World Meteorological Organization (WMO) network were included in the processing for the essential vertical information. The closest sites with respect to the project area were selected (see Fig. 5.6).

The data collection was prepared and processed using the software package COMEDIE (see Geiger et al., 1995; Hirter, 1998; Troller et al., 2002b). The control parameters were optimized with respect to the geometrical and sampling configuration of the whole network as well as in view of a high CPU time efficiency.

The mean values and the corresponding standard deviations (σ) for all collocated data are shown in Tabs. 5.4 and 5.5 for the July and October 2005 campaigns. X-

[12] See also http://www.meteoschweiz.admin.ch for further information about the automated meteorological monitoring networks of MeteoSwiss.

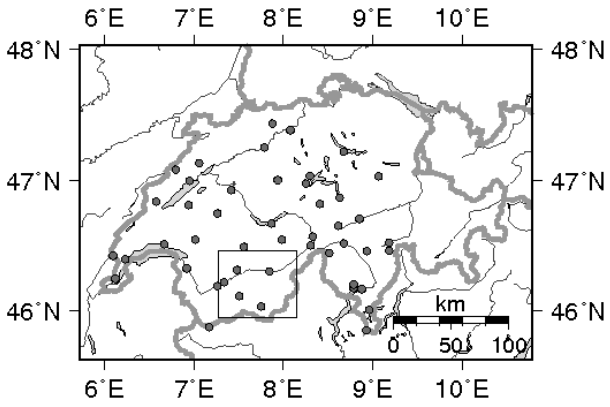

Fig. 5.5: Map of a part of the automated Swiss national ground meteorological network ANETZ (dots), taken into account for the meteorological data preprocessing. The network, operated by MeteoSwiss, provides data of pressure every hour and data of temperature and humidity every 10 min. The project area in the canton of Valais is marked by a black rectangle.

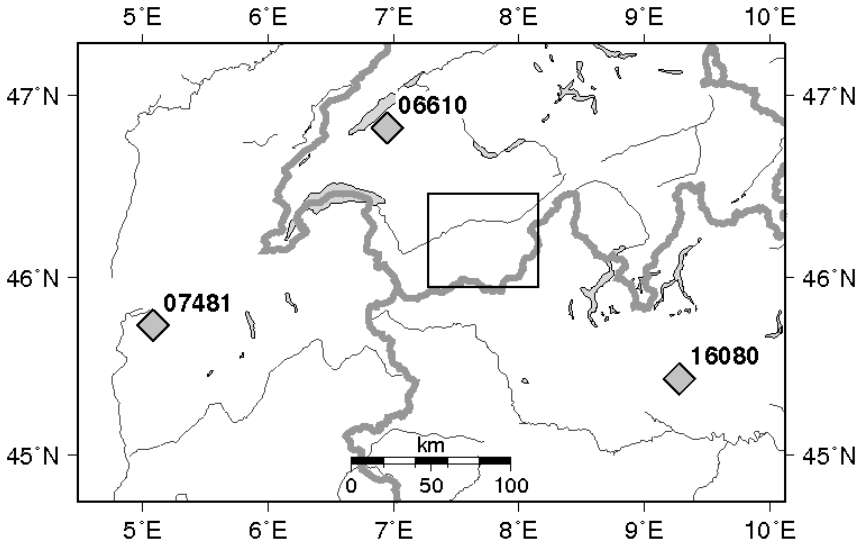

Fig. 5.6: WMO radiosondes used for the COMEDIE processing and the location of the project area (black rectangle). The data of radio soundings officially available from the world wide network usually includes pressure, temperature and humidity profiles twice a day. It covers the atmosphere from the launch site on the ground up to 30 km altitude. The labels of the sites on the map correspond to the WMO numbering (see Tab. 5.3).

direction of the horizontal gradients means Easting, Y-direction Northing and the constant temperature in the higher area (i.e. at and above the tropopause) is related to the typical temperature profile shown in Fig. 2.1(a), p. 13 (see also Troller et al., 2002b).

Comparing the July and October 2005 campaigns, all estimated values differ mainly in the horizontal gradients. In July, there was a horizontal pressure gradient

WMO No.	Site name	Country
06610	Payerne	Switzerland
07481	Nancy Essey	France
16080	Milano Linate	Italy

Tab. 5.3: WMO numbering of the international radiosonde launch sites.

July 2005	value	σ
pressure at sea level	1022.31 hPa	0.32 hPa
scaling height	7803.54 m	6.54 m
horizontal gradient in X-direction	-0.74 hPa/100 km	0.11 hPa/100 km
horizontal gradient in Y-direction	2.10 hPa/100 km	0.15 hPa/100 km
time gradient	0.07 hPa/h	0.03 hPa/h
temperature at sea level	20.41 °C	0.40 °C
temperature gradient	-6.85 °C/km	0.07 °C
horizontal gradient in X-direction	0.12 °C/100 km	0.06 °C/100 km
horizontal gradient in Y-direction	-0.16 °C/100 km	0.10 °C/100 km
time gradient	0.01 °C/h	0.01 °C/h
constant temperature in the higher area	-50.60 °C	0.65 °C
water vapor pressure at sea level	16.79 hPa	0.27 hPa
scaling height	2613.15 m	92.03 m
horizontal gradient in X-direction	0.09 hPa/100 km	0.14 hPa/100 km
horizontal gradient in Y-direction	0.24 hPa/100 km	0.19 hPa/100 km
time gradient	0.03 hPa/h	0.03 hPa/h

Tab. 5.4: Results of the meteorological data collocation from the July 2005 campaign using the software package COMEDIE.

in Y-direction (Northing) of +2.10 hPa/100 km, whereas in October, the gradient is in opposite direction (–3.60 hPa/100 km). Temperature and water vapor pressure gradients in July in contrast to October 2005 have opposite signs in X-direction. Overall, the absolute gradients in longitudinal direction are larger than in latitudinal direction. This is mainly due to the special west-east topography of the Swiss Alps in the target region. The temperature at sea level is higher in July 2005 with a larger vertical gradient than in October 2005. Also, water vapor pressure is slightly higher in July than in October.

After the successful collocation of the meteorological data, the obtained values were interpolated to the GPS station locations. In the tomographic processing, the total path delay is then separated into the dry and wet part. Furthermore, the total path delays from this collocated meteorological data were calculated and compared to the path delay time series of the other methods (see e.g. Sec. 5.4).

October 2005	value	σ
pressure at sea level	1022.28 hPa	0.32 hPa
scaling height	7870.47 m	7.73 m
horizontal gradient in X-direction	-0.17 hPa/100 km	0.10 hPa/100 km
horizontal gradient in Y-direction	-3.60 hPa/100 km	0.12 hPa/100 km
time gradient	0.03 hPa/h	0.03 hPa/h
temperature at sea level	16.94 °C	0.41 °C
temperature gradient	-5.99 °C/km	0.09 °C
horizontal gradient in X-direction	-0.21 °C/100 km	0.05 °C/100 km
horizontal gradient in Y-direction	-0.07 °C/100 km	0.07 °C/100 km
time gradient	-0.01 °C/h	0.01 °C/h
constant temperature in the higher area	-58.85 °C	0.63 °C
water vapor pressure at sea level	14.78 hPa	0.27 hPa
scaling height	2319.69 m	81.32 m
horizontal gradient in X-direction	-0.27 hPa/100 km	0.13 hPa/100 km
horizontal gradient in Y-direction	0.17 hPa/100 km	0.18 hPa/100 km
time gradient	-0.01 hPa/h	0.03 hPa/h

Tab. 5.5: Results of the meteorological data collocation from the October 2005 campaign using the software package COMEDIE.

5.4 Path delay comparison

Before entering the obtained and preprocessed data into the GPS tomographic analysis, the zenith delays are validated with external and independent measurements (see also e.g. Ruffini et al., 1999; Haase et al., 2001b; Pacione et al., 2001b). Figs. 5.7 and 5.8 visualize the comparison between the solar spectrometer GEMOSS mounted at HOHT and the GPS-ZTD time series as well as the time series derived from the meteorological data processing with COMEDIE and the radiosondes at the stations SUST. The data of GEMOSS was previously adjusted to the height of SUST for this purpose by calculating the differences of total delay on the basis of meteorological surface measurements at both stations.

The time series of GPS with respect to solar spectrometry at station HOHT are in very good agreement. The mean values over the seven days in the October 2005 campaign differ by only 5.8 mm (GPS minus GEMOSS). It has to be considered that GEMOSS only measures at day time during sunshine whereas GPS is an all-weather 24-hour a day observing system. The overestimation in the COMEDIE solution is mainly due to an inappropriate modeling of the dry part in the zenith total delay (see e.g. the time series of zenith wet delay in Chapter 8, pp. 111).

By adjusting the GEMOSS data from HOHT with respect to the GPS and radiosonde station SUST (see Fig. 5.8), two major differences can be extracted: The time series do not fit similarly to Fig. 5.7 on October 22 and 24, 2005. This is at the day before and the day after the cold front passage with intense rainfall. Thus, such extreme meteorological events change the behavior of the environment significantly

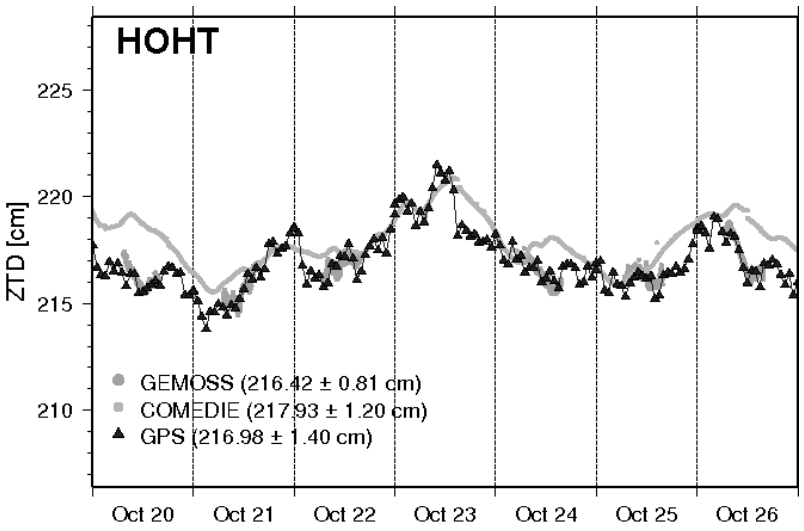

Fig. 5.7: Comparison of the ZTD time series from solar spectrometry (GEMOSS; thick dark points), meteorological surface measurements preprocessed with COMEDIE (continuous light-gray line) and GPS data from the GPS station at Hohtenn of the AGNES network (station HOHT at 935 m AMSL; line with dark triangles) during the seven days of the October 2005 campaign. There is an agreement between the time series of GEMOSS and GPS of better than 1 cm. In the time series of GPS and COMEDIE, the cold front passage on October 23 is clearly visible by the increasing value of ZTD due to the larger amount of water vapor in the atmosphere.

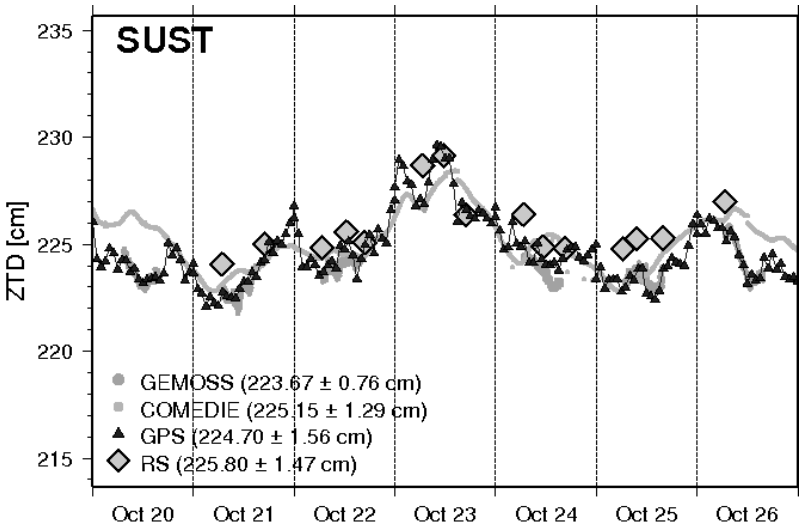

Fig. 5.8: Comparison of the ZTD time series from COMEDIE, GPS and integrated balloon soundings (RS) at the campaign station in Susten (at 678 m AMSL) and GEMOSS at Hohtenn (at 935 m AMSL). The GEMOSS data is adjusted to station SUST based on the differences of the meteorological measurements at the two stations concerned and processed with the software package COMEDIE.

for stations about 10 km away from each other.

The time series of zenith total delays from the methods discussed so far, coincide well. Especially, the characteristics of the cold front passage in the middle of the October 2005 campaign is visible by the increase of the zenith delay. The ZTD from the balloon soundings shows an almost systematic overestimation. This may be due to an inaccurate self-calibration of the sensors or a lack of data in the upper atmosphere. The latter may further cause an incorrect extrapolation of the meteorological parameters with the standard Saastamoinen model (see Eq. 2.9).

Further investigations in zenith path delay comparison based on this campaign data is carried out in the bachelor work by F. Forrer (see Forrer, 2007).

Chapter 6

The numerical weather model COSMO-7

6.1 Model description

The Swiss Federal Office of Meteorology and Climatology (MeteoSwiss) uses the COSMO model (see Doms and Schättler, 2002; Steppeler et al., 2003), formerly known as the Alpine Model aLMo, for its operational numerical weather forecasts. Boundary conditions are taken from the global model (Integrated Forecast System, IFS) of the European Center for Medium-Range Weather Forecasts (ECMWF). The domain of COSMO extends from 35.11 ° North/–9.33 ° East (lower left corner) to 57.03 ° North/23.41 ° East (upper right corner), a covers parts of western and central Europe.

The model domain is covered by a spherical grid of 385 x 325 points with a horizontal resolution of about 7 km (COSMO-7). The model consists of 45 levels vertically distributed between the ground (filtered orography) and 22.5 km altitude. The western and southern borders were placed over the sea to reduce negative interferences generated in the transition zone between the orographies of the driving model (IFS) and COSMO (see Doms and Schättler, 2002). COSMO is particularly suited to capture regional weather phenomena and serves as the basis for the MeteoSwiss short-term forecasts. On the one hand, it gives quantitative hints for daily forecasts and for early warnings of severe weather, on the other hand it provides a variety of automated products. The quality of COSMO is permanently monitored, a prerequisite for a high forecast quality.[13]

In order to assess the impact of ground-based GPS water vapor tomography in meteorological (and hydrological hazard) forecasting applications, the results have to be compared and validated with the actual state of the art procedure in this domain, which is the COSMO-7 model for the specific target area. A new model with 2 km horizontal resolution (COSMO-2) is under development at MeteoSwiss. It will be launched in early 2008 on the new Super-Computer at the Swiss National Super Computing Center CSCS[14]. The quality of the tomographic analysis in this new resolution domain will be assessed as well by defining comparable voxel models (see Sec. 7.2.1 on pp. 93f.).

[13] For further information see the COSMO website at http://www.cosmo-model.org and the model related site at http://www.meteoschweiz.admin.ch.

[14] For further information on the CSCS see http://www.cscs.ch.

6.2 Distribution of the available data

For comparing and validating the results of the two measurement campaigns systematically, a subset of the postprocessed COSMO-7 vertical grid point profile data was available (see Figs. 6.1 and 6.2). The reanalysis of the COSMO data includes the vertical radiosonde measurements from the meteorological atmosphere sounding station in Payerne (see Fig. 6.1).

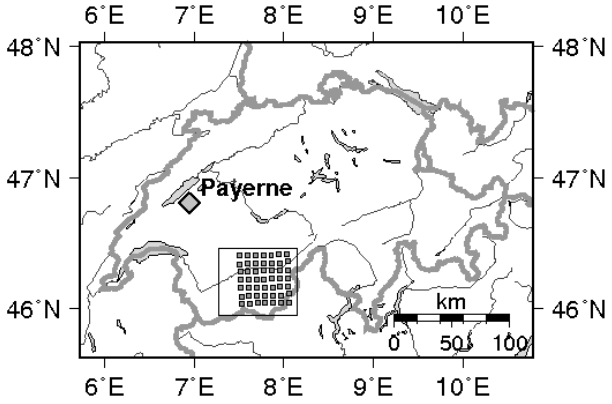

Fig. 6.1: Project area within Switzerland (black rectangle) and locations of the base points of the available COSMO grid point profile data. The site of the meteorological radiosonde station of MeteoSwiss in Payerne is labeled and indicated with a light-colored diamond.

The data used in this work consists of 49 profiles within the project area in the canton of Valais (see Fig. 6.2). The internal profile number, for example, 28 for the COSMO data is used to validate the results at station Susten (SUST). Profile number 33 is utilized in conjunction with station St. Niklaus (SNIK).

Due to the filtered orography, the COSMO model base points do not represent the real topography very well in the small-scale and mountainous project area (see also Bica and Steinacker, 2006). Furthermore, the mean height of the base points is between 200 and 600 m above the earth's surface. Thus, it has to be considered that there is no data below this height, where thermal stratification plays an important role in the atmospheric structure (see e.g. Panofsky, 1974). This may cause problems comparing this data to ground-based solutions (e.g. GPS derived zenith path delays).

6.3 Data processing workflow

To obtain suitable data sets for the comparison with the zenith path delays from the GPS processing and with the refractivity profiles from the tomographic analysis with AWATOS, the following processing steps were taken:

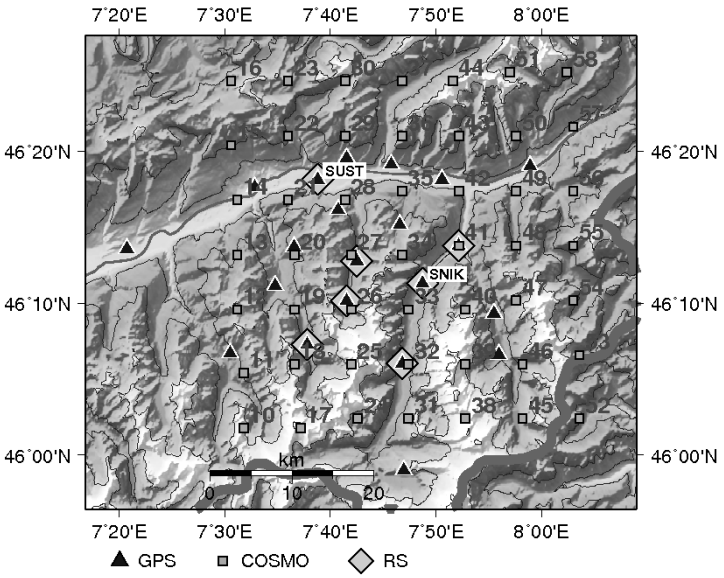

Fig. 6.2: Project area in the eastern part of the mountainous canton of Valais with GPS station network during the July 2005 campaign (dark triangles), the locations of the base points of the available COSMO model profiles (squares with internal profile numbers between 10 in the south-west and 58 in the north-east) and the balloon sounding launch sites of the reference radiosondes (RS; big light-colored diamonds). Data samples from stations SNIK and SUST are shown in Sec. ??.

1. Conversion of the COSMO model grid point indices and coordinates from the model definition file `aLMo_EXTparam.pri` to internal profile numbers with respect to the geographical coordinates and the orography on a spherical earth.
2. Extraction of the relevant information from the daily generated raw data files (the data comprises date and time in UTC, grid point index, parameters pressure in 0.1 hPa, height in m, temperature in 0.1 °C, specific humidity in kg/kg and relative humidity in %)
3. Compilation to hourly files for each grid point's vertical profile and conversion of temperature and relative humidity to water vapor pressure according to Eq. (2.1a) (see examples of profile 21 and 33 and the corresponding radiosondes in Fig. 6.3).
4. Conversion of the meteorological parameters pressure, temperature and water vapor pressure to radio wave refractivity using Eqs. (2.4) and (2.5) (examples of profile 21 and 33 in Fig. 6.4) and calculation of the integrated dry, wet and total path delays according to Eq. (2.15).
5. Extraction and compilation of time series of both, the meteorological parameters at the lowest level of the model and the integrated path delays from the preceding step (examples of the path delay time series in Figs. 6.5 and 6.6). For the geographical COSMO coordinates, the earth is approximated by a rotated and WGS84-like mounted sphere, whereas the altitude is taken from the GTOPO30 model, orthometric heights. Thus, the geographical grid point

coordinates were converted into the Swiss horizontal projection system by the following program sequence[15]:

```
llh2xyz -e GRS 80 |
xyz2xyz -s WGS84 -t ETRF |
xyz2xyz -s ETRF -t CH1903+ |
xyz2llh -e bessel |
llh2proj -P swissyxh
```

6. Spatial and temporal collocation of the integrated path delays and interpolation to the coordinates of the GPS station sites using the software package COITROPA (see Eq. (2.17) and Troller and Brockmann, 2002) (for some examples see Appendix D).

6.4 Data analysis

6.4.1 Comparison with balloon sounding profiles

With respect to the order of the processing steps discussed above, the profile data with the meteorological parameters pressure, temperature and water vapor pressure (Fig. 6.3) as well as the refractivity profiles (Fig. 6.4) are shown and examined together with the radiosondes. The COSMO profile is selected as the temporally and spatially nearest neighbor to the corresponding radiosonde profile (see also Fig. 6.2).

Two profiles are chosen from nearly the same time but with a horizontal distance of about 20 km to show the characteristics of the model compared to the radiosondes. COSMO profile number 28 is next to the GPS and radiosonde station in Susten (SUST) in the main valley (see Fig. 6.2). Profile number 33 is about 4 km to the south of station St. Niklaus (SNIK).

The data of all COSMO profiles reach an altitude of 22.5 km whereas the radiosondes ascend up to the point of their breakdown. The data of pressure and temperature matches the entire profiles with high correspondence. Especially in the lower part of the troposphere, the local water vapor pressure calculated for the numerical weather model do mostly not reproduce the reference profile of the radiosonde very well. This is due to the high variability of this parameter. The discrepancies in the water vapor profiles are mainly causing the differences in the wet refractivity profiles (N_{wet} in Fig. 6.4) in the same order of magnitude, whereas the profiles of the dry delay (N_{dry}) correspond considerably well.

In general, the estimated parameters by the COSMO model match the radiosonde data to a large extent. They are just a little below the values of the corresponding radiosondes (see Tabs. 6.1 and 6.2). Especially the water vapor pressure and therefore also the wet refractivity is underestimated during the October 2005 campaign.

[15] The programs used are internal software libraries for specific purposes:
`llh2xyz` and `xyz2ll` for the conversion between ellipsoidal coordinates (`llh`) and geocentric Cartesian coordinates (`xyz`) on the ellipsoid `e`, `xyz2xyz` for the geodetic datum transformation of geocentric coordinates (`xyz`) from source frame `s` to target frame `t` and `llh2proj` for the projection of ellipsoidal coordinates (`llh`) on a plane applying the map projection algorithm specified by the letter `P`.

Notice that an offset of a radiosonde profile outside the 95 % interval of confidence leads to the removal of this profile from further processing and statistics.

Jul 8–14, 2005	p hPa	T °C	e_p hPa	N_{tot} ppm	N_{dry} ppm	N_{wet} ppm
COSMO data						
mean value at base points	780.75	6.61	7.42	251.92	214.65	37.28
mean standard deviation	3.50	3.29	1.30	4.79	2.03	5.94
COSMO minus radiosonde						
mean offset to 10 radiosondes	-3.18	-0.74	-0.01	-0.77	-0.75	-0.03
mean standard deviation	1.28	0.85	0.32	1.90	0.45	1.75

Tab. 6.1: Mean values and standard deviation of the meteorological parameters at the COSMO model base points (not earth's surface) as well as mean offsets and standard deviations of the weather model profiles minus the corresponding reference balloon soundings for the July 2005 campaign.

Oct 20–26, 2005	p hPa	T °C	e_p hPa	N_{tot} ppm	N_{dry} ppm	N_{wet} ppm
COSMO data						
mean value at base points	778.24	3.58	5.56	245.46	216.83	28.63
mean standard deviation	3.73	2.20	1.19	5.88	1.38	6.16
COSMO minus radiosonde						
mean offset to 32 radiosondes	-3.26	-0.53	-0.12	-1.40	-0.77	-0.62
mean standard deviation	1.21	0.95	0.34	1.95	0.50	1.84

Tab. 6.2: Mean values and standard deviation of the meteorological parameters at the COSMO model base points as well as mean offsets and standard deviations of the weather model profiles minus the corresponding reference balloon soundings for the October 2005 campaign.

There is a mean offset of the COSMO profiles minus the corresponding radiosondes which is systematically negative. For October, the mean temperature of all COSMO model base points within the project area was about 3 °C lower than in July. Also the mean water vapor pressure was below the value in July (about 2 hPa).

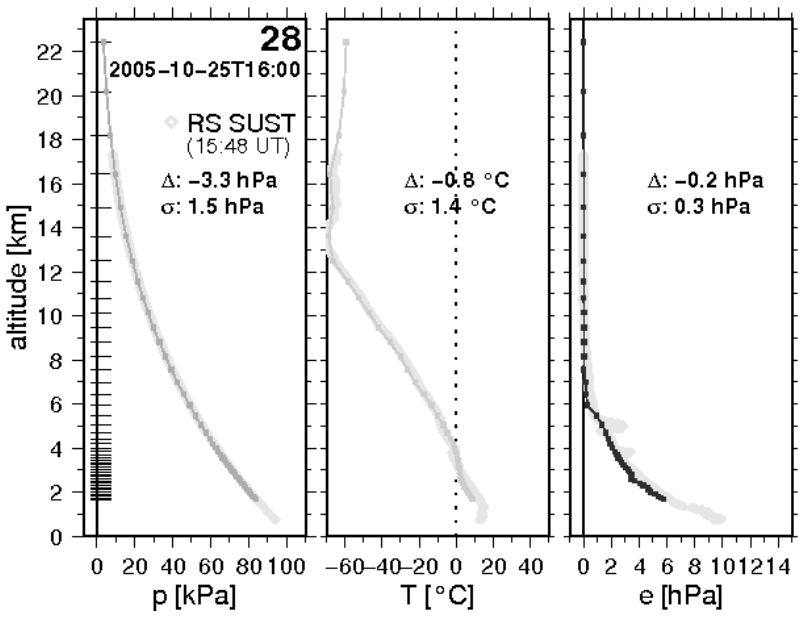

(a) COSMO profile no. 28 at 16 UT and corresponding radiosonde observations from station Susten (RS SUST).

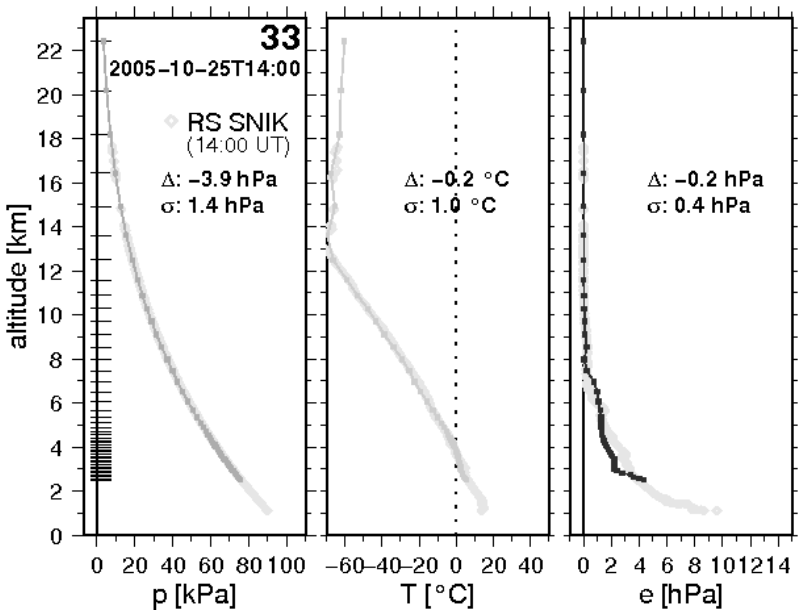

(b) COSMO profile no. 33 at 14 UT and corresponding radiosonde observations from station St. Niklaus (RS SNIK).

Fig. 6.3: Data of pressure p (left panels), temperature T (middle panels) and water vapor pressure e (panels on the right-hand side), calculated according to Eq. (2.1a), of the COSMO profiles number 28 and 33 (for their geographical location see Fig. 6.2) on the same day (October 25, 2005) with only two hours difference. The data is compared to the radiosonde measurements (RS) from station SUST at 15:48 UT and from station SNIK at 14:00 UT (light-colored profile in the background). The vertical distribution of the 45 COSMO model layers is indicated on the left side of the pressure panels. Furthermore, the unweighted mean offset (Δ) and the standard deviation (σ) of the parameters with respect to the radiosonde data is given for each parameter profile.

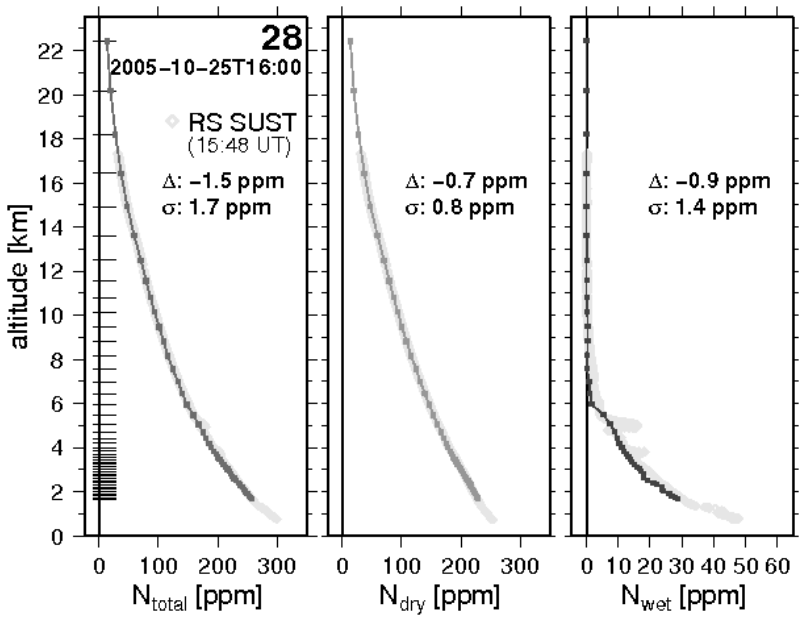

(a) COSMO profile no. 28 at 16 UT and corresponding radiosonde observations from station Susten (RS SUST).

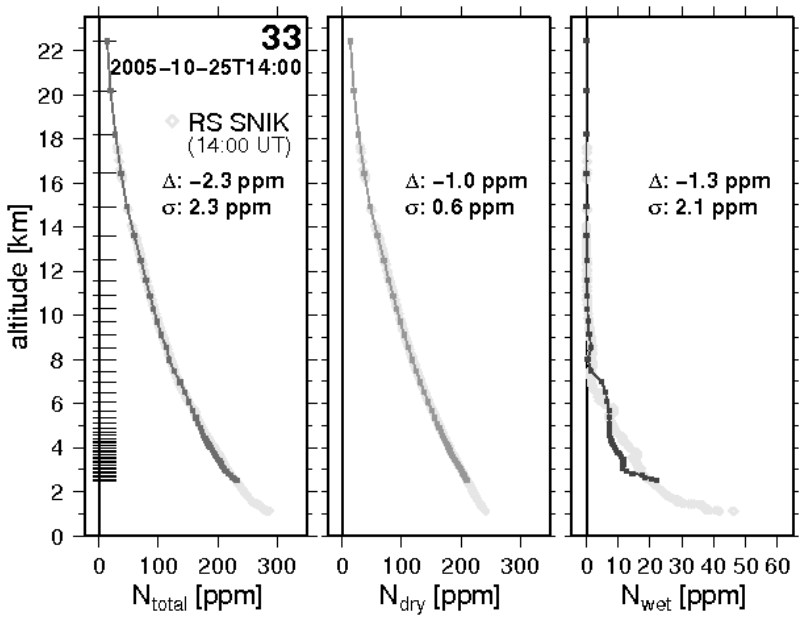

(b) COSMO profile no. 33 at 14 UT and corresponding radiosonde observations from station St. Niklaus (RS SNIK).

Fig. 6.4: Converted total (left panels), dry (middle panels) and wet (panels on the right-hand side) refractivity data calculated according to Eq. (2.4) of the COSMO profile number 28 and 33 on October 25, 2005, compared to the corresponding radiosonde data (light-colored profile in the background).

6.4.2 Time series of integrated path delays

After integrating the refractivity profiles above the base point (according to Eq. 2.15), time series for zenith total, dry and wet path delays (ZTD, ZDD and ZWD) are obtained with an hourly resolution (see Figs. 6.5 and 6.6).

The time series plots of the integrated zenith path delays (Figs. 6.5 and 6.6) reflect the evolution of the general meteorological situation during the two field campaigns (see also Sec. 6.4.4 and Appendix A). Along the seven days from July 8 to 14, 2005, both, the air pressure and the mean daily temperature were rising continuously (see the time series of the meteorological surface data in Fig. A.2, p. 180) and correspond with the ZDD progression.

There was rainfall in the main valley in the north of the project area in the evening of the second day (high value in the ZWD time series of profile 28). The fifth, sixth and seventh day of the campaign were warm and sunny. The weather situation during the field campaign in October 2005 was dominated by a cold front passage with heavy rain fall in the middle of the seven days followed by high-pressure dominated weather (see also the meteorological surface data in Fig. A.3, p. 181).

Overall, the time series of the wet delay has a much stronger amplitude at profile 28 (in the main valley) than at profile 33 (in a tributary valley). The sensitivity of the zenith total delay with respect to the meteorological parameters given in Geiger (1987) and on Tab. 2.2, p. 30, can be confirmed. Pursuant to Tabs. 6.1 and 6.2 the meteorological environment of the project area was dryer in October than in July.

For a cooler atmosphere, the smaller amount of water vapor in the air (see water vapor parameter e_p depending on temperature and relative humidity) leads to smaller wet delays and, therefore, smaller zenith total delays. Examining the absolute values of the dry and total delays, the influence of the altitude of the base points is obvious. In Figs. 6.7(a) and 6.7(b), this influence is shown together with the variation of the time series.

There are slight discontinuities in the data of the absolute value of ZWD between 1500 m and 2000 m altitude in July (see Fig. 6.7(a)). This independence from the base point height from which the delay was integrated could be an indicator of vertical mass transport of wet air in the project area due to strong uplift winds modeled by COSMO-7 during this campaign.

Regarding the variation of the ZWD time series depicted in Figs. 6.5 and 6.6 and visualized by the error band with respect to the ZWD dots in Fig. 6.7, there is a difference between the two campaigns. In October, the cold front passage with heavy rain fall on the fourth day dominates the weather dynamics. This is represented in the large variation of the ZWD parameter.

In general, the variation of the time series reduces with increasing height. This indicates the influence of the variability and atmospheric turbulences within the planetary boundary layer and the lower troposphere (see also e.g. Stull, 1999). The strong negative correlation between height and ZDD/ZTD is well known. The difference of more than 2 cm between mean ZTD in July and mean ZTD in October confirms the empirically determined partial derivatives presented on Tab. 2.2, p. 30, and in Geiger (1987), taking into account the changes in the meteorological parameters at the base points given on Tabs. 6.1 and 6.2. This difference is mostly due to the wet delay, whereas the ZDD remains almost the same in July and October.

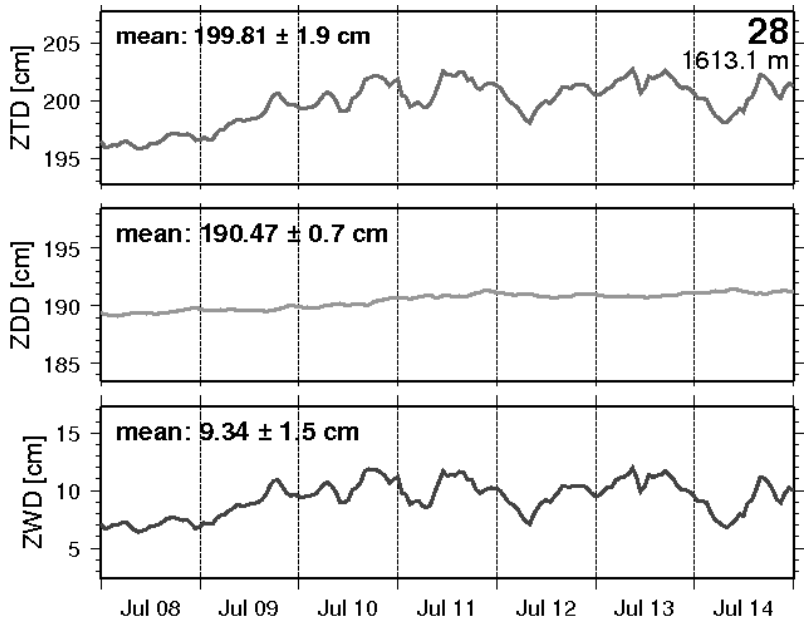

(a) COSMO profile no. 28, July 2005 campaign.

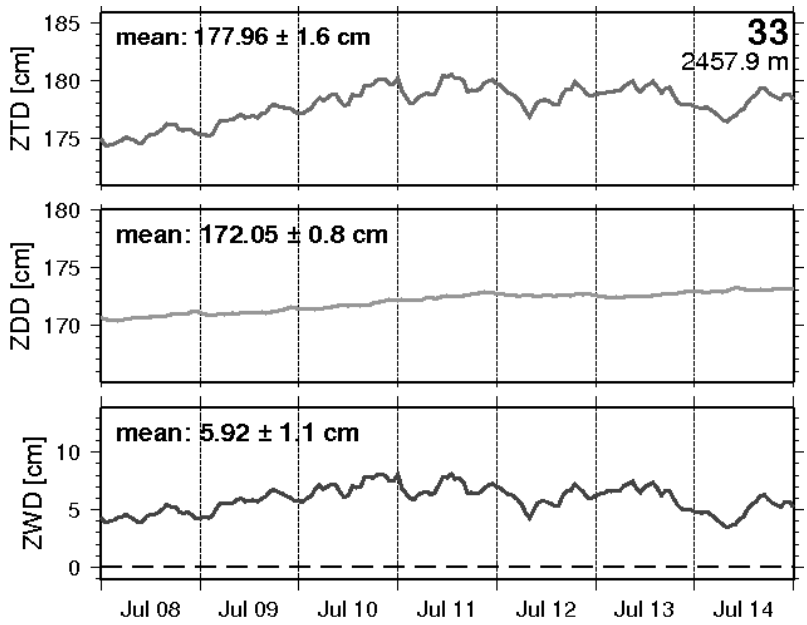

(b) COSMO profile no. 33, July 2005 campaign.

Fig. 6.5: Time series of integrated path delays from COSMO model data of profile 28 (next to station SUST, base point height 1613.1 m AMSL) and profile 33 (next to station SNIK, base point height 2457.9 m AMSL) during the field campaign in July 2005.

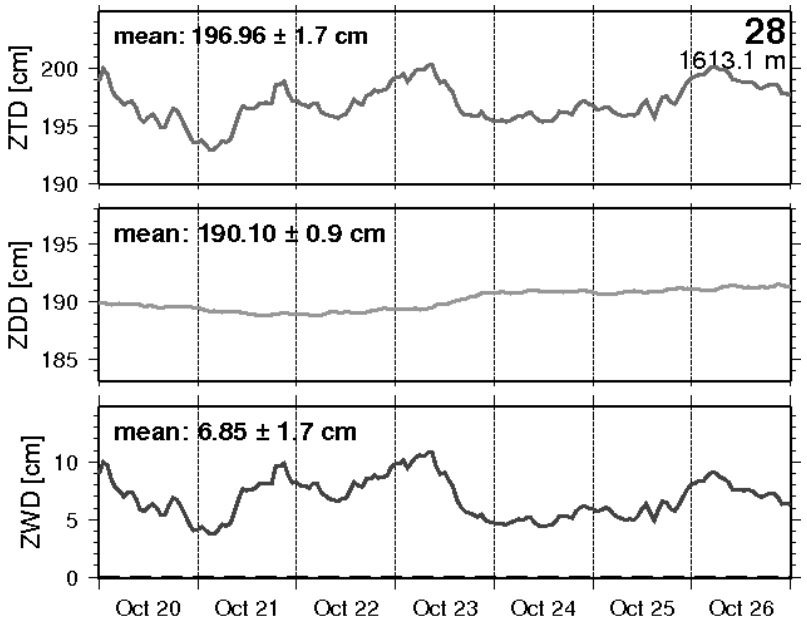

(a) COSMO profile no. 28, October 2005 campaign.

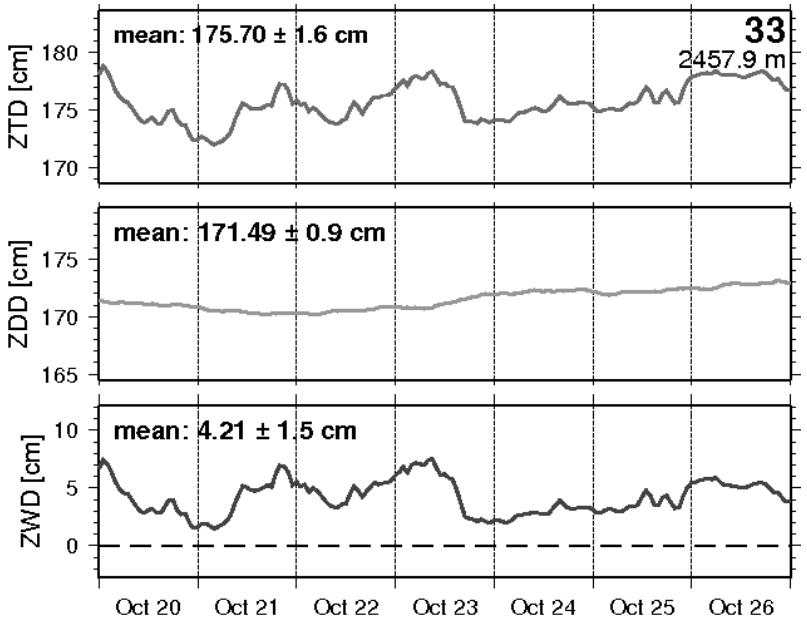

(b) COSMO profile no. 33, October 2005 campaign.

Fig. 6.6: Time series of integrated path delays from COSMO model data of profile 28 (next to station SUST) and profile 33 (next to station SNIK) during the field campaign in October 2005.

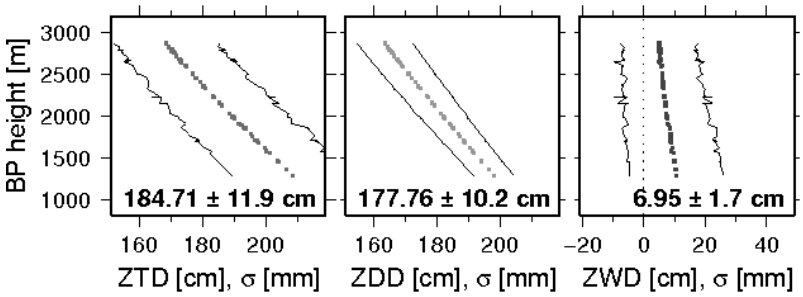

(a) July 2005 campaign.

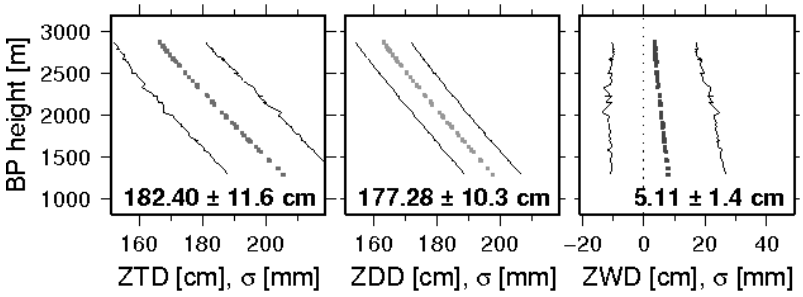

(b) October 2005 campaign.

Fig. 6.7: Dependence of the integrated total (ZTD, panels on the left-hand side), dry (ZDD, middle panels) and wet (ZWD, panels on the right-hand side) path delays with respect to the base point (BP) heights of the COSMO profiles. The indicated standard deviations (σ in mm) show with some exceptions a slightly decreasing variability of the time series of the parameter ZWD with increasing base point height. The standard deviation of the dry delay (ZDD) is almost independent from the height. The mean value of the path delays of all profiles is given as well together with the corresponding variance.

6.4.3 Comparison with time series of hourly GPS-ZTD

The correction for vertical offsets between GPS, radiosondes, the base points from the numerical weather model and the profiles from AWATOS with respect to the integrated path delays is a critical issue (see also Vedel et al., 2001).

The zenith total delays (ZTD) time series with an hourly resolution derived from GPS measurements are compared to the integrated and spatially and temporally interpolated total path delays from the COSMO model data (see Eqs. 2.17 and 2.18). The following parameters have been used for the functional (see Tab. 6.3) and the stochastic (see Tab. 6.4) models:

Functional model	ZPD_0 m	a 1/100 km	b 1/100 km	c h^{-1}	h_s m
ZTD	2.00	0.0	0.0	0.0	7500
ZDD	2.00	0.0	0.0	0.0	7500
ZWD	0.20	0.0	0.0	0.0	2400

Tab. 6.3: Initial values of the functional model Eq. (2.17) for the zenith total (ZTD), dry (ZDD) and wet (ZWD) delays derived from the integrated COSMO-7 grid point profiles. ZPD_0 refers to mean sea level height.

Stochastic model	σ_0^2	Δx_0 km	Δy_0 km	Δz_0 km	Δt_0 h
ZTD	2.00	100	100	1	6.0
ZDD	2.00	100	100	1	6.0
ZWD	0.01	100	100	1	6.0

Tab. 6.4: Parameters of the stochastic model Eq. (2.18) for the time series of the zenith total (ZTD), dry (ZDD) and wet (ZWD) delays derived from the integrated COSMO-7 data.

The mean values of the functional model after the collocation are given in Tabs. 6.5 and 6.6. For comparison purpose of e.g. the resulted scaling heights with the COMEDIE processed ground-based meteorological data, see Tabs. 5.4 on p. 70 and 5.5, p. 71.

The mean values of the integrated zenith total delays over the time of the field campaigns and the correlation coefficient between the ZTD time series of the interpolated COSMO and the GPS data are calculated on an hourly basis. Time series for selected GPS stations are shown in the Appendix D in Figs. D.2, D.3, D.4 and D.5. Regrading the power spectra, the repeat rates of one day in the ZTD time series (about 24 h in July and in October, the sampling time is about 30 h) are primarily due to the wet delay variation (see also Figs. 6.5 and 6.6). For most stations, this

July 2005	ZPD_0 m	a 1/100 km	b 1/100 km	c h^{-1}	h_s m
ZTD	2.48	$0.8 \cdot 10^{-3}$	$4.1 \cdot 10^{-3}$	$0.4 \cdot 10^{-3}$	7375.01
ZDD	2.31	$-0.9 \cdot 10^{-3}$	$1.1 \cdot 10^{-3}$	$0.2 \cdot 10^{-3}$	8303.90
ZWD	0.21	$6.6 \cdot 10^{-3}$	$-4.4 \cdot 10^{-3}$	$0.2 \cdot 10^{-3}$	1977.61

Tab. 6.5: Estimations of the parameters of the functional model Eq. (2.17), p. 23, after collocation of the COSMO-7 data for the July 2005 campaign.

October 2005	ZPD_0 m	a 1/100 km	b 1/100 km	c h^{-1}	h_s m
ZTD	2.44	$3.0 \cdot 10^{-3}$	$4.8 \cdot 10^{-3}$	$-0.1 \cdot 10^{-3}$	7538.79
ZDD	2.31	$2.3 \cdot 10^{-3}$	$1.0 \cdot 10^{-3}$	$0.1 \cdot 10^{-3}$	8218.74
ZWD	0.16	$0.1 \cdot 10^{-3}$	$31.2 \cdot 10^{-3}$	$-1.0 \cdot 10^{-3}$	1897.42

Tab. 6.6: Estimations of the parameters of the functional model Eq. (2.17) after collocation of the COSMO-7 data for the October 2005 campaign.

frequency is dominating the spectrum for both, the GPS data and the COSMO data. However, GPS is sensing also higher frequency variations in the ZTD estimates.

Overall, there is a good agreement between the time series of the integrated and interpolated path delays from the COSMO model and the ZTD from the GPS processing, especially by processing final orbits. The general behavior of the parameter development is similar. The time series correlate with about +70 %. The experience of large differences between the ZTD values derived from the GPS observations and the numerical weather model for the maximum activity of a mesoscale convective system described in Cucurull et al. (2002b) can be reconfirmed. After the intense rainfall event in the middle of the October 2005 campaign, where most of the water vapor above 4 km altitude precipitated, large positive offsets between the time series of GPS minus COSMO are apparent as well (apart from station ZINA).

Due to the GPS station configuration and maintenance problems (short observation time) in the July campaign, the time series of the sites SUST (at 678 m AMSL) and SSTU (at 2182 m AMSL) correlate with less than 50 %. Furthermore, in July, the correlation coefficients between the ZTD time series of GPS and the COSMO-7 data mostly seem to depend on the station heights. In October, the correlation is much more homogeneously centered around +70 % with no significant or obvious dependencies (see Fig. 6.8). On average, the absolute values from COSMO are below the GPS estimates (see Tabs. 6.7 and 6.8).

Iwabuchi et al. (2000) attempt to explain this difference by the fact that the base point heights of the numerical weather model are generally above the GPS station heights in a mountainous area. Hence, the extrapolation algorithm for the path delays of the model data down to the earth's surface underestimates the impact of

the lowest and more complex part of the atmosphere. There is either a small dry bias in the reanalysis data of the weather model or a wet bias in the GPS data (see e.g. Hagemann et al., 2003; Morland et al., 2006).

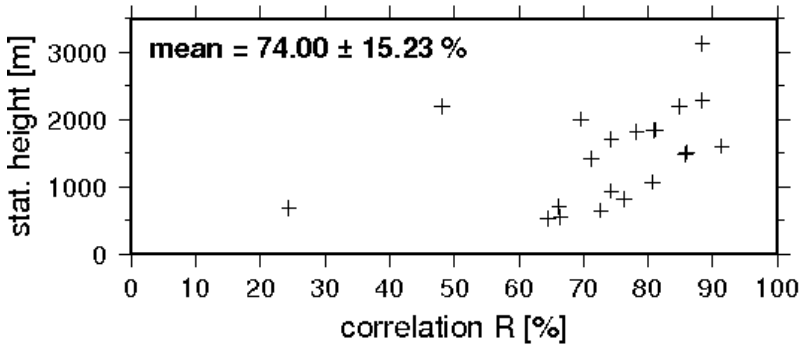

(a) ZTD correlation coefficients of GPS and COSMO during the July 2005 campaign.

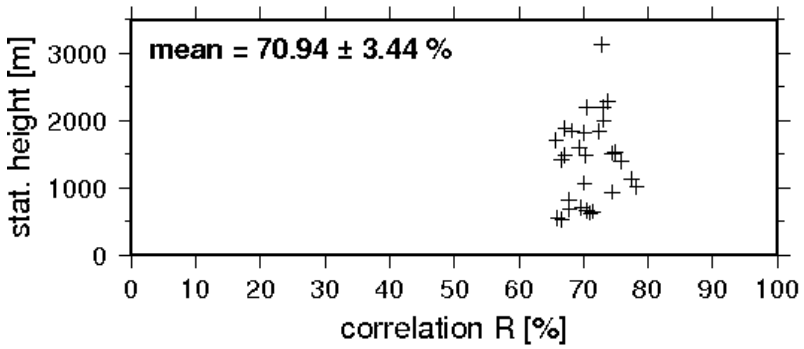

(b) ZTD correlation coefficients of GPS and COSMO during the October 2005 campaign.

Fig. 6.8: Correlation coefficients of the ZTD time series from GPS and interpolated COSMO-7 data versus station heights during the July (top panel) and October (bottom panel) campaigns.

Jul 8–14, 2005	COSMO		GPS		difference	correlation
	mean	σ	mean	σ		
orbits/clocks	cm		cm		cm	%
final	204.26	1.86	206.23	1.74	-1.97 ± 0.83	74.00 ± 15.23
rapid	204.26	1.86	206.23	1.74	-1.97 ± 0.83	74.10 ± 15.11
ultra-rapid	204.26	1.86	206.24	1.75	-1.98 ± 0.83	74.21 ± 14.59
broadcast	204.26	1.86	206.62	2.59	-2.36 ± 0.82	54.45 ± 13.46

Tab. 6.7: Mean values, offset and correlation coefficients comparing the ZTD time series of COSMO-7 minus GPS (processed with different orbit qualities) for all stations within the project area during the field campaign in July 2005.

Oct 20–26, 2005	COSMO		GPS		difference	correlation
	mean	σ	mean	σ		
orbits/clocks	cm		cm		cm	%
final	203.25	1.78	204.53	1.43	-1.29 ± 0.87	70.94 ± 3.44
rapid	203.25	1.78	204.54	1.42	-1.29 ± 0.87	71.06 ± 3.45
ultra-rapid	203.25	1.78	204.50	1.44	-1.25 ± 0.87	68.36 ± 3.25
broadcast	203.25	1.78	204.76	2.72	-1.51 ± 0.90	35.89 ± 3.61

Tab. 6.8: Mean values, offset and correlation coefficients comparing the ZTD time series of COSMO-7 minus GPS (processed with different orbit qualities) for all stations within the project area during the field campaign in October 2005.

The standard deviations for both time series (COSMO and GPS) are larger in July than in October, similar to the absolute mean values over the seven campaign days. For all time series, the mean values of the interpolated COSMO data are smaller than the GPS derived ZTD. In July, the offset is about 2.0 cm whereas in October, the difference is only 1.3 cm. Yang et al., 1999 remarked that in several numerical weather models there is a systematic underestimation of wet refractivity in the reanalysis, especially under humid conditions. Another reason for the difference might be an overestimation in the GPS data.

Comparing the COSMO-7 data with the GPS data processed with broadcast ephemerides instead of postprocessed and/or predicted (i.e. ultra-rapid) orbits, the correlation coefficients decrease significantly. The decrease of quality in the GPS derived ZTD time series with broadcast ephemerides have already been discussed in Sec. 5.2.4, pp. 64f. There is also a significant decrease of the correlation compared to the COSMO results and an increase of the difference between the mean values, i.e. an increase of the GPS derived zenith total delays.

6.4.4 ZTD comparison with rainfall data

During the July 2005 campaign, three GPS stations were in use near meteorological stations operated by MeteoSwiss. The stations SION and VISP were located in the main valley northwest and northeast of the project area, whereas EVOL was set up in a tributary valley in the southwest of the project area (see also Fig. 6.2). In October 2005, there was a fourth GPS station mounted next to an ANETZ station: ZER1, located in the southeast of the project area. Figs. 6.9 and 6.10 show the time series of ZTD derived from GPS and the numerical weather model together with rainfall data of the ANETZ stations. For the geographical locations of these stations see in the Appendix, Fig. A.1 on p. 179.

By visual inspection, the ZTD time series correlate well with rainfall data. Usually, the impact of local precipitation is more clearly represented in the GPS data than in the data of the numerical weather model. The COSMO-7 time series seem to be too smooth.

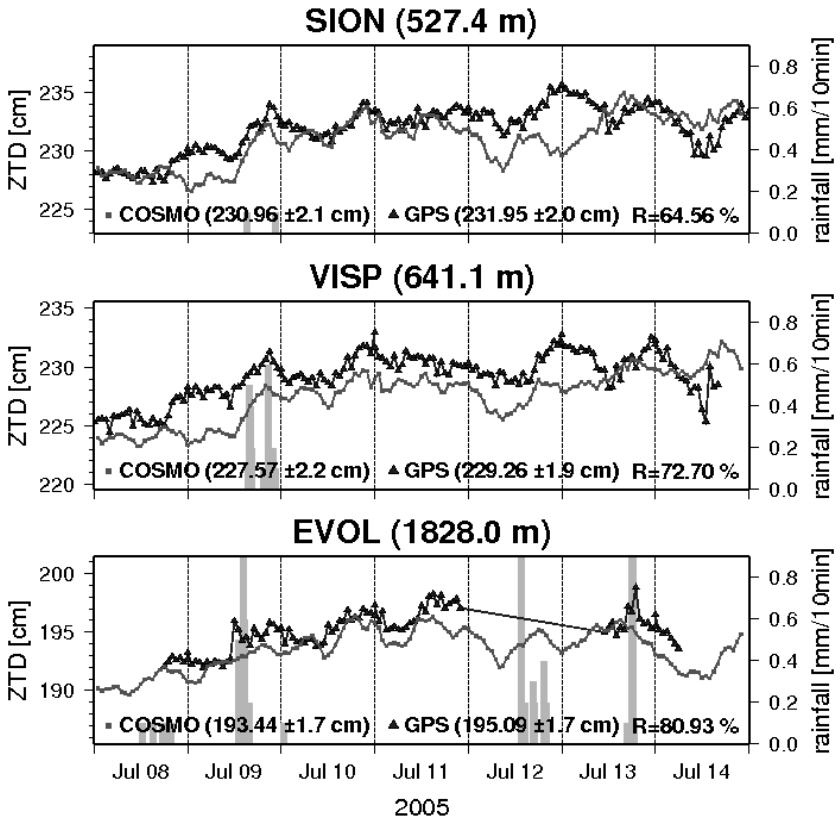

Fig. 6.9: Zenith total path delay time series of COSMO and GPS related to the ANETZ stations Sion (abbreviated by "SIO" in Fig. A.1, p. 179), Evolène (EVO) and Visp (VIS) shown together with rainfall data, visualized by light-colored bars, during the field campaign in July 2005.

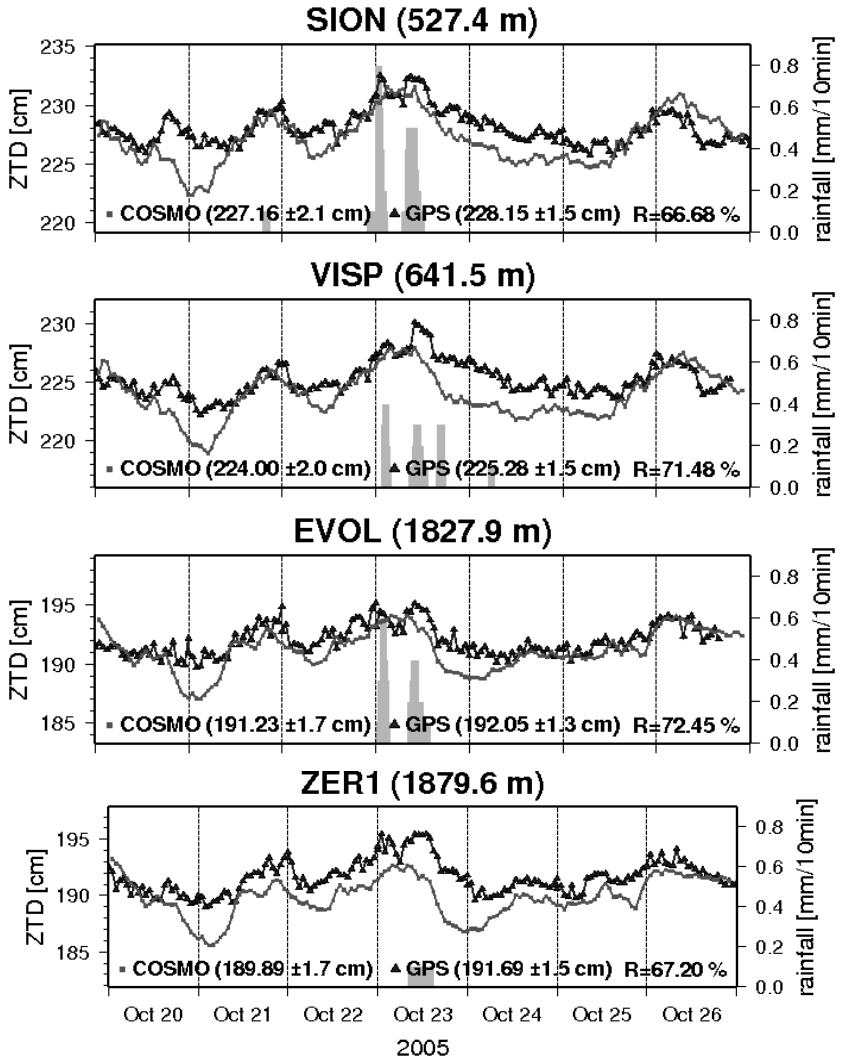

Fig. 6.10: Zenith total path delay time series of COSMO and GPS related to the ANETZ stations Sion (abbreviated by "SIO" in Fig. A.1, p. 179), Evolène (EVO), Visp (VIS) and Zermatt (ZER) shown together with rainfall data, visualized by light-colored bars, during the field campaign in October 2005.

Chapter 7

Enhancements of AWATOS

7.1 Introduction

As mentioned before, this study has three main objectives (see Sec. 1.4): The second one is to investigate the possibilities and limitations of GPS tomography for high-resolution applications using the software package AWATOS (see Sec. 3.2). For that, different horizontal, vertical and temporal resolutions were computed, analyzed and evaluated by comparing the results with profiles from radiosondes and the numerical weather prediction model COSMO-7 (see Chapter 6). The second objective is to consider the use of precise orbits, rapid and ultra-rapid orbits and even broadcast GPS satellite ephemerides in view of near real-time processing. The related data is taken directly from the GPS processing.

This chapter will give an overview of the tools, which were developed to address the objectives mentioned above. Chapter 8 will then show different results and discuss some effects of the tools. Besides error corrections and bug-fixing, the core functionalities of the software package AWATOS have not been changed. However, several tools and modules were added to meet the requirements for the extensive analysis studies based on the data of the two dedicated field campaigns (see Chapter 4).

7.2 New models and algorithms

7.2.1 Designing the voxel model

The tomographic voxel model for the software package AWATOS is a three-dimensional geometrical structure with ellipsoidal borders. The grid spacing defines the resulting resolution of the tomographic analysis.

In the horizontal plane, the voxel model has to cover the whole catchment's area. So far, the horizontal extension of the whole model can be divided by an integer number to get the required resolution. There is a frame around the target area, the inner model, of the so called outer boxes or buffer area with infinite extension. In Chapter 8, pp. 111f., voxel models of 15 km down to 2 km horizontal grid spacing are discussed.

In the vertical direction, the variability and flexibility of the spatial resolution by introducing additional voxel model layers is much higher. The distribution of the layers and the corresponding and related thickness is a critical issue in GPS tomographic analysis. Theoretically, any layer distribution is possible. Including

and enabling inter-voxel constraints in the processing with the software package AWATOS, refractivity values can be estimated even in those voxels without real measurements or observations, e.g. below the natural topography. Nevertheless, usually, the bottom layer of the voxel models investigated is an ellipsoidal surface at mean sea level. To minimize the number of unknowns in the tomographic inversion problem (see Eq. 3.2 on p. 34), the upper boundary of the first layer can be taken from the approximate minimum elevation of the topography within the target area. Therefore, the first tomographic layer lies completely beneath the earth's surface.

The upper limitation of the voxel model depends on the application. Investigating the wet refractivity field, it is recommended to cover the atmosphere up to the tropopause. There, the water vapor pressure has only a negligible influence on the radio wave refractivity. In central Europe, this is the part of the atmosphere at an altitude between 10 and 12 km AMSL. Nilsson (2005) investigated the impact of the remaining water vapor above 8 km AMSL on the GPS signals in zenith direction. The information were obtained using radiosonde data. The error is in general less than 1 mm (the average is 0.7 mm). The error is larger in the summer than in the winter period (see Nilsson, 2005).

Within the first and the highest layer, the intermediate layers can be distributed either freely, with a constant thickness or in a way that the integral of the refractivity in each layer is approximately constant. This means, the thickness increases with altitude. Due to quasi-exponential behavior of the refractivity profile (see e.g. Fig. 2.2 and Hall, 1979), the following geometric series, based on the first rules of arithmetic, has been established and successfully applied.

$$h_i = \begin{cases} 0, & \text{if } i = 0 \\ h_{min}, & \text{if } i = 1 \\ h_{max}, & \text{if } i = n \\ h_{i-1} + \dfrac{h_{max} - h_{i-1}}{d \cdot (n - i)} & \text{in all other cases} \end{cases} \tag{7.1}$$

h_i	height of the upper boundary of layer number i in m
h_{min}	minimal surface elevation within the target area in m
h_{max}	upper boundary of the highest layer in m
n	total number of layers
d	design factor

In the following examples applying Eq. (7.1) for the layer distribution in the vertical, the relation $d = e \approx 2.718...$ (Euler's number) was used as design factor. The higher the value of d (e.g. $d = 4.0$), the more layers are created in the lowest troposphere and the smaller d (e.g. $d = 1.5$), the more the layer distribution approximates a layer distribution with uniform thickness. The geometry of the whole voxel model is written into a file, which serves as input for the estimation and interpolation of the a priori values and the actual tomographic analysis.

The comparison between three different layer distributions will show the advantages and disadvantages of this new formula Eq. (7.1). In the first place, an empirically determined distribution with 16 layers up to 15 km altitude is used (see Fig. 7.2(a)). It was introduced and investigated in Troller (2004) to determine the wet refractivity field above the Swiss territory. This layer distribution was used

to account for the strong gradients in wet refractivity at the edge of the planetary boundary layer, usually within the first 1000 m to 2000 m above the surface layer (see e.g. Stull, 1999). In the second place, a tomographic analysis is carried out with the same number of layers but with equidistant thickness up to 12.5 km altitude (see Fig. 7.2(b)). In the third place, another model with 16 layers is generated using the formula described in Eq. (7.1) (see Fig. 7.2(c)).

The horizontal resolution of the voxel model for all three cases is 7.5 km (see Fig. 7.1). The observation data for this comparison is taken from the October 2005 campaign (see Sec. 4.4). The vertical distribution of the GPS stations within the project area and the cross sections of the three voxel models compared are shown in Fig. 7.2.

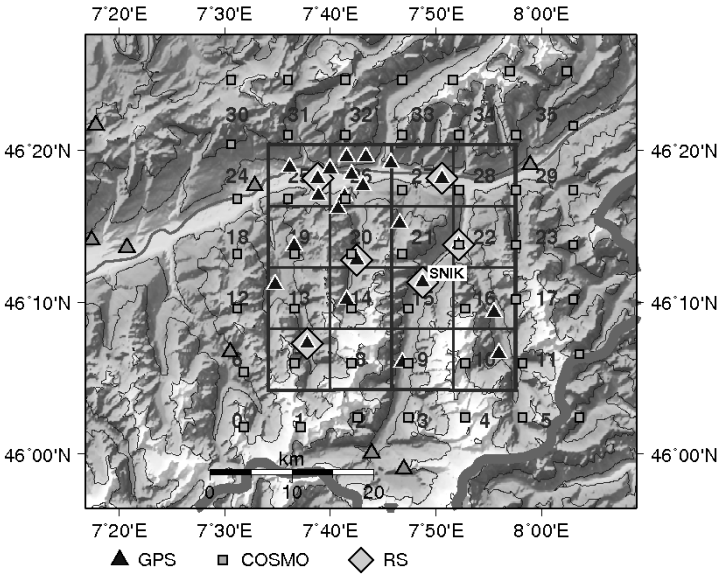

Fig. 7.1: Plan view of the 7.5 km voxel model including voxel column numbers (between 0 in the south-west and 35 in the north-east) and the GPS and radiosonde network as well as the base points of the data available from the numerical weather model COSMO-7 during the field campaign in October 2005. This data is used for the comparison of different layer distributions. The GPS and radiosonde station SNIK at 1116 m AMSL within the voxel model column 15 is highlighted for locating the following results.

In order to assess the quality of the results obtained by applying the high-resolution GPS tomographic technique further developed in this work, special time series plots were created. The main part are the wet refractivity profiles between mean sea level and 10 km altitude from the tomographic solution (AWATOS) and the results from the numerical weather model (COSMO-7), respectively. The scale of the height component is shown on the left hand side. The profiles of one particular site were selected for the period of a measurement campaign (seven days).

According to the temporal resolution, the wet refractivity values in ppm were linearly interpolated, and contour lines with 5 ppm distance could be added. On

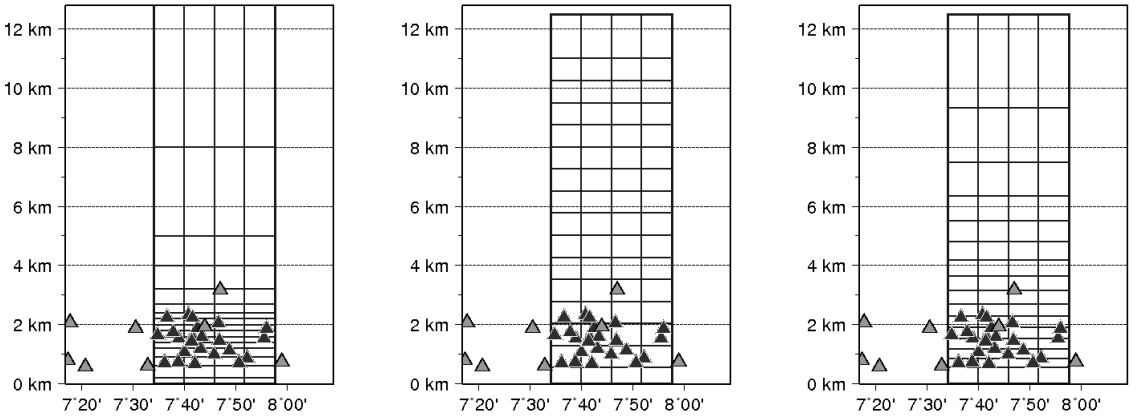

(a) Voxel model with 16 empirically distributed layers. The top layer reaches up to 15 km altitude.

(b) Voxel model with 16 layers of the same thickness (747 m) from the surface up to 12.5 km altitude.

(c) Voxel model with 16 layers defined according to Eq. (7.1) up to 12.5 km altitude. The first layer has a thickness of 314 m.

Fig. 7.2: Layer distribution of three different voxel model definitions with a horizontal resolution of 7.5 km together with the locations of the GPS stations during the field campaign in October 2005. Analog to Fig. 7.1, the GPS symbols distinguish stations inside the outer boundary front of the voxel model (dark triangles) and those outside (light-colored triangles).

the left vertical axis, the altitude above mean sea level is given together with the corresponding vertical distribution of the model layer center points or level heights (denoted by short black horizontal lines). The estimated parameters are available for this range.

Because the tomographic voxel model's lowest layers do not usually account for the topography, refractivity values may be calculated for beneath the earth's surface based on the intervoxel constraints. The gray section below the continuous thin black horizontal line depicts the part, which lays beneath the topography of the corresponding voxel model. The top of this part is evaluated by the intersection of the specific tomographic profile with a high-resolution digital elevation model or, in the case of the COSMO-7 results, with the filtered orography of the model. If the profile is related to a specific station (GPS or meteorological station), the station abbreviation is given on the top left corner, and a dashed black line indicates the height of that station or observation ward. In the case of comparison with additional data (e.g. meteorological surface measurements or integrated path delays), there is a second corresponding vertical scale on the right hand side.

Independent from the layer distribution of the tomographic voxel model, the wet refractivity profiles, derived from the numerical weather model COSMO-7, are shown in the first place (Fig. 7.3). The data is taken from the profile about 5 km south of the GPS station in St. Niklaus (SNIK, see Fig. 7.1). The time series of the zenith total delays (ZTD) from the GPS station SNIK (Bernese processed) and the values derived from COSMO-7 (according to Eq. 2.15b on p. 21 and Eq. 2.17 on

p. 23), as well as the corresponding reference radiosondes, are given for comparison purpose. Regarding the second and third balloon sounding, Guerova et al. (2003) have identified that in some particular weather situations with low stratus clouds and temperature inversion, radiosondes significantly overestimates the water vapor amount (see also e.g. Figs. 6.3(b) and 6.4(b) on pp. 80 and 81). Nevertheless, the data from the radiosondes are taken as first reference for the following analyses.

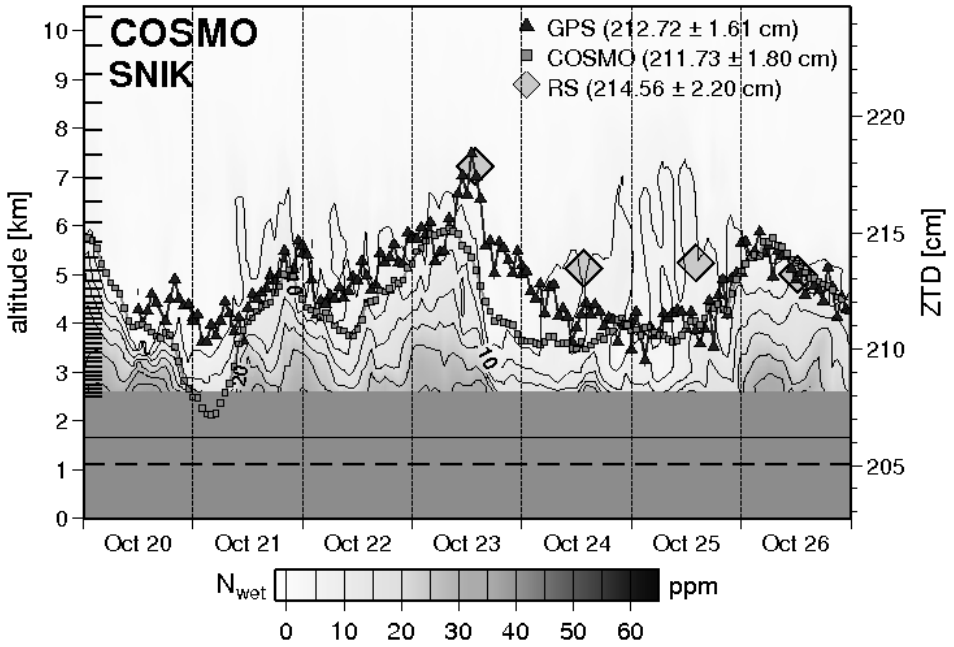

Fig. 7.3: Vertical distribution and temporal variation of wet refractivity (contour lines in ppm) between October 20 and 26, 2005, derived from the COSMO-7 hourly postprocessed data. The values are taken from the profile within the voxel model column 15 about 5 km south of the station in St. Niklaus SNIK (see Fig. 7.1). The COSMO model consists of 45 vertically distributed levels up to 22.5 km altitude (see also e.g. Fig. 6.3). The time series of zenith total delay (ZTD) from the Bernese GPS processing are shown together with the integrated and interpolated values from COSMO-7 and the four reference balloon soundings ("RS") launched at station SNIK. Mean values and standard deviation of the time series are shown in the upper right corner of the figure.

Secondly, the temporal variation and vertical distribution of the wet refractivity profiles from the different voxel models estimated using the software package AWATOS are given (Figs. 7.4, 7.5 and, finally, Fig. 7.6). Here, the time series of integrated zenith wet delays (ZWD) are plotted together with the values derived from COSMO-7.

The empirical model (Figs. 7.2(a) and 7.4) has the advantage of the pre-estimated wet refractivity values from the a priori model in the top layers with large thickness of the voxel model (see also Sec. 7.2.2). Because the two top layers have a large extension (down to 5 km AMSL), there is a strong impact on the results. The progression of the integrated path delay values of ZWD are very smooth compared to the ZTD time series of the Bernese processed GPS data displayed in Fig. 7.3.

They match the values derived from the reference radiosondes quite well. But the characteristics (e.g. the distinct minimum on the second day) of the profile evolution do not correspond with the numerical weather model in high accordance.

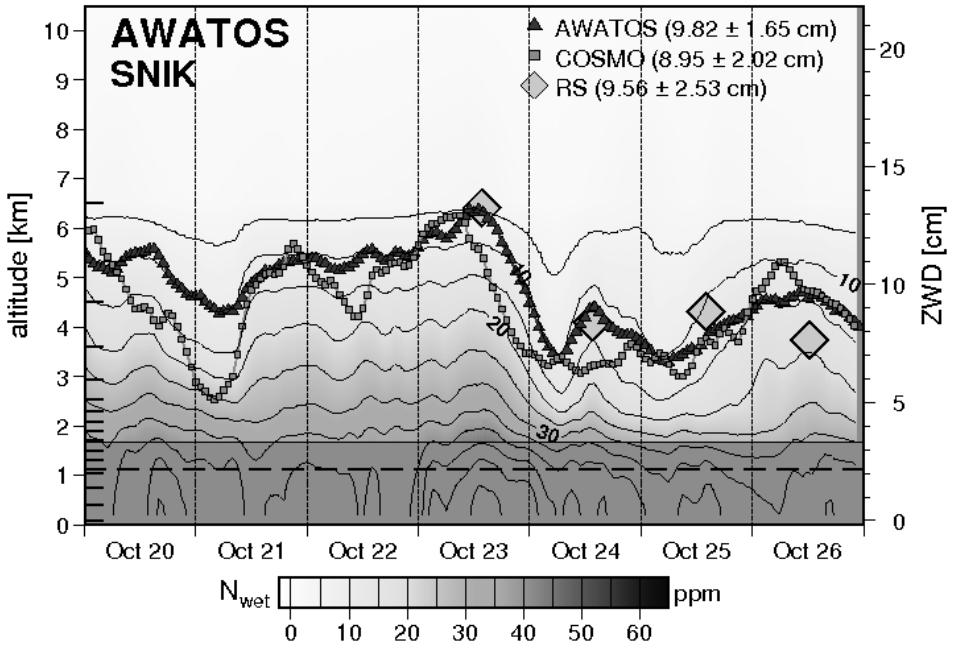

Fig. 7.4: Wet refractivity variation from the AWATOS analysis with the empirical layer distribution (Fig. 7.2(a)). Here, the same voxel column 15 is selected (see Fig. 7.1). The time series of the integrated wet path delays (ZWD) from the tomographic solution (AWATOS), the interpolated COSMO-7 data (see Fig. 7.3) and that from the reference radiosondes ("RS") are shown for qualitative comparison purposes.

The linear model with a layer thickness of 747 m (Figs. 7.2(b) and 7.5) seems to be too smooth below an altitude of 3 km. Above this, however, the wet refractivity changes rapidly and causes a large variation in the time series of the integrated ZWD. Also negative values of refractivity can occur in the higher troposphere. They are represented by the white areas in the figure.

The new model of layer distribution applying Eq. (7.1) (see the result in Fig. 7.6) seems to track also the higher variability of wet refractivity in the lower troposphere. Unlike the first model, it is still sensitive enough in the middle segment to reproduce vertical and temporal gradients and changes in the water vapor content. Under extreme atmospheric conditions (e.g. the day after heavy rainfall on October 23, 2005), the data analysis may also lead to refractivity values below 0 ppm in the upper troposphere, evoked by the tomographic least-squares adjustment. Here, this effect is not as strong as in the linear model.

An increase of accuracy in the spatial high-resolution domain could be obtained by applying Eq. (7.1) for generating the tomographic voxel model layer distribution compared to other layer distributions. The mean offset to all wet refractivity profiles of the radiosondes in the October 2005 campaign for the empirical formula (see Fig. 7.2(a)) is +0.80 ppm. The linear model with constant layer thickness (see

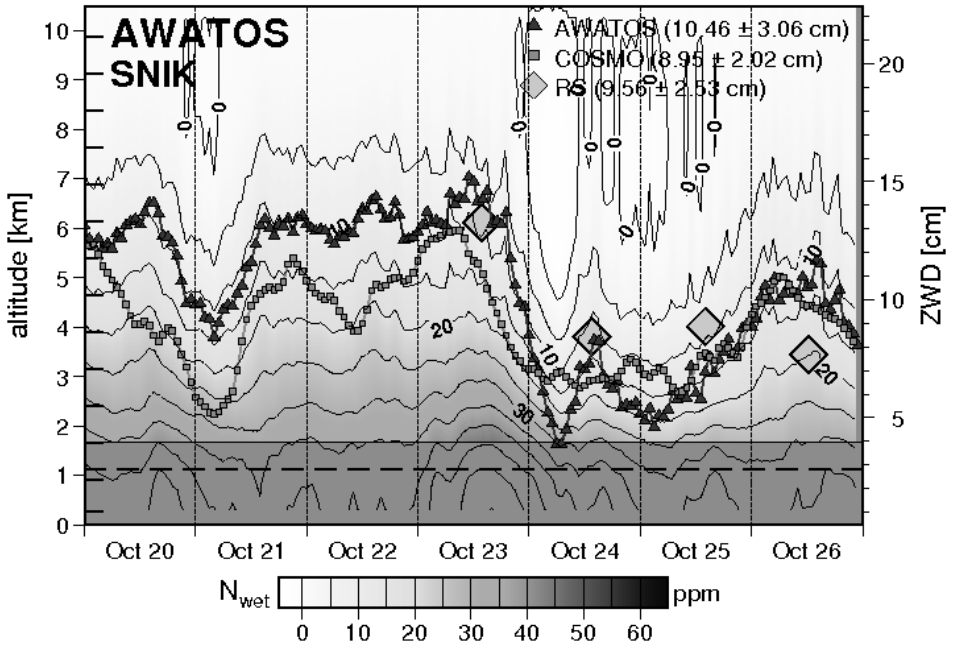

Fig. 7.5: Wet refractivity variation in voxel column 15 (see Fig. 7.1) from the tomographic analysis with the equidistant layer distribution (Fig. 7.2(b)) and the time series of the corresponding integrated ZWD.

Fig. 7.2(b)) reaches a mean offset of +0.65 ppm, whereas the new developed formula applied to the tomographic voxel model definition (see Fig. 7.2(c)) gets a mean offset of only +0.55 ppm compared to the radiosondes. Due to its rather simple mathematical formulation, its high flexibility and the benefits discussed above, this model is recommended for further investigations. Maybe with refined a priori values (see Sec. 7.2.2).

Compared to the COSMO-7 results with its 45 vertical levels, all three voxel models with only 16 layers and hourly resolution are not able to reproduce the higher vertical and temporal gradients shown in the variation of wet refractivity data of the numerical weather model in Fig. 7.3. Therefore, an increase of the number of layers is investigated and presented in Sec. 8.1.1, pp. 111f. Fig. 8.1 shows different implementations of the layer distribution applying Eq. (7.1), which was used for the further data analysis of high-resolution GPS tomography. The temporal variation of wet refractivity profiles using these voxel models is discussed in Sec. 8.1.1.

In general, the mean height of the lower wet refractivity contour lines (e.g. 10 ppm line) decrease in height along with the increasing number of layers. Intense precipitation events are much better reproduced as well. Unlike the COSMO-7 result in the case of Zermatt, the tomographic solution seems to recognize all precipitation incidences.

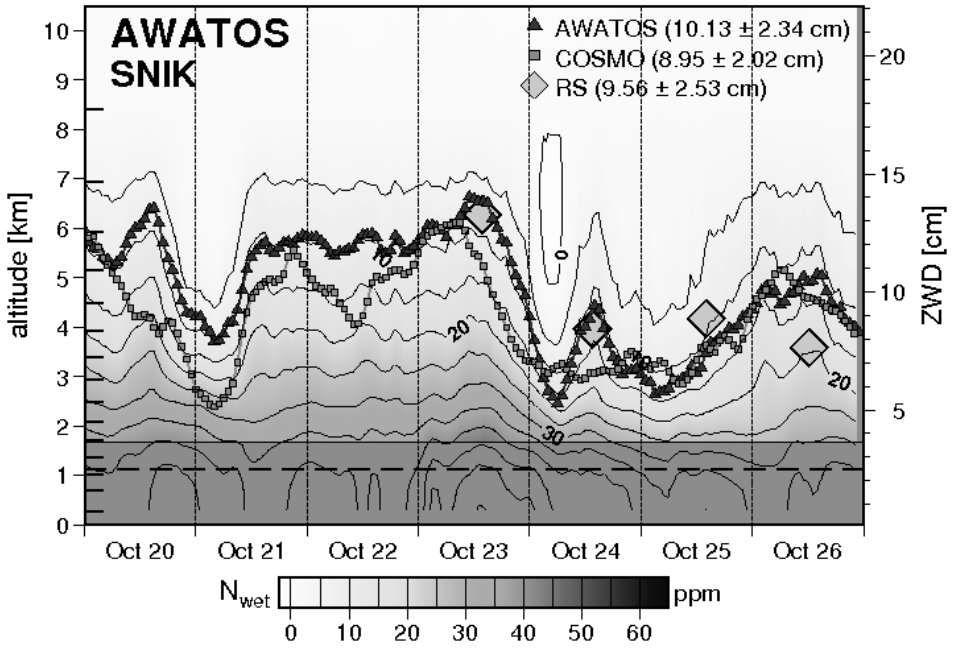

Fig. 7.6: Wet refractivity distribution in voxel column 15 (see Fig. 7.1) from the tomographic analysis with the newly developed layer distribution function (see Eq. 7.1) and the time series of integrated ZWD. Compared to Fig. 7.4, especially the variation of the integrated value with the new function is closer to the reference radiosondes, and the mean value of ZWD is achieved with better agreement than in Fig. 7.5.

7.2.2 Obtaining a priori information

A priori or initial values for unknown refractivities are used to constrain and stabilize the tomographic inversion problem (see Eq. 3.7 on p. 39). In principle, any value with an appropriate weighting factor can be introduced for any or each voxel. Usually, the a priori values are taken from the spatially and temporally distributed meteorological observation data collocated and interpolated with respect to the tomographic voxel center coordinates. The parameters atmospheric pressure, temperature and partial water vapor pressure are preprocessed with the software package COMEDIE (see Sec. 2.5, pp. 30f.), and are converted into dry, wet and total refractivity according to Eq. (2.4). This can be chosen with respect to the desired tomographic output.
A priori or initial values for unknown refractivities are used to constrain and stabilize the tomographic inversion problem (see Eq. 3.7 on p. 39). In principle, any value with an appropriate weighting factor can be introduced for any or each voxel. Usually, the a priori values are taken from the spatially and temporally distributed meteorological observation data collocated and interpolated with respect to the tomographic voxel center coordinates. The parameters atmospheric pressure, temperature and partial water vapor pressure are preprocessed with the software package COMEDIE (see Sec. 2.5, pp. 30f.), and are converted into dry, wet and total refractivity according to Eq. (2.4). This can be chosen with respect to the desired tomographic output.

There are several options how to associate appropriate voxel numbers to be connected with those a priori values and estimated corresponding standard deviations. It is a promising approach to tie the boxes of the two top layers to such a priori values with predefined standard deviation (see also Liou et al., 2003). The voxel model should, therefore, be constructed in order to obtain accurate parameters from COMEDIE at this upper boundary (e.g. above the tropopause). Moreover, the voxels cutting the ground may be associated with the a priori values from the nearest ground based meteorological stations. A range of about ± 100 m in altitude is suitable, if longer distances to the voxel centroids are represented by higher standard deviations of the a priori values, which act in the sense of reduced weights. In order to let the GPS observations having the highest impact on the tomographic solution, the weights for all a priori values are at least five times lower than for the GPS data (i.e. double-difference slant path delays and ZTD), realized by setting up the weight matrix $\mathbf{P}$ in Eq. 3.7, p. 39, accordingly.

Another approach is to fill up the whole voxel model by COMEDIE preprocessed and converted values. But this is not recommended because the COMEDIE output comprises only the ground-based meteorological measurements and the few radiosondes from the WMO network for the middle and upper tropospheric situation. In the ground based GPS measurements, though, the effects of the entire troposphere from the surface up to the tropopause over the catchment area are included. They would not be appropriately approximated by the other method, and related biases interfere with the tomographic processing.

7.2.3 Allocation of meteorological data

Meteorological data of air pressure, temperature and humidity is used to divide the total path delays of the GPS processing into a dry and a wet part (see Eq. 2.13 on p. 19). The parameters have to be available for each GPS station included in the tomographic analysis.

Within AWATOS, the data is interpolated to the required times of each double-difference introduced. Therefore, according to the temporal correlation length, data before the first and after the last point of the time range for one tomographic analysis have to be available. The software COMEDIE is used to collocate and interpolate the meteorological data at the desired locations in space and time.

7.2.4 Selection of beneficial stations

The selection of the GPS stations, whose data has to be processed in the tomographic analysis, is a very important issue. An optimum has to be found between the number of estimated zenith path delays from stations in the target area and the total number of uncorrelated double-differenced observations, which intersect with the voxel model.

Stations too far away from the tomographic voxel model have a negative impact on the final solution. The reason for this may be that they are in a completely different atmospheric environment. Thus, related to the cutoff angle, those stations and their

connected baselines were pre-eliminated before the processing. The remaining data is shown in Figs. 7.7(a) and 7.7(b) for the July and October 2005 campaigns.

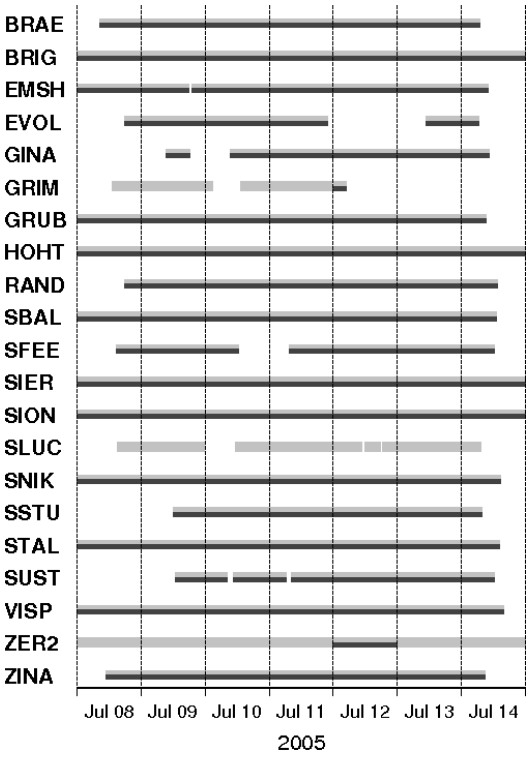

(a) Data availability of the GPS stations in the project area for the July 2005 campaign.

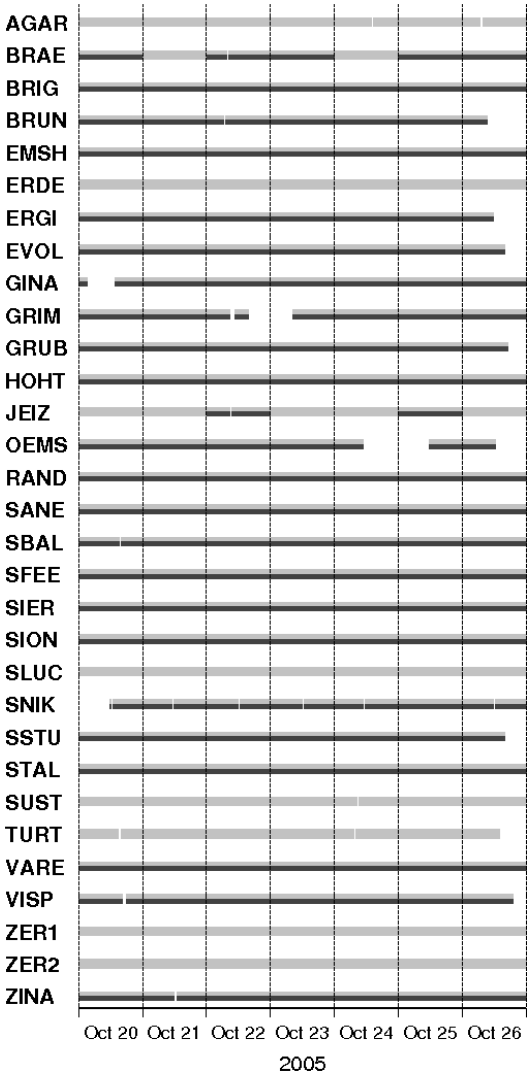

(b) Data availability of the GPS stations in the project area for the October 2005 campaign.

Fig. 7.7: Availability of GPS observations for the stations within the project area after the double-difference postprocessing with the Bernese GPS Software Version 5.0. The light-colored bars denote the data before removal of the baselines to far distant stations. The dark-colored lines represent the remaining observations.

There is a drastic reduction of the number of double-difference observations (baselines and corresponding phase residuals) after filtering out far distant stations. Unlike the phase residuals, the zenith path delays of all the stations in the project area remain for further processing. In the following, an example of a GPS tomography analysis with and without including data from three distant IGS stations is presented.

Although in Fig. 7.9(b) the total number of observations to generate the solution is larger than in Fig. 7.9(a), the negative influence of the three stations left

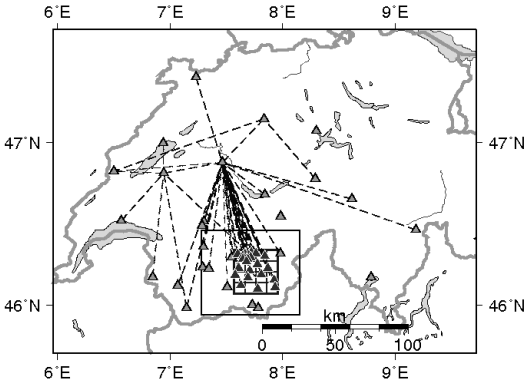

(a) Baseline map of the reduced network of GPS receivers to the beneficial stations for the analysis of the voxel model indicated.

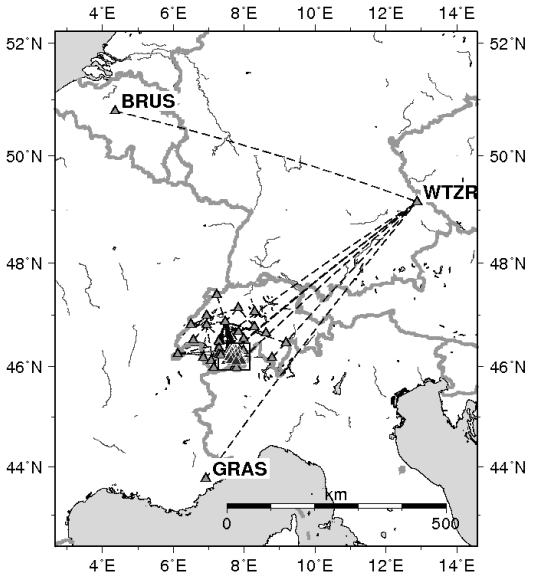

(b) Baseline map of the GPS receiver network from Subfig. (a) incorporating the three IGS stations in Brussels (BRUS), Caussols (GRAS) and Bad Koetzting (WTZR).

Fig. 7.8: Typical baselines generated by the GPS processing software with maximum observation strategy (OBS-MAX) with the campaign stations network during the October 2005 campaign. Keeping the three additional stations shown in Subfig. (b), many baselines from station WTZR remain for the tomographic analysis together with the zenith path delays from all three stations.

is significant, especially above an altitude of 3.5 to 4 km. Below this height, the solutions correspond with high agreement due to the similar a priori model from the meteorological surface data and the vertical inter-voxel constraints. The effect of the additional stations is mainly a strong variability (more than +10 ppm) of the estimated wet refractivity values in the middle troposphere between 4 and 8 km AMSL.

The results revealed the sensitivity of the tomographic software package AWATOS concerning data to far distant GPS receivers (ZPD estimates and double-difference residuals). There is a negative influence of this data mainly on the border boxes of the voxel model. By means of intervoxel constraints and also direct impact of the measurements to the boxes outside the inner model, all voxels in the whole model are contaminated. The effect becomes manifest in a high variation of overestimated refractivity values in the middle and upper troposphere.

In Fig. 7.10, the time series of the zenith total delay estimated by GPS processing are shown for a station in the north of the project area (see station HOHT in Fig. 4.9(a)) and the three distant IGS stations BRUS, GRAS and WTZR mentioned in this section (see Fig. 7.8(b)). The time series significantly disagree in both the general shape and the variation due to completely different meteorological conditions. Thus, a combination in GPS tomography has to be omitted unless the impact of this measurements can be handled appropriately.

To avoid the removal of double-differences of baselines from local stations to far distant stations, it could be considered to implement a distance dependent down-weighting function for the ZTD estimates with respect to the station coordinates. In this case, all double-difference observations could remain in the tomographic equation system to improve the condition of the design matrix (see Eq. 3.7). Without such a function, the tomographic system cannot distinguish between far distant stations and stations outside but close to the boundary of the voxel model.

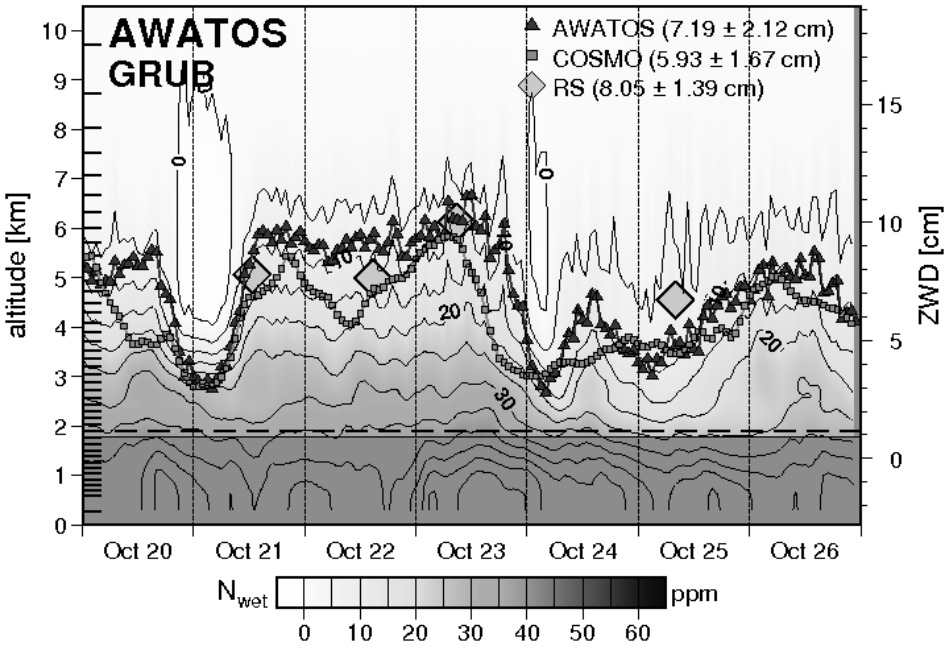

(a) Wet refractivity variation in ppm above station GRUB processing the reduced GPS network shown in Fig. 7.8(a).

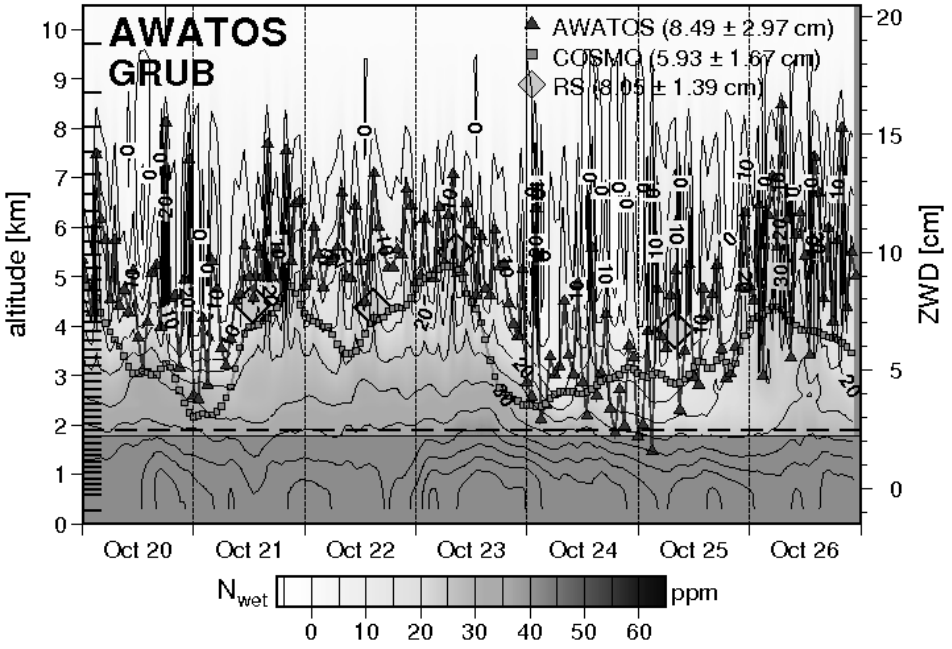

(b) Tomographic solution processing the GPS network including the three distant stations BRUS, GRAS and WTZR (see Fig. 7.8(b)).

Fig. 7.9: Tomographic determined wet refractivity variation in ppm above the station GRUB in a voxel model with 7.5 km horizontal resolution and 43 layers (see Figs. 8.2 and 8.1(c)) during the October 2005 campaign. The integrated zenith wet delays from the tomographic solution and the data of the numerical weather model COSMO-7 are shown as well.

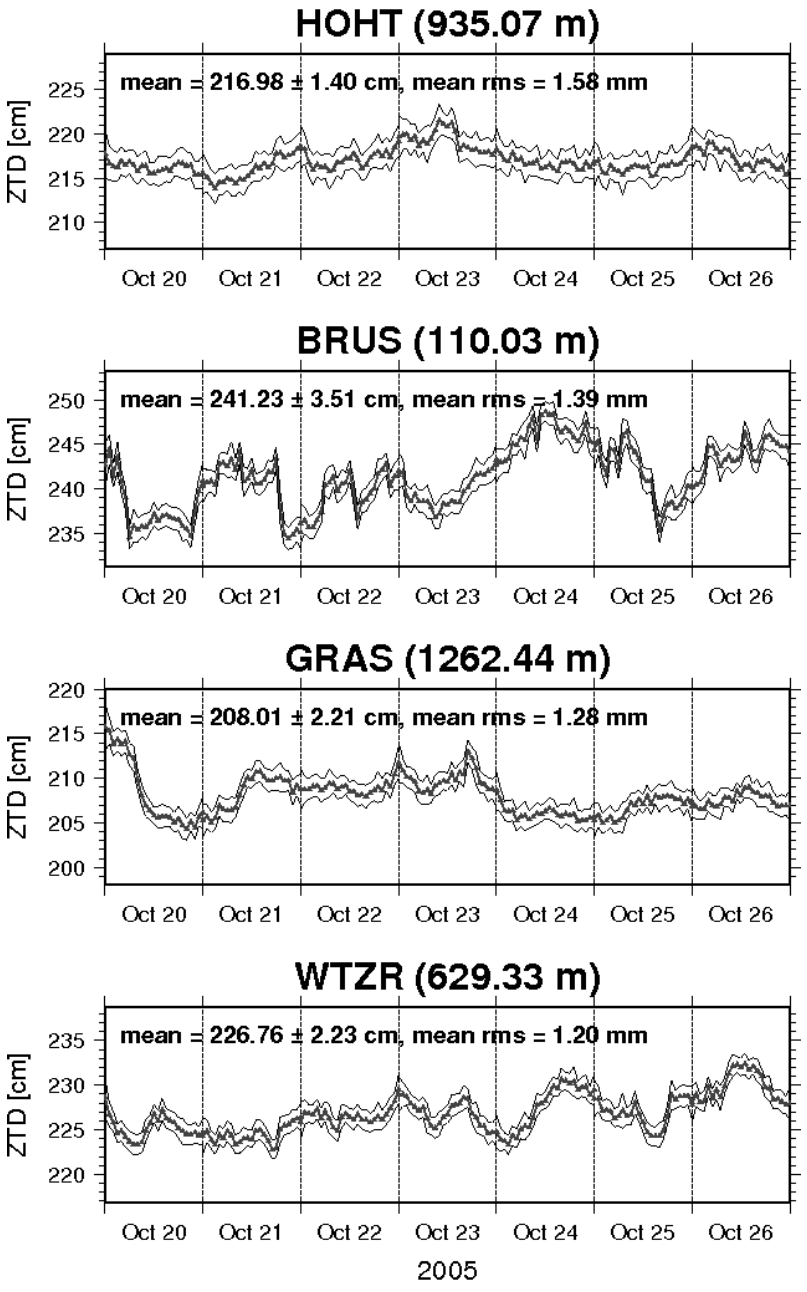

Fig. 7.10: Zenith total delay time series from GPS postprocessing of station HOHT (in the project area) and the three distant stations BRUS, GRAS and WTZR for the field campaign in October 2005.

7.3 Further analysis tools

To investigate the design matrix of the tomographic inversion problem (see Eq. 3.7 on p. 39), the estimation of the condition number is implemented in the AWATOS processing (see Sec. 3.2.5).

To improve the resolvability of the problem, the weight matrix may be updated iteratively by changing the a priori standard deviations of the input data. This also gives valuable information about the network design (horizontal and vertical station distribution) of the measurement system with respect to the voxel model resolution.

7.4 Notes on near real-time analysis and predictive algorithms

Investigations were carried out in terms of near real-time determination of the refractivity field by GPS tomography. Furthermore, predictive algorithms were developed and tested based on temporal correlation analysis.

The most limiting factor in near real-time analysis with GPS tomography is the availability of the auxiliary input data. The use of rapid orbits or broadcast ephemerides instead of precise orbits for the GPS processing is discussed in Sec. 5.2. The same orbit data has to be introduced into the tomographic software package AWATOS. Compared to the processing with precise orbits, Rocken et al. (1993) has already demonstrated a degradation of the quality of line-of-sight wet path delays by 30 % using broadcast ephemerides.

Another issue in this context is the limitation of the tomographic analysis in the temporal domain. Tools have been developed to introduce data of different sampling intervals into the processing.

7.5 Accuracy and reliability assessment

The accuracy and reliability of high-resolution GPS tomography is investigated by comparing the results derived from the data of the dedicated field campaigns with GPS-independent measurements and the numerical weather model COSMO-7 of MeteoSwiss.

In a first step, the integrated zenith path delays were examined. The GPS derived ZTD were compared to data from a solar spectrometer, radiosondes, the numerical weather model COSMO-7 and the meteorological data acquired during the measurement campaigns. Additional to the analysis in space domain, the time series were also transformed into frequency domain (see e.g. Forrer, 2007). The next focus is on the comparison between the actual profiles (wet refractivity) from AWATOS, the local radiosondes and COSMO-7. Due to the different temporal and spatial resolution of all of these methods, interpolation algorithms had to be applied and optimized for this purpose. Fig. 7.11 shows wet refractivity profiles at the three locations Visp (VISP), Susten (SUST) and St. Niklaus (SNIK) at three different times (the first on October 24, 2005, the second and third on October 25).

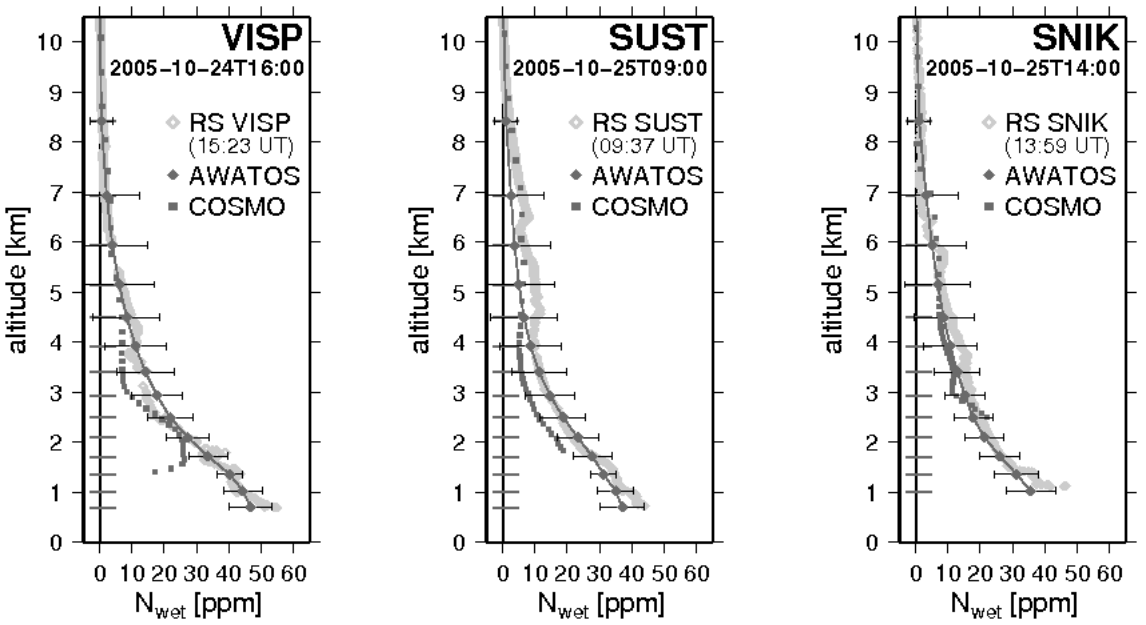

(a) Station VISP on October 24, 16:00 UT.

(b) Station SUST on October 25, 09:00 UT.

(c) Station SNIK on October 25, 14:00 UT.

Fig. 7.11: Wet refractivity profile comparison of AWATOS, COSMO and radiosonde (RS) data. On the left side, the vertical distribution of the sixteen center points of the tomographic voxel model is indicated. The horizontal error bars show the formal a priori errors of the tomographic result. They are calculated in terms of square root of the diagonal elements of the cofactor matrix $(\mathbf{A^T P A})^{-1}$ (see Eq. 3.7 on p. 39).

model	VISP		SUST		SNIK	
	Δ	σ	Δ	σ	Δ	σ
	ppm	ppm	ppm	ppm	ppm	ppm
COSMO-7	-0.86	2.98	-1.19	2.50	-1.59	2.71
AWATOS	-0.05	1.10	-1.71	2.55	-1.26	1.89

Tab. 7.1: Mean unweighted offset (Δ) of the COSMO-7 profile or AWATOS profile minus the profile of the corresponding radiosonde and standard deviation (σ) of the three examples shown in Fig. 7.11. The first and last profiles are represented better by GPS tomography than by the numerical weather model. The wet refractivity profile taken at SUST in the morning of a cloudy day (see also Fig. A.3 in the Appendix) is more difficult to recover due to a meteorological inversion situation at around 5 km altitude. At this height, there are not enough unknowns introduced in the tomographic voxel model analyzed here (only 16 layers from the bottom to the top).

For each common section of the profiles the mean offsets AWATOS minus radiosonde and COSMO-7 minus radiosonde were calculated (represented by the symbol Δ). For this, the model levels from both, the COSMO-7 model and the tomographic voxel model, were linearly interpolated to the data points of the reference radiosonde. The standard deviation (σ) of the different profiles is another indicator for accordance (see Tab. 7.1).

Uncertainties related to a non-vertical ascension of the radiosondes have not been taken into account. Hence, it is possible that the weather balloon leaves the voxel model column in a certain height, and rigid comparison statistics will be disturbed. In a prospective project of high-resolution GPS tomography, the localization of the radio sondes and effects of wind should be considered. The time component is another issue: The ascension of a radiosonde takes typically about one hour from the earth's surface up to the tropopause. During this time, the wet refractivity at the ground certainly changes. These variations are not considered in this work either.

Chapter 8

Results and discussion

8.1 Towards high spatial resolution

8.1.1 Impact of vertical spacing

In order to study the impact of different vertical resolutions of the tomographic voxel model the newly introduced function Eq. (7.1), explained on p. 94, was applied. The wet refractivity profiles are compared to the rainfall data of the station Zermatt of the automated meteorological network ANETZ of MeteoSwiss during the July 2005 campaign (July 8 to 14, 2005) and the results of the postprocessed data of the numerical weather model COSMO-7. For the weather dynamics at the two related stations Evolène and Visp during this period see Fig. A.2 on p. 180.

Fig. 8.1 gives the cross sections through the different voxel models discussed in this part, and Fig. 8.2 shows the geographical setup in the horizontal plane. The result obtained by data conversion from a COSMO-7 profile is given in Fig. 8.3. Figs. 8.4, 8.5 and 8.6 give the solutions of the high-resolution GPS tomography using the enhanced software package AWATOS with three different layer distributions. The nearest COSMO-7 profiles were used to validate the different vertical resolutions of the voxel model profiles.

The conclusions of this section are summarized in Sec. 8.1.7 on pp. 135f. The vertical correlation length (Δz_0) for the inter-voxel constraints discussed in Sec. 3.1.3, pp. 35f., is set to 200 m for all examples. Furthermore, the weights for all inter-voxel constraints are five times lower than the GPS input data (double-difference slant path delays and ZTD) in the weight matrix $\mathbf{P}$ of the tomographic equation system (see Eq. 3.7, p. 39). In this way, vertical inhomogeneities and meteorological inversion situations near the earth's surface may still be reproducible and the refractivity profiles are not forced to a standard profile.

The general behavior of the wet refractivity variation in temporal as well as in vertical dimension in the 16 layer case (see Fig. 8.4) is comparable to the COSMO result (Fig. 8.3). Yet, also in this tomographic analysis, rainfall events are hardly detectable. Only the 5 ppm wet refractivity contour line seems to be far to high (in the upper troposphere above 7 km altitude) regarding the numerical weather model solution. Compared to the solution with 16 layers (see Fig. 8.4), the first and last rainfall events at the ANETZ station Zermatt leave a clearer signature in the vertical wet refractivity profiles of the 26 layer solution (Fig. 8.5), especially in the middle troposphere between 4 and 7 km AMSL.

Processing 43 layers in the tomographic voxel model (see Fig. 8.6), precipitation is well represented by the gradients of the vertical distribution of wet refractivity. Furthermore, the 5 ppm wet refractivity contour line decreased significantly to a more

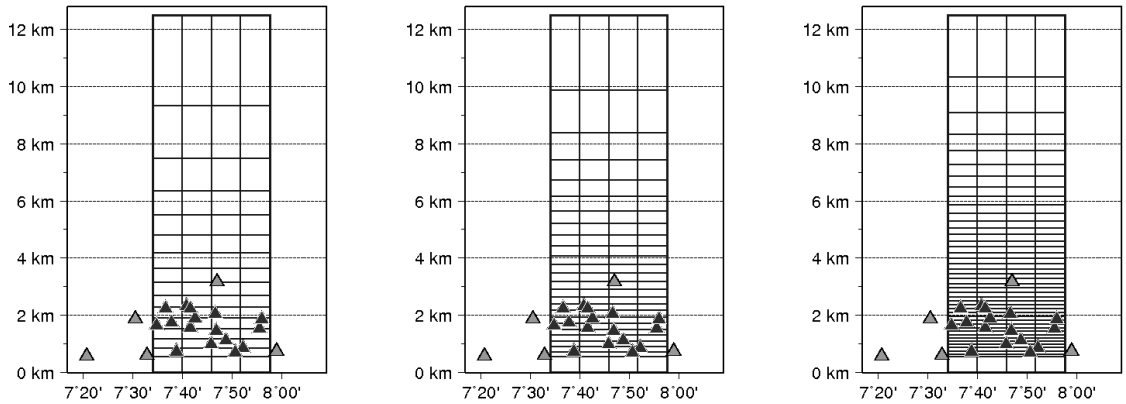

(a) Voxel model with 16 layers up to 12.5 km altitude.

(b) Voxel model with 26 layers up to 12.5 km altitude.

(c) Voxel model with 43 layers up to 12.5 km altitude.

Fig. 8.1: Latitudinal cross sections through three different voxel models with 7.5 km horizontal resolution. The vertical distribution of the GPS stations in the project area during the campaign in July 2005 is added for each case.

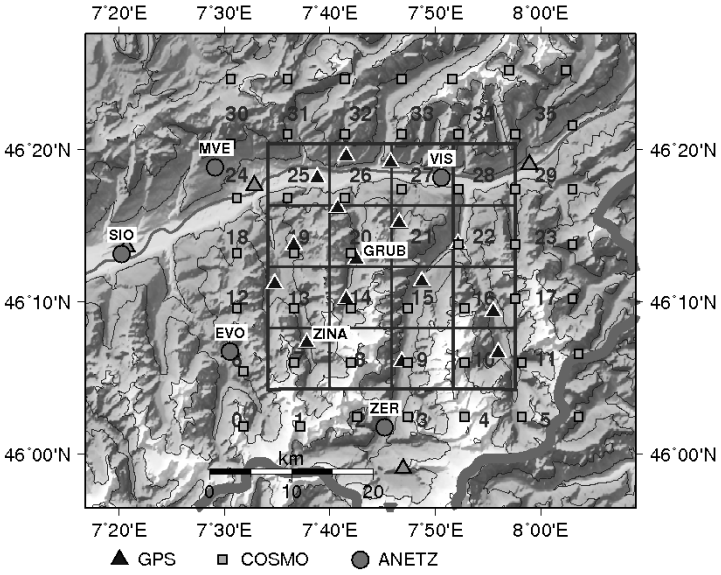

Fig. 8.2: Plan view of the 7.5 km voxel model including the profile numbers, the local GPS network during the field campaign in July 2005 and the stations of the automated meteorological network of MeteoSwiss (ANETZ). Furthermore, the base points of the available data from the numerical weather model COSMO-7 are shown.

realistic height compared to the 16 layer solution (see Fig. 8.1(a)). The sensitivity of the tomographic analysis with respect to the vertical resolution of the voxel model is strongest in the middle troposphere compared to the lower and upper parts.

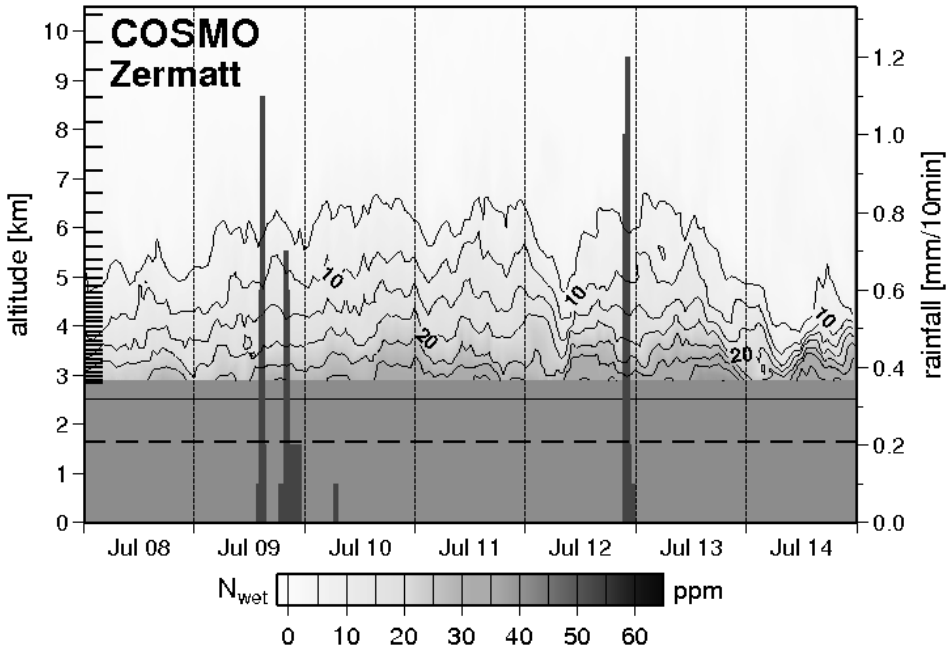

Fig. 8.3: Temporal variation of the vertical distribution of wet refractivity (contour lines in ppm) between July 8 and 14, 2005, derived from the reanalyzed COSMO-7 profile 5 km to the west of the ANETZ station in Zermatt at 1638 m AMSL (see station ZER in Fig. 8.2). Due to the height of the base point, only data above 2.8 km altitude is available. The rainfall data (in mm/10 min) of the station Zermatt is shown for validation purpose. There are no clear patterns in the refractivity field from COSMO indicating the local intense rainfall events at station Zermatt on the second and on the fifth day.

The difference of the best result with 43 voxel model layers compared to the COSMO solution is shown in Fig. 8.7 (profiles next to ANETZ station Zermatt) and Fig. 8.8 (profiles next to ANETZ station Evolène). Figs. 8.7 and 8.8 are generated by differencing the values within the homogeneous rasterized images of Fig. 8.6 minus Fig. 8.3, respectively the analogue results for Evolène.

There is an agreement of better than 2.7 ppm in average and a standard deviation of about 3.0 ppm for the common section between the profiles of the two solutions. In the case of 16 layers (see Fig. 8.4) the mean offset exceeds 3.7 ppm with a higher standard deviation. It is remarkable that the tomographic result exceeds the values from the numerical weather model especially at those times (fifth and sixth day), when the water vapor pressure increases rapidly and, therefore, a high concentration of water vapor is expected. These local effects are amplified in the processing of the GPS observations.

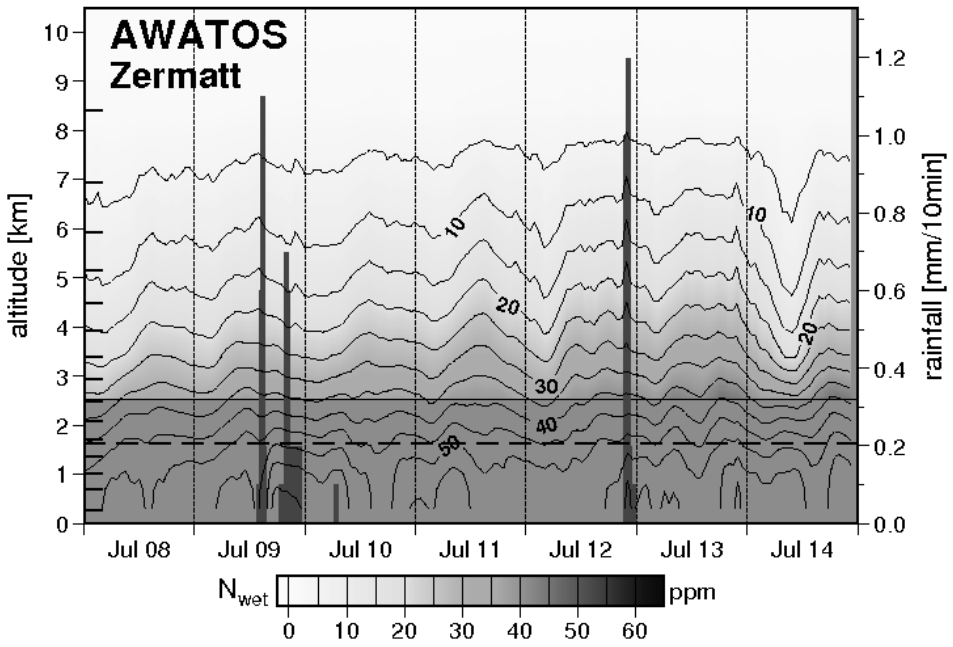

Fig. 8.4: Variation of wet refractivity in ppm from tomographic analysis of the voxel model with 16 layers (see Fig. 8.1(a)). The figure shows the profile number 2 next to the ANETZ station Zermatt (see Fig. 8.2) and the rainfall data measured at this station.

Studying the results based on single profiles (see e.g. Fig. 8.9 for the radiosonde station ZINA), the weakness of a small number of layers in the voxel model becomes evident. Especially in the middle troposphere (between 4 and 7 km altitude), the number and thickness of the voxel model layers have to be appropriate with respect to the vertical gradient of wet refractivity. Applying Eq. (7.1) for the layer distribution, this can be obtained by increasing the total number of model layers (see Figs. 8.4, 8.5 and 8.6 for examples with 16, 26 and 43 layers).

Due to the larger number of unknown refractivity values in Eq. (3.7) or the smaller number of observations for the case with more layers (e.g. Fig. 8.9(c)), the diagonal elements of the cofactor matrix $(\mathbf{A^T P A})^{-1}$ increase (see also Fig. 7.11). Comparing the solution with 43 layers to that one with 16 layers, the degradation of the related a priori quality is up to 40 %.

The increase of processing time analyzing a model with 26 layers compared to a model with sixteen layers is about factor 1.2 of CPU time. Reprocessing 36 profiles for seven days with sixteen layers needs less than 20 h of CPU time, which is about a tenth of the data time span. Analyzing a model with 43 layers instead enlarges this factor in the order of 1.5 of CPU time. This limitation has to be kept in mind when regarding near real-time processing strategies with high-resolution GPS tomography.

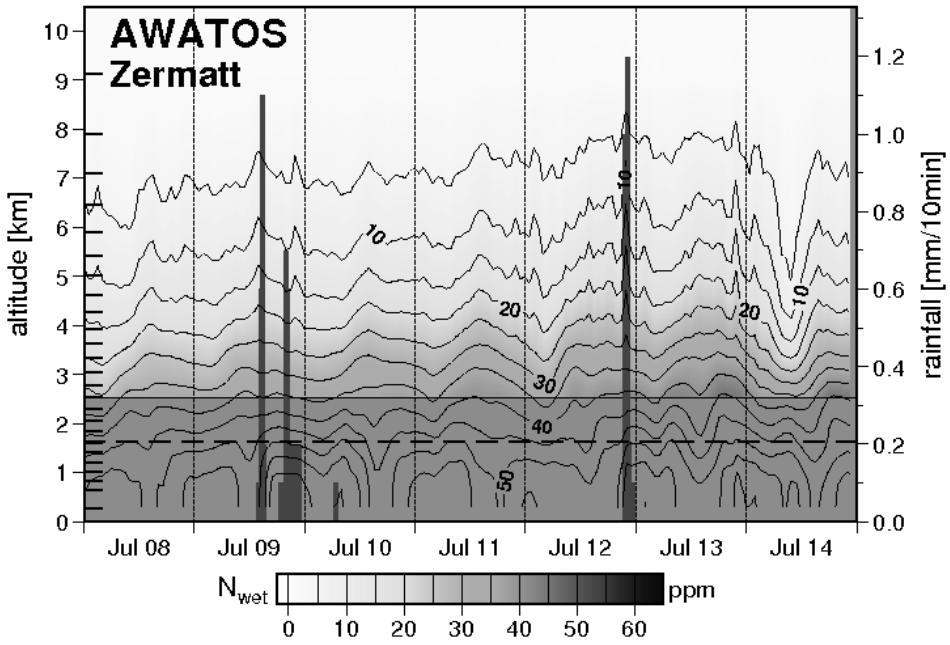

Fig. 8.5: Variation of wet refractivity in ppm from tomographic analysis of the voxel model with 26 layers (see Fig. 8.1(b)) and the rainfall data from Zermatt. Compared to Fig. 8.4, this solution shows higher variations and stronger vertical gradients in the wet refractivity profiles, what corresponds more to the data of the numerical weather model (see Fig. 8.3). Also the precipitation events are recognizable in local maxima in the time series.

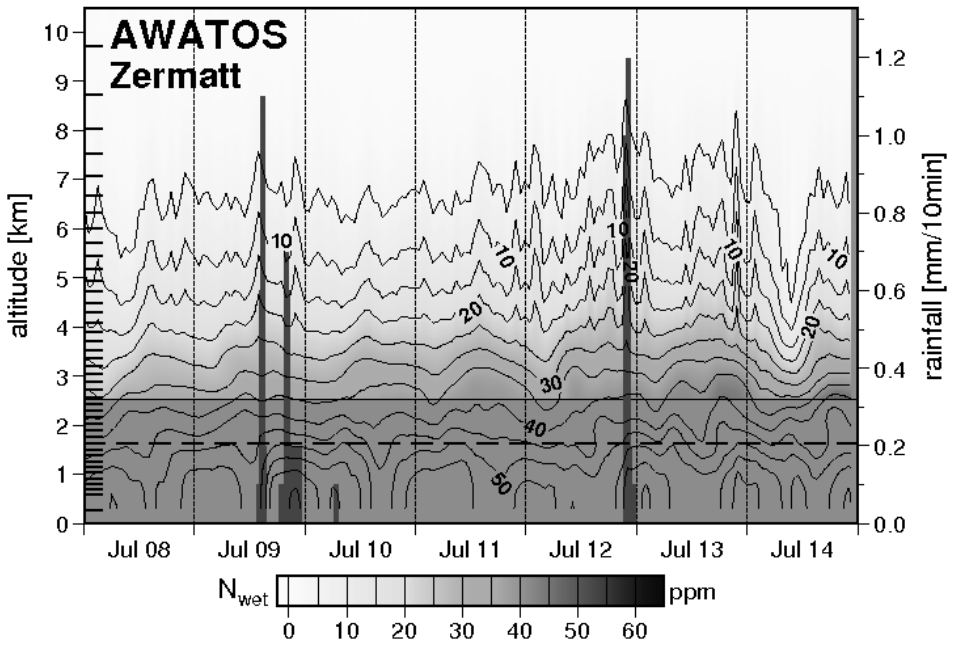

Fig. 8.6: The last example of different vertical voxel model resolutions shows the wet refractivity distribution in ppm above the ANETZ station Zermatt of the tomographic analysis with 43 layers (see Fig. 8.1(c)) and the observed rainfall data at Zermatt during the July 2005 campaign. The peak in wet refractivity in the middle troposphere before midnight of July 14 is related to an intense precipitation event observed at station Evolène (see also Fig. A.2 in Appendix A).

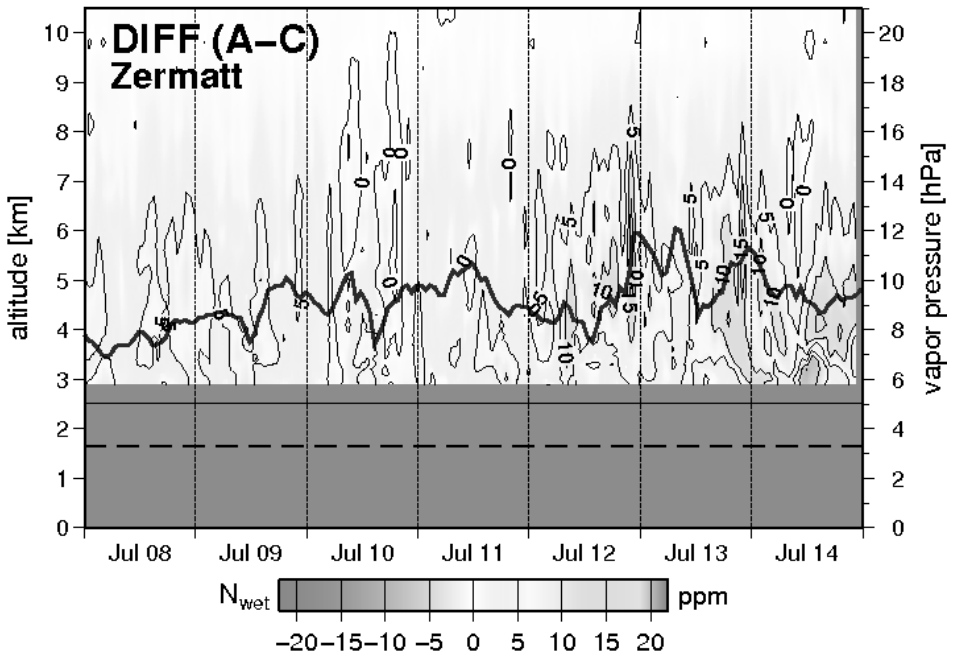

Fig. 8.7: Difference of the distribution and variation of wet refractivity in ppm next to Zermatt during the July 2005 campaign. The tomographic result (*A*WATOS) with 43 layers is shown (see Fig. 8.6) minus the solution of the numerical weather model *C*OSMO (see Fig. 8.3). There is a good agreement of the wet refractivity values between both methods during the first four days. On the fifth day, GPS tomography estimates more water vapor around five km altitude. On the sixth and seventh day, the differences are most pronounced around four km altitude. The time series of the surface-based water vapor pressure measurements, which are used for the a priori model of the tomographic solution at station height, are shown as well. The positive differences from the tomographic solution (AWATOS) minus the numerical weather model (COSMO-7) precede intense rainfall events at this station coupled with increasing vapor pressure.

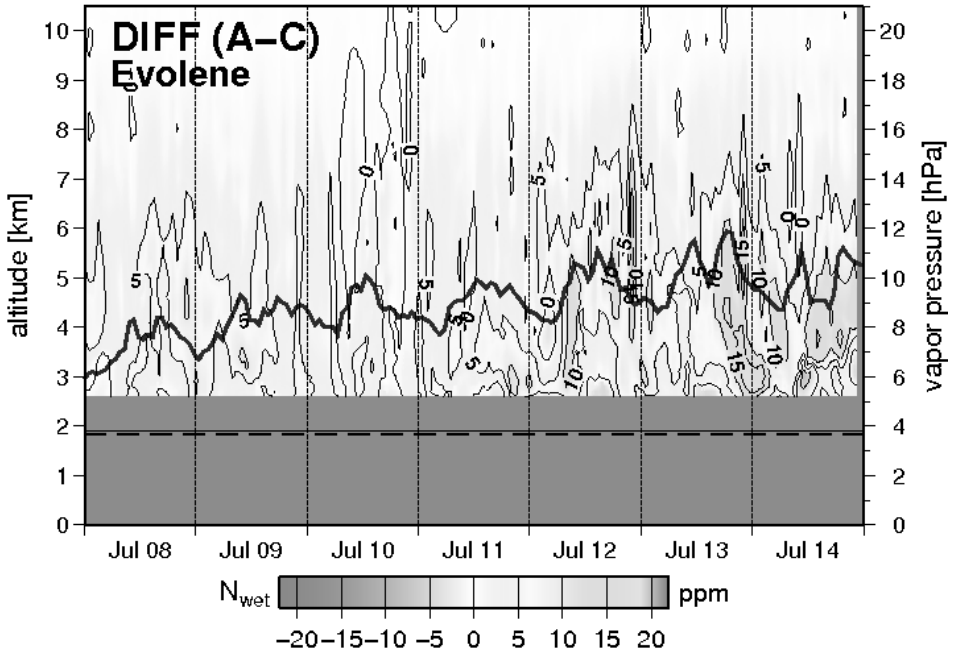

Fig. 8.8: Difference of the distribution and variation of wet refractivity in ppm next to Evolène (at 1825 m AMSL) from the tomographic result minus the solution of the numerical weather model. The time series of the surface-based water vapor pressure measurements are shown as well. Similar to Fig. 8.7, the positive offsets of the comparison of the AWATOS solution minus the COSMO-7 solution (*A-C*) in the second half of the campaign, come together with approaching rainfall events (see also Fig. A.2 in Appendix A).

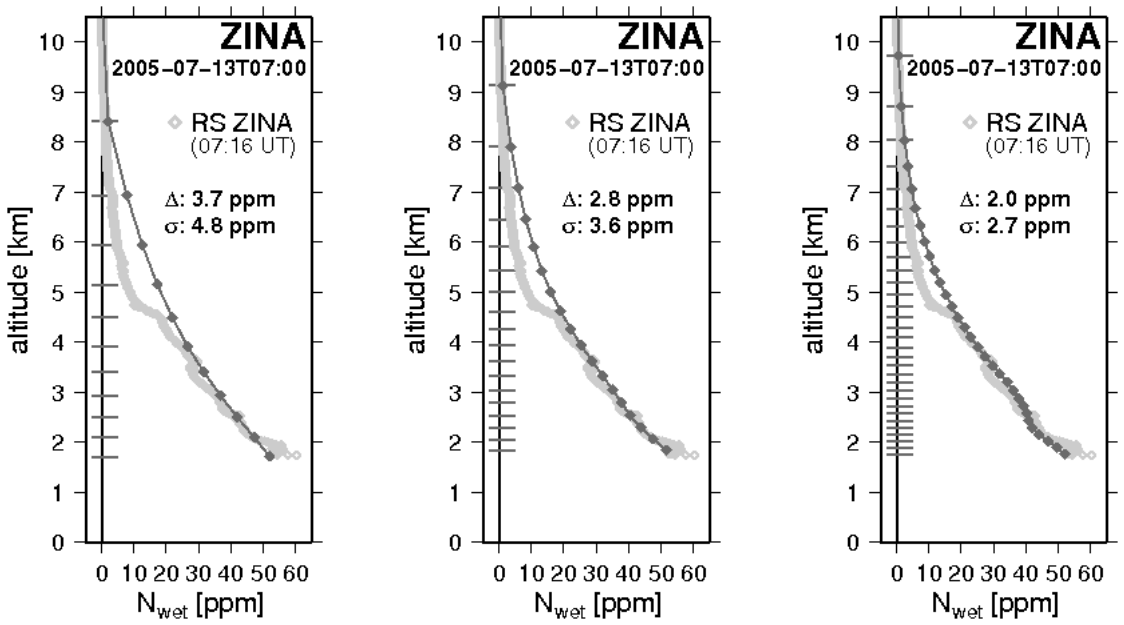

(a) Station ZINA on July 13, 07:00 UT. 16 layers.

(b) Station ZINA on July 13, 07:00 UT. 26 layers.

(c) Station ZINA on July 13, 07:00 UT. 43 layers.

Fig. 8.9: Wet refractivity profiles from tomographic voxel column number 7 (see Fig. 8.2) analyzing three different vertical resolutions. Only the layers above the earth's surface are indicated on the left side. The profile of the reference radio sounding is represented, too, together with the mean offset Δ (tomographic solution minus radiosonde) and the standard deviation σ in ppm.

8.1.2 Vertical resolution and cutoff elevation angle

The previous results were obtained by processing all slant path delays available. Thus, the elevation cutoff angle was adopted from the GPS processing and set to 3 ° (see also Sec. 5.2.3 on pp. 59). In order to study the influence of a changing cutoff angle, the GPS observation data was reduced accordingly within the tomographic analysis. That means, no double-differenced slant path delays were reconstructed for ray tracing below the specified elevation. Some results are shown in Tab. 8.1.

layers	cutoff elevation							
	3 °		5 °		10 °		15 °	
	Δ	σ	Δ	σ	Δ	σ	Δ	σ
#	ppm	ppm	ppm	ppm	ppm	ppm	ppm	ppm
16	0.55	2.69	0.54	2.69	0.65	3.29	0.54	2.69
43	0.32	2.35	0.31	2.34	-0.26	2.29	-0.17	2.29

Tab. 8.1: Mean offset (Δ) and mean standard deviation (σ) of the tomographic wet refractivity profiles minus the reference radiosondes based on the data of the October 2005 campaign. The voxel model has a horizontal resolution of 7.5 km. Two vertical resolutions are shown. The results with cutoff elevation angles of 3 °, 5 °, 10 ° and 15 ° are presented.

The observations with low elevation angles carry more information about the troposphere (see e.g. Bender and Raabe, 2005, 2007). But the uncertainty in modeling these effects and the influence of multipath in this domain has a negative impact on the final solution, especially in the case of a high vertical resolution (with 43 layers, see also e.g. Fig. 8.1(c) for the model cross section). Here, the absolute values of the offset as well as the standard deviation decrease with increasing elevation cutoff angle. This is because in high resolution mode more layers and voxels are affected by deficient slant path delays. With 16 layers (see e.g. Fig. 8.1(a)), no significant influence of the cutoff angle can be recognized.

8.1.3 Impact of horizontal spacing

Because of the mountainous topography of the project area, a horizontal resolution of 7.5 km (as discussed in Sec. 8.1.1) does not seem to be appropriate. In the presented target region some side valleys have a spacing distance of only a few kilometers. Therefore, investigations were carried out for higher resolution voxel models also in the horizontal plane.

Resolutions of 15, 5 and 3 km grid spacing of the tomographic voxel models with 32 layers were compared. The layers are distributed according to the new function Eq. (7.1). The ground plan and cross section of the three cases are shown in Figs. 8.11, 8.13 and 8.15. Data of the field campaign in October 2005 was processed. For validation purposes, the profile next to the ANETZ station in Visp in the main valley was selected. In the GPS tomography processing the same a priori model and intervoxel constraint parametrization were used for all three cases. The horizontal correlation lengths discussed in Sec. 3.1.3, pp. 35f., are set to 5000 m for both in west-east (Δx_0) and south-north (Δy_0) direction.

Increasing the horizontal resolution of the tomographic voxel model yields to an increase of the wet refractivity especially in the upper troposphere. This can be verified by the time series of the integrated zenith wet delays compared to the COSMO data.

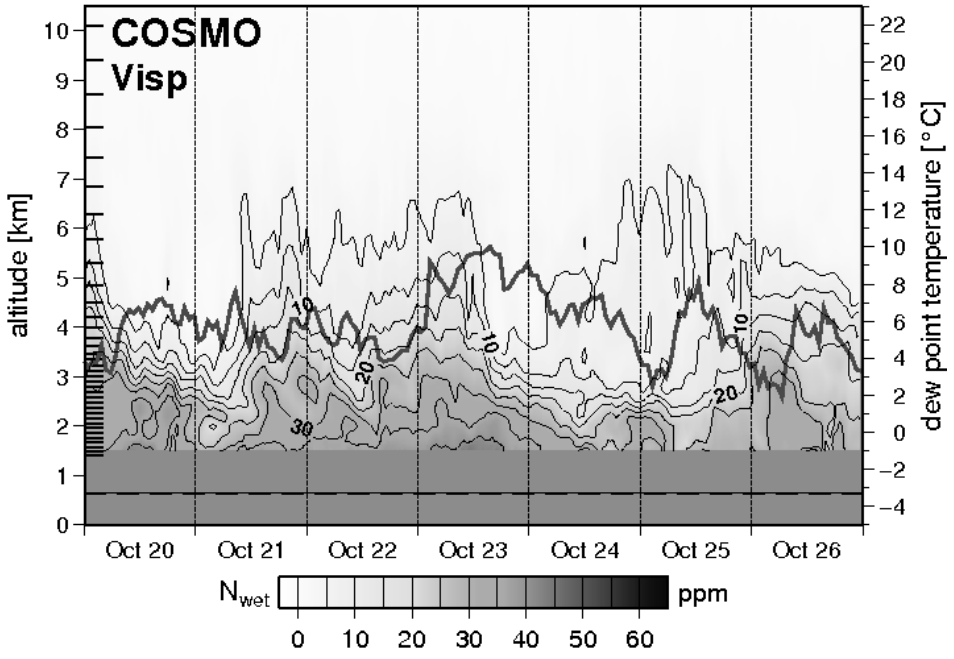

Fig. 8.10: Wet refractivity variation above ANETZ station Visp (640 m AMSL) from the numerical weather model COSMO during the campaign in October 2005. The surface-based measurements of dew point temperature are shown as well (see Eq. 2.2 on p. 12). For further time series of meteorological parameters at this time see in Appendix A, Fig. A.3 on p. 181.

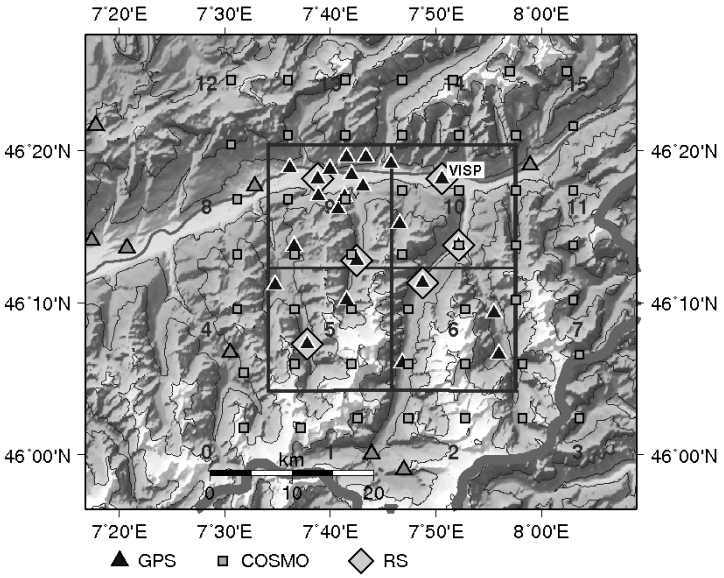

(a) 15 km voxel model with profile numbers between 0 (south-west) and 15 (north-east) and local GPS network of the October 2005 campaign including the launch sites of the radiosondes and the COSMO-7 model base points.

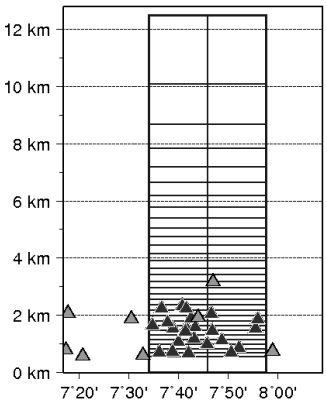

(b) Voxel model cross section with 32 layers and 15 km horizontal grid spacing.

Fig. 8.11: Ground plan and cross section of the voxel model with 15 km horizontal grid spacing in the project area with GPS network during the field campaign in October 2005.

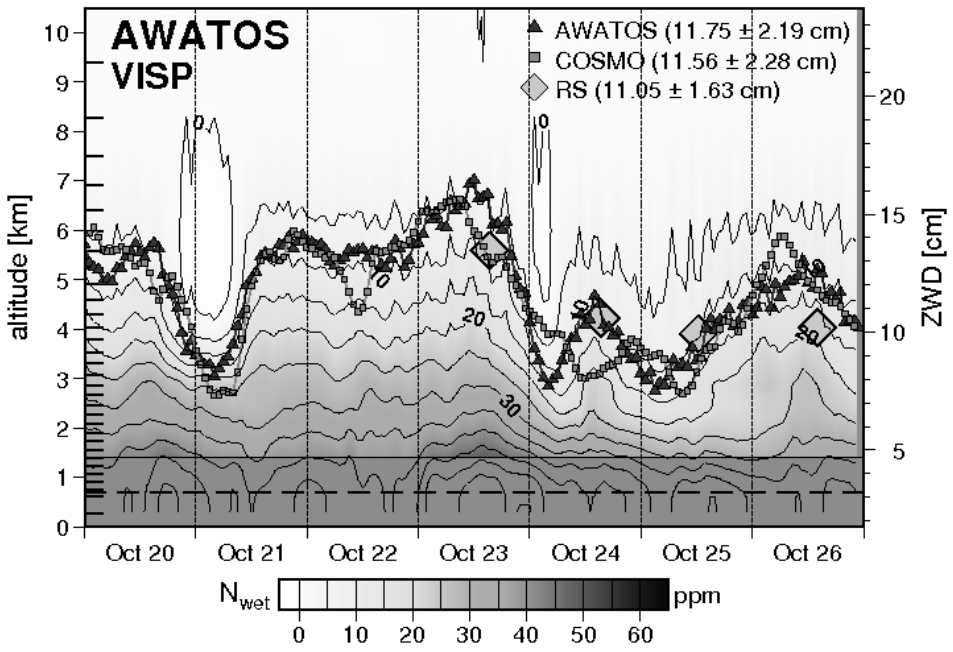

Fig. 8.12: Variation of wet refractivity determined by GPS tomography based on a voxel model with 15 km horizontal resolution. The integrated zenith wet delays (ZWD) of the solution are shown together with the corresponding data of COSMO-7 (interpolated to the surface height) and the reference radiosondes.

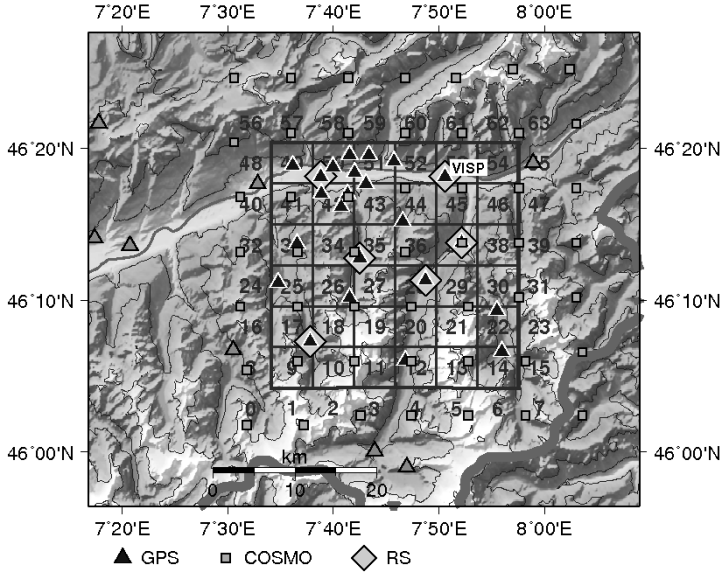

(a) 5 km voxel model with profile numbers between 0 (south-west) and 63 (north-east) and local GPS network of the October 2005 campaign including the launch sites of the radiosondes and the COSMO-7 model base points.

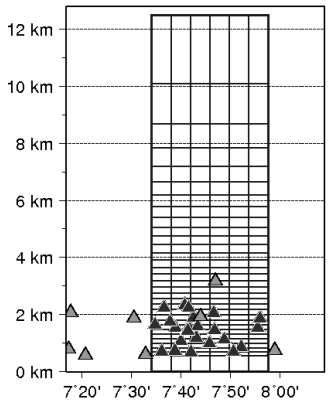

(b) Voxel model cross section with 32 layers and 5 km horizontal grid spacing.

Fig. 8.13: Ground plan and cross section of the voxel model with 5 km horizontal grid spacing in the project area with GPS network during the field campaign in October 2005.

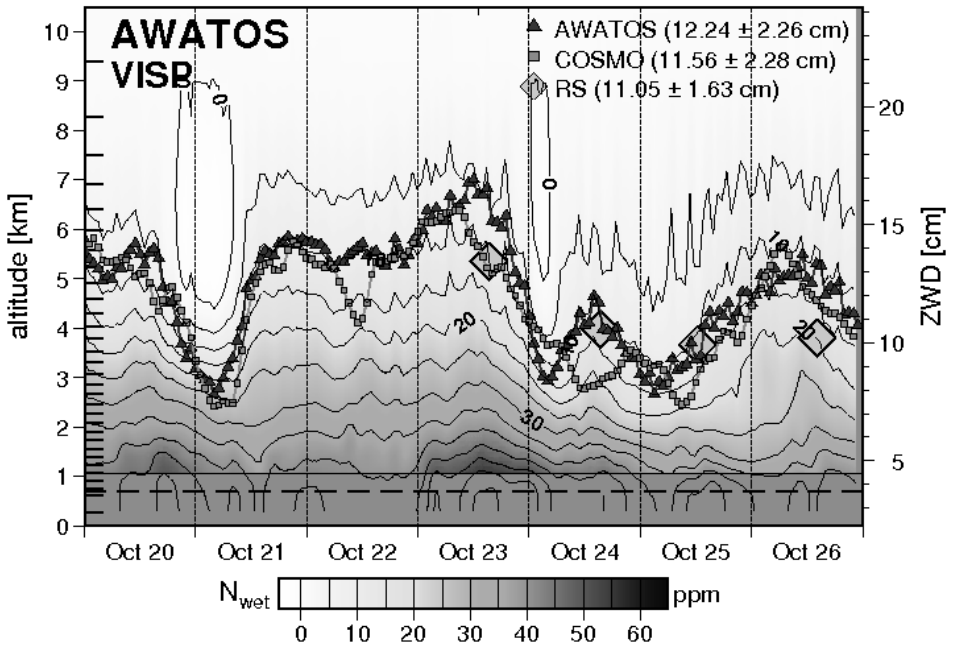

Fig. 8.14: Variation of wet refractivity determined by GPS tomography based on a voxel model with 5 km horizontal resolution. The integrated zenith wet delays of the solution are shown together with the data of COSMO-7 and reference radiosondes.

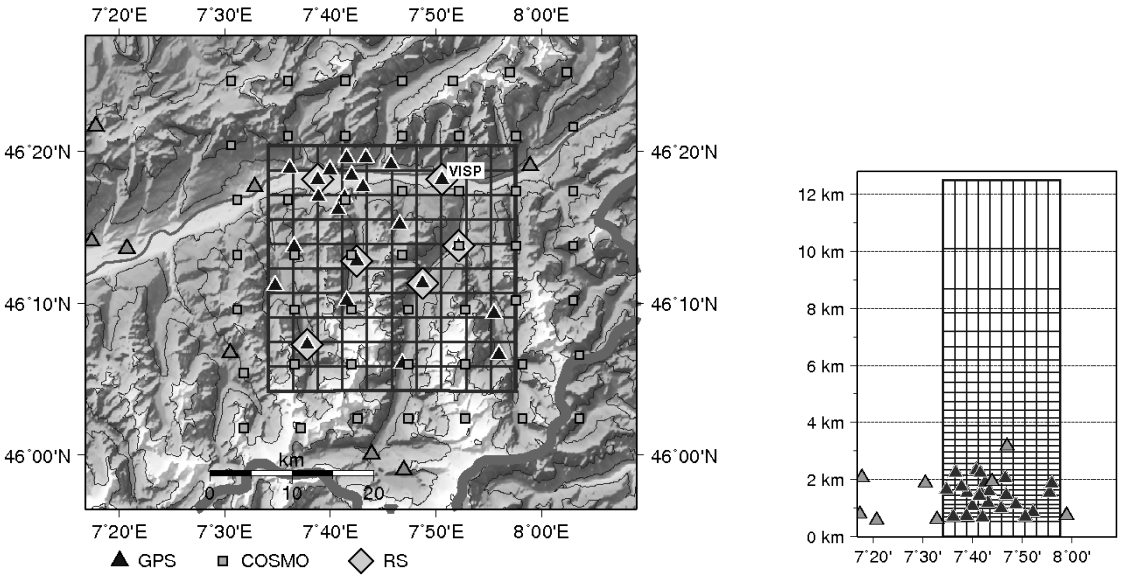

(a) 3 km voxel model with 144 columns and local GPS network of the October 2005 campaign including the launch sites of the radiosondes and the COSMO-7 model base points.

(b) Voxel model cross section with 32 layers and 3 km horizontal grid spacing.

Fig. 8.15: Ground plan and latitudinal cross section of the voxel model with 3 km horizontal grid spacing in the project area with GPS network during the field campaign in October 2005.

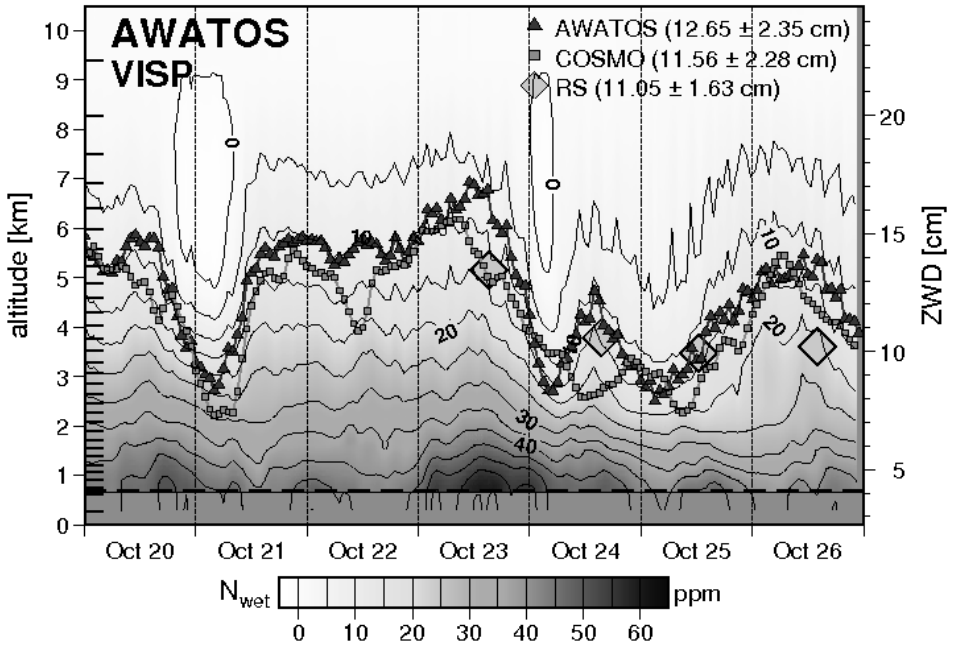

Fig. 8.16: Variation of wet refractivity determined by GPS tomography based on a voxel model with 3 km horizontal resolution. The integrated zenith wet delays of the solution are shown together with the data of COSMO-7 and reference radiosondes.

8.1.4 Summary on the July 2005 campaign data

Tab. 8.2 gives an overview over the results from the July 2005 campaign. The comparison of the tomographic wet refractivity profiles determined with a cutoff elevation angle of 3° to the corresponding radiosondes are given. Tab. 8.3 shows the same comparison with the COSMO-7 profiles and the reference radiosondes. The "synthetic" profiles of the GPS tomography and the numerical weather model were interpolated to the radiosonde profile for the calculation of the mean offset and mean standard deviation. The COSMO-7 profile was selected according to the voxel model's horizontal grid (nearest profile to the center line of a tomographic voxel column). I.e. this selection depends on the horizontal resolution of the voxel model.

The offset is defined as the difference of the modeled (COSMO-7) or estimated (AWATOS) profiles and the reference profiles (radiosonde) (see also Sec. 7.5, pp. 107f., especially Tab. 7.1). Here, the mean offset (or mean standard deviation) is the arithmetic mean of all offsets (or all standard deviations) derived with respect to the total of the radiosonde profiles launched during the campaign.

layers	horizontal resolution											
	15 km		10 km		7.5 km		5 km		3.75 km		3 km	
	Δ	σ	Δ	σ	Δ	σ	Δ	σ	Δ	σ	Δ	σ
#	ppm	ppm	ppm	ppm	ppm	ppm	ppm	ppm	ppm	ppm	ppm	ppm
16			3.33	4.52	3.85	5.03	4.49	5.52	4.24	5.43		
26			2.21	3.61	3.24	4.30	3.40	4.39	3.91	5.14	4.01	5.16
32	2.03	3.42	2.10	3.45	2.75	3.85	3.20	4.19	3.14	4.36	3.65	4.75
43	1.99	3.46	1.96	3.34	2.42	3.57	2.29	3.54	2.53	3.82		

Tab. 8.2: Mean offset and standard deviation of AWATOS wet refractivity profile solutions minus the corresponding radiosonde profiles for the July 2005 campaign. A total of 16 or 17 radiosondes was used, depending on the rejected profiles with an exceeding deviation compared to the relevant COSMO profile (see Sec. 6.4.1, pp. 78). The GPS data was processed with final orbits.

In general, the AWATOS solution overestimates the wet refractivity values with the data of the July 2005 campaign compared to the radiosondes by more than 2 ppm. On the one hand, the results of the tomographic solution get the better, the more layers are introduced into the voxel model (i.e. a higher vertical resolution) because of the optimized vertical inter-voxel constraints. On the other hand, the results get the worse, the higher the horizontal resolution is chosen, because the horizontal constraints are more difficult to determine, especially in the lower troposphere or planetary boundary layer in a region with rugged topography. Both, the offset and standard deviation of the AWATOS results (Tab. 8.2) increase with higher horizontal voxel model resolution independent from the vertical resolution. This effect has been discussed in Sec. 8.1.3. In the vertical direction, offset and standard deviation are decreasing the more layers are introduced into the model (see also Sec. 8.1.1).

The results of the numerical weather model in October 2005 are close to the radiosondes with an offset of about –0.5 to –0.2 ppm (depending on which profiles

layers	horizontal resolution											
	15 km		10 km		7.5 km		5 km		3.75 km		3 km	
	Δ	σ	Δ	σ	Δ	σ	Δ	σ	Δ	σ	Δ	σ
#	ppm	ppm	ppm	ppm	ppm	ppm	ppm	ppm	ppm	ppm	ppm	ppm
16			-0.56	3.36	-0.21	3.15	-0.18	3.18	-0.32	3.24		
26			-0.54	3.32	-0.20	3.12	-0.17	3.14	-0.30	3.21	-0.35	3.07
32	-0.23	3.11	-0.53	3.30	-0.19	3.10	-0.17	3.12	-0.30	3.20	-0.34	3.05
43	-0.23	3.09	-0.52	3.28	-0.17	3.08	-0.39	3.31	-0.29	3.18		

Tab. 8.3: Mean offset and standard deviation of COSMO-7 wet refractivity profiles minus the corresponding radiosonde profiles during the July 2005 campaign. As in these statistics, the selection of the COSMO-7 profile used for the comparison depends on the tomographic voxel model horizontal spacing, the results diverge slightly.

were selected according to the corresponding tomographic voxel model) with a mean standard deviation of 3.2 ppm.

Despite these statistics concerning the advantage of COSMO-7 and regarding not only the mean values but also the vertical distribution of wet refractivity, GPS tomography achieves good results. An example of a voxel model with 7.5 km horizontal spacing and 43 layers is given in Fig. 8.17. The ground plan of this model is shown in Fig. 8.2, where column number 20 indicates the location of the profiles at station GRUB. Mean offset and standard deviation of the example are summarized in Tab. 8.4.

model	July 11, 12:00		July 12, 17:00		July 13, 18:00	
	Δ	σ	Δ	σ	Δ	σ
	ppm	ppm	ppm	ppm	ppm	ppm
COSMO-7	-0.59	2.31	-4.05	6.62	-3.83	6.34
AWATOS	0.71	1.37	0.11	4.01	0.02	3.70

Tab. 8.4: Mean offset (Δ) and standard deviation (σ) of the three examples shown in Fig. 8.17. The differences of the COSMO-7 and AWATOS wet refractivity profiles minus the parameters of the corresponding radiosondes, launched at station GRUB in July 2005, are presented. The meteorological situation within the project area on July 12 and July 13 was inhomogeneous: There was rainfall at Evolène but not in Visp (see also Fig. A.2 in the Appendix). The numerical weather model is not able to reproduce such local phenomenas. Also GPS tomography cannot estimate the tropospheric profiles very accurately for these conditions.

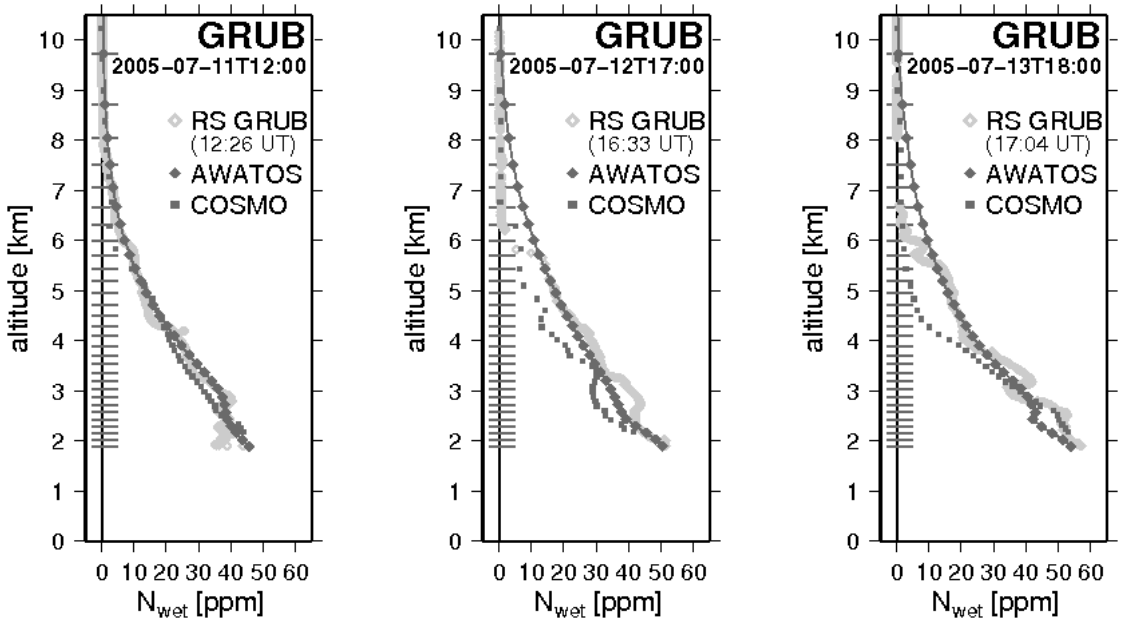

(a) Wet refractivity profiles on July 11, 2005.

(b) Wet refractivity profiles on July 12, 2005.

(c) Wet refractivity profiles on July 13, 2005.

Fig. 8.17: Wet refractivity profiles of the tomographic solution (AWATOS) with 43 layers, taken from the numerical weather model COSMO-7 as well as from the reference radio sounding at station GRUB at 1844 m AMSL within voxel column 20 (see Fig. 8.2, p. 112).

On July 11, 12 and 13, 2005, there was rainfall in the project area (see also in the Appendix, Fig. A.2, p. 180). The COSMO-7 data is not able to represent this higher amount of water vapor. In the differences shown on the time series plot (Fig. 8.18), precipitation is better predicted by GPS tomography than by the numerical weather model at this location (see also Sec. 8.1.1). The data of the integrated zenith wet delays from AWATOS are verified and confirmed by the radiosondes (see Fig. 8.18).

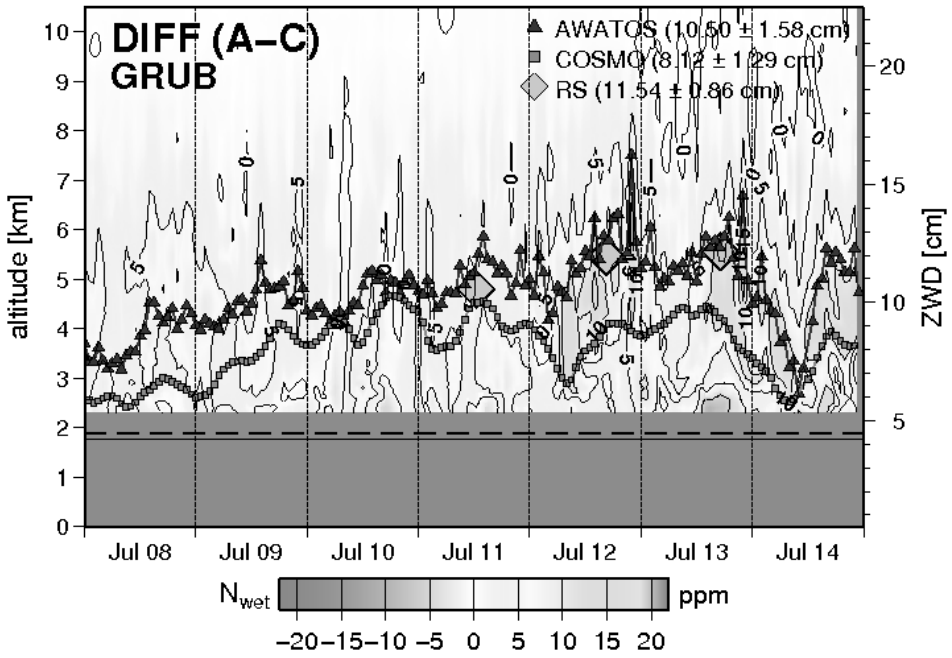

Fig. 8.18: Differences in wet refractivity from the AWATOS solution (A) minus the COSMO-7 solution (C). The mean offset is +2.5 ppm with a standard deviation of 3.2 ppm. Additionally, the time series of the integrated zenith wet delays (ZWD) from both methods together with the integrated data from the three radio soundings, which correspond to Figs. 8.17(a), 8.17(b) and 8.17(c), are given.

8.1.5 Summary on the October 2005 campaign data

The mean offsets and standard deviation of different tomographic analyses minus all suitable reference radiosondes are shown in Tab. 8.5. Fig. 8.19 gives three examples of wet refractivity profiles at station SUST from three consecutive days. The voxel model with 5 km horizontal spacing and 16 layers was processed. The data of the corresponding radiosondes represents the reference profiles. Further profiles were shown in Fig. 7.11, p. 108.

layers	horizontal resolution											
	15 km		10 km		7.5 km		5 km		3.75 km		3 km	
	Δ	σ	Δ	σ	Δ	σ	Δ	σ	Δ	σ	Δ	σ
#	ppm	ppm	ppm	ppm	ppm	ppm	ppm	ppm	ppm	ppm	ppm	ppm
16			0.08	2.24	0.55	2.69	0.67	2.61	0.76	2.84	0.84	2.93
26			-0.47	2.08	0.41	2.40	0.57	2.42	0.65	2.54	0.90	2.82
32	0.15	2.18	-0.48	2.09	0.42	2.39	0.58	2.45	0.39	2.26	0.92	2.76
43	0.17	2.21	-0.55	2.08	0.32	2.35	0.13	2.13	0.07	2.08		

Tab. 8.5: Comparison of the tomographic wet refractivity profiles with the total of 32 radiosonde profiles from the October 2005 campaign.

The wet refractivity profiles from GPS tomography match the radiosonde profiles better in the October 2005 campaign than in the July 2005 campaign with a mean offset of less than 1 ppm. The standard deviation does not exceed 3 ppm for all models presented. The same statistics for the data of the numerical weather model COSMO-7 is given in Tab. 8.6. There are small differences in the results because the selection of the COSMO-7 profiles and the common vertical section COSMO, GPS tomography and the radiosondes depends on the voxel model in use. Nevertheless, the variation of all values is very small. The mean offset is about −0.85 ppm (about 60 % larger than in July), and the mean standard deviation is 2.4 ppm (about 20 % smaller than in July).

layers	horizontal resolution											
	15 km		10 km		7.5 km		5 km		3.75 km		3 km	
	Δ	σ	Δ	σ	Δ	σ	Δ	σ	Δ	σ	Δ	σ
#	ppm	ppm	ppm	ppm	ppm	ppm	ppm	ppm	ppm	ppm	ppm	ppm
16			-0.90	2.49	-0.91	2.47	-0.80	2.32	-0.94	2.44	-0.91	2.43
26			-0.88	2.46	-0.89	2.44	-0.78	2.30	-0.91	2.42	-0.88	2.38
32	-0.79	2.36	-0.87	2.45	-0.88	2.43	-0.78	2.28	-0.91	2.48	-0.88	2.39
43	-0.77	2.36	-0.86	2.51	-0.87	2.41	-0.75	2.39	-0.90	2.47		

Tab. 8.6: Mean offset and standard deviation of the COSMO wet refractivity profiles minus the corresponding radiosonde profiles in October 2005.

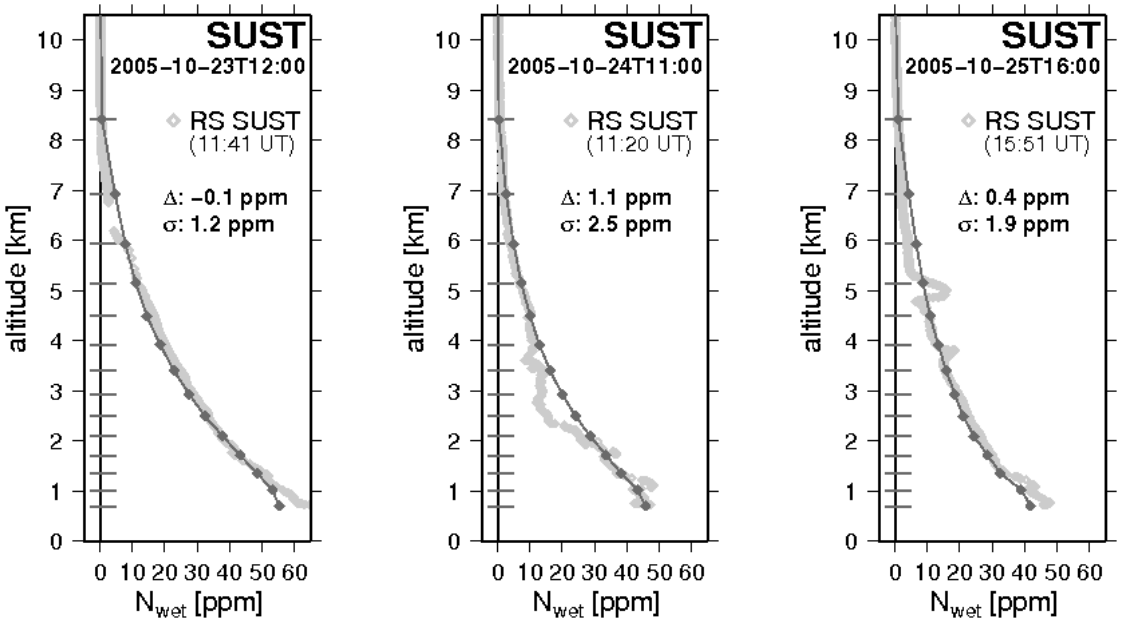

(a) Wet refractivity profiles at SUST on October 23, 2005, 12 UT.

(b) Wet refractivity profiles at SUST on October 24, 2005, 11 UT.

(c) Wet refractivity profiles at SUST on October 25, 2005, 16 UT.

Fig. 8.19: Comparison of tomographic wet refractivity profiles minus corresponding radiosondes from SUST on October 23, 24 and 25, 2005. The mean offset of the two profiles and the standard deviation is shown on the panels, too.

Figs. 7.6 on p. 100 and 7.9(a) on p. 105 as well as the results given in Sec. 8.1.3, pp. 121, have already shown examples of wet refractivity variation derived from GPS tomography and COSMO-7 during the October 2005 campaign. Fig. 8.20 shows the temporal variation and vertical distribution of wet refractivity above the station SUST during the same campaign. Fig. 8.20(a) gives the results obtained by tomographic analysis with AWATOS (5 km horizontal resolution and 16 layers) together with the ZTD time series from the Bernese processing and the integrated COSMO-7 data. Fig. 8.20(b) depicts the wet refractivity data derived from the numerical weather model COSMO-7 together with the time series of corresponding ZWD (this time not the Bernese solution but the integrated AWATOS profiles).

Concerning the ZTD time series, the Bernese results are highly correlated with the data from the reference radiosondes. The integrated COSMO-7 profiles shows a systematic offset to the GPS-ZTD results with increasing drift in time in drier weather conditions. If the ZTD value increases, the COSMO-7 data increases disproportionally, too. In terms of ZWD, the integrated tomographic results are slightly above the reference data. This is due to the modeling with only 16 layers. Here, the COSMO-7 data agree well with the radiosondes in the first half of the campaign. After the cold front passage, short-term increases of atmospheric water vapor are not represented very well.

High-resolution tomography with 3.75 km horizontal spacing and 43 layers, distributed according to Eq. (7.1) on p. 94, is able to reproduce almost each integrated radiosonde profile taken at station SUST during the field campaign in October 2005

with high accuracy (see Fig. 8.21).

Fig. 8.22 gives the graphical representation of the offsets and standard deviation of the profile comparison at station SUST (see also Fig. 7.11(b) on p. 108) during the October 2005 campaign.

There is one profile (the last one taken on October 23, 2005), that could not be reproduced accurately by both numerical methods. Although the zenith total delay from the GPS processing (see Fig. 8.20(a)) corresponds well with the integrated ZTD from the radio sounding, the tomographic determined wet refractivity field does not show the same profiles. This profile was taken at the end of intense rainfall affecting the whole project area due to a cold front passage (see also Fig. 4.8 on p. 51 for the diagram of weather fronts). Also the second radiosonde profile with strong decrease of atmospheric water vapor above 4 km altitude right after the rainfall could not be attained with high agreement. The tomographic analysis did not respond fast enough to the strong vertical gradient. On the contrary, there is local maximum in the ZWD time series right before the rapid decrease. Usually, weather simulations are unable to capture abrupt moisture changes and small-scale variations in the non-isotropic component of slant wet delays, too (see also Ha et al., 2002). With respect to the zenith total delay time series (see Fig. 8.20(a)), the GPS data fits the integrated radiosonde measurements with good correspondence.

Fig. 8.23 depicts the change of vertical wet refractivity distribution on October 23, 2005. The rapid decrease of water vapor above 4 km altitude due to the rainfall cannot be reproduced by high-resolution GPS tomography with good agreement. The second profile (Fig. 8.23(b)) was taken at station VISP. For further analysis referring to this site see also the examples in Sec. 8.1.3.

In the Appendix, Fig. E.2 on p. 202, shows results from four stations in different valleys and at different heights within the project area. This provides a basis for a spatial analysis of high-resolution GPS tomography. The tomographic results are determined for a voxel model with 3.75 km horizontal resolution and 43 layers.

Firstly, the absolute values of the integrated zenith wet delays highlights its dependency on the station height. Secondly, based on visual analysis, the ZWD time series of GPS tomography correspond well compared to the values derived from the numerical weather model COSMO-7. They agree better for the stations at lower heights in the main valley (SIER and BRIG) than at ZINA and RAND in two narrow tributary valleys. And thirdly, the vertical wet refractivity distribution varies in the four examples mostly in the first kilometers above the surface. In the higher troposphere above 5 km, the distribution is more similar for all stations.

The time series of integrated zenith wet delays and the vertical distribution of wet refractivity analyzed by GPS tomography for the four stations presented are similar during calm weather conditions. They decorrelate stronger especially before and after the cold front passage in the middle of the campaign or other rapid changes in the atmosphere (see also Lawrence et al., 2006). The figures point out the importance of estimating the vertical structure of the wet refractivity field. Atmospheric disorders may be identified with high spatial and temporal accuracy.

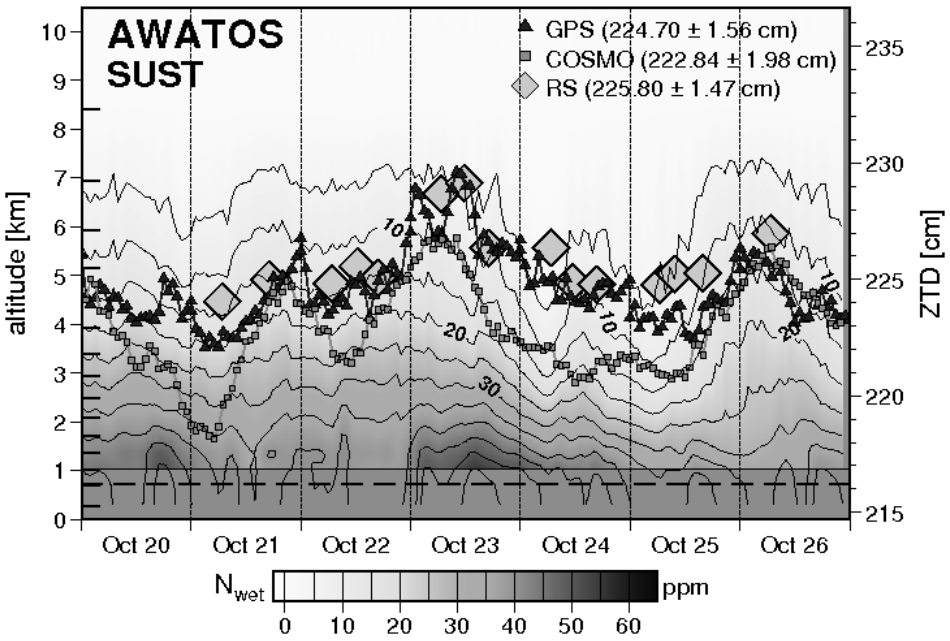

(a) Wet refractivity distribution in ppm by tomographic analysis in a 5 by 5 km voxel column with 16 layers above the station SUST. The time series of zenith total delay (ZTD) from the GPS processing (Bernese), the integrated and interpolated COSMO data and data from the reference radiosondes are shown for comparison purposes.

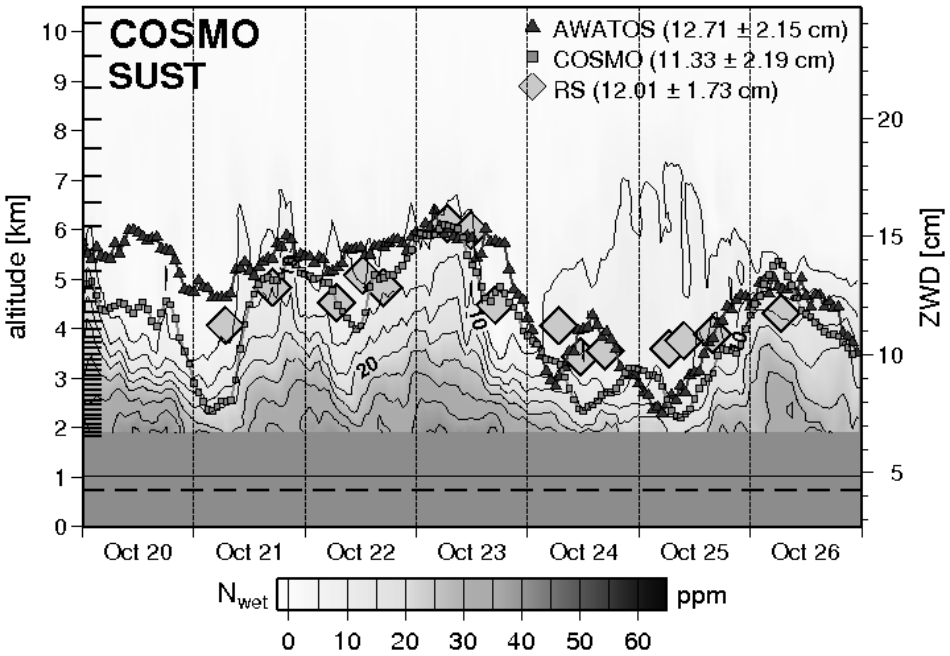

(b) Wet refractivity distribution in ppm derived from the data of the numerical weather model COSMO-7 of the nearest profile to the tomographic voxel model column shown in Subfig. (a). For comparison purposes, the time series of the integrated zenith wet delays (ZWD) are represented with the corresponding scale on the right side.

Fig. 8.20: Temporal change of the vertical distribution of wet refractivity above the station SUST in the northwest of the project area during the field campaign in October 2005.

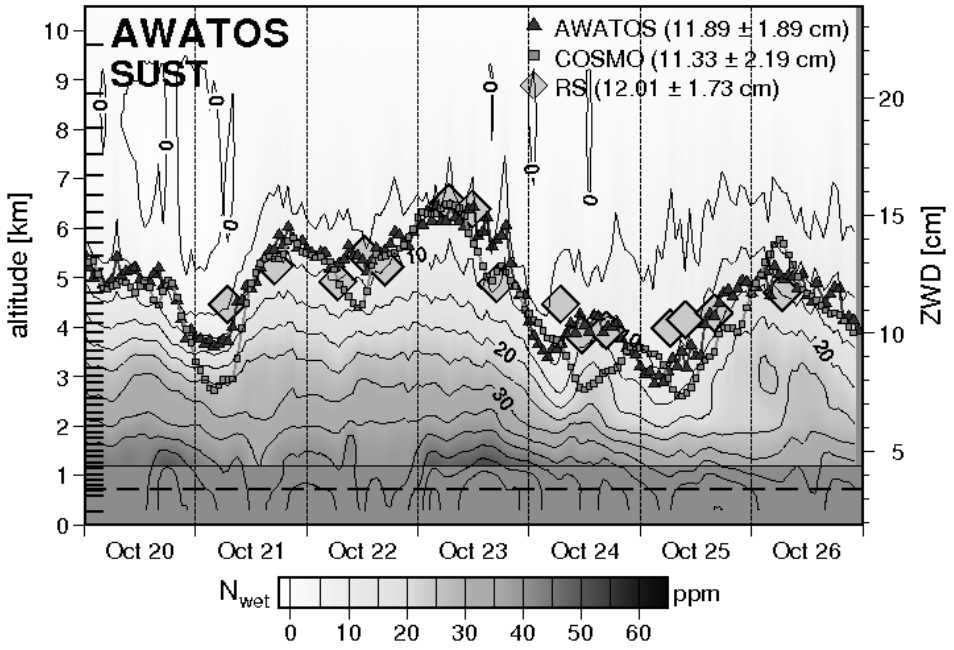

Fig. 8.21: Wet refractivity distribution in a 3.75 by 3.75 km voxel column with 43 layers. The tomographic solution of the voxel column above the station SUST is shown together with the ZWD time series of the integrated wet refractivity values from AWATOS, COSMO-7 and the reference radiosondes.

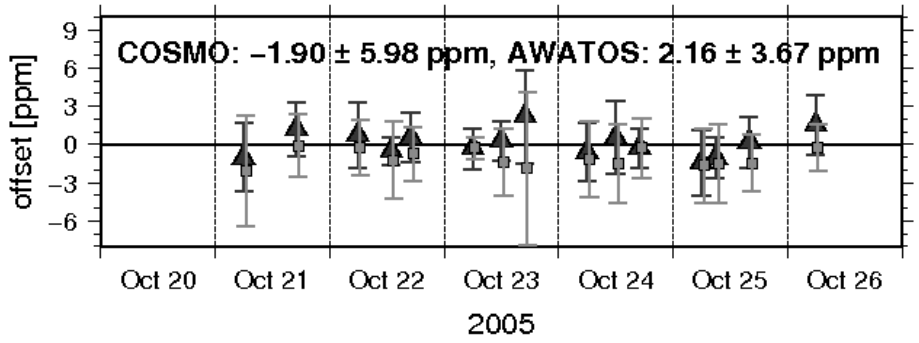

Fig. 8.22: Mean offsets and standard deviations (error bars) of the wet refractivity profiles of AWATOS (big triangles) and COSMO (small squares) minus the corresponding radiosondes launched at the station in Susten (SUST) during the October 2005 field campaign.

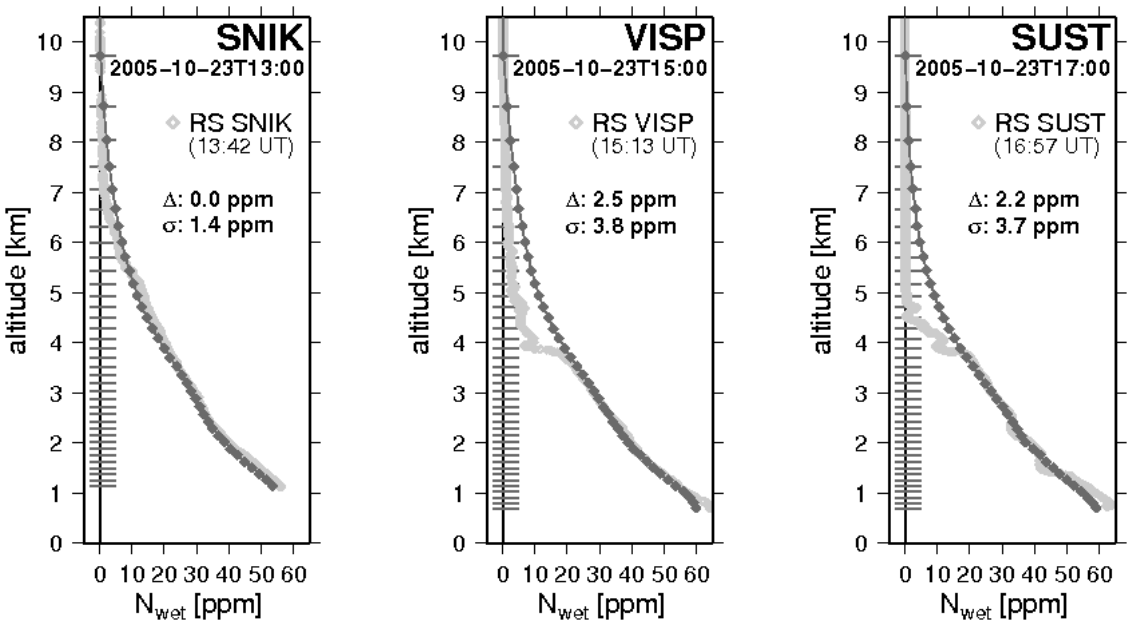

(a) Wet refractivity profiles at SNIK on October 23, 2005, 13 UT.

(b) Wet refractivity profiles at VISP on October 23, 2005, 15 UT.

(c) Wet refractivity profiles at SUST on October 23, 2005, 17 UT.

Fig. 8.23: Three wet refractivity profiles from AWATOS (column numbers 45, 76 and 72 of the 3.75 km voxel model used) and the corresponding radiosondes in the October 2005 field campaign. One profile is taken during (Fig. (a), see also e.g. Fig. 8.19(a)) and right after (Figs. (b) and (c)) the intense rainfall event on October 23, 2005. The results from the radio soundings and the corresponding tomographic analysis with 43 layers are shown together with the offsets Δ (AWATOS minus radiosonde) and their standard deviations σ. The numbers in the upper right corner represent the number of the tomographic voxel column in the model.

8.1.6 Impact of a reduced network in October 2005

To assess the impact of the season apart from the influence of the denser GPS network during the October 2005 campaign (especially due to the additional Turtmann network in the project area, see also Sec. B.3 in the Appendix), this data was processed using only the stations from July 2005 (see Fig. 8.24). Based on a few voxel models analyzed (see Tab. 8.7 compared to Tab. 8.5 on p. 129), it can be concluded that the negative effect of the smaller network gets stronger the higher the horizontal resolution of the voxel model (degradation in the order of 10 % for a model with 3 km grid spacing). There is also a correlation of the negative effect with the number of layers processed (more than 20 % increase of the mean offset with more than 30 layers). The absolute offsets (Δ) are now similar to those of the COSMO results (see Tab. 8.6).

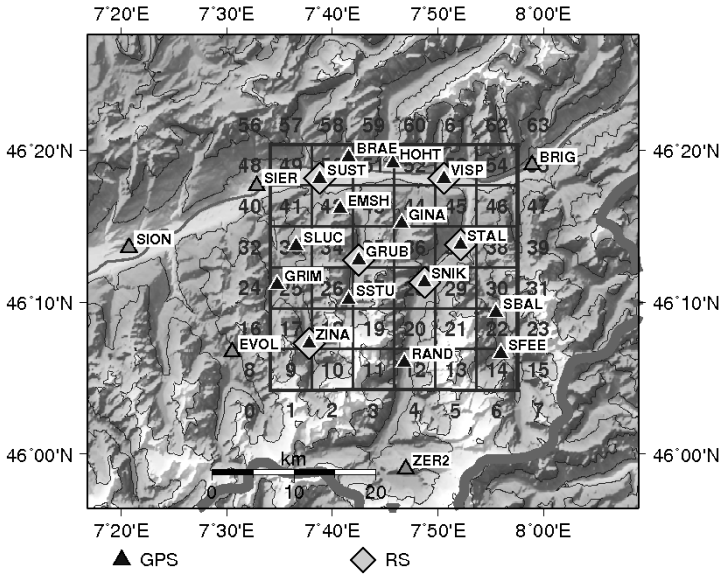

Fig. 8.24: Plan view of a 5 km voxel model including the profile numbers, the local GPS network during the field campaign in July 2005 and the radiosonde launch sites.

Especially with a higher horizontal resolution, the results of the reduced GPS network get a bigger offset in October.

8.1.7 Discussion on spatial resolution

The comparison of the COSMO-7 wet refractivity profiles with the radiosondes are very similar for July (Tab. 8.3) and for October (Tab. 8.6) 2005. The mean offset COSMO-7 minus radiosonde is about –0.85 ppm.

The tomographic processing of GPS zenith and slant path delays with final orbits shows larger offsets and standard deviations in July (Tab. 8.2) than in October (Tab. 8.5) 2005. There is a positive mean bias of the AWATOS solutions minus reference radiosondes of more than 2.0 ppm in July, whereas in October, depending on the voxel model resolution, the results differ between –0.5 ppm and 0.9 ppm. A

layers	horizontal resolution							
	7.5 km		5 km		3.75 km		3 km	
	Δ	σ	Δ	σ	Δ	σ	Δ	σ
#	ppm	ppm	ppm	ppm	ppm	ppm	ppm	ppm
16			0.73	2.72	0.82	2.94	0.94	3.05
26	0.41	2.44	0.67	2.50	0.65	2.58	0.83	2.79
32			0.71	2.54	0.45	2.35		
43			0.26	2.19				

Tab. 8.7: Statistic of the tomographic results minus reference radiosondes for the October 2005 campaign. The GPS network processed corresponds to the network during the July campaign.

seasonal variation of this bias comparing GPS with radiosondes is due to the amount of humidity and the much higher variability of water vapor in the summer month. This phenomenon has already been reported in different studies (see e.g. Haase et al., 2003; Ruckstuhl et al., 2007; Troller et al., 2007a,b).

For both campaigns, the results get the better the more layers are introduced. Investigating different horizontal resolutions, the wet refractivity distribution is worse determined in a voxel model with smaller spacing. Despite the larger offsets of the AWATOS solution compared to the radiosondes, these dependencies are visible also in the results of the July 2005 campaign, but even better in October. Reducing the GPS network for the October 2005 campaign to the size of the network in July (see Tab. 8.7) has an impact on the results, especially in the higher-resolution domain.

In terms of rainfall prediction, the GPS data shows high potential. The variation of the integrated zenith wet delays is consistent with the trend of rainfall with a little advance. Cheng et al. (2003) concluded that the increase of precipitable water vapor is a necessary but not sufficient condition of actual rainfall. Guo et al. (2000); de Pondeca and Zou (2001a,b) have already identified that the assimilation of ground-based GPS precipitable water vapor data (or integrated zenith wet delays) into numerical weather forecast models has a significant impact on the short-range rainfall prediction, but has a relatively small influence on the recovery of moisture structure.

Comparing the tomographic profiles with the numerical weather model COSMO-7 and the radiosondes, the wet refractivity is generally higher in the AWATOS processed data. This could be due to an insufficient modeling of the dry delay, which evokes an overestimated wet delay. Another reason might be an underestimation of wet refractivity in the reanalysis of the numerical weather model especially if the concentration of precipitable water vapor in the atmosphere becomes high (see also Yang et al., 1999).

8.2 Correlation analysis with meteorological surface data

8.2.1 Comparison with air temperature

Kursinski and Hajj (2001) concluded from a global data analysis that occultation results from limb soundings below an altitude of 6 km are generally drier than those of the numerical weather model of ECMWF (European Centre for Medium-Range Weather Forecasts). The bias is generally increasing with warmer surface temperatures. Near the height of the trade wind inversion, the ECMWF reanalyses are significantly moister than the occultation results due to vertical smoothing and overextension of the top of the boundary layer in the analyses (see Kursinski and Hajj, 2001).

Fig. 8.25 shows the differences of the tomographic solution of the vertical wet refractivity distribution minus the data from the numerical weather model COSMO-7 for both, the July and the October 2005 campaigns. Here, the GPS derived wet refractivity values are generally higher than those from the numerical weather model, especially between 4 and 6 km in July and between 3 and 5 km in October.

Performing high-resolution ground-based local GPS tomography in an area of 40 km by 40 km, no strong correlation between the surface temperature and the differences against the numerical weather model can be recognized. In July 2005, when the mean surface temperature at station Visp was about 10 °C higher than in October 2005, there is an overall slightly positive offset. This bias is also verified by the comparison of the integrated ZWD. During the fifth day (July 12, 2005), the GPS tomography senses significantly more water vapor than the numerical weather model. There was rainfall on the evening of that day.

8.2.2 Wet refractivity variation and sunshine duration

In order to validate the correlation between wet refractivity distribution and sunshine duration, the profiles from the ANETZ station Visp in October 2005 are shown. Gaffen and Elliott (1993) found that the climatological column water vapor content in clear skies is significantly lower than in cloudy skies. Based on the observations of the meteorological station, the parameter sunshine duration can help to identify cloud covered skies during daytime additional to the rainfall data.

Fig. 8.26(a) shows the variation of wet refractivity from GPS tomography during the October 2005 campaign for the station Visp. The tomographic voxel model has 7.5 horizontal resolution and 43 layers. Together with the wet refractivity, the sunshine duration is given in yellow vertical bars. Gaps in the time series of the sunshine duration (on October 21 and 22, 2005) indicate the existence of clouds above the station. On October 23, 2005, no sunshine is measured. This was the day of the cold front passage with heavy rainfall (see also Appendix, Fig. A.3, p. 181). On October 25, the sun appears only for a short time in the afternoon.

As seen in Fig. 8.26(a), there is a substantial increasing of wet refractivity above 3 km altitude before the first and second gap in the time series of the sunshine duration (on October 21 and 22, 2005). This indicates the development of a cloud

system in the middle troposphere. Also on October 25, the wet refractivity increases strongly above 5 km altitude before sunrise and prevents direct sunshine on the meteorological stations through clouds. The analysis of the wet refractivity data derived from the numerical weather model COSMO-7 (see Fig. 8.27) shows similar results regarding possible cloud development on that day.

The findings of Gaffen and Elliott (1993) cannot be confirmed completely. The zenith wet delay (ZWD) shown in Fig. 8.26(b), which is proportional to the column water vapor (see Eq. 2.16), is not significantly lower on clear sky days that on cloudy days (see Fig. 8.26(a)). Much more obvious is the diurnal variation of the GPS derived precipitable water vapor with a local maximum in the late afternoon (see also Dai et al., 2002).

Within the lower troposphere, where most of the precipitable water resides, several processes, including surface evapotranspiration, vertical mixing, low-level moisture convergence and precipitation, all affect the diurnal variation of water vapor. The integrated data of the numerical weather model does not follow this systematic behavior strictly, probably because of the missing data in the lowest part of the troposphere above the topography.

Comparing the results with sunshine duration, it could be confirmed that the determination of the vertical distribution of wet refractivity by GPS tomography is useful to distinguish accumulation of evaporated water vapor from the surface (e.g. due to sunshine radiation) and wind induced medium-scale variations of the water vapor content in the lower and middle troposphere. However, the comparison is limited to daytime and does not account for sky-cover amounts. Furthermore, the parameters do not represent the situation in zenith direction. An all-day comparison method for the correlation of clouds and column water vapor content would be possible using the analysis with images of weather satellites or radar data.

8.2.3 Dew point temperature and atmospheric water vapor

Several former studies concluded that there is a high positive correlation between the surface dew point temperature and the integrated precipitable water vapor (see e.g. Reitan, 1963; Smith, 1966; Lowry and Glahn, 1969).

Fig. 8.28(a) shows the development of the dew point temperature together with the tomographic result for the meteorological station Visp in July 2005. There is a good agreement between the time series of dew point temperature and the wet refractivity near the surface of the ground (see the wet refractivity variation near the dashed line in Fig. 8.28(a)). However, only a weak correlation can be recognized in relation to the integrated zenith wet delay time series (see Fig. 8.28(b)), neither for the tomographic solution nor for the data of the numerical weather model.

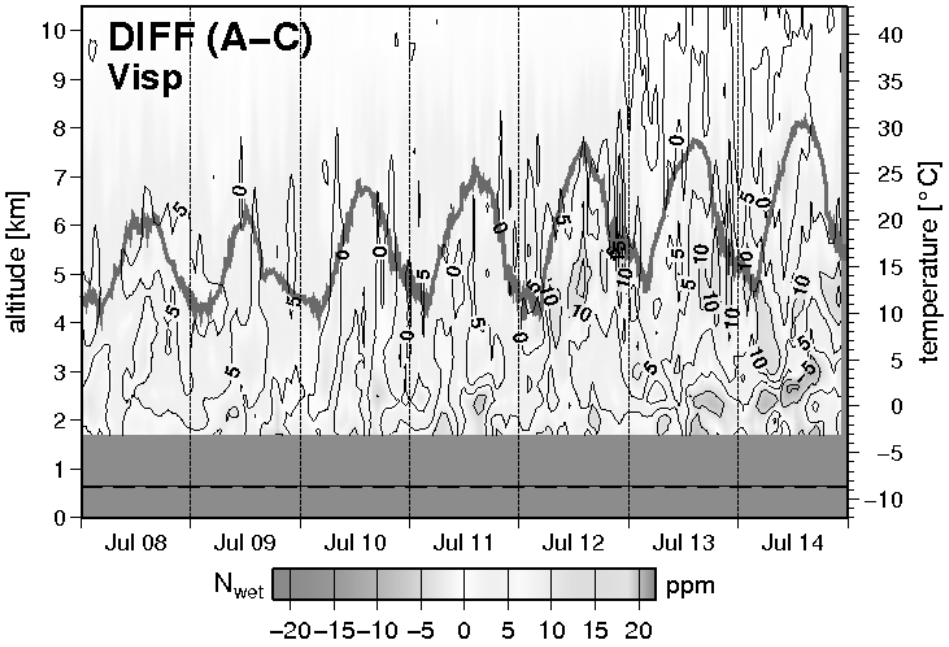

(a) Difference of the tomographic solution of wet refractivity profiles above the ANETZ station Visp minus COSMO during the July 2005 campaign.
Offset = $+2.3 \pm 3.1$ ppm.

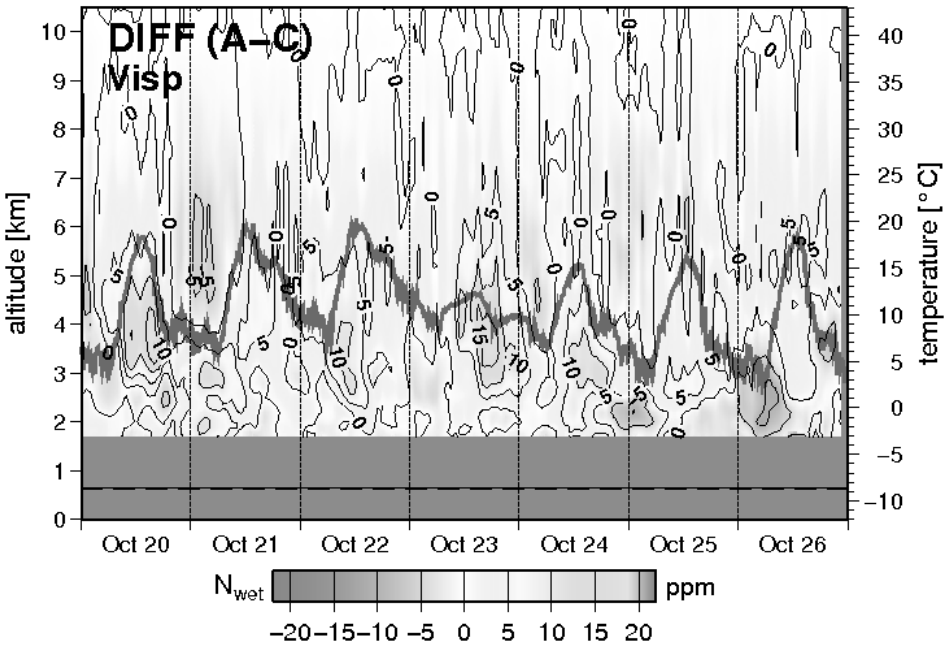

(b) Difference of the tomographic solution (*A*WATOS) of wet refractivity profiles above the ANETZ station Visp minus *C*OSMO during the October 2005 campaign.
Offset = $+1.1 \pm 3.3$ ppm.

Fig. 8.25: Correlation analysis between the differences of the results from AWATOS minus COSMO (*A*-*C*) and the time series of surface temperature is given by the continuous oscillating line.

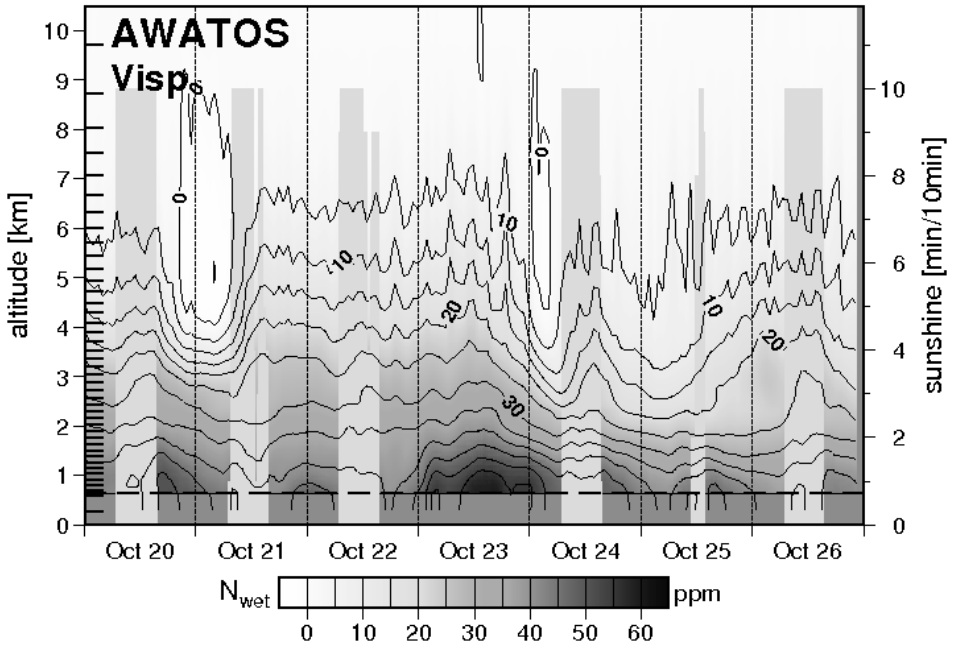

(a) Variation of wet refractivity (in ppm) from GPS tomography above the meteorological ANETZ station Visp and sunshine duration in min/10 min (light-colored vertical bars). The tomographic solution is calculated based on a voxel model with 43 layers, which are indicated on the left side of the figure.

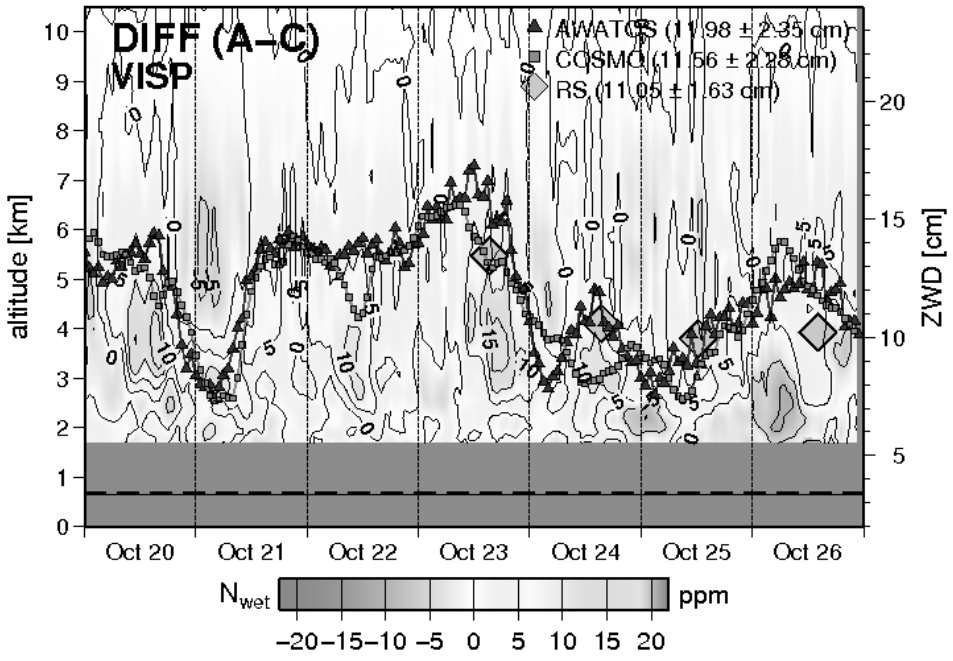

(b) Differences of wet refractivity profiles from AWATOS minus corresponding COSMO data. The time series of integrated ZWD is given for comparison purpose.

Fig. 8.26: Correlation analysis between wet refractivity distribution and variation of a GPS tomography solution and sunshine.

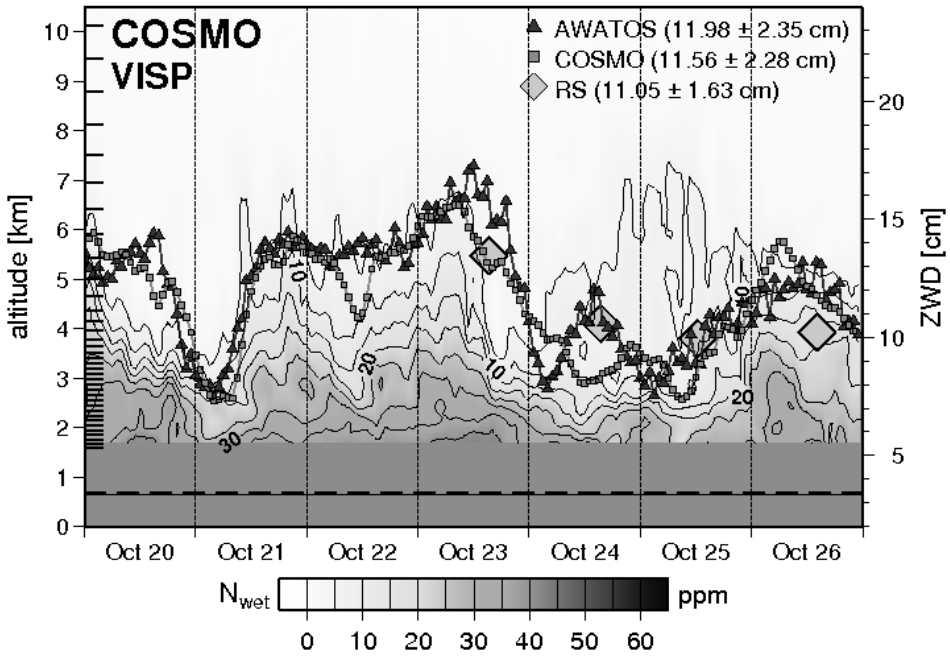

Fig. 8.27: Variation of wet refractivity (in ppm) from the numerical weather model COSMO-7 above the meteorological ANETZ station Visp and time series of zenith wet delay (ZWD). The heights of the model levels are indicated on the left side on the figure. The ZWD are integrated values from the wet refractivities of the tomographic solution AWATOS (see Fig. 8.26(a)), COSMO and the radiosondes launched at Visp.

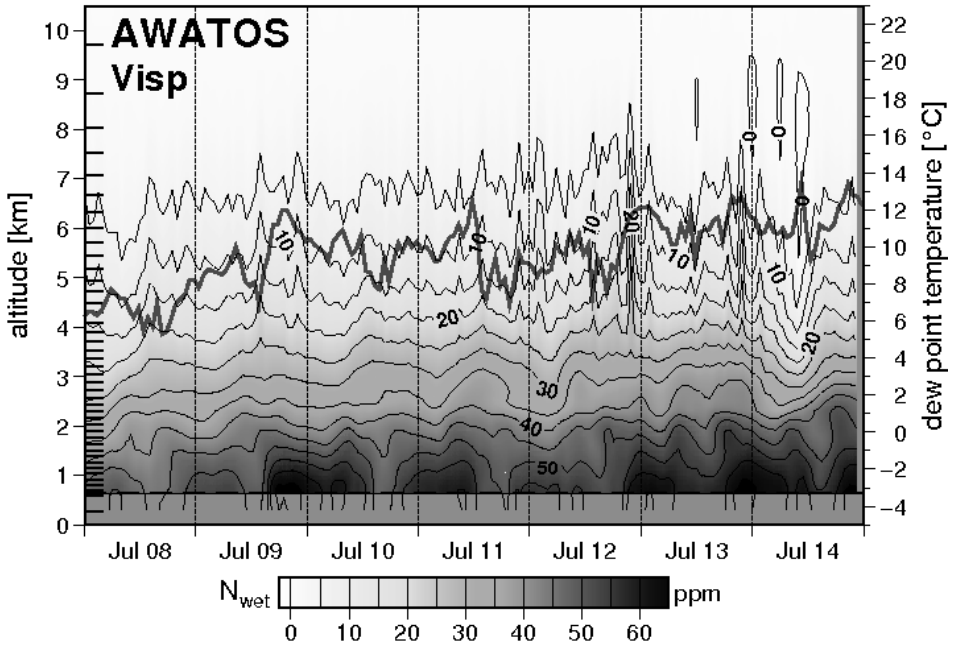

(a) Variation of wet refractivity (in ppm) from GPS tomography above the meteorological ANETZ station Visp and dew point temperature in °C. The tomographic solution is calculated based on a voxel model with 43 layers.

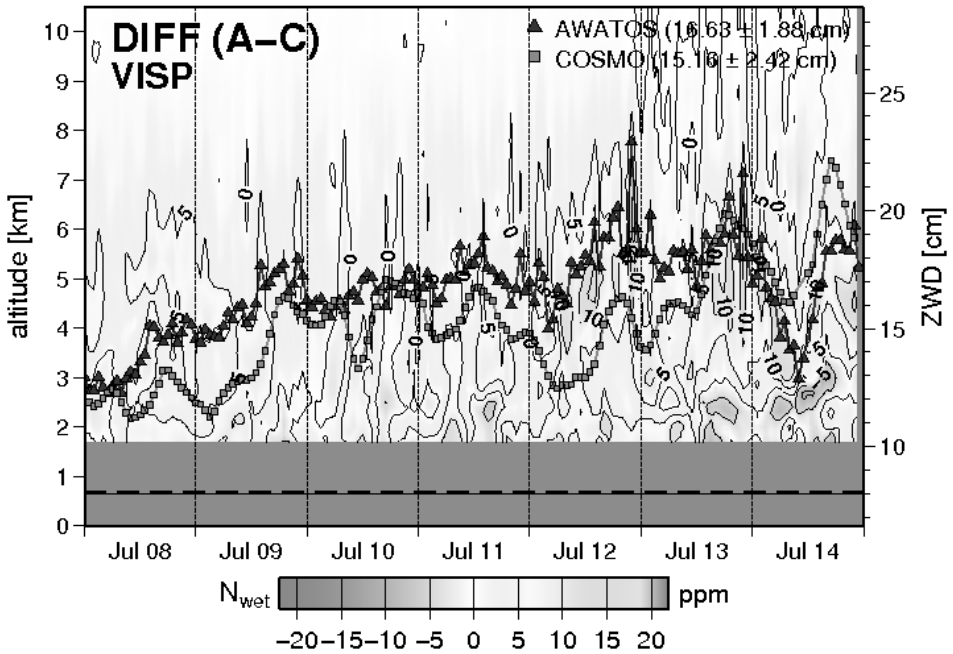

(b) Differences of wet refractivity profiles from AWATOS minus corresponding COSMO data. The time series of integrated ZWD is given for comparison purpose.

Fig. 8.28: Comparison of dew point temperature, wet refractivity variation and the integrated zenith wet delays from the numerical weather model and GPS tomography with respect to the ANETZ station Visp during the July 2005 campaign.

8.3 Aspects of changing temporal resolution

Until now, tomographic results have been presented based on one hour time windows for the GPS double-difference data. Also higher update rates are possible without changing the input options. The voxel model with 5 km horizontal resolution and 26 layers processed with the data of the July 2005 campaign is shown as example. Tab. 8.8 gives the mean offsets (Δ) and mean standard deviation (σ) of the comparison AWATOS minus radiosondes with three different temporal resolutions: one hour, 30 min and 10 min, without any temporal constraints (see also Sec. 8.4.2).

model	temporal resolution					
	1 h		30 min		10 min	
	Δ	σ	Δ	σ	Δ	σ
	ppm	ppm	ppm	ppm	ppm	ppm
5 km resolution, 26 layers	3.40	4.39	3.13	4.12	3.18	4.18

Tab. 8.8: Mean offset (Δ) and mean standard deviation (σ) of the tomographic wet refractivity profiles minus the reference radiosondes based on the data of the July 2005 campaign. The voxel model has a horizontal resolution of 5 km and 26 layers. Results with 1 h, 30 min and 10 min time windows are presented.

According to Tab. 8.8 a shorter time window leads to better results. This indicates mainly two important points:

- Induced by the meteorological condition within the small-scale project area, changes in N_{wet} have a dynamic which is below one hour.
- The GPS derived tropospheric parameters taken into account for the tomographic analysis of one hour sampling period are highly correlated in time (see also Stoew and Elgered, 2005). They do not provide much additional information compared to only 10 min of data. In the case of hourly estimated zenith path delays, they are linearly interpolated, which also influence the epoch-wise double-differenced phase residuals.

In Sec. 8.1.1, the time series of ANETZ station Zermatt were presented. The rainfall events caused clear signals in the wet refractivity profiles derived from GPS tomography. Fig. 8.5 on p. 115 is the result for the voxel model with 26 layers, 7.5 km horizontal resolution and one hour temporal resolution. In Figs. 8.29 and 8.30 the wet refractivity profiles are shown for a 5 km voxel model with 26 layers and a temporal resolution of 30 min and 10 min, respectively. Water vapor pressure is used for the a priori wet refractivity model of the tomographic analysis.

The impact of the short precipitation events at this location on the second and fifth day (see e.g. Fig. 8.5) is still recognizable even with an update rate of 10 min. Despite the smaller number of double-differenced observations, the information on the rainfall is stored in the residuals. Limitations in carrying out GPS tomography with high temporal resolution are given in terms of processing time (for one day of data) and the physical size of the output generated (result files and statistics).

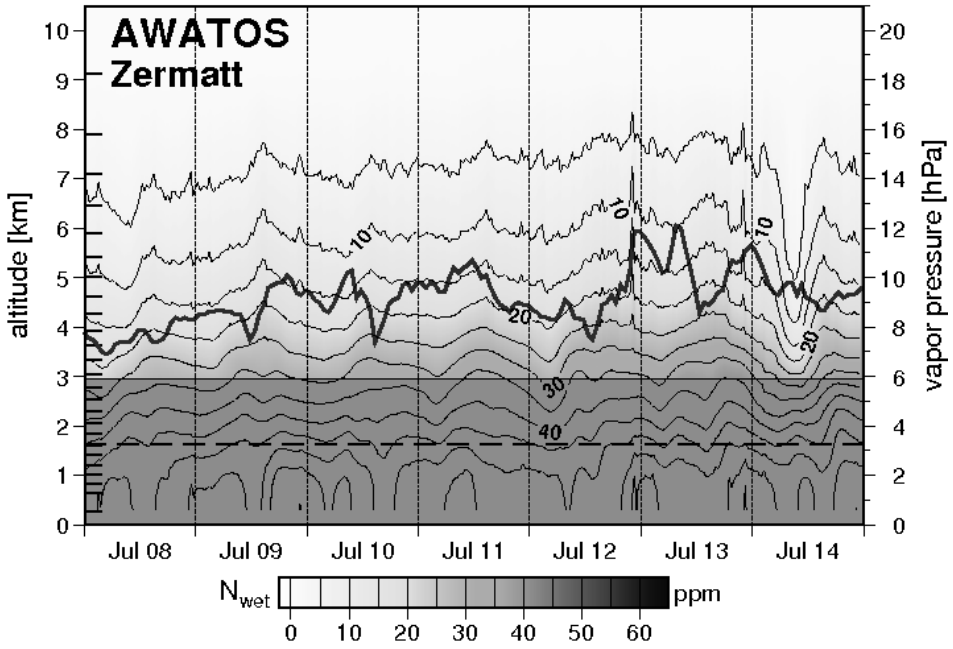

Fig. 8.29: 30 min variation of wet refractivity (in ppm) from GPS tomography above the meteorological ANETZ station Zermatt and water vapor pressure time series in hPa (dark-colored broad continuous line). The tomographic solution is calculated based on a voxel model with 26 layers and 5 km horizontal resolution.

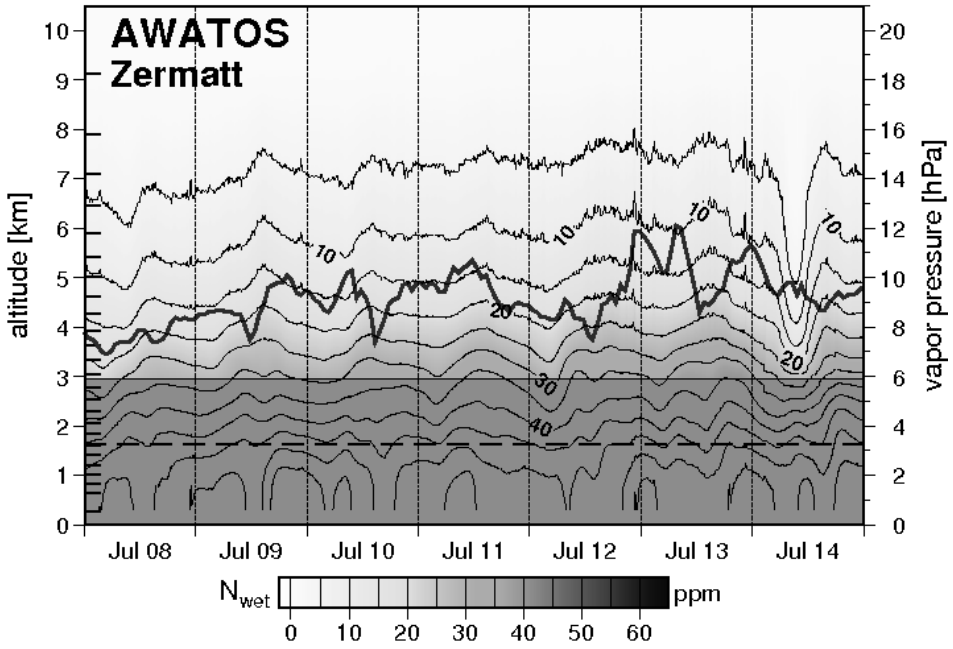

Fig. 8.30: 10 min variation of wet refractivity (in ppm) from GPS tomography above the meteorological ANETZ station Zermatt and water vapor pressure in hPa (dark-colored broad continuous line). The same voxel model as in Fig. 8.29 was analyzed.

8.4 Investigations in near real-time analysis

8.4.1 Processing real-time GPS orbits

In order to analyze the quality of the tomographic processing using GNSS orbits with a higher update rate than the final orbits, calculations were done with ultra-rapid orbits and broadcast ephemerides (see Tabs. 8.9 and 8.10).

layers	final orbits		ultra-rapid orbits		broadcast ephemerides	
	Δ	σ	Δ	σ	Δ	σ
#	ppm	ppm	ppm	ppm	ppm	ppm
16	4.49	5.52	4.68	5.68	4.87	5.89
26	3.40	4.39	2.95	4.50	3.89	4.75
32	3.20	4.19	3.53	4.43	3.76	4.67
43	2.29	3.54	2.66	3.65	3.11	4.07

Tab. 8.9: Mean offset and standard deviation of AWATOS profiles minus radiosondes for the July 2005 campaign. The tomographic voxel model has a horizontal resolution of 5 km. The GPS data is preprocessed with final, ultra-rapid and broadcast orbits.

For the data of the July 2005 campaign (see Tab. 8.9), a continuous degradation of accuracy between the tomographic solution and the radiosondes is detected for both, the mean offsets and the mean standard deviations, introducing orbits with lower quality. There is no strong effect for voxel models with low vertical resolution. The influence is more significant in the high-resolution domain. But an appropriate choice of the inter-voxel constraints is damping the negative effect.

layers	final orbits		ultra-rapid orbits		broadcast ephemerides	
	Δ	σ	Δ	σ	Δ	σ
#	ppm	ppm	ppm	ppm	ppm	ppm
16	0.67	2.61	0.76	2.69	0.77	2.75
26	0.57	2.42	0.64	2.48	0.66	2.55
32	0.58	2.45	0.64	2.51	0.68	2.60
43	0.13	2.13	0.20	2.18	0.22	2.25

Tab. 8.10: Tomographic profiles minus radiosondes for the October 2005 campaign. The GPS data is preprocessed with final, ultra-rapid and broadcast orbits.

Compared to the results of the July 2005 campaign (see Tab. 8.9), the mean offsets and standard deviations for the October 2005 campaign are generally smaller. The negative influence on the offsets processing broadcast orbits compared to the other

IGS products is also more significant in July, especially for high vertical resolution models. The values in the upper troposphere are mostly considered. In October, the different orbit qualities are generally lead to higher variations of the mean offsets. Regarding the shorter latency of ultra-rapid orbits compared to final orbits, the first can be recommended for near real-time GPS tomography.

8.4.2 Examination of time correlation strategies

Considering the application of time correlation algorithms into the tomographic processing, the method described in Sec. 7.2.2 has been examined. Hence, the solution of one analysis can be introduced as a priori field for the following run. This method was successfully employed in Troller et al. (2007b) for a voxel model with approximately 50 km horizontal grid spacing and 16 layers (for the layer distribution see also Sec. 7.2.1 and Fig. 7.2(a) on p. 96).

The results shown in Sec. 8.3 revealed that the sensitivity of the tomographic algorithm presented in this work is sensitive enough to detect changes in the wet refractivity field in a 10 minute sampling interval. The introduction of time correlation for a high-resolution voxel model with less than 10 km horizontal resolution would produce an unneeded filtering of the results.

Chapter 9

Conclusions

Water vapor plays an essential role in the context of atmospheric storm systems and the hydrological cycle on local, regional and global scale. It is both, a precursor for precipitation and a source of latent heat, which drives the weather dynamics. Furthermore, it has a positive feedback in model projections of climate change. The spatial distribution and temporal variation of the water vapor content are key elements in analyzing its impact on the environment.

An extensive review of the literature revealed the difficulty in finding a solution to determine the vertical distribution of atmospheric water vapor. In previous studies, the potential of GPS derived estimates of integrated precipitable water vapor assimilated into numerical weather prediction models was investigated and is commonly accepted by meteorological institutes. Yet, not only the moisture analysis and short-range rainfall forecasts, but also the determination of mesoscale frontal structures and energy fluxes benefit significantly from this integrated GPS data. Information on the vertical distribution of water vapor would even have a larger positive impact. In order to gain knowledge about the vertical structure, ground-based GPS tomography has been investigated in this research project. It is a dedicated method, which provides profiles of wet refractivity at any location with a high update rate.

Concerning the three superordinate objectives, the following conclusions could be drawn:

1. The tomographic method has been successfully applied in a small-scale, Alpine region. Based on campaign-type measurements, the Atmospheric Water Vapor Tomography Software (AWATOS) has been further developed and the parameters have been optimized for the target area.
2. High-resolution GPS tomography in mountainous regions is especially well suited to investigate the capability of the method in view of hydrological hazard assessment. The wet refractivity field have been estimated with a resolution comparable with the current and the next generation of numerical weather models.
3. To dispose of the main limitation in near real-time applications, the high-precision, so-called final satellite orbits were replaced by broadcast and/or predicted ephemerides. This data was prepared and processed for the GPS analysis and for the tomographic processing.

Five major tasks were pursued and carried out in this project. The results lead to the following conclusions:

- Based on simulation studies, an optimized network geometry for GPS stations and meteorological measurement systems could be designed despite of the difficult topography in the mountainous target area. Two field campaigns were carried out, one in July and another in October 2005.
  Input data for both, the spatially and temporally high-resolution GPS tomographic analysis and the validation of the results were collected. The network geometry for the second campaign was based on the same locations as the first one but was densified by additional GPS receivers and more systems recording data for comparison and validation purposes.
  The larger amount of systematic radiosonde profiles and the measurement of more independent data sets during the October 2005 campaign were beneficial for extensive statistics. The inhomogeneous distribution of rainfall in the local area (especially in July 2005) would ask for even more precipitation sensors in the meteorological measurement network to account for the hydrological hazard assessment.
- Within the second task, the first objective to achieve was, on the one hand, the estimation of tropospheric parameters, i.e. zenith path delays and corresponding phase residuals of the slant observations, based on GPS measurements. On the other hand, the GPS data was to be validated in view of capturing weather dynamics.
  The GPS observations were processed with the Bernese GPS Software Version 5.0 in double-difference mode. Previous to the tomographic analysis, the quality of the results had to be assessed. This was achieved by confronting the GPS time series to independent techniques: Radiosondes, the best available operational numerical weather model COSMO-7 of MeteoSwiss, solar spectrometry and meteorological surface data. Mainly, the GPS derived ZTD time series were compared with the continuous data sets of converted and interpolated zenith total delays of the weather model.
  The comparison showed that the time series agree within 2 cm on average, which is approximately 1 % of the absolute value, and correlate with more than 70 %. The general weather dynamics are reproduced by all techniques. However, local showers of rain are sometimes more clearly represented by the data of the dense GPS network. This reconfirms the potential of GPS measurements for monitoring integrated tropospheric water vapor and supporting numerical weather models.
- Looking at these results, it seemed most promising to analyze the GPS path delays within a four-dimensional tomographic system to obtain vertical water vapor profiles. In the third step, the feasibility of ground-based GPS tomography in view of hydrological hazard assessment was evaluated.
  The tomographic software package AWATOS was utilized to determine the variation of the wet refractivity field above the target area by assimilating GPS data and meteorological surface measurements. The tomographic profiles were compared with the numerical weather model COSMO-7. The examination of the meteorological profiles of the weather model revealed deficiencies in

the determination of the wet refractivity field in the lower troposphere. This problem is especially significant over the local and mountainous project area due to the filtered orography in the numerical weather model, which is not congruent with the observations of the reference radiosondes and GPS. Yet, both results show a similar behavior with respect to the temporal and vertical gradients of the wet refractivity parameter in the section the two models cover. This indicates that the reconstructed GPS slant path delays were assigned to the correct locations by the tomographic least-squares inversion system.

- Operational numerical weather prediction models compute meteorological data with a high spatial and temporal resolution. New tomographic voxel models towards higher resolution are being developed in the forth step of this work. To fulfill the same requirements, the existing algorithms of GPS tomography were further developed in this study. It was investigated, whether GPS tomography can contribute to better weather forecasts and whether it is possible to obtain satisfying results using non-permanent measurement networks with lower technical standards.
  A minimum horizontal spacing of the voxel model of 3 km was analyzed. Due to optimized inter-voxel constraints and a new function for the layer distribution in the vertical, the tomographic analysis with 43 layers from the surface up to 12.5 km altitude corresponds to collocated reference radiosonde profiles with a mean offset of less than 4.5 $\pm$5.5 ppm in July and less than 0.9 $\pm$2.9 ppm in October 2005. The sensitivity of the tomographic solution with respect to the vertical resolution of the voxel model is mostly accentuated in the middle troposphere between 4 and 6 km altitude.
  In terms of high temporal resolution, an update rate of 10 min of the tomographic processing was investigated. This examination revealed that it still reflects the vertical structure of the wet atmosphere accurately. The comparison with the results based on an hourly processing showed the high correlation of GPS measurements (not only the ZTD but also the phase residuals) within the voxel model during one hour of observation.
  Three conclusions can be drawn from this task: Firstly, it is possible to increase the spatial and temporal resolution in GPS tomography, so it can compete with numerical weather models. Secondly, the better agreement of the tomographic profiles with radiosonde data, compared to the COSMO-7 estimates, indicates that the numerical weather prediction models will benefit from additional vertical water vapor information provided by high-resolution GPS tomography. Thirdly, it was shown that also campaign-type measurements can be used to determine the wet refractivity field in high-resolution GPS tomography.
- Near real-time GPS processing for high-precision applications is mainly limited by the availability of precise satellite orbits and clocks. Thus, the possibilities of predicted products was examined in the fifth and last topic.
  In order to assess the potential of near real-time GPS tomography, IGS products with short latency (e.g. three hours or even real-time) and fast update rates (e.g. four times daily) were introduced into the GPS processing. Analyzing the Up-component of daily coordinates processed with broadcast ephemerides, the formal rms error reaches values in the order of 3 mm and

a standard deviation (repeatability) of more than 1.6 cm in July and 1.2 cm in October 2005. Furthermore, the time series of the resulting ZTD shows large systematic errors. With ultra-rapid orbits instead, satisfying results (repeatability of 9.1 mm in July and 7.7 mm in October 2005) can be obtained in almost real-time mode. The use of predicted orbits for the GPS processing degrades the results by up to 50 % (mean offset to radiosondes) compared to final products. The degradation of the GPS solution due to the broadcast ephemerides has a relatively small influence on the refractivity profiles.
It is concluded that for GPS meteorological applications like GPS tomography, it is not advised to use broadcast ephemerides if predicted ultra-rapid orbits and clocks are available. The impact of the orbit's accuracy on the wet refractivity profiles determined by GPS tomography depends on the spatial voxel model resolution and on seasonal differences of the atmospheric condition.

High-resolution GPS tomography is a promising tool in view of hydrological hazard assessment even in small-scale catchment areas with rough topography. It may further contribute to an enhanced estimation in the water vapor distribution and thus to a better initial condition for numerical weather forecast.

Chapter 10

Outlook

Several beneficial aspects of GPS tomography to support high-resolution numerical weather prediction models were shown in this work. Tomographically determined wet refractivity fields may also be used in conjunction with directly estimated integrated slant path delays to correct the GPS observations, especially at low elevation angles. Implemented into a GPS processing software, GPS tomography could provide completely anisotropic tropospheric corrections.

As a consequence of the good results obtained by analyzing voxel models with a large number of layers (e.g. 43 instead of 16) and the related increase of consumption of the processing time (CPU time), the parametrization of the unknown refractivity could result in a more flexible and dynamic tomographic procedure. The refractivity value in one voxel has no longer to be considered as constant but can be treated as a function of time and space. By optimizing this approach, the number of unknowns and, therefore, also the processing time, could be minimized without any loss of information. The determination of lower-stratospheric water vapor (see e.g. Oltmans and Hofmann, 1995; Gerber et al., 2004), which is difficult to detect by traditional techniques, is another interesting topic in the domain of high-resolution GPS water vapor tomography.

An additional set of important topics is related to the space segment of the GPS or GNSS domain and its impact on GPS tomography. Examination of possible biases due to the special satellite constellation and lack of data around the earth rotation axis should be carried out (see e.g. Santerre, 1991). The results could give insight into the dependency of latitude of the tomographic ray tracing algorithm on a global scale. In this domain, sensitivity tests with removing satellites (artificial obstructions) could be performed. Furthermore, the impact of additional GNSS Satellites (e.g. GLONASS and Galileo, see also Nilsson et al., 2004; Nilsson and Gradinarsky, 2006; Perler et al., 2007) could be studied. The introduction of further satellite systems would probably lead to enhanced double-difference processing and estimation of the corresponding residuals. Furthermore, a densified satellite constellation allows to detect and mitigate some systematic errors. Due to more frequencies available, a further benefit will result in uncorrelated observations and new linear combinations.

Considerations of GPS receivers and antennas used within the GPS processing are valuable, too. The introduction of absolute phase center variation models or multipath stacking maps for each antenna in use has to be considered to obtain optimized tropospheric estimates (see e.g. Rothacher et al., 1995; Rothacher, 2001; Iwabuchi et al., 2004; Shoji et al., 2004). This is an important issue especially if networks with a mixture of different receiver and antenna types are involved in the analysis. Rothacher (2001) and others found that there is an overestimation of about 8 mm mean bias observed in the GPS processed ZTD parameters due to

relative antenna calibration compared to absolute calibration. In order to enlarge the amount of low elevation measurements, multipath effects and correlations will be worthwhile being investigated in detail as well. The incorporation of low cost GNSS receivers in a tomographic network would help to make GPS tomography available for a wide range of users. But it requires knowledge of correction terms, especially related to the ionospheric refraction.

Regarding near real-time processing, Foster et al. (2005) and others presented methods of sliding-window analysis, which could be used to preprocess the GPS data for the tomographic analysis. Casually, hourly or near epoch-wise processed GPS data could be used for ZPD and double-differenced path delay retrieval. In a permanent and operational mode, GPS tomography would become a real-time sensing technique for the three-dimensional distribution of one of the most important constituents of the earth's atmosphere for weather dynamics, the tropospheric water vapor.

Bibliography

Abdullah, M., Strangeways, H. J., and Walsh, D. M. A. (2007). Effects of ionospheric horizontal gradients on differential GPS. *Acta Geophysica*, 55(4):509–523.

Ahmad, B. and Tyler, G. L. (1999). Systematic errors in atmospheric profiles obtained from Abelian inverion of radio occultation data: Effects of large-scale horizontal gradients. *J. Geophys. Res.*, 104(D4):3971–3992.

Allinson, C. R., Clarke, P. J., Edwards, S. J., King, M. A., Baker, T. F., and Cruddace, P. R. (2004). Stability of direct GPS estimates of ocean tide loading. *Geophys. Res. Lett.*, 31.

Ao, C. O., Meehan, T. K., Hajj, G. A., Mannucci, A. J., and Beyerle, G. (2003). Lower troposphere refractivity bias in GPS occultation retrievals. *J. Geophys. Res.*, 108(D18).

Aparicio, J. M. and Rius, A. (2004). A raytracing inversion procedure for the extraction of the atmospheric refractivity from GNSS travel-time data. *Phys. Chem. Earth*, 29:213–224.

Arpagaus, M. (2007). MAP D-PHASE Implementation Plan. Version 3.2.

Askne, J. and Nordius, H. (1987). Estimation of tropospheric delay for microwaves from surface weather data. *Radio Science*, 22(3):379–386.

Baker, H. C., Dodson, A. H., Penna, N. T., Higgings, M., and Offiler, D. (2001). Ground-based GPS water vapour estimation: potential for meteorological forecasting. *J. Atmos. Solar-Terr. Phys.*, 63:1305–1314.

Bar-Sever, Y. E. (1996). Strategies for GPS-Based Estimates of Troposphere Delay. In *Proceedings of the ION-GPS*, Kansas City, MO.

Bar-Sever, Y. E., Kroger, P. M., and Borjesson, J. A. (1998). Estimating horizontal gradients of tropospheric path delay with a single GPS receiver. *J. Geophys. Res.*, 103(B3):5019–5035.

Barlag, S., Offiler, D., and de Haan, S. (2005). User Requirements. In Elgered, G., Plag, H.-P., van der Marel, H., Barlag, S., and Nash, J., editors, *Exploitation of ground-based GPS for operational numerical weather prediction and climate applications*. COST. COST Action 716: Final report.

Bassiri, S. and Hajj, G. A. (1993). Higher-order ionospheric effects on the global positioning system observables and means of modeling them. *mnuscripta geodaetica*, 18:280–289.

Bastin, S., Champollion, C., Bock, O., Drobinski, P., and Masson, F. (2005). On the use of GPS tomography to investigate water vapor variability during a Mistral/sea breeze event in southeastern France. *Geophys. Res. Lett.*, 32.

Baueršíma, I. (1983). NAVSTAR/Global Positioning System (GPS), II. *Mitteilungen der Satelliten-Beobachtungsstation Zimmerwald*, 10.

Belloul, M. B. and Hauchecorne, A. (1997). Effect of periodic horizontal gradients on the retrieval of atmospheric profiles from occultation measurements. *Radio Science*, 32(2):469–478.

Bender, M. and Raabe, A. (2005). Bodengestützte GPS-Wasserdampf-Tomographie. *Meteorologische Arbeiten aus Leipzig (X)*, 37.

Bender, M. and Raabe, A. (2007). Preconditions to ground based GPS water vapour tomography. *Ann. Geophys.*, 25:1727–1734.

Bender, M., Wickert, J., Dick, G., Rothacher, M., and Raabe, A. (2007). GPS water vapour tomography with the German GPS network. *Geophys. Res. Abstr.*, 9.

Bengtsson, L., Robinson, G., Anthes, R., Aonashi, K., Dodson, A., Elgered, G., Gendt, G., Gurney, R., Jietai, M., Mitchell, C., Mlaki, M., Rhodin, A., Silvestrin, P., Ware, R., Watson, R., and Wergen, W. (2003). The Use of GPS Measurements for Water Vapor Determination. *Bull. Am. Meteorol. Soc.*, 84(9):1249–1258.

Berg, H. (1948). *Allgemeine Meteorologie: Einführung in die Physik der Atmophäre*. Dümmler, Bonn.

Beutler, G., Baueršíma, I., Botton, S., Gurtner, W., Rothacher, M., and Schildknecht, T. (1989a). Accuracy and biases in the geodetic application of the Global Positioning System. *manus. geod.*, 14:28–35.

Beutler, G., Baueršíma, I., Gurtner, W., Rothacher, M., Schildknecht, T., and Geiger, A. (1989b). Atmospheric refraction and other important biases in GPS carrier phase observations. In Brunner, F. K., editor, *Atmospheric Effects on Geodetic Space Measurements*, volume 12 of *Monograph*, pages 15–44. School of Geomatic Engineering (formerly Surveying), The University of New South Wales, Kensington, Australia.

Beutler, G., Geiger, A., Rothacher, M., Schaer, S., Schneider, D., and Wiget, A. (1995a). *Dreidimensionales Testnetz Turtmann 1985 - 1993, Teil II (GPS-Netz)*, volume 51 of *Geodätisch-geophysikalische Arbeiten in der Schweiz*. Swiss Geodetic Commission.

Beutler, G., Kouba, J., and Springer, T. (1995b). Combining the orbits of the IGS Analysis Centers. *Bull. Géod.*, 69:200–222.

Beutler, G., Rothacher, M., Schaer, S., Springer, T. A., Kouba, J., and Neilan, R. E. (1999). The International GPS Service (IGS): An Interdisciplinary Service in Support of Earth Sciences. *Adv. Space Res.*, 23(4):631–653.

Bevis, M., Businger, S., Chiswell, S., Herring, T. A., Anthes, R. A., Rocken, C., and Ware, R. H. (1994). GPS Meteorology: Mapping Zenith Wet Delays onto Precipitable Water. *J. Appl. Meteor.*, 33:379–386.

Bevis, M., Businger, S., Herring, T. A., Rocken, C., Anthes, R. A., and Ware, R. H. (1992). GPS Meteorology: Remote Sensing of Atmospheric Water Vapor Using the Global Positioning System. *J. Geophys. Res.*, 97(D14):15787–15801.

Bevis, M., Chiswell, S., Businger, S., Herring, T. A., and Bock, Y. (1996). Estimating wet delays using numerical weather analyses and predictions. *Radio Science*, 31(3):477–487.

Beyerle, G., Wickert, J., Schmidt, T., and Reigber, C. (2004). Atmospheric sounding by global navigation satellite system radio occultation: An analysis of the negative refractivity bias using CHAMP observations. *J. Geophys. Res.*, 109.

Bi, Y., Mao, J., and Li, C. (2006). Preliminary Results of 4-D Water Vapor Tomography in the Troposphere Using GPS. *Adv. Atmos. Sci.*, 23(4):551–560.

Bica, B. and Steinacker, R. (2006). High Resolution Precipitation Analysis over Complex Terrain and Recognition of Orographic Patterns in Meteorological Fields. In *Proceedings of the 1st MAP D-PHASE Scientific Meeting*, pages 69–72. De-

partement of Meteorology and Geophysics, Univerity of Vienna.

Bock, O. and Doerflinger, E. (2001). Atmospheric Modeling in GPS Data Analysis for High Accuracy Positioning. *Phys. Chem. Earth (A)*, 26(6–8):373–383.

Bock, O., Doerflinger, E., Masson, F., Walpersdorf, A., van Baelen, J., Tarniewicz, J., Troller, M., Somieski, A., Geiger, A., and Bürki, B. (2002a). GPS water vapor project associated to the ESCOMPTE programme: description and first results of the field experiment. *Phys. Chem. Earth*, 29:149–157.

Bock, O., Tarniewicz, J., Thom, C., and Pelon, J. (2001). Effect of Small-Scale Atmospheric Inhomogeneity on Positioning Accuracy with GPS. *Geophys. Res. Lett.*, 28(11):2289–2292.

Bock, O., Tarniewicz, J., Thom, C., and Pelon, J. (2002b). The effect of inhomogeneities in the lower atmosphere on coordinates determined from GPS measurements. *Phys. Chem. Earth*, 27:323–328.

Boehm, J. (2004). *Troposphärische Laufzeitverzögerungen in der VLBI*, volume 68 of *Geowissenschaftliche Mitteilungen*. Institut für Geodäsie und Geophysik, Wien.

Boehm, J., Cerveira, P. J. M., Schuh, H., and Tregoning, P. (2006a). The impact of tropospheric mapping functions based on numerical weather models on the determination of geodetic parameters. In *IAG General Assembly, Cairns, Australia*. International Association of Geodesy, Springer.

Boehm, J., Niell, A., Tregoning, P., and Schuh, H. (2006b). Global Mapping Function (GMF): A new empircal mapping function based on numerical weather model data. *Geophys. Res. Lett.*, 33.

Boehm, J. and Schuh, H. (2004). Vienna mapping functions in VLBI analyses. *Geophys. Res. Lett.*, 31.

Booth, S. (2003). GPS+GLONASS: Vale la pena? *Engineering surveying showcase*, 2.

Borbás, E. (1998). Derivation of Precipitable Water from GPS Data: an Application to Meteorology. *Phys. Chem. Earth*, 23(1):87–90.

Bos, M. S. and Scherneck, H.-G. (2007). Ocean tide loading provider.

Braun, J. and Rocken, C. (2003). Water vapor tomography within the planetary boundary layer using GPS. In *International Workshop on GPS Meteorology, Tsukuba, Japan*, pages 3–09–1–4.

Braun, J., Rocken, C., and Liljegren, J. (2003). Comparisons of Line-of-Sight Water Vapor Observations Using the Global Positioning System and a Pointing Microwave Radiometer. *J. Atmos. Oceanic Technol.*, 20:606–612.

Brockmann, E. (2007). TURT'05: Partnerschaftliche Messkampagne TURT/-TECVAL/WATEC von ETHZ und swisstopo. Report (A) 05–27, swisstopo, Wabern.

Brockmann, E., Calais, E., Douša, J., Gendt, G., Ge, M., Higgins, M., Johansson, J., van der Marel, H., Offiler, D., Rius, A., and Vespe, F. (2001). The COST-716 Benchmark GPS Campaign for Numerical Weather Prediction Applications. In *Proceedings of the European Geophysical Society General Assembly*, Nice.

Brockmann, E., Grünig, S., Ineichen, D., and Schaer, S. (2006). Monitoring the Automated GPS Network of Switzerland AGNES. In *Report on the Symposium of the IAG Subcommission for Europe (EUREF) held in Riga, Latvia, 14–17 June 2006*. Slides.

Brunner, F. K. (1992). Refraction, refractive index and dispersion: some relevant

history. In de Munck, J. C. and Spoelstra, T. A. T., editors, *Refraction of Transatmospheric Signals in Geodesy*, number 36 in Publications on Geodesy, pages 3–9. Netherlands Geodetic Commission, Delft.

Brunner, F. K. and Gu, M. (1991). An improved model for the dual frequency ionospheric correction of GPS observations. *manus. geod.*, 16:205–214.

Budden, K. G. (1985). *The propagation of radio waves: the theory of radio waves of low power in the ionosphere and magnetosphere*. Cambridge University Press, Cambridge.

Businger, S., Chiswell, S. R., Bevis, M., Duan, J., Anthes, R. A., Rocke, C., Ware, R. H., Exner, M., van Hove, T., and Sohlheim, F. S. (1996). The promise of GPS in atmospheric monitoring. *Bull. Am. Meteorol. Soc.*, 77(1).

Cao, Y., Chen, Y., and Li, P. (2006). Wet Refractivity Tomography with an Improved Kalman-Filter Method. *Adv. Atmos. Sci.*, 23(5):693–699.

Champollion, C., Masson, F., Bouin, M.-N., Walpersdorf, A., Doerflinger, E., Bock, O., and van Baelen, J. (2005). GPS water vapour tomography: preliminary results from the ESCOMPTE field experiment. *Atmos. Res.*, 74:253–274.

Chapman, S. and Lindzen, R. S. (1970). *Atmospheric Tides: Thermal and Gravitational*. D. Reidel, Dordrecht.

Cheng, X., Zhang, Y., Dongchen, E., and Shao, Y. (2003). GPS Water Vapour Estimation Using Meteorological Data from Chinese Antarctic Research Stations. In *Proceedings of the Geoscience and Remote Sensing Symposium*, pages 2356–2358. IEEE International.

Cocard, M. (1987). Geodätische Auswertung von GPS-Messungen (im GPS-Testnetz Turtmann, Wallis). Technical Report 129, Inst. of Geodesy and Photogrammetry, ETH Zurich.

Cocard, M., Eckert, V., Geiger, A., Bürki, B., and Neininger, B. (1992). Three-dimensional modelling of atmospheric parameters for automatic path delay corrections. In de Munck, J. C. and Spoelstra, T. A. T., editors, *Refraction of transatmospheric signals in geodesy*, pages 175–178. Netherlands Geodetic Commission.

Coster, A. J., Niell, A. E., Solheim, F. S., Mendes, V. B., Toor, P. C., Buchmann, K. P., and Upham, C. A. (1996). Measurements of Precipitable Water Vapor by GPS, Radiosondes, and a Microwave Water Vapor Radiometer. In *Proceedings of the ION-GPS, Kansas City, Kansas*.

Coster, A. J., Niell, A. E., Solheim, F. S., Mendes, V. B., Toor, P. C., and Langley, R. B. (1997). The Effect of Gradients in the GPS Estimation of Tropospheric Water Vapor. In *Proceedings of the ION 53rd Annual Meeting, Albuquerque, New Mexico*.

Cros, B., Durand, P., Cachier, H., Drobinsk, P., Fréjafon, E., Kottmeier, C., Perros, P. E., Peuch, V.-H., Ponche, J.-L., Robin, D., Saïd, F., Toupance, G., and Wortham, H. (2004). The ESCOMPTE program: an Overview. *Atmos. Res.*, 69:241–279.

Cucurull, L., Kuo, Y.-H., Barker, D., and Rizvi, S. R. H. (2006). Assessing the Impact of Simulated COSMIC GPS Radio Occultation Data on Weather Analysis over the Antarctic: A Case Study. *Monthly Weather Review*, 134:3283–3296.

Cucurull, L., Navascues, B., Ruffini, G., Elósegui, P., Rius, A., and Vilà, J. (2000). The Use of GPS to Validate NWP Systems: The HIRLAM Model. *J. Atmos.*

Oceanic Technol., 17:773–787.

Cucurull, L., Sedó, P., Behrend, D., Cardellach, E., and Rius, A. (2002a). Integrating NWP products into the analysis of GPS observables. *Phys. Chem. Earth*, 27:377–383.

Cucurull, L., Vandenberghe, F., Barker, D., Vilaclara, E., and Rius, A. (2004). Three-Dimensional Variational Data Assimilation of Ground-Based GPS ZTD and Meteorological Observations during the 14 December 2001 Storm Event over the Western Mediterranean Sea. *Monthly Weather Review*, 132:749–763.

Cucurull, L., Vilà, J., and Rius, A. (2002b). Zenith total delay study of a mesoscale convective system: GPS observations and fine-scale modeling. *Tellus*, 54A:138–147.

Dach, R. and Dietrich, R. (2000). Influence of the ocean loading effect on GPS derived precipitable water vapor. *Geophys. Res. Lett.*, 27(18):2953–2958.

Dach, R., Hugentobler, U., Fridez, P., and Meindl, M., editors (2007). *Bernese GPS Software Version 5.0*. Astronomical Institute, University of Bern.

Dai, A., Wang, J., Ware, R. H., and Hove, T. V. (2002). Diurnal variation in water vapor over North America and its implications for sampling errors in radiosonde humidity. *J. Geophys. Res.*, 107(D10).

Davies, K. and Rush, C. M. (1985). High-frequency ray paths in ionospheric layers with horizontal gradients. *Radio Science*, 20(1):95–110.

Davies, O. T. and Watson, P. A. (1998). Comparison of integrated precipitable water vapour obtained by GPS and radiosondes. *Electronics Letters*, 34(7):645–646.

Davis, J. L., Cosmo, M. L., and Elgered, G. (1996). Using the Global Positioning System to study the atmosphere of the earth: Overview and prospects. In Beutler, G., Hein, G. W., Melbourne, W. G., and Seeber, G., editors, *GPS Trends in Precise Terrestrial, Airborne, and Spaceborne Applications*, volume 115 of *IAG Symposium*, pages 233–242. Springer, Berlin.

Davis, J. L. and Elgered, G. (1998). The Spatio-Temporal Structure of GPS Water-Vapor Determinations. *Phys. Chem. Earth*, 23(1):91–96.

Davis, J. L., Elgered, G., Niell, A. E., and Kuehn, C. E. (1993). Ground-based measurement of gradients in the "wet" radio refractivity of air. *Radio Science*, 28(6):1003–1018.

Davis, J. L., Herring, T. A., Shapiro, I. I., Rogers, A. E. E., and Elgered, G. (1985). Geodesy by radio interferometry: Effects of atmospheric modeling errors on estimates of baseline length. *Radio Science*, 20(6):1593–1607.

de Haan, S. (2006). National/Regional operational procedures of GPS water vapour networks and agreed international procedures. Instruments and observing methods report 92, World Meteorological Organization.

de Haan, S., Barlag, S., Klein Baltink, H., Debie, F., and van der Marel, H. (2004). Synergetic Use of GPS Water Vapor and Meteosat Images for Synoptic Weather Forecasting. *J. Appl. Meteor.*, 43:514–518.

de la Torre Juárez, M. and Nilsson, M. (2003). On the detection of water vapor profiles and thin moisture layers from atmospheric radio occultations. *J. Geophys. Res.*, 108(D9).

de Munck, J. C. (1992). The influence of horizontal tropospheric gradients derived by assuming spherical, but sloping layers. In de Munck, J. C. and Spoelstra, T. A. T., editors, *Refraction of transatmospheric signals in geodesy*, pages 29–32.

Netherlands Geodetic Commission.

de Munck, J. C. and Spoelstra, T. A. T., editors (1992). *Refraction of transatmospheric signals in geodesy*. Number 36 in Publications on Geodesy. Netherlands Geodetic Commission, Delft. Proceedings of the Symposium, The Hague, The Netherlands.

de Pondeca, M. S. F. V. and Zou, X. (2001a). A Case Study of the Variational Assimilation of GPS Zenith Delay Observations into a Mesoscale Model. *J. Appl. Meteor.*, 40:1559–1576.

de Pondeca, M. S. F. V. and Zou, X. (2001b). Moisture retrievals from simulated zenith delay "observations" and their impact on short-range precipitation forecasts. *Tellus*, 53A:192–214.

Dick, G., Gendt, G., and Reigber, C. (2001). First experience with near real-time water vapor estimation in a German GPS network. *J. Atmos. Solar-Terr. Phys.*, 63(12):1295–1304.

Ding, J., Yang, Y., Ye, Y., Huang, Y., Ma, X., Ma, L., and Guo, Y. R. (2007). Moisture Analysis of a Squall Line Case Based on Preciptiable Water Vapor Data from a Ground-Based GPS Network in the Yangtze River Delta. *Adv. Atmos. Sci.*, 24(3):409–420.

Dodson, A. H. and Baker, H. C. (1998). Accuracy of Orbits for GPS Atmospheric Water VApour Estimation. *Phys. Chem. Earth*, 23(1):119–124.

Dodson, A. H., Shardlow, P. J., Hubbard, L. C. M., Elgered, G., and Jarlemark, P. O. J. (1996). Wet tropospheric effects on precise relative GPS height determination. *J. Geod*, 70:188–202.

Doerflinger, E., Bayer, R., Chéry, J., and Bürki, B. (1998). The Global Positioning System in mountainous areas: effect of the troposphere on the vertical GPS accuracy. *Earth & Planetary Sciences*, 326:319–325.

Doms, G. and Schättler, U. (2002). *A Description of the Nonhydrostatic Regional Model LM. Part I: Dynamics and Numerics*. COSMO.

Dong, D., Fang, P., Bock, Y., Cheng, M. K., and Miyazaki, S. (2002). Anatomy of apparent seasonal variations from GPS-derived site position time series. *J. Geophys. Res.*, 107(B4).

Douša, J. (2001). Towards an operational near real-time precipitable water vapor estimation. *Phys. Chem. Earth (A)*, 26(3):189–194.

Douša, J. (2004). Evaluation of tropospheric parameters estimated in various routine GPS analysis. *Phys. Chem. Earth*, 29:167–175.

Dow, J. M., Neilan, R. E., and Gendt, G. (2005). The International GPS Service: Celebrating the 10th anniversary and looking to the next decade. *Adv. Space Res.*, 36:320–326.

Dragert, H., James, T. S., and Lambert, A. (2000). Ocean Loading Corrections for Continuous GPS: A Case Study at the Canadian Coastal Site Holberg. *Geophys. Res. Lett.*, 27(14):2045–2048.

Duan, J., Bevis, M., Fang, P., Bock, Y., Chiswell, S., Businger, S., Rocken, C., Solheim, F., van Hove, T., Ware, R., McClusky, S., Herring, T. A., and King, R. W. (1996). GPS Meteorology: Direct Estimation of the Absolute Value of Precipitable Water. *J. Appl. Meteor.*, 35:830–838.

Eckert, V., Cocard, M., and Geiger, A. (1992). COMEDIE (Collocation of Meteorological Data for Interpretation and Estimation of Tropospheric Pathdelays): Soft-

ware. Technical Report 195, Inst. of Geodesy and Photogrammetry, ETH Zurich.

Elgered, G. (2001). An Overview of COST Action 716: Exploitation of Ground-Based GPS for Climate and Numerical Weather Prediction Applications. *Phys. Chem. Earth (A)*, 26(6-8):399–404.

Elgered, G., Johansson, J. M., Rönnäng, B. O., and Davis, J. L. (1997). Measuring regional atmospheric water vapor using the Swedish permanent GPS network. *Geophys. Res. Lett.*, 24(21):2663–2666.

Elgered, G., Plag, H.-P., van der Marel, H., Barlag, S., and Nash, J., editors (2005). *Exploitation of ground-based GPS for operational numerical weather prediction and climate applications*. COST. COST Action 716: Final report.

Elgered, G. and van der Marel, H. (2005). Theoretical Physical Background. In Elgered, G., Plag, H.-P., van der Marel, H., Barlag, S., and Nash, J., editors, *Exploitation of ground-based GPS for operational numerical weather prediction and climate applications*. COST. COST Action 716: Final report.

Elliott, W. P. (1995). On detecting long-term changes in atmospheric moisture. *Climatic Change*, 31:349–367.

Elósegui, P. and Davis, J. L. (2001). Sensing Atmospheric Structure: GPS Water-Vapor Tomography to Improve Severe Weather Forecasts. Technical report, Smithsonian Astrophysical Observatory.

Elósegui, P., Davis, J. L., Gradinarsky, L. P., Elgered, G., Johansson, J. M., Tahmoush, D. A., and Rius, A. (1999). Sensing atmospheric structure using small-scale space geodetic networks. *Geophys. Res. Lett.*, 26(16):2445–2448.

Elósegui, P., Davis, J. L., Jaldehag, R. T. K., Johansson, J. M., Niell, A. E., and Shapiro, I. I. (1995). Geodesy using the Global Positioning System: The effects of signal scattering on estimates of site position. *J. Geophys. Res.*, 100(B7):9921–9934.

Elósegui, P., Ruis, A., Davis, J. L., Ruffini, G., Keihm, S. J., Bürki, B., and Kruse, L. P. (1998). An Experiment for Estimation of the Spatial and Temporal Variations of Water Vapor Using GPS Data. *Phys. Chem. Earth*, 23(1):125–130.

Emardson, T. R. and Derks, H. J. P. (2000). On the relation between the wet delay and the integrated precipitable water vapour in the European atmosphere. *Meteorol. Appl.*, 7(1):61–68.

Emardson, T. R. and Jarlemark, P. O. J. (1999). Atmospheric modelling in GPS analysis and its effect on the estimated geodetic parameters. *J. Geod*, 73:322–331.

Eresmaa, R., Järvinen, H., and Salonen, K. (2006). Potential of Ground-Based GPS Slant Delays for Numerical Weather Prediction.

Essen, L. and Froome, K. D. (1951). The Refractive Indices and Dielectric Constants of Air and its Principal Constituents at 24,000 Mc/s. In *Proceedings of the Physical Society, Section B*, volume 64/10, pages 862–875.

Estey, L. H. and Meertens, C. M. (1999). TEQC: The Multi-Purpose Toolkit for GPS/GLONASS Data. *GPS Solut.*, 3(1):42–49.

Faccani, C., Ferretti, R., Pacione, R., Paolucci, T., Vespe, F., and Cucurull, L. (2005). Impact of a high density GPS network on the operational forecast. *Advances in Geosciences*, 2:73–79.

Fadil, A. and Sari, D. B. (2006). Correlation between precipitable water and rainfall using Global Positioning System (GPS) technique. In Perrin, A., Sari-Zizi, N. B., and Demaison, J., editors, *Remote Sensing of the Atmosphere for Environmental*

Security. Springer, Dordrecht.

Fang, P., Bevis, M., Bock, Y., Gutman, S., and Wolfe, D. (1998). GPS meteorology: Reducing systematic errors in geodetic estimates for zenith delay. *Geophys. Res. Lett.*, 25(19):3583–3586.

Farrell, W. E. (1972). Deformation of the Earth by Surface Loads. *Reviews of Geophysics and Space Physics*, 10(3):761–797.

Feng, D. D. and Herman, B. M. (1999). Remotely Sensing the Earth's Atmosphere Using the Global Positioning System (GPS) – The GPS/MET Data Analysis. *J. Atmos. Oceanic Technol.*, 16:989–1002.

Flores, A. (1999). *Atmospheric Tomography Using Satellite Radio Signals*. PhD thesis, Departament de Teoria del Senyal i Comunicacions, Universitat Politècnica de Catalunya, Barcelona.

Flores, A., de Arellano, J. V.-G., Gradinarsky, L. P., and Rius, A. (2001). Tomography of the Lower Troposphere Using a Small Dense Network of GPS Receivers. *IEEE Transactions on Geoscience and Remote Sensing*, 39(2):439–447.

Flores, A., Escudero, A., Sedó, M. J., and Rius, A. (2000a). A near real time system for tropospheric monitoring using IGS hourly data. *Earth Planets Space*, 52:681–684.

Flores, A., Gradinarsky, L. P., Elósegui, P., Elgered, G., Davis, J. L., and Rius, A. (2000b). Sensing atmospheric structure: Tropospheric tomographic results of the small-scale GPS campaign at the Onsala Space Observatory. *Earth Planets Space*, 52:941–945.

Flores, A., Ruffini, G., and Rius, A. (1999). 4D Tropospheric Tomography using GPS Estimated Delays. In *Geoscience and Remote Sensing Symposium, IGARSS'99*, volume 1, pages 675–677. IEEE.

Flores, A., Ruffini, G., and Rius, A. (2000c). 4D tropospheric tomography using GPS slant wet delays. *Ann. Geophys.*, 18:223–234.

Foelsche, U. and Kirchengast, G. (2001). Tropospheric water vapor imaging by combination of ground-based and spaceborne GNSS sounding data. *J. Geophys. Res.*, 106(D21):27,221–27,231.

Forrer, F. (2007). Geodäsie für Wettervorhersage: ZTD-Untersuchungen (Projekt WATEC). Zürich. Bachelor thesis.

Foster, J., Bevis, M., and Businger, S. (2005). GPS Meteorology: Sliding-Window Analysis. *J. Atmos. Oceanic Technol.*, 22:687–695.

Fragner, E. and Weber, R. (2003). Estimation of the Tropospheric Delay from GNSS Data over the Austrian Territory. *Österreichische Zeitschrift für Vermessung und Geoinformation*, 3:48–53.

Gaffen, D. J. and Elliott, W. P. (1993). Column Water Vapor Contetn in Clear and Cloudy Skies. *J. Climate*, 6:2278–2287.

Ge, M., Calais, E., and Haase, J. (2000). Reducing satellite orbit error effects in near real-time GPS zenith tropospheric delay estimation for meteorology. *Geophys. Res. Lett.*, 27(13):1915–1918.

Geiger, A. (1987). Einfluss richtungsabhängiger Fehler bei Satellitenmessungen. Bericht 130, Inst. of Geodesy and Photogrammetry, ETH Zurich.

Geiger, A. (1988). Modeling of Phase Center Variation and its Influence on GPS-Positioning. In Groten, E. and Strauss, R., editors, *GPS-Techniques Applied to Geodesy and Surveying*, pages 210–222, Berlin. Springer-Verlag. Proceedings of

the International GPS-Workshop, Darmstadt, April 10 to 13, 1988.

Geiger, A. and Cocard, M. (1992). Collocational methods in atmospheric ray tracing. In de Munck, J. C. and Spoelstra, T. A. T., editors, *Refraction of transatmospheric signals in geodesy*, pages 191–195. Netherlands Geodetic Commission.

Geiger, A., Cocard, M., and Hirter, H. (1995). Dreidimensionale Modellierung des Refraktivitätsfeldes in der Atmosphäre. *Vermessung, Photogrammetrie, Kulturtechnik*, 4.

Geiger, A., Hirter, H., Cocard, M., Bürki, B., Wiget, A., Wild, U., Schneider, D., Rothacher, M., Schaer, S., and Beutler, G. (1996). Mitigation of tropospheric effects in local and regional GPS networks. In Beutler, G., Hein, G. W., Melbourne, W. G., and Seeber, G., editors, *GPS Trends in Precise Terrestrial, Airborne, and Spaceborne Applications*, volume 115 of *IAG Symposium*, pages 263–267. Springer, Berlin.

Geiger, A., Kahle, H.-G., Köchle, R., Meier, D., Neiniger, B., Schneider, D., and Wirth, B. (1992). *Dreidimensionales Testnetz Turtmann 1985 - 1990, Teil I*, volume 45 of *Geodätisch-geophysikalische Arbeiten in der Schweiz*. Swiss Geodetic Commission.

Gendt, G., Dick, G., Reigber, C., Tomassini, M., Liu, Y., and Ramatschi, M. (2004). Near Real Time GPS Water Vapor Monitoring for Numerical Weather Prediction in Germany. *J. Meteor. Soc. Japan*, 82(1B):361–370.

Gendt, G., Reigber, C., and Dick, G. (2001). Near Real-Time Water Vapor Estimation in a German GPS Network: First Results from the Ground Program of the HGF GASP Project. *Phys. Chem. Earth (A)*, 26(6–8):413–416.

Genio, A. D. D. (1994). Climatic implicaitons of the seasonal variation of upper troposphere water vapor. *Geophys. Res. Lett.*, 21(24):2701–2704.

Gerber, D., Balin, I., Feist, D. G., Kämpfer, N., Simeonov, V., Calpini, B., and van den Bergh, H. (2004). Ground-based water vapour soundings by microwave radiometry and Raman lidar on Jungfraujoch (Swiss Alps). *Atmos. Chem. Phys.*, 4:2171–2179.

Gorbunov, M. E. (2002). Canonical transform method for processing radio occultation data in the lower troposphere. *Radio Science*, 37(5).

Gorbunov, M. E. and Gurvich, A. S. (1998). Microlab-1 experiment: Multipath effects in the lower troposphere. *J. Geophys. Res.*, 103(D12):13,819–13,826.

Gorbunov, M. E. and Kornblueh, L. (2001). Analysis and validation of GPS/MET radio occultation data. *J. Geophys. Res.*, 106(D15):17,161–17,169.

Gorbunov, M. E. and Kornblueh, L. (2003). Principles of variational assimilation of GNSS radio occultation data. Technical report, Max Planck Insitute for Meteorology, Hamburg.

Gossard, E. E. (1978). The height distribution of refractive index structure parameter in an atmosphere being modified by spatial transition at its lower boundary. *Radio Science*, 13(3):489–500.

Gradinarsky, L. and Jarlemark, P. (2002). GPS Tomography Using the Permanent Network in Göteborg: Simulations. In *Position Location and Navigation Symposium*, pages 128–133. IEEE.

Gradinarsky, L. P. (2002). *Sensing Atmospheric Water Vapor Using Radio Waves*. PhD thesis, Chalmers University of Technology, Göteborg, Sweden.

Gradinarsky, L. P. and Jarlemark, P. (2004). Ground-Based GPS Tomography of

Water Vapor: Analysis of Simulated and Real Data. *J. Meteor. Soc. Japan*, 82(1B):551–560.

Gradinarsky, L. P., Johansson, J. M., Bouma, H. R., Scherneck, H.-G., and Elgered, G. (2002). Climate monitoring using GPS. *Phys. Chem. Earth*, 27:335–340.

Grebner, D. (1996). Räumlich-zeitliche Verteilung von Niederschlägen. In Oddsson, B., editor, *Instabile Hänge und andere risikorelevante natärliche Prozesse*. Birkhäuser, Basel.

Gregorius, T. L. H. and Blewitt, G. (1999). Modeling weather fronts to improve GPS heights: A new tool for GPS meteorology? *J. Geophys. Res.*, 104(B7):15,261–15,279.

Grzeschik, M., Zus, F., Bauer, H.-S., Wulfmeyer, V., Wickert, J., Dick, G., and Gendt, G. (2006). Assimilation of GPS water vapor observations into the MM5 4D-Var system. In *Proceedings of the 1st MAP D-PHASE Scientific Meeting*, pages 28–31. Departement of Meteorology and Geophysics, Univerity of Vienna.

Guerova, G. (2003a). *Application of GPS derived water vapour for Numerical Weather Prediction in Switzerland*. PhD thesis, Institue of Applied Physics, University of Bern, Berne.

Guerova, G. (2003b). Derivation of Integrated Water Vapour (IWV) from the ground-based GPS estimates of Zenith Total Delay (ZTD). Technical Report 2003-08, Institute of Applied Physics, University of Bern, Bern.

Guerova, G., Bettems, J.-M., Brockmann, E., and Matzler, C. (2006). Assimilation of COST 716 Near-Real Time GPS data in the nonhydrostatic limited area model used at MeteoSwiss. *Meteorol. Atmos. Phys.*, 91:149–164.

Guerova, G., Brockmann, E., Quiby, J., Schubiger, F., and Matzler, C. (2003). Validation of NWP Mesoscale Models with Swiss GPS Network AGNES. *J. Appl. Meteor.*, 42:141–150.

Guo, J. and Langley, R. B. (2003). A new tropospheric propagation delay mapping function for elevation angles down to 2°. In *Proceedings of the ION GPS/GNSS, Portland, ORE*.

Guo, Y.-R., Kuo, Y.-H., Dudhia, J., Parsons, D., and Rocken, C. (2000). Four-Dimensional Variational Data Assimilation of Heterogeneous Mesoscale Observations for a Strong Convective Case. *Monthly Weather Review*, 128:619–643.

Gurtner, W., Beutler, G., Botton, S., Rothacher, M., Geiger, A., Kahle, H.-G., Schneider, D., and Wiget, A. (1989). The use of the Global Positioning System in mountainous areas. *manus. geod.*, 14:53–60.

Gurtner, W. and Estey, L. (2006). *RINEX: The Receiver Independent Exchange Format Version 2.11*.

Gutman, S. I., Sahm, S. R., Benjamin, S. G., and Smith, T. L. (2004). GPS Water Vapor Observation Errors. In *8th Symposium on Integrated Observing and Assimilation Systems for Atmosphere, Oceans, and Land Surface*.

Ha, S.-Y., Kuo, Y.-H., Guo, Y.-R., and Lim, G.-H. (2003). Variational Assimilation of Slant-Path Wet Delay Measurements from a Hypothetical Ground-Based GPS Network. Part I: Comparison with Precipitable Water Assimilation. *Monthly Weather Review*, 131:2635–2655.

Ha, S.-Y., Kuo, Y.-H., Guo, Y.-R., Rocken, C., and Hove, T. V. (2002). Comparison of GPS slant wet delay measurements with model simulations during the passage of a squall line. *Geophys. Res. Lett.*, 29(23).

Haase, J., Calais, E., Talaya, J., Rius, A., Vespe, F., Santangelo, R., Huang, X.-Y., Davila, J. M., Ge, M., Cucurull, L., Flores, A., Sciarretta, C., Pacione, R., Boccolari, M., Pugnaghi, S., Vedel, H., Mogensen, K., Yang, X., and Garate, J. (2001a). The Contributions of the MAGIC Project to the COST 716 Objectives of assessing the Operational Potential of Ground-Based GPS Meteorology on an International Scale. *Phys. Chem. Earth (A)*, 26(6–8):433–437.

Haase, J., Ge, M., Vedel, H., and Calais, E. (2003). Accuracy and Variability of GPS Tropospheric Delay Measurements of Water Vapor in the Western Mediterranean. *J. Appl. Meteor.*, 42:1547–1568.

Haase, J. S., Vedel, H., Ge, M., and Calais, E. (2001b). GPS Zenith Tropospheric Delay (ZTD) Variability in the Mediterranean. *Phys. Chem. Earth (A)*, 26(6–8):439–443.

Haefele, P., Martin, L., Becker, M., Brockmann, E., Morland, J., Nyeki, S., Matzler, C., and Kirchner, M. (2004). Impact of Radiometric Water Vapor Measurements on Troposphere and Height Estimates by GPS. In *Proceedings of the ION GNSS*, Long Beach.

Hagemann, S., Bengtsson, L., and Gendt, G. (2003). On the determination of atmospheric water vapor from GPS measurements. *J. Geophys. Res.*, 108(D21).

Hajj, G. A., Kursinski, E. R., Romans, L. J., Bertiger, W. I., and Leroy, S. S. (2002). A technical description of atmospheric sounding by GPS occultation. *J. Atmos. Solar-Terr. Phys.*, 64:451–469.

Hall, A. and Manabe, S. (1999). The Role of Water Vapor Feedback in Unperturbed Climate Variability and Global Warming. *J. Climate*, 12:2327–2346.

Hall, M. P. M. (1979). *Effects of the troposphere on radio communication*, volume 8 of *IEE Electromagnetic Waves*. Institution of Electrical Engineers, London.

Hardy, K. R., Hajj, G. A., and Kursinski, E. R. (1994). Accuracies of atmospheric profiles obtained from GPS occultations. *Int. J. Sat. Comm.*, 12:463–473.

Hartmann, G. K. and Leitinger, R. (1984). Range errors due to ionospheric and tropospheric effects for signal frequencies above 100 MHz. *Bull. Géod.*, 58:109–136.

Healy, S. B., Jupp, A. M., and Marquardt, C. (2005). Forecast impact experiment with GPS radio occultation measurements. *Geophys. Res. Lett.*, 32.

Healy, S. B. and Thépaut, J.-N. (2006). Assimiliation experiments with CHAMP GPS radio occultation measurements. *Q. J. R. Meteorol. Soc.*, 132:605–623.

Heise, S., Wickert, J., Beyerle, G., Schmidt, T., and Reigber, C. (2006). Global monitoring of tropospheric water vapor with GPS radio occultation aboard CHAMP. *Adv. Space Res.*, 37:2222–2227.

Heller, O., Geiger, A., Hollenstein, C., and Kahle, H.-G. (2005a). Satellitengestützte Kontrollnetzwerke im Gebirge im Hinblick auf die Erkennung seismischer Gefahren. In *Proceedings of the AHORN meeting 2005*.

Heller, O., Geiger, A., and Kahle, H.-G. (2005b). TECVAL: GPS based determination of crustal deformation in the canton Valais and its correlation with seismicity. In *Alpine Valley & HazNETZ Ph.D.-Workshop on Natural Hazards*, volume 6. Abstract.

Heller, O., Hollenstein, C., Geiger, A., Kahle, H.-G., Jonsson, S., Deichmann, N., and Giardini, D. (2005c). Continuous local GPS network for the assessment of small-scale Alpine geodynamics. In *3rd Swiss Geoscience Meeting, Zürich*, page 54.

Abstract.

Herring, T. A. (1992). Modeling atmospheric delays in the analysis of space geodetic data. In de Munck, J. C. and Spoelstra, T. A. T., editors, *Refraction of transatmospheric signals in geodesy*, pages 157–164. Netherlands Geodetic Commission.

Herschke, P. M. (2002). Modeling and Extrapolation of Path Delays in GPS Signals. Master's thesis, ETH Zurich, Zürich.

Higgins, M. (2001). Progress in 3D-Variational Assimilation of Total Zenith Delay at the Met Office. *Phys. Chem. Earth (A)*, 26(6–8):445–449.

Hill, R. J., Lawrence, R. S., and Priestley, J. T. (1982). Theoretical and calculational aspects of the radio refractive index of water vapor. *Radio Science*, 17(5):1251–1257.

Hilla, S. (2004). Plotting pseudorange multipath with respect to satellite azimuth and elevation. *GPS Solut.*, 8:44–48.

Hirahara, K. (2000). Local GPS tropospheric tomography. *Earth Planets Space*, 52:935–939.

Hirter, H. (1998). Mehrdimensionale Interpolation von Meteorologischen Feldern zur Berechnung der Brechungsbedingungen in der Geodäsie. Mitteilung 64, Inst. of Geodesy and Photogrammetry, ETH Zurich.

Höflinger, W. (1993). Entwicklung von 3D Meteo-Modellen zur Korrektion der troposphärischen Refraktion bei GPS-Messungen. Bericht 216, Inst. of Geodesy and Photogrammetry, ETH Zurich.

Hofmann-Wellenhof, B., Lichtenegger, H., and Collins, J. (2001). *Global Positioning System: Theory and Practice*. Springer, Wien.

Hogg, D. C., Guiraud, F. O., and Decker, M. T. (1981). Measurement of Excess Radio Transmission Length on Earth-space Paths. *Astron. Astrophys.*, 95:304–307.

Hopfield, H. S. (1969). Two-quadratic tropospheric refractivity profile for correcting satellite data. *J. Geophys. Res.*, 74:4487–4499.

Hopfield, H. S. (1971). Tropospheric effect on electromagnetically measured range: Prediction from surface weather data. *Radio Science*, 6(3):357–367.

Hoyle, V. A. (2005). Data Assimilation for 4-D Wet Refractivity Modelling in a Regional GPS Network. Master's thesis, Department of Geomatics Enineering, University of Calgary, Calgary, Alberta.

Huang, C.-Y., Kuo, Y.-H., Chen, S.-Y., Prasad-Rao, A. S. K. A. V., and Wang, C.-J. (2007). The Assimilatino of GPS Radio Occultation Data and its Impact on Rainfall Prediction along the West Coast of India during Monsoon 2002. *Pure appl. geophys.*, 164:1577–1591.

Huang, J. and van Graas, F. (2007). Comparison of Tropospheric Decorrelation Errors in the Presence of Severe Weather Conditions in Different Areas and Over Different Baseline Lengths. *Navigation*, 54(3):207–226.

Huang, J. Y. and Wang, Y. P. (1992). Depolarization effects of the rainy medium in millimeter wave propagation. In de Munck, J. C. and Spoelstra, T. A. T., editors, *Refraction of transatmospheric signals in geodesy*, pages 33–36. Netherlands Geodetic Commission.

Hugentobler, U., Meindl, M., Beutler, G., Bock, H., Dach, R., Jäggi, A., Urschl, C., Mervart, L., Rothacher, M., Schaer, S., Brockmann, E., Ineichen, D., Wiget, A., Wild, U., Weber, G., Habrich, H., and Boucher, C. (2004). CODE IGS Analysis

Center Technical Report 2003/2004. Technical report, Astronomical Institute, University of Bern.

Ifadis, I. M. and Savvaidis, P. (2001). Space to Earth Geodetic Observations: Approaching the Atmospheric Effect. *Phys. Chem. Earth (A)*, 26(3):195–200.

IGS Central Bureau (2005). IGS Products.

Iwabuchi, T., Naito, I., and Mannoji, N. (2000). A comparison of Global Positioning System retrieved precipitable water vapor with the numericla weather prediction analysis data over the Japanese Islands. *J. Geophys. Res.*, 105(D4):4573–4585.

Iwabuchi, T., Rocken, C., Mervart, L., and Kanzaki, M. (2006). Nowcasting and Weather Forecasting: Real-time Estimation of ZTD in GEONET, Japan. *Location*, pages 44–49.

Iwabuchi, T., Shoji, Y., Shimada, S., and Nakamura, H. (2004). Tsukuba GPS Dense Net Campaign Observations: Comparison of the Stacking Maps of Post-fit Phase Residuals Estimated from Three Software Packages. *J. Meteor. Soc. Japan*, 82(1B):315–330.

Jakowski, N., Heise, S., Wehrenpfennig, A., Schläter, S., and Reimer, R. (2002). GPS/GLONASS-based TEC measurements as a contributor for space weather forecast. *J. Atmos. Solar-Terr. Phys.*, 64:729–735.

Janes, H. W., Langley, R. B., and Newby, S. P. (1991). Analysis of tropospheric delay prediction models: comparisons with ray-tracing and implications for GPS relative positioning. *Bull. Géod.*, 65:151–161.

Jensen, A. S., Lohmann, M. S., Benzon, H.-H., and Nielsen, A. S. (2003). Full Spectrum Inversion of radio occultation signals. *Radio Science*, 38(3).

Jerrett, D. and Nash, J. (2001). Potential Uses of Surface Based GPS Water Vapour Measurements for Meteorological Purposes. *Phys. Chem. Earth (A)*, 26(6–8):457–461.

Johansson, J. M. (1998). GPS Antenna and Site Effects. In Brunner, F. K., editor, *Advances in Positioning and Reference Frames*, volume 118 of *International Association of Geodesy Symposia*, pages 229–236. Springer, Berlin.

Johns, J. W. C. (1965). The Absorption of Radiation by Water Vapor. In Ruskin, R. E., editor, *Principles and Methods of Measuring Humidity in Gases*, volume 1 of *Humidity and Moisture: Measurement and Control in Science and Industry*, pages 417–427. Reinhold Publishing Corporation, New York.

Kaniuth, K., Kleuren, D., and Tremel, H. (1998). Sensitivity of GPS Height Estimates to Tropospheric Delay Modelling. *Allgemeine Vermessungs-Nachrichten*, 6.

Kaplan, E. D. and Hegarty, C. J., editors (2006). *Understanding GPS: Principles and Applications*. Artech House, Boston, 2 edition.

Katsaros, K. B., Bhatti, I., McMurdie, L. A., and Petty, G. W. (1989). Identification of Atmospheric Fronts over the Ocean with Microwave Measurements of Water Vpor and Rain. *Weather and Forecasting*, 4(4):449–460.

Kiehl, J. T. and Trenberth, K. E. (1997). Earth's Annual Global Mean Energy Budget. *Bull. Am. Meteorol. Soc.*, 78(2).

King, R. W., Masters, E. G., Rizos, C., Stolz, A., and Collins, J. (1987). *Surveying with Global Positioning System GPS*. Dümmler, Bonn.

Kleijer, F. (2004). *Troposphere Modeling and Filtering for Precise GPS Leveling*, volume 56 of *Publications on Geodesy*. Nederlandse Commissie voor Geodesie,

Delft.

Klein Baltink, H., van der Marel, H., and van der Hoeven, A. G. A. (2002). Integrated atmospheric water vapor estimates from a regional GPS network. *J. Geophys. Res.*, 107(D3).

Klobuchar, J. A. (1996). Ionospheric Effects on GPS. In Parkinson, B. W. and Spilker, Jr, J. J., editors, *Global Positioning System: Theory and Applications: Volume I*, chapter 12. American Institue of Aeronautics and Astronautics, Inc.

Klobuchar, J. A. and Kunches, J. M. (2003). Comparative range delay and variability of the earth's troposphere and the ionosphere. *GPS Solut.*, 7:55–58.

Kolesnik, S. N., Tinin, M. V., and Afanasiev, N. T. (2002). Statistical characteristics of a wave propagating through a layer with random irregularities. *Waves in Random Media*, 12:417–431.

Köpken, C. (2001). Validation of Integrated Water Vapor from Numerical Models Using Ground-Based GPS, SSM/I, and Water Vapor Radiometer Measurements. *J. Appl. Meteor.*, 40:1105–1117.

Kruse, L. P. (2001). *Spatial and Temporal Distribution of Atmospheric Water Vapor using Space Geodetic Techniques*, volume 61 of *Geodätisch-geophysikalische Arbeiten in der Schweiz*. Swiss Geodetic Commission.

Kruse, L. P., Sierk, B., Springer, T., and Cocard, M. (1999). GPS-Meteorology: Impact of Predicted Orbits on Precipitable Water Estimates. *Geophys. Res. Lett.*, 26(14):2045–2049.

Kunitsyn, V. E. and Tereshchenko, E. D. (2003). *Ionospheric Tomography*. Springer, Berlin, Heidelberg.

Kuo, Y.-H., Guo, Y.-R., and Westwater, E. R. (1993). Assimilation of precipitable water measurements into a mesoscale numerical model. *Monthly Weather Review*, 121:1215–1238.

Kuo, Y.-H., Sokolovskiy, S., Anthes, R. A., and Vandenberghe, F. (2000). Assimilation of GPS Radio Occultation Data for Numerical Weather Prediction. *Terr. Atmos. Oceanic Sci.*, 11(1):157–186.

Kuo, Y.-H., Wee, T.-K., Sokolovskiy, S., Rocken, C., Schreiner, W., Hunt, D., and Anthes, R. A. (2004). Inversion and Error Estimation of GPS Radio Occultation Data. *J. Meteor. Soc. Japan*, 82(1B):507–531.

Kursinski, E. R. and Hajj, G. A. (2001). A comparison of water vapor derived from GPS occultations and global weather analyses. *J. Geophys. Res.*, 106(D1):1113–1138.

Kursinski, E. R., Hajj, G. A., Hardy, K. R., Romans, L. J., and Schofield, J. T. (1995). Observing tropospheric water vapor by radio occultation using the global positioning system. *Geophys. Res. Lett.*, 22(17):2365–2368.

Kursinski, E. R., Hajj, G. A., Leroy, S. S., and Herman, B. (2000). The GPS Radio Occultation Technique. *Terr. Atmos. Oceanic Sci.*, 11(1):53–114.

Lawrence, D., Langley, R. B., Kim, D., Chan, F.-C., and Pervan, B. (2006). Decorrelation of Troposphere Across Short Baselines. In *Proceedings of the Position, Location and Navigation Symposium IEEE/ION*, pages 94–102.

Leitinger, R. (1994). Data from Orbiting Navigation Satellites for Tomographic Reconstruction. *Int. J. Imaging Sys. Tech.*, 5:86–96.

Leitinger, R., Ladreiter, H.-P., and Kirchengast, G. (1997). Ionosphere tomography with data from satellite reception of Global Navigation Satellite System signals

and ground reception of Navy Navigation Satellite System signals. *Radio Science*, 32(4):1657–1669.

LeVine, D. M. (1972). Propagation delay in the atmosphere. *Radio Science*, 7(6):625–629.

Liou, K.-N. (1980). *An Introduction to Atmospheric Radiation*. Academic Press, New York.

Liou, Y.-A. and Huang, C.-Y. (2000). GPS observations of PW during the passage of a typhoon. *Earth Planets Space*, 52:709–712.

Liou, Y.-A., Huang, C. Y., and Teng, Y.-T. (2000a). Precipitable water observed by ground-based GPS receivers and microwave radiometry. *Earth Planets Space*, 52:445–450.

Liou, Y.-A., Huang, C.-Y., and Wu, C.-C. (2000b). GPS observations of preciptiable water dynamics associated with typhoon Zeb (1998). In *Proceedings of the IEEE*, pages 3027–3029.

Liou, Y.-A., Lin, Y.-J., Chiang, C.-C., and Huang, C.-Y. (2003). Reconstructing 3D wet refractivity structures of the lower troposphere from GPS measurements. In *International Workshop on GPS Meteorology, Tsukuba, Japan*, pages 3–23–1–6.

Liou, Y.-A., Pavelyev, A. G., Wickert, J., Schmidt, T., and Pavelyev, A. A. (2005). Analysis of atmospheric and ionospheric structures using the GPS/MET and CHAMP radio occultation database: a methodological review. *GPS Solut.*, 9:122–143.

Lowry, D. A. and Glahn, H. R. (1969). Relationships Between Integrated Atmospheric Moisture and Surface Weather. *J. Appl. Meteor.*, 8:762–768.

Lutz, S., Troller, M., Geiger, A., and Kahle, H.-G. (2005). High-resolution GPS-tomography in view of hydrological hazard assessment in the Canton of Valais (Switzerland). *Geophys. Res. Abstr.*, 7.

MacDonald, A. E., Xie, Y., and Ware, R. H. (2002). Diagnosis of Three-Dimensional Water Vapor Using a GPS Network. *Monthly Weather Review*, 130:386–397.

Mao, H., Mao, J. T., Bi, Y. M., Li, C. C., and Liu, X. Y. (2007). Constructing temporal and spatial water vapor figures by GPS remote sensing along slant rays. *Science in China Series D: Earth Sciences*, 50(2):296–305.

Marshall, J. (2002). Creating and viewing skyplots. *GPS Solut.*, 6:118–120.

Marshall, J., Schenewerk, M., Snay, R., and Gutman, S. (2001). The Effect of the MAPS Weather Model on GPS-Determined Ellipsoidal Heights. *GPS Solut.*, 5(1):1–14.

McBean, G. A. and Elliott, J. A. (1981). Pressure and humidity effects on optical refractive-index fluctuations. *Boundary-Layer Meteorology*, 20:101–109.

McCaskill, T. B., Reid, W. G., Buisson, J. A., and Warren, H. E. (1994). Effect of Broadcast and Precise Ephemerides on Estimates of the Frequency Stability of GPS Navstar Clocks. *Interantional Journal of Satellite Communications*, 12:435–441.

Meindl, M., Schaer, S., Hugentobler, U., and Beutler, G. (2004). Tropospheric Gradient Estimation at CODE: Results from Global Solutions. *J. Meteor. Soc. Japan*, 82(1B):331–338.

Melbourne, W. G., Davis, E. S., Duncan, C. B., Hajj, G. A., Hardy, K. R., Kursinski, E. R., Meehan, T. K., Young, L. E., and Yunck, T. P. (1994). *The Application of Spaceborne GPS to Atmospheric Limb Sounding and Global Change Monitor-*

ing. Number 94-18 in JPL Publication. Jet Propulsion Laboratory, Pasadena, California.

Melfi, S. H., Whiteman, D., and Ferrare, R. (1989). Observation of Atmospheric Fraonts Using Raman Lidar Moisture Measurements. *J. Appl. Meteor.*, 28:789–806.

Mendes, V. B. (1999). Modeling the neutral-atmospheric propagation delay in radiometric space techniqes. Ph.D. dissertation 199, University of New Brunswick, Canada.

Mendes, V. B. and Langley, R. B. (1998). Optimization of tropospheric delay mapping function performance for high-precision geodetic applications. In *Proceedings of DORIS Days*, Toulouse, France.

Moritz, H. (1973). *Least-Squares Collocation*. Number 75 in Reihe A: Theoretische Geodäsie. Deutsche Geodätische Kommission, Mänchen.

Morland, J., Liniger, M. A., Kunz, H., Balin, I., Nyeki, S., Mätzler, C., and Kämpfer, N. (2006). Comparison of GPS and ERA40 IWV in the Alpine region, including correction of GPS observations at Jungfraujoch (3584 m). *J. Geophys. Res.*, 111.

Morland, J. and Mätzler, C. (2007). Spatial interpolation of GPS integrated water measurements made in the Swiss Alps. *Meteorol. Appl.*, 14:15–26.

Murray, F. W. (1967). On the Computation of Saturation Vapor Pressure. *J. Appl. Meteor.*, 6:203–204.

Nakamura, H., Koizumi, K., and Mannoji, N. (2004). Data Assimilation of GPS Precipitable Water Vapor into the JMA Mesoscale Numerical Weather Prediction Model and its Impact on Rainfall Forecasts. *J. Meteor. Soc. Japan*, 82(1B):441–452.

Niell, A. E. (1996). Global mapping functions for the atmosphere dely at radio wavelengths. *J. Geophys. Res.*, 101:3227–3246.

Niell, A. E. (2000). Improved atmospheric mapping functions for VLBI and GPS. *Earth Planets Space*, 52:699–702.

Niell, A. E. (2001). Preliminary Evaluation of Atmospheric Mapping Functions Based on Numerical Weather Models. *Phys. Chem. Earth*, 26(6–8):475–480.

Niell, A. E., Coster, A. J., Solheim, F. S., Mendes, V. B., Toor, P. C., Langley, R. B., and Upham, C. A. (2001). Comparison of Measurements of Atmospheric Wet Delay by Radiosonde, Water Vapor Radiometer, GPS, and VLBI. *J. Atmos. Oceanic Technol.*, 18:830–850.

Nilsson, T. (2005). Assessment of Tomographic Methods for Estimation of Atmospheric Water Vapor Using Ground-Based GPS. Master's thesis, Chalmers University of Technology, Göteborg, Sweden.

Nilsson, T. and Gradinarsky, L. (2006). Water Vapor Tomography Using GPS Phase Observations: Simulation Results. *IEEE Transactions on Geoscience and Remote Sensing*, 44(10):2927–2941.

Nilsson, T., Gradinarsky, L., and Elgered, G. (2004). GPS Tomography Using Phase Observations. In *Geoscience and Remote Sensing Symposium, IGARSS'04*, volume 4, pages 2756–2759. IEEE.

Noguchi, W., Yoshihara, T., Tsuda, T., and Hirahara, K. (2004). Time-Height Distribution of Water Vapor Derived by Moving Cell Tomography During Tsukuba GPS Campaigns. *J. Meteor. Soc. Japan*, 82(1B):561–568.

Norquist, D. C. and Chang, S. S. (1994). Diagnosis and Correction of Systematic Humidity Error in a Global Numerical Weather Prediction Model. *Monthly Weather Review*, 122:2442–2460.

Ohtani, R. and Naito, I. (2000). Comparisons of GPS-derived precipitable water vapors with radiosonde observations in Japan. *J. Geophys. Res.*, 105(D22):26,917–26,929.

Oltmans, S. J. and Hofmann, D. J. (1995). Increase in lower-stratospheric water vapour at a mid-latitude Northern Hemisphere site from 1981 to 1994. *Nature*, 374.

Owens, J. C. (1967). Optical Refractive Index of Air: Dependence on Pressure, Temperature and Composition. *Applied Optics*, 6(1):51–59.

Pacione, R., Sciarretta, C., Faccani, C., Ferretti, R., and Vespe, F. (2001a). GPS PW Assimilation into MM5 with the Nudging Technique. *Phys. Chem. Earth (A)*, 26(6–8):481–485.

Pacione, R., Sciarretta, C., Vespe, F., Faccani, C., Ferretti, R., Fionda, E., Ferraro, C., and Nardi, A. (2001b). GPS Meteorology: Validation and Comparisons with Ground-Based Microwave Radiometer and Mesoscale Model for the Italian GPS Permanent Stations. *Phys. Chem. Earth (A)*, 26(3):139–145.

Pacione, R. and Vespe, F. (2003). GPS Zenith Total Dealy Estimation in the Mediterranean Area for Climatological and Meteorologcial Applications. *J. Atmos. Oceanic Technol.*, 20:1034–1042.

Panofsky, H. A. (1974). The atmospheric boundary layer below 150 meters. *Annu. Rev. Fluid Mech.*, 6:147–177.

Pany, T. (2002). Measuring and modeling the slant wet delay with GPS and the ECMWF NWP model. *Phys. Chem. Earth*, 27:347–354.

Pany, T., Pesec, P., and Stangl, G. (2001). Atmospheric GPS Slant Path Delays and Ray Tracing Through Numerical Weather Models, a Comparison. *Phys. Chem. Earth (A)*, 26(3):183–188.

Parkinson, B. W. and Spilker, Jr, J. J., editors (1996a). *Global Positioning System: Theory and Applications: Volume I*, volume 163 of *Progress in Astronautics and Aeronautics*. American Institue of Aeronautics and Astronautics, Inc., Washington.

Parkinson, B. W. and Spilker, Jr, J. J., editors (1996b). *Global Positioning System: Theory and Applications: Volume II*, volume 164 of *Progress in Astronautics and Aeronautics*. American Institue of Aeronautics and Astronautics, Inc., Washington.

Peng, S.-Q. and Zou, X. (2004). Impact on Short-Range Precipitation Forecasts from Assimilation of Ground-Based GPS Zenith Total Delay and Rain Gauge Precipitation Observations. *J. Meteor. Soc. Japan*, 82(1B):491–506.

Penna, N. T. and Stewart, M. P. (2003). Aliased tidal signatures in continuous GPS height time series. *Geophys. Res. Lett.*, 30(23).

Perler, D., Troller, M., Leuenberger, D., Brockmann, E., Geiger, A., and Kahle, H.-G. (2007). GPS-Tomographie: Was bringt Galileo? In *Proceedings of the AHORN meeting*, Bad Reichenhall.

Philipona, R., Dürr, B., Ohmura, A., and Ruckstuhl, C. (2005). Anthropogenic greenhouse forcing and strong water vapor feedback increase temperature in Europe. *Geophys. Res. Lett.*, 32.

Poli, P., Ao, C. O., de la Torre Juárez, M., Joiner, J., Hajj, G. A., and Hoff, R. M. (2003). Evaluation of CHAMP radio occultation refractivity using data assimilation office analyses and radiosondes. *Geophys. Res. Lett.*, 30(15).

Poli, P., Joiner, J., and Kursinski, E. R. (2002). 1DVAR analysis of temperature and humidity using GPS radio occultation refractivity data. *J. Geophys. Res.*, 107(D20).

Poli, P., Moll, P., Rabier, F., Desroziers, G., Chapnik, B., Berre, L., Healy, S. B., Andersson, E., and ElGuelai, F.-Z. (2007). Forecast impact studies of zenith total delay data from European near real-time GPS stations in Météo France 4DVAR. *J. Geophys. Res.*, 112.

Poli, P., Moll, P., Rabier, F., Healy, S., and Andersson, E. (2006). Assimilation of GPS data over Europe in Meteo France global forecasting system. *Geophys. Res. Abstr.*, 8.

Pryse, S. E. (2003). Radio Tomography: A New Experimental Technique. *Surveys in Geophysics*, 24:1–38.

Pugnaghi, S., Boccolari, M., Fazlagić, S., Pacione, R., Santangelo, R., Vedel, H., and Vespe, F. (2002). Comparison of independent integrated water vapour estimates from GPS and sun photometer measurements and a meteorological model. *Phys. Chem. Earth*, 27:355–362.

Ray, R. D. (1999). A Global Ocean Tide Model From TOPEX/POSEIDON Altimetry: GOT99.2. Technical report, Goddard Space Flight Center.

Reigber, C., Gendt, G., Dick, G., and Tomassini, M. (2002). Water Vapor Monitoring for Weather Forecasts. *GPS World*, 13(1):18–27.

Reigber, C., Lühr, H., Schwintzer, P., and Wickert, J., editors (2005). *Earth Observation with CHAMP: Results from Three Years in Orbit*. Springer, Berlin.

Reitan, C. H. (1963). Surface Dew Point and Water Vapor Aloft. *J. Appl. Meteor.*, 2:776–779.

Remondi, B. W. (1984). *Using the Global Posititioning System (GPS) Phase Observable for Relative Geodesy: Modeling, Processing, and Results*. Noaa reprint, University of Texas at Austin.

Rey, L. (2006). Impact de l'atmosphère sur la localisation GPS pour la surveillance étendue d'ouvrage d'art. Master's thesis, École Polytechnique Fédérale de Lausanne, Lausanne.

Richner, H., Joss, J., and Ruppert, P. (1996). A Water Hypsometer Utilizing High-Precision Thermocouples. *J. Atmos. Oceanic Technol.*, 13:175–182.

Richner, H., Rieker, J., and Ruppert, P. (1999). Die Auswertung von Radiosondendaten. In Richner, H. and v. Hünerbein, S., editors, *Grundlagen aerologischer Messungen speziell mittels der Schweizer Sonde SRS 400*, number 61 in Veröffentlichungen der SMA-MeteoSchweiz, chapter 1.1. SMA-MeteoSchweiz.

Rieder, M. J. and Kirchengast, G. (2001). Error analysis and characterization of atmospheric profiles retrieved from GNSS occultation data. *J. Geophys. Res.*, 106(D23):31,755–31,770.

Rind, D., Chiou, E.-W., Chu, W., Larsen, J., Oltmans, S., Lerner, J., McCormick, M. P., and McMaster, L. (1991). Positive water vapour feedback in climate models confirmed by satellite data. *Nature*, 349:500–503.

Rius, A., Ruffini, G., and Cucurull, L. (1997). Improving the vertical resolution of ionospheric tomography with GPS occultations. *Geophys. Res. Lett.*, 24(18):2291–

2294.

Rocken, C., Anthes, R., Exner, M., Hunt, D., Sokolovskiy, S., Ware, R., Gorbunov, M., Schreiner, W., Feng, D., Herman, B., Kuo, Y.-H., and Zou, X. (1997a). Analysis and validation of GPS/MET data in the neutral atmosphere. *J. Geophys. Res.*, 102(D25):29,849–29,866.

Rocken, C., Sokolovskiy, S., Johnson, J. M., and Hunt, D. (2001). Improved Mapping of Tropospheric Delays. *J. Atmos. Oceanic Technol.*, 18:1205–1213.

Rocken, C., van Hove, T., Johnson, J., Solheim, F., Ware, R., Bevis, M., Chiswell, T., and Businger, S. (1995). GPS/STORM — GPS sensing of atmospheric water vapor for meteorology. *J. Atmos. Oceanic Technol.*, 12:468–478.

Rocken, C., van Hove, T., and Ware, R. (1997b). Near real-time GPS sensing of atmospheric water vapor. *Geophys. Res. Lett.*, 24(24):3221–3224.

Rocken, C., Ware, R., van Hove, T., Solheim, F., Alber, C., Johnson, J., Bevis, M., and Businger, S. (1993). Sensing atmospheric water vapor with the Global Positioning System. *Geophys. Res. Lett.*, 20(23):2631–2634.

Ross, R. J. and Rosenfeld, S. (1997). Estimating mean weighted temperature of the atmosphere for Global Positioning System applications. *J. Geophys. Res.*, 102(D18):21,719–21,730.

Rothacher, M. (2001). Comparison of Absolute and Relative Antenna Phase Center Variations. *GPS Solut.*, 4(4):55–60.

Rothacher, M. and Beutler, G. (1998). The Role of GPS in the Sutdy of Global Change. *Phys. Chem. Earth*, 23(9-10):1029–1040.

Rothacher, M., Schaer, S., Mervart, L., and Beutler, G. (1995). Determination of Antenna Phase Center Variations Using GPS Data. In *Proceedings of the IGS Workshop*, Potsdam, Germany.

Rothacher, M., Springer, T. A., Schaer, S., and Beutler, G. (1998). Processing Strategies for regional GPS networks. In Brunner, F. K., editor, *Advances in Positioning and Reference Frames*, volume 118 of *International Association of Geodesy Symposia*. Springer, Berlin.

Ruckstuhl, C., Philipona, R., Morland, J., and Ohmura, A. (2007). Observed relationship between surface specific humidity, integrated water vapor, and longwave downward radiation at different altitudes. *J. Geophys. Res.*, 112.

Rueeger, J. M. (2002). Refractive Index Formulae for Radio Waves. In *Integration of Techniques and Corrections to Achieve Accurate Engineering*.

Ruffini, G., Cardellach, E., Flores, A., Cucurull, L., and Rius, A. (1998a). Ionospheric calibration of radar altimeters using GPS tomography. *Geophys. Res. Lett.*, 25(20):3771–3774.

Ruffini, G., Flores, A., and Rius, A. (1998b). GPS Tomography of the Ionospheric Electron Content with a Correlation Functional. *IEEE Transactions on Geoscience and Remote Sensing*, 36(1).

Ruffini, G., Kruse, L. P., Rius, A., Bürki, B., Cucurull, L., and Flores, A. (1999). Estimation of Tropospheric Zenith Delay and Gradients over the Madrid Area Using GPS and WVR Data. *Geophys. Res. Lett.*, 26(4):447–450.

Rührnössl, H., Brunner, F. K., and Rothacher, M. (1998). Modellierung der troposphärischen Korrektur für Deformationsmessungen mit GPS im alpinen Raum. *Allgemeine Vermessungs-Nachrichten*, 1.

Saastamoinen, J. (1972). Atmospheric Correction for Troposphere and Stratosphere

in Radio Ranging of Satellites. In Henriksen, S. W., Macini, A., and Chovitz, B. H., editors, *The Use of Artificial Satellites for Geodesy*, volume 15 of *Geophysics Monograph*, pages 247–251. American Geophysical Union, Washington, D.C.

Saastamoinen, J. (1973a). Contributions to the theory of atmospheric refraction. *Bull. Géod.*, 105:279–298.

Saastamoinen, J. (1973b). Contributions to the theory of atmospheric refraction: Introduction to practical computation of astronomical refraction. *Bull. Géod.*, 107:383–397.

Saastamoinen, J. (1973c). Contributions to the theory of atmospheric refraction: Part II. Refraction corrections in satellite geodesy. *J. Geod*, 47(1):13–34.

Salstein, D. A., Rosen, R. D., and Peixoto, J. P. (1983). Modes of Variability in Annual Hemispheric Water Vapor and Transport Fields. *J. Atmos. Sci.*, 40:788–803.

Santerre, R. (1991). Impact of GPS satellite sky distribution. *manus. geod.*, 16:28–53.

Scherneck, H.-G. (1991). A parametrized solid earth tide model and ocean tide loading effects for global geodetic baseline measurements. *Geophys. J. Int.*, 106:677–694.

Scherneck, H.-G. (1993). Ocean tide loading: propagation of errors from the ocean tide into loading coefficients. *manuscripta gedaetica*, 18:59–71.

Schneider, E. K., Kirtman, B. P., and Lindzen, R. S. (1999). Tropospheric Water Vapor and Climate Sensitivity. *J. Atmos. Sci.*, 56:1649–1658.

Schueler, T., Hein, G. W., and Eissfeller, B. (2000). Improved Tropospheric Delay Modeling Using an Integrated Approach of Numerical Weather Models and GPS. In *Proceedings of the ION GPS 2000*, Salt Lake City, USA.

Seeber, G. (2003). *Satellite Geodesy*. Walter de Gruyter, Berlin, New York, 2 edition.

Seko, H., Kawabata, T., Tsuyuki, T., Nakamura, H., Koizumi, K., and Iwabuchi, T. (2004a). Impacts of GPS-derived Water Vapor and Radial Wind Measured by Doppler Radar on Numerical Prediction of Precipitation. *J. Meteor. Soc. Japan*, 82(1B):473–489.

Seko, H., Nakamura, H., Shoji, Y., and Iwabuchi, T. (2004b). The Meso-γ scale Water Vapor Distribution Associated with a Thunderstrom Calculated from a Dense Network of GPS Receivers. *J. Meteor. Soc. Japan*, 82(1B):569–586.

Seko, H., Shimada, S., Nakamura, H., and Kato, T. (2000). Three-dimensional distribution of water vapor estimated from tropospheric delay of GPS data in a mesoscale precipitation system of the Baiu front. *Earth Planets Space*, 52:927–933.

Shine, K. P. and Sinha, A. (1991). Sensititviy of the Earth's climate to height-dependent changes in the water vapour mixing ratio. *Nature*, 354:382–384.

Shoji, Y., Nakamura, H., Iwabuchi, T., Aonashi, K., Seko, H., Mishima, K., Itagaki, A., Ichikawa, R., and Ohtani, R. (2004). Tsukuba GPS Dense Net Campaign Observation: Improvement in GPS Analysis of Slant Path Delay by Stacking One-way Postfit Phase Residuals. *J. Meteor. Soc. Japan*, 82(1B):301–314.

Shrestha, S. M. (2003). Investigations into the Estimation of Tropospheric Delay and Wet Refractivity Using GPS Measurements. Master's thesis, Department of Geomatics Enineering, University of Calgary, Calgary, Alberta.

Shum, C. K., Woodworth, P. L., Andersen, O. B., Egbert, G. D., Francis, O., King, C., Klosko, S. M., LeProvost, C., Li, X., Molines, J.-M., Parke, M. E., Ray,

R. D., Schlax, M. G., Stammer, D., Tierney, C. C., Vincent, P., and Wunsch, C. I. (1997). Accuracy assessment of recent ocean tide models. *J. Geophys. Res.*, 102(C11):25,173–25,194.

Sierk, B. (2001). *Solar Spectrometry for Determination of Tropospheric Water Vapor*, volume 62 of *Geodätisch-geophysikalische Arbeiten in der Schweiz*. Swiss Geodetic Commission.

Sierk, B., Bürki, B., Becker-Ross, H., Florek, S., Neubert, R., Kruse, L. P., and Kahle, H.-G. (1997). Tropospheric water vapor derived from solar spectrometer, radiometer, and GPS measurements. *J. Geophys. Res.*, 102(B10):22,411–22,424.

Skone, S. and Hoyle, V. (2005). Troposphere modeling in a regional GPS network. *Journal of Global Positioning Systems*, 4(1-2):230–239.

Smith, Jr, E. K. and Weintraub, S. (1953). The Constants in the Equation for Atmospheric Refractive Index at Radio Frequencies. In *Proceedings of the Institute of Radio Engineers*, volume 41/8, pages 1035–1037.

Smith, T. L., Benjamin, S. G., Gutman, S. I., and Sahm, S. (2004). Ongoing Assessment of GPS-IPW Impact on RUC Forecasts. In *Proceedings of the 20th Conference on Weather Analysis and Forecasting/16th Conference on Numerical Weather Prediction*.

Smith, T. L., Benjamin, S. G., Gutman, S. I., and Sahm, S. (2007). Short-Range Forecast Impact from Assimilation of GPS-IPW Observations into the Rapid Update Cycle. *Monthly Weather Review*, 135:2914–2930.

Smith, W. L. (1966). Note on the Relationship Between Total Precipitable Water and Surface Dew Point. *J. Appl. Meteor.*, 5:726–727.

Soden, B. J., Wetherald, R. T., Stenchikov, G. L., and Robock, A. (2002). Global Cooling After the Eruption of Mount Pinatubo: A Test of Climate Feedback by Water Vapor. *Science*, 296:727–730.

Sokolovskiy, S. (2003). Effect of superrefraction on inversions of radio occultation signals in the lower troposphere. *Radio Science*, 38(3).

Sokolovskiy, S. V. (2001). Tracking tropospheric radio occultation signals from low Earth orbit. *Radio Science*, 36(3):483–498.

Solheim, F. S., Vivekanandan, J., Ware, R. H., and Rocken, C. (1999). Propagation delays induced in GPS signals by dry air, water vapor, hydrometeors, and other particulates. *J. Geophys. Res.*, 104(D8):9663–9670.

Solomon, S., Qin, D., Manning, M., Marquis, M., Averyt, K., Tignor, M. M. B., Miller, Jr, H. L., and Chen, Z., editors (2007). *Climate Change 2007: The Physical Science Basis. Contribution of Working Group I to the Fourth Assessment Report of the Intergovernmental Panel on Climate Change*. Cambridge University Press, Cambridge and New York.

Somieski, A. (2005). *Geodetic Mobile Solar Spectrometer*, volume 68 of *Geodätisch-geophysikalische Arbeiten in der Schweiz*. Swiss Geodetic Commission.

Song, S., Zhu, W., Ding, J., and Peng, J. (2006). 3D water-vapor tomography with Shanghai GPS network to improve forecasted moisture field. *Chin. Sci. Bull.*, 51(5):607–614.

Spilker, Jr, J. J. (1996). Tropospheric Effects on GPS. In Parkinson, B. W. and Spilker, Jr, J. J., editors, *Global Positioning System: Theory and Applications: Volume I*, chapter 13, pages 517–546. American Institue of Aeronautics and Astronautics, Inc.

Spoelstra, T. A. T. (1992). The ionosphere as a refractive medium. In de Munck, J. C. and Spoelstra, T. A. T., editors, *Refraction of transatmospheric signals in geodesy*, pages 69–76. Netherlands Geodetic Commission.

Springer, T. A. and Hugentobler, U. (2001). IGS Ultra Rapid Products for (Near-) Real-Time Applications. *Phys. Chem. Earth*, 26(6–8):623–628.

Steiner, A. K., Kirchengast, G., and Ladreiter, H. P. (1999). Inversion, error andalysis, and validation of GPS/MET occultation data. *Ann. Geophys.*, 17:122–138.

Steppeler, J., Doms, G., Schättler, U., Bitzer, H. W., Gassmann, A., Damrath, U., and Gregoric, G. (2003). Meso-gamma scale forecasts using the nonhydrostatic model LM. *Meteorol. Atmos. Phys.*, 82:75–96.

Stoew, B. and Elgered, G. (2004). Characterization of Atmospheric Parameters using a Ground Based GPS Network in North Europe. *J. Meteor. Soc. Japan*, 82(1B):587–596.

Stoew, B. and Elgered, G. (2005). Spatial and temporal correlations of the GPS estimation errors. Technical report, TOUGH, Onsala.

Stull, R. B. (1999). *An Introduction to Boundary Layer Meteorology*. Kluwer Academic Publishers, Dordrecht. Reprint.

Sturm, P., Leuenberger, M., and Schmidt, M. (2005). Atmospheric $O2$, $CO2$ and $\delta^{13}C$ observations from the remote sites Jungfraujoch, Switzerland, and Puy de Dôme, France. *Geophys. Res. Lett.*, 32.

Sun, H.-P., Ducarme, B., and Dehant, V. (1995). Effect of the atmospheric pressure on surface displacements. *J. Geod*, 70:131–139.

Syndergaard, S. (2002). A new algorithm for retrieving GPS radio occultation total electron content. *Geophys. Res. Lett.*, 29(16).

Tarniewicz, J., Bock, O., Pelon, J., and Thom, C. (2002). Raman lidar for external GPS path delay calibration devoted to high accuracy height determination. *Phys. Chem. Earth*, 27:329–333.

Tatarskii, V. I. (1971). *The effects of the turbulent atmosphere on wave propagation*. Israel Program for Scientific Translations Ltd. translated from russian by IPST Staff.

Thayer, G. D. (1974). An improved equation for the radio refractive index of air. *Radio Science*, 9:803–807.

Tralli, D. M. and Lichten, S. M. (1990). Stochastic estimation of tropospheric path delays in Global Positioning System geodetic measurements. *Bull. Géod.*, 64:127–159.

Tranquilla, J. M. and Al-Rizzo, H. M. (1993). Theoretical and experimental evaluation of precise relative positioning during periods of snowfall precipitation using the global positioing system. *manus. geod.*, 18:362–379.

Tregoning, P., Boers, R., O'Brien, D., and Hendy, M. (1998). Accuracy of absolute precipitable water vapor estimates from GPS observations. *J. Geophys. Res.*, 103(D22):28,701–28,710.

Tregoning, P. and Herring, T. A. (2006). Impact of a priori zenith hoydrostatic dealy errors on GPS estimates of station heights and zenith total delays. *Geophys. Res. Lett.*, 33.

Trenberth, K. E. and Guillemot, C. J. (1994). The total mass of the atmosphere. *J. Geophys. Res.*, 99(D11):23,079–23,088.

Troller, M. (2004). *GPS based Determination of the Integrated and Spatially Distributed Water Vapor in the Troposphere*, volume 67 of *Geodätisch-geophysikalische Arbeiten in der Schweiz*. Swiss Geodetic Commission.

Troller, M. and Brockmann, E. (2002). Troposphäreninterpolation aus AGNES: Benutzeranleitung und Resultate anhand der GPS Verdichtungsmessungen 2001. Report (B) 02-25, swisstopo.

Troller, M., Bürki, B., Cocard, M., Geiger, A., and Kahle, H.-G. (2002a). 3-D refractivtiy field from GPS double difference tomography. *Geophys. Res. Lett.*, 29(24).

Troller, M., Cocard, M., and Geiger, A. (2002b). *Softwarepackage Comedie: Collocation of Meteorological Data for Interpolation and Estimation of Tropospheric Pathdelays. User documentation.* Version 1.1.

Troller, M., Geiger, A., Brockmann, E., Bettems, J.-M., Bürki, B., and Kahle, H.-G. (2006a). Tomographic determination of the spatial distribution of water vapor using GPS observations. *Adv. Space Res.*, 37:2211–2217.

Troller, M., Geiger, A., Brockmann, E., and Kahle, H.-G. (2006b). Determination of the spatial and temporal variation of tropospheric water vapour using CGPS networks. *Geophys. J. Int.*, 167(2):509–520.

Troller, M., Leuenberger, D., Brockmann, E., Geiger, A., and Kahle, H.-G. (2007a). GPS-Tomography: Results and Analyses of the Operational Determination of Humidity Profiles over Switzerland. *Geophys. Res. Abstr.*, 9.

Troller, M., Leuenberger, D., Brockmann, E., Geiger, A., and Kahle, H.-G. (2007b). Impact of GPS-Tomography on Operational Weather Forecast: Determination of the 3D Distribution of Humidity. In *Proceedings of the European Navigation Conference (ENC-GNSS)*, pages 174–179, Geneva, Switzerland.

Tsuda, T., Heki, K., Miyazaki, S., Aonashi, K., Hirahara, K., Nakamura, H., Tobita, M., Kimata, F., Tabei, T., Matsushima, T., Kimura, F., Satomura, M., Kato, T., and Naito, I. (1998). GPS meteorology project of Japan: Exploring frontiers of geodesy. *Earth Planets Space*, 50(10):i–v.

Urfer-Henneberger, C. and Turner, H. (1982). Bodennahes Windsystem und Temperaturgradienten bei verschiedenen Wetterlagen in einem von Süden nach Norden führenden V-förmigen Alpental. *Arch. Met. Geoph. Biokl.*, 31:253–271.

Urschl, C., Dach, R., Hugentobler, U., Schaer, S., and Beutler, G. (2005). Validating ocean tide loading models using GPS. *J. Geod*, 78:616–625.

van Dam, T. M., Blewitt, G., and Heflin, M. B. (1994). Atmospheric pressure loading effects on Global Positioning System coordinate determinations. *J. Geophys. Res.*, 99(B12):23,939–23,950.

van der Hoeven, A., Hanssen, R. F., and Ambrosius, B. (2002). Tropospheric delay estimation and analysis using GPS and SAR interferometry. *Phys. Chem. Earth*, 27:385–390.

van der Marel, H. and The COST-716 Team (2004). COST-716 demonstration project for the near real-time estimation of integrated water vapour from GPS. *Phys. Chem. Earth*, 29:187–199.

Vedel, H., Huang, X.-Y., Haase, J., Ge, M., and Calais, E. (2004). Impact of GPS Zenith Tropospheric Delay data on precipitation forecasts in Mediterranean France and Spain. *Geophys. Res. Lett.*, 31.

Vedel, H., Mogensen, K. S., and Huang, X.-Y. (2001). Calculation of Zenith Delays

From Meteorological Data Comparison of NWP Model, Radiosonde and GPS Delays. *Phys. Chem. Earth (A)*, 26(6–8):497–502.

Vedel, H. and Sattler, K. (2002). Impact study of assimilation of GPS slant delays. Technical Report D41, Danish Meterological Institute, Copenhagen.

Verdun, J., Brockmann, E., Geiger, A., Kahle, H.-G., and Schneider, D. (2001). GPS time series analysis of the permanent GPS Swiss network AGNES. In *Proceedings of the 2nd EUCOR-URGENT Workshop*, Strasbourg, France.

Vespe, F., Benedetto, C., and Pacione, R. (2004). The use of refractivity retrieved by radio occultation technique for the derivation of atmospheric water vapor content. *Phys. Chem. Earth*, 29:257–265.

Ware, R., Exner, M., Feng, D., Gorbunov, M., Hardy, K., Herman, B., Kuo, Y., Meehan, T., Melbourne, W., Rocken, C., Schreiner, W., Sokolovkiy, S., Solheim, F., Zou, X., Anthes, R., Businger, S., and Trenberth, K. (1996). GPS Sounding of the Atmosphere from Low Earth Orbit: Preliminary Results. *Bull. Am. Meteorol. Soc.*, 77(1).

Ware, R. H., Alber, C., Rocken, C., and Solheim, F. (1997). Sensing integrated water vapor along GPS ray paths. *Geophys. Res. Lett.*, 24(4):417–420.

Ware, R. H., Fulker, D. W., Stein, S. A., Anderson, D. N., Avery, S. K., Clark, R. D., Droegemeier, K. K., Kuettner, J. P., Minster, J. B., and Sorooshian, S. (2000). SuomiNet: A Real-Time National GPS Network for Atmospheric Research and Education. *Bull. Am. Meteorol. Soc.*, 81(4):677–694.

Warren, D. L. M. and Raquet, J. F. (2003). Broadcast vs. precise GPS ephemerides: a historical perspective. *GPS Solut.*, 7:151–156.

Webb, E. K. (1984). Temperature and Humidity Structure in the Lower Atmosphere. In Brunner, F. K., editor, *Geodetic Refraction: Effects of Electromagnetic Wave Propagation Through the Atmosphere*, pages 85–141. Springer, Berlin.

Wessel, P. and Smith, W. H. F. (2007). *The Generic Mapping Tools Version 4.2.1. Technical Reference and Cookbook.*

Wickert, J., Reigber, C., Beyerle, G., König, R., Marquardt, C., Schmidt, T., Grunwaldt, L., Galas, R., Meehan, T. K., Melbourne, W. G., and Hocke, K. (2001). Atmosphere sounding by GPS radio occultation: First results from CHAMP. *Geophys. Res. Lett.*, 28(17):3263–3266.

Wild, U., Brockmann, E., Hug, R., Just, C., Kummer, P., Signer, T., and Wiget, A. (2000). Automatisches GPS-Netz Schweiz (AGNES). Ein multifunktionales Referenznetz für Navigation und Vermessung. *Vermessung, Photogrammetrie, Kulturtechnik*, 6:389–392.

Wirth, B. (1990). *Höhensysteme, Schwerepotentiale und Niveauflächen: Systematische Untersuchungen zur zukünftigen terrestrischen und GPS-gestätzten Höhenbestimmung in der Schweiz*, volume 42 of *Geodätisch-geophysikalische Arbeiten in der Schweiz*. Swiss Geodetic Commission.

Wolfe, D. E. and Gutman, S. I. (2000). Developing an Operational, Surface-Based, GPS, Water Vapor Observing System for NOAA: Network Design and Results. *J. Atmos. Oceanic Technol.*, 17:426–440.

Yang, X., Sass, B. H., Elgered, G., Johansson, J. M., and Emardson, T. R. (1999). A Comparison of Precipitable Water Vapor Estimates by an NWP Simulation and GPS Observations. *J. Appl. Meteor.*, 38:941–956.

Yeh, K. C. and Liu, C. H. (1972). Propagation and Application of Waves in the Ionosphere. *Reviews of Geophysics and Space Physics*, 10(2):631–709.

Yeh, K. C. and Raymund, T. D. (1991). Limitations of ionospheric imaging by tomography. *Radio Science*, 26(6):1361–1380.

Yuan, L. L., Anthes, R. A., Ware, R. H., Rocken, C., Bonner, W. D., Bevis, M. G., and Businger, S. (1993). Sensing climate change using the Global Positioning System. *J. Geophys. Res.*, 98(D8):14925–14937.

Yunck, T. P. and Hajj, G. A. (2005). Atmospheric and Ocean Sensing with GNSS. In Reigber, C., Lühr, H., Schwintzer, P., and Wickert, J., editors, *Earth Observation with CHAMP: Results from Three Years in Orbit*. Springer, Berlin.

Yunck, T. P., Lindal, G. F., and Liu, C.-H. (1988). The role of GPS in precise Earth observation. In *Proceedings of the IEEE Postion Location and Navigation Symposium PLANS88*, Orlando, Florida.

Zhang, M., Ni, Y., and Zhang, F. (2007). Variational Assimilation of GPS Precipitable Water Vapor and Hourly Rainfall Observations for a Meso-β Scale Heavy Precipitation Event During the 2002 Mei-Yu Season. *Adv. Atmos. Sci.*, 24(3):509–526.

Zou, X., Kuo, Y.-H., and Guo, Y.-R. (1995). Assimilation of Atmospheric Radio Refractivity Using a Nonhydrostatic Adjoint Model. *Monthly Weather Review*, 123:2229–2249.

Zuev, V. E. and Komarov, V. S. (1987). *Statistical models of the temperature and gaseous components of the atmosphere*. Atmospheric Sciences Library. Reidel, Dordrecht.

Appendix A

Weather dynamics during the two field campaigns

In this chapter, the weather dynamics during the two field campaigns are described. The time series of the meteorological surface parameters air pressure, water vapor pressure, relative humidity, rainfall, air temperature and sunshine duration are shown. The observations were recorded by the automated ground-based measurement network (ANETZ) at two stations in the project area: Evolène (EVO) at 1825 m AMSL (left panels in Figs. A.2 and A.3) and Visp (VIS) at 640 m AMSL (right panels).

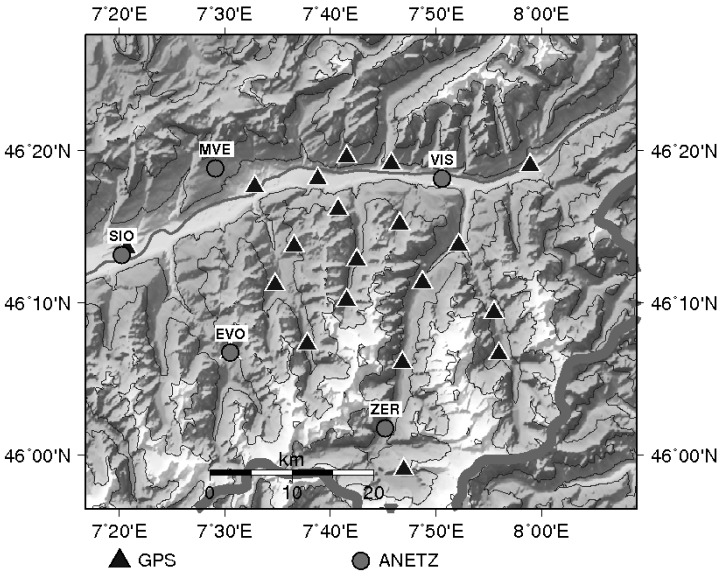

Fig. A.1: Plan view of the project area in the canton of Valais. The local, densified GPS network during the field campaign in July 2005 and the stations of the automated meteorological network (ANETZ) of MeteoSwiss are marked.

In the top panels of Figs. A.2 and A.3, air pressure p (broad line) and water vapor pressure e_p (thin line) are shown. The middle panels display relative humidity H_r (continuous line) and rainfall (dark-colored columns). In the bottom panels, the variation of air temperature T (continuous line) and, if available, sunshine duration (light-colored bars) are indicated.

Tabs. A.1 and A.2 on p. 182 summarize the mean values and variations of the meteorological parameters observed at all five ANETZ stations within the project area (see Fig. A.1).

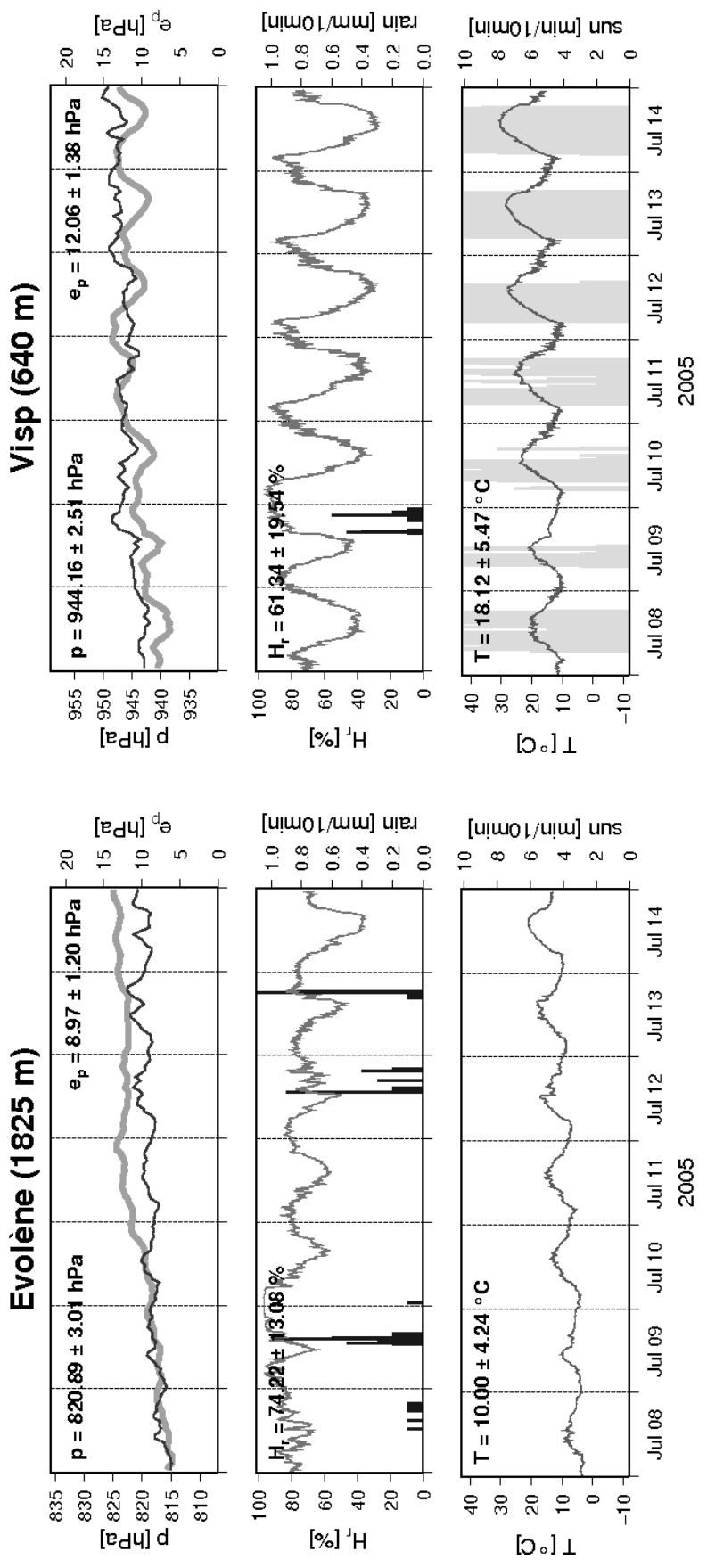

Fig. A.2: Time series, mean values and variation (standard deviation) of the major meteorological parameters (pressure p, partial water vapor pressure e_p, relative humidity H_r, rainfall, air temperature T and sunshine duration) at the stations Evolène and Visp during the field campaign in July 2005. Sunshine duration is not available for station Evolène. In the daily variation of the time series of air pressure at station Visp (see top panels on the right hand side, similar in A.3), the influence of a strong mountain-valley-breeze circulation is recognizable.

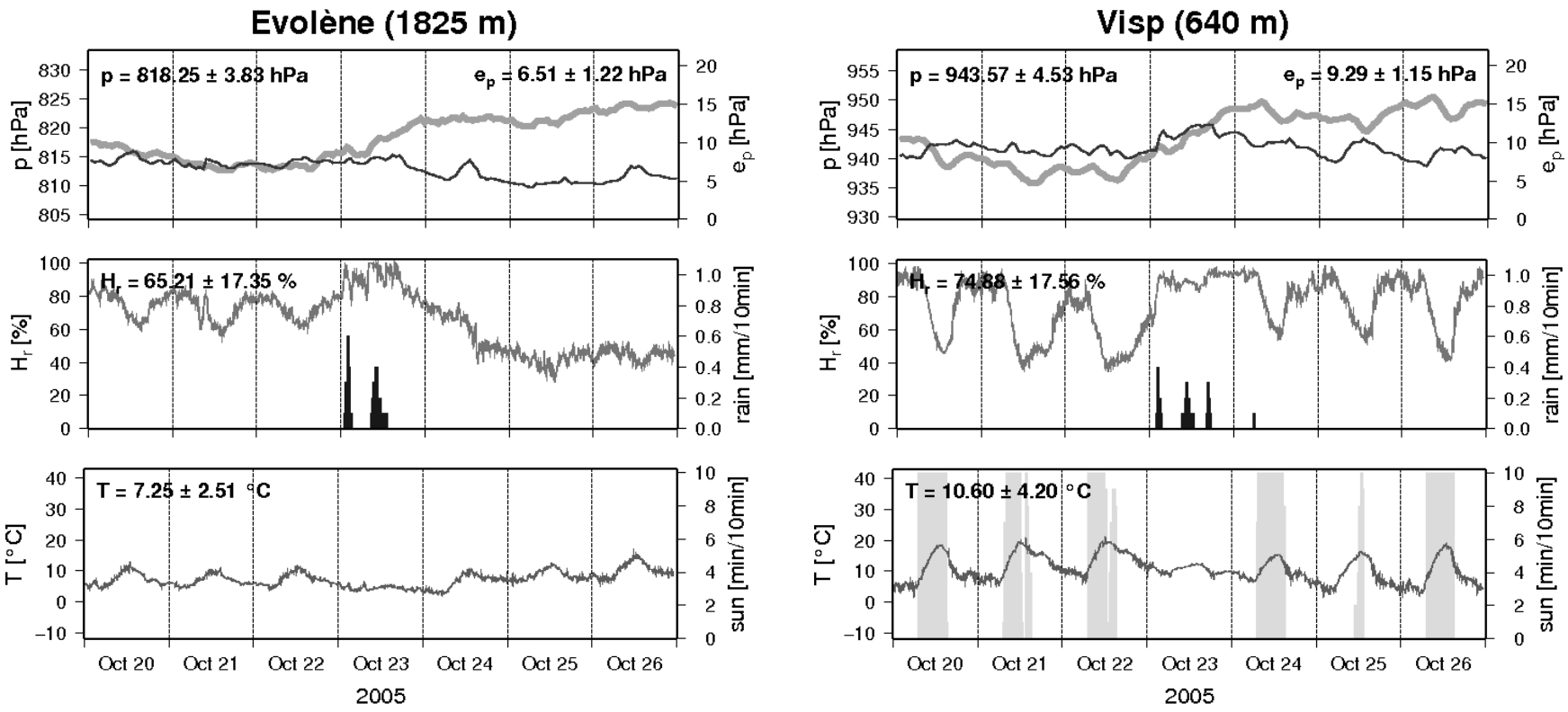

Fig. A.3: Time series, mean values and variation (standard deviation) of the major meteorological parameters (pressure p, partial water vapor pressure e_p, relative humidity H_r, rainfall, air temperature T and sunshine duration) at the stations Evolène and Visp during the field campaign in October 2005. Sunshine duration is not available at station Evolène.

Station	Height	p		e_p		H_r		T	
		mean	σ	mean	σ	mean	σ	mean	σ
	m AMSL	hPa	hPa	hPa	hPa	%	%	°C	°C
EVO	1825	820.9	3.0	9.0	1.2	74.2	13.1	10.0	4.2
MVE	1508	853.3	2.8	10.1	1.4	70.5	16.5	12.7	4.7
SIO	482	961.5	2.3	13.4	1.6	61.9	14.9	19.2	4.9
VIS	640	944.2	2.5	12.1	1.4	61.3	19.5	18.1	5.5
ZER	1638	840.0	3.0	9.2	1.1	69.0	19.9	11.9	4.8
Average	1218.6	884.0	2.7	10.8	1.3	67.4	16.8	14.4	4.8

Tab. A.1: Mean values and standard deviation (σ) of the major meteorological constituents measured at five ANETZ stations in the canton of Valais from July 8–14, 2005.

Station	Height	p		e_p		H_r		T	
		mean	σ	mean	σ	mean	σ	mean	σ
	m AMSL	hPa	hPa	hPa	hPa	%	%	°C	°C
EVO	1825	818.2	3.8	6.5	1.2	65.2	17.4	7.2	2.5
MVE	1508	851.3	3.9	7.4	1.0	66.8	16.1	8.8	2.6
SIO	482	961.6	4.7	10.5	1.5	77.7	16.9	11.7	3.8
VIS	640	943.6	4.5	9.3	1.1	74.9	17.6	10.6	4.2
ZER	1638	837.3	3.9	6.3	1.1	66.0	17.6	6.6	3.3
Average	1218.6	882.4	4.2	8.0	1.2	70.1	17.1	9.0	3.3

Tab. A.2: Mean values and standard deviation (σ) of the major meteorological constituents measured at five ANETZ stations in the canton of Valais from October 20–26, 2005.

Based on the average values of all stations shown in Tabs. A.1 and A.1, two major aspects in terms of weather dynamics during the two campaigns can be pointed out:

- Firstly, in October the mean air temperature is about five degrees below the value in July due to the seasonal variation. Also, all other mean values decreased between July and October 2005, except the relative humidity at the two stations SIO and VIS in the main valley.
- Secondly, the larger variation of the pressure time series in October refers to the cold front passage in the middle of the campaign (see also Sec. 4.4, pp. 50f.). The variation is most accentuated in the main valley (stations SIO and VIS).

The expected differences in the zenith total delay estimates caused by changing meteorological surface data can be pre-estimated according to Tab. 2.2, p. 30.

Appendix B

Description of the GPS networks in the project area

B.1 Introduction

In this chapter, the different GPS networks operated during the two field campaigns in the project area in July and October 2005 are shortly described with respect to the receiver and antenna specifications as well as to the site dependent skyplots. Among these networks, there are

- the non-permanent network WATEC (see Sec. B.2), purposely installed for the present investigation in high-resolution GPS tomography,
- the geodetic three-dimensional network TURTMANN (see Sec. B.3) of the Swiss Geodetic Commission operated by swisstopo and
- the permanent geodynamic network TECVAL (see Sec. B.4), which belongs to an ongoing project of ETH Zurich.

Furthermore, the stations of the national permanent networks of swisstopo and Swissat, which are located within the target region, are described (see Sec. B.5). Fig. 4.3 on p. 46 and Fig. 4.9 on p. 52 show the geographical distribution of all stations during the campaigns in July and October, respectively.

The skyplots shown on the following pages are north-aligned and include the approximate GPS satellite tracks down to 0 ° elevation angle visible from the particular GPS station. Furthermore, the topography from a high-resolution digital elevation model is displayed. The percentage value in the middle of the plot (degree of visibility V) is calculated by division of the number of real observations (n_{real}), accounting for the natural and artificial obstructions as well as for the vegetation, by the number of expectable observations ($n_{no\ obstructions}$) due to the satellite orbits, but without obstructions and a cutoff elevation of 0 °.

$$V = \frac{n_{real}}{n_{no\ obstructions}} \tag{B.1}$$

For further information on the software and the algorithms used for the generation of the skyplots see Marshall (2002); Hilla (2004); Wessel and Smith (2007).

B.2 The non-permanent network WATEC

To get an adequate covering for high-resolution GPS tomography, the existing national permanent GPS networks within the mountainous project area (see Sec. B.5) were densified. With a spatial resolution of less than 5 km in average, non-permanent GPS stations were installed and operated at fifteen sites during a week in July and October 2005.

Tab. B.1 summarizes the configurations of receiver and antenna types of the WATEC stations for both campaigns.

Station	Receiver type	Antenna type	Receiver type	Antenna type
	July 8–14, 2005		October 20–26, 2005	
EVOL	Leica SR530	LEIAT502	Leica SR530	LEIAT502
GINA	Leica SR399	LEISR399_INT	Leica SR530	LEIAT502
GRIM	Trimble 4000 SSi	TRM41249.00	Leica SR530	LEIAT502
GRUB	Trimble 5700	TRM41249.00	Leica SR530	LEIAT502
RAND	Trimble NetRS	TRM41249.00	Leica GRX1200	LEIAX1202
SBAL	Trimble NetRS	TRM41249.00	Leica GRX1200	LEIAX1202
SFEE	Trimble NetRS	TRM41249.00	Trimble NetRS	TRM41249.00
SIER*	TPS HE_GGD	JPSLEGANT_E	Trimble NetRS	TRM41249.00
SLUC	Trimble 4000 SSi	TRM41249.00	Leica SR530	LEIAT502
SNIK	Trimble NetRS	TRM41249.00	Leica GRX1200	LEIAX1202
SSTU	Trimble 5700	TRM41249.00	Leica SR530	LEIAT502
STAL	Trimble NetRS	TRM41249.00	Leica GRX1200	LEIAX1202
VISP	Trimble NetRS	TRM41249.00	Leica GRX1200	LEIAX1202
ZINA	Leica SR530	LEIAT502	Leica SR530	LEIAT502

Tab. B.1: Receiver and antenna configuration of the fourteen stations of the WATEC network in July and October 2005.
*During the first campaign in July 2005, the station SIER was operated by the agency Geosat S.A. in Sierre.

Figs. B.1 and B.2 show the corresponding skyplots for all station of the WATEC network. The number of real observations over the number of hypothetical observations down to 0° cutoff elevation (degree of visibility V, see Eq. B.1) varies between 96 % (station SLUC) and 63 % (station SNIK). Seven stations have 80 % or more available observations, and four stations are located, where the satellite visibility is below 70 %.

Concerning the stations of the non-permanent network WATEC, the choice of a cutoff elevation below 10° in the data processing is noncritical (except in terms of multipath intensification), because in most cases the natural obstructions exceed this limit already.

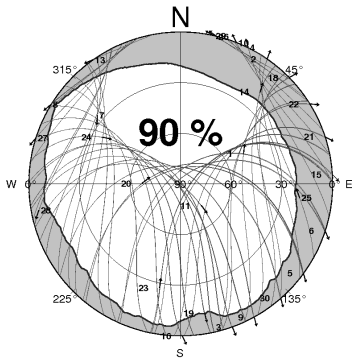

(a) EVOL at 1827.9 m AMSL.

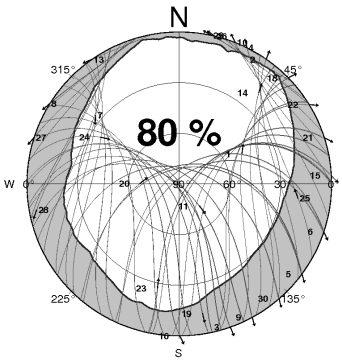

(b) GINA at 2003.5 m AMSL.

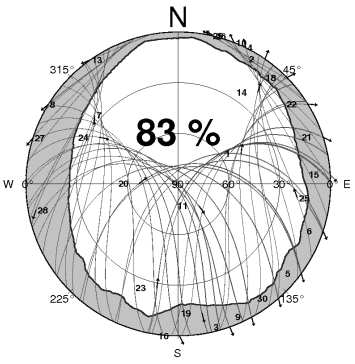

(c) GRIM at 1596.9 m AMSL.

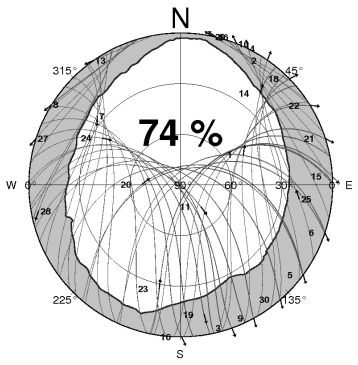

(d) GRUB at 1844.2 m AMSL.

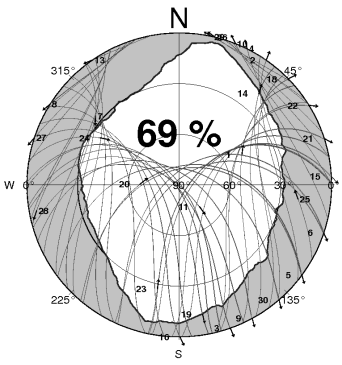

(e) RAND at 1406.9 m AMSL.

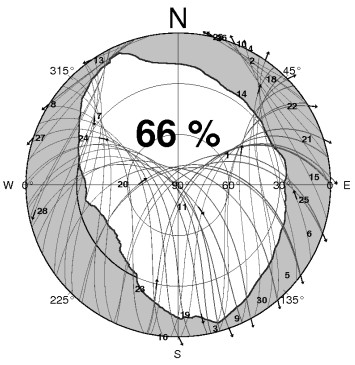

(f) SBAL at 1483.1 m AMSL.

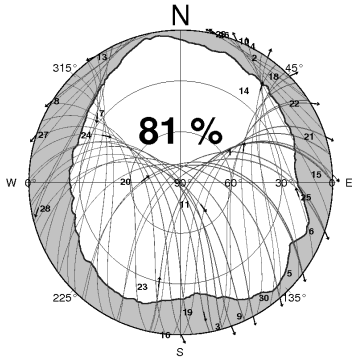

(g) SFEE at 1810.3 m AMSL.

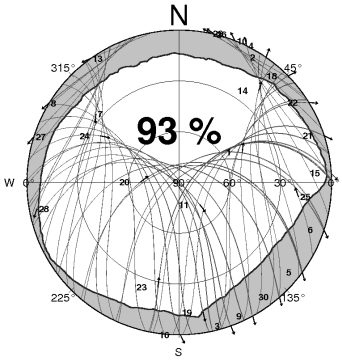

(h) SIER at 551.2 m AMSL.

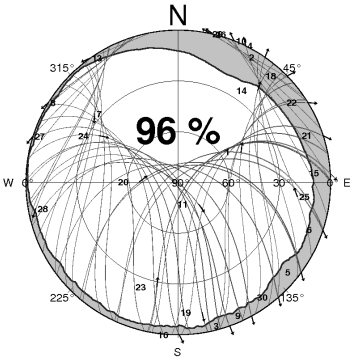

(i) SLUC at 2186.7 m AMSL.

Fig. B.1: Skyplots from the stations of the WATEC network (first part).

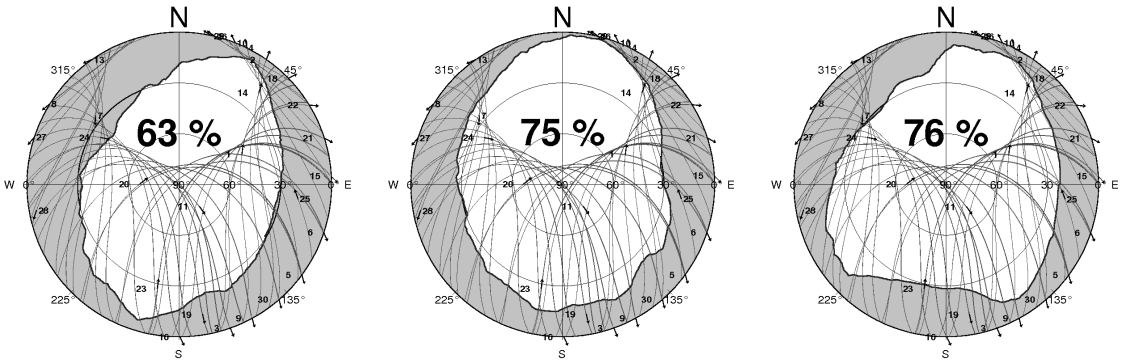

(a) SNIK at 1065.7 m AMSL. (b) SSTU at 2181.7 m AMSL. (c) STAL at 805.1 m AMSL.

(d) VISP at 641.1 m AMSL. (e) ZINA at 1694.1 m AMSL.

Fig. B.2: Second part of skyplots from the stations of the WATEC network.

B.3 The geodetic 3-D network Turtmann

During the field campaign in October 2005, the Swiss Federal Office of Topography swisstopo ran a high-precision geodetic three-dimensional network of nine GPS stations for a remeasurement campaign. The network was established and designed for investigating different effects on geodetic observations and corresponding correction models in an alpine region (see e.g. Cocard, 1987; Gurtner et al., 1989; Geiger et al., 1992; Beutler et al., 1995a; Rührnössl et al., 1998; Brockmann, 2007).

In July 2005, three of these sites had been occupied and operated as well (see Fig. 4.9(b) on p. 52). For the October 2005 campaign, the data were cleaned and preprocessed by swisstopo before delivering and usage in this work.

Tab. B.2 summarizes the hardware configuration utilized at the stations of the Turtmann network for both campaigns.

Station	Receiver type	Antenna type	Receiver type	Antenna type
	July 8–14, 2005		October 20–26, 2005	
AGAR	-	-	Trimble 4000 SSi	TRM41249.00
BRAE	Trimble 5700	TRM41249.00	Trimble 5700	TRM41249.00
BRUN	-	-	Trimble 5700	TRM41249.00
EMSH	Trimble 5700	TRM41249.00	Trimble 5700	TRM41249.00
ERGI	-	-	Trimble 5700	TRM41249.00
JEIZ	-	-	Trimble 5700	TRM41249.00
OEMS	-	-	Trimble 5700	TRM41249.00
SUST	Leica SR399	LEISR399_INT	Trimble 4000 SSi	TRM41249.00*
TURT	-	-	Trimble 4000 SSi	TRM41249.00*

Tab. B.2: Specifications of the receiver and antenna types mounted at the nine sites of the Turtmann network.
*At stations SUST and TURT, the antennas first used were replaced in the middle of the campaign by two TRM22020.00+GP antennas.

Fig. B.3 shows the skyplots for the stations of the Turtmann network. Compared to the locations of the WATEC network (see Sec. B.2), the satellite visibility of all but one station is fairly good and above 80 %.

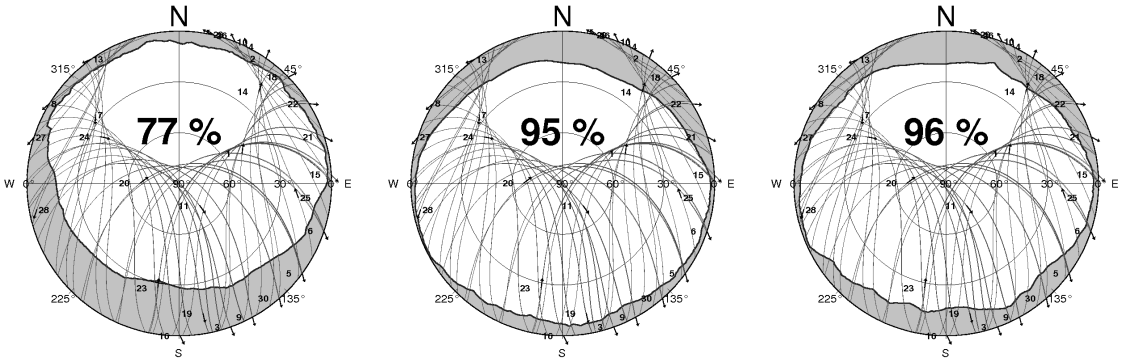

(a) AGAR at 1474.6 m AMSL. (b) BRAE at 1508.6 m AMSL. (c) BRUN at 1010.4 m AMSL.

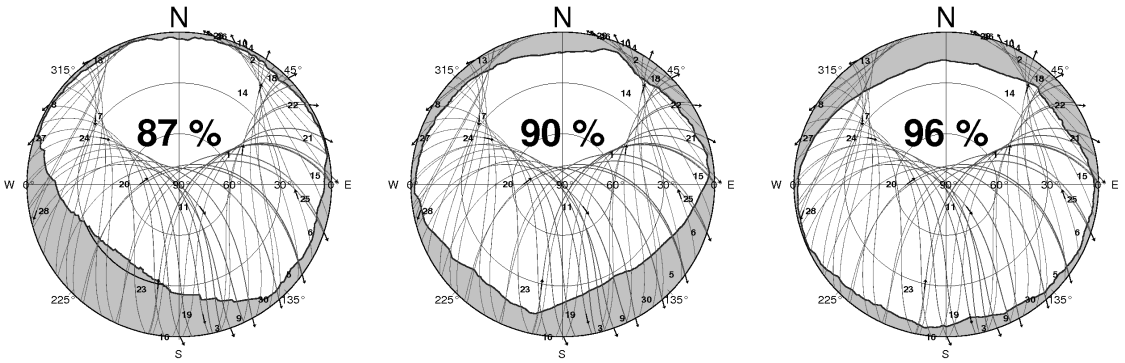

(d) EMSH at 2271.3 m AMSL. (e) ERGI at 1133.3 m AMSL. (f) JEIZ at 1527.1 m AMSL.

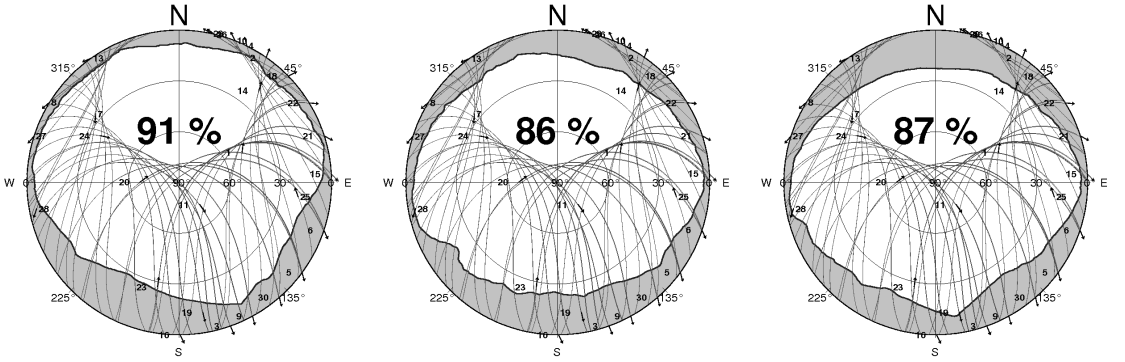

(g) OEMS at 1387.1 m AMSL. (h) SUST at 678.3 m AMSL. (i) TURT at 627.3 m AMSL.

Fig. B.3: Skyplots from the nine Turtmann network stations.

B.4 The permanent geodynamic network TECVAL

In summer 2005, a new GPS network was established within a project supported by the Swiss National Science Foundation to study tectonic movements by modern geodetic methods. A major objective of this study is to correlate the GPS observations with seismic activity in view of seismic hazard assessment in the canton of Valais (see also Heller et al., 2005a,b,c; Rey, 2006; Brockmann, 2007).

During the field campaign in July, the network had not yet been ready for use. For the campaign in October 2005, however, three stations were built up, and their data was available for the present analysis. The same receiver and antenna types were used for all stations (see Tab. B.4).

Station	Receiver type July 8–14, 2005	Antenna type July 8–14, 2005	Receiver type October 20–26, 2005	Antenna type October 20–26, 2005
ERDE	-	-	Trimble NetRS	TRM41249.00
SANE	-	-	Trimble NetRS	TRM41249.00
VARE	-	-	Trimble NetRS	TRM41249.00

Tab. B.3: Receiver and antenna types of the TECVAL network stations.

The sites of the three TECVAL stations ERDE, SANE and VARE have been selected carefully in terms of satellite visibility. All stations, dedicated for permanent operation, receive more than 80 % of the hypothetically expectable signals from the GPS satellites.

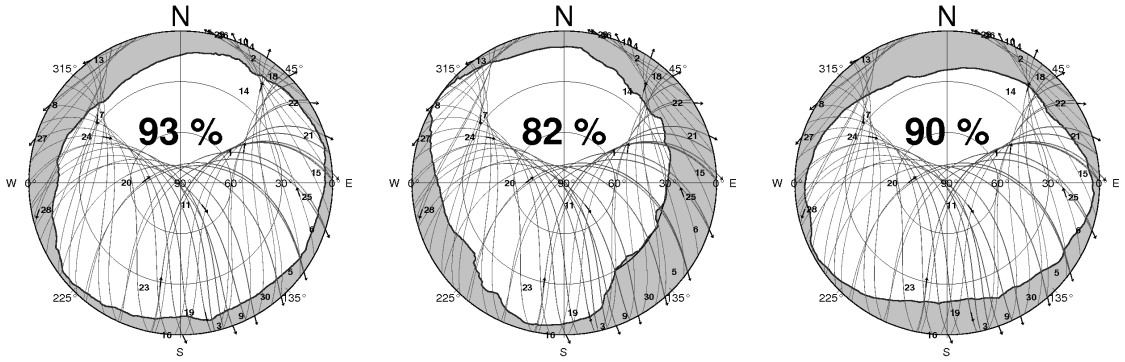

(a) ERDE at 730.8 m AMSL. (b) SANE at 2025.8 m AMSL. (c) VARE at 652.3 m AMSL.

Fig. B.4: Skyplots from the TECVAL network stations.

B.5 National permanent networks AGNES and Swissat

There were two national permanent GNSS (GPS and GLONASS) networks ongoing during the time of the measurement campaigns. The Automated GPS Network for Switzerland (AGNES), maintained and processed by the Swiss Federal Office of Topography swisstopo, consists of 30 permanently operating GPS stations well distributed over the territory of Switzerland (see e.g. Wild et al., 2000; Verdun et al., 2001; Brockmann et al., 2006).[16] Only one respectively two of the stations were located in the project area during the two field campaigns (see Tab. B.4).

The data of this permanent network is primarily used for actively providing users with the new Swiss reference frame LV95 and for maintaining the reference frame at all times with high accuracy. For this purpose, the data is processed daily, occasionally even hourly. This allows detecting possible interferences and changes of the stations' coordinates, e.g. due to tectonic movements, rather quickly.

Station	Receiver type	Antenna type	Receiver type	Antenna type
	July 8–14, 2005		October 20–26, 2005	
HOHT	Trimble 4700	TRM33429.20+GP	Trimble 4700	TRM33429.20+GP
ZER1	-	-	Trimble NetRS	TRM41249.00

Tab. B.4: Configuration of receiver and antenna types of the national GPS network AGNES of swisstopo within the project area.

The Virtual Reference Stations (VRS) network of the private company Swissat was a network of 24 reference stations at this time.[17] In both campaigns, three of those stations were located in the project area.

All stations of the VRS network were equipped with receivers and antennas of the company TOPCON. The stations received the signals of the American GPS (Global Positioning System) and of the Russian GLONASS (Global Navigation Satellite System). With GPS and GPS+GLONASS units (rovers), the Swissat VRS Network permitted a measurement accuracy of a few centimeters within the area of Switzerland. Regarding the use of GPS and GLONASS receivers at the Swissat stations, see e.g. Booth (2003).

[16] For further information on the permanent GPS network AGNES see the website at http://www.swisstopo.ch.

[17] The VRS network is briefly described on the website http://www.swissat.ch. In 2007, the Swiss Federal Office of Topography swisstopo took over the VRS network of Swissat and incorporated parts of the hardware into AGNES.

Station	Receiver type	Antenna type	Receiver type	Antenna type
	July 8–14, 2005		October 20–26, 2005	
BRIG	Javad Legacy	JPSREGANT	Javad Legacy	JPSREGANT
SION	Javad Legacy	JPSREGANT	Javad Legacy	JPSREGANT
ZER2	Javad Legacy	JPSREGANT	Javad Legacy	JPSREGANT

Tab. B.5: Configuration of receiver and antenna types of the Virtual Reference Stations network VRS of the company Swissat within the project area.

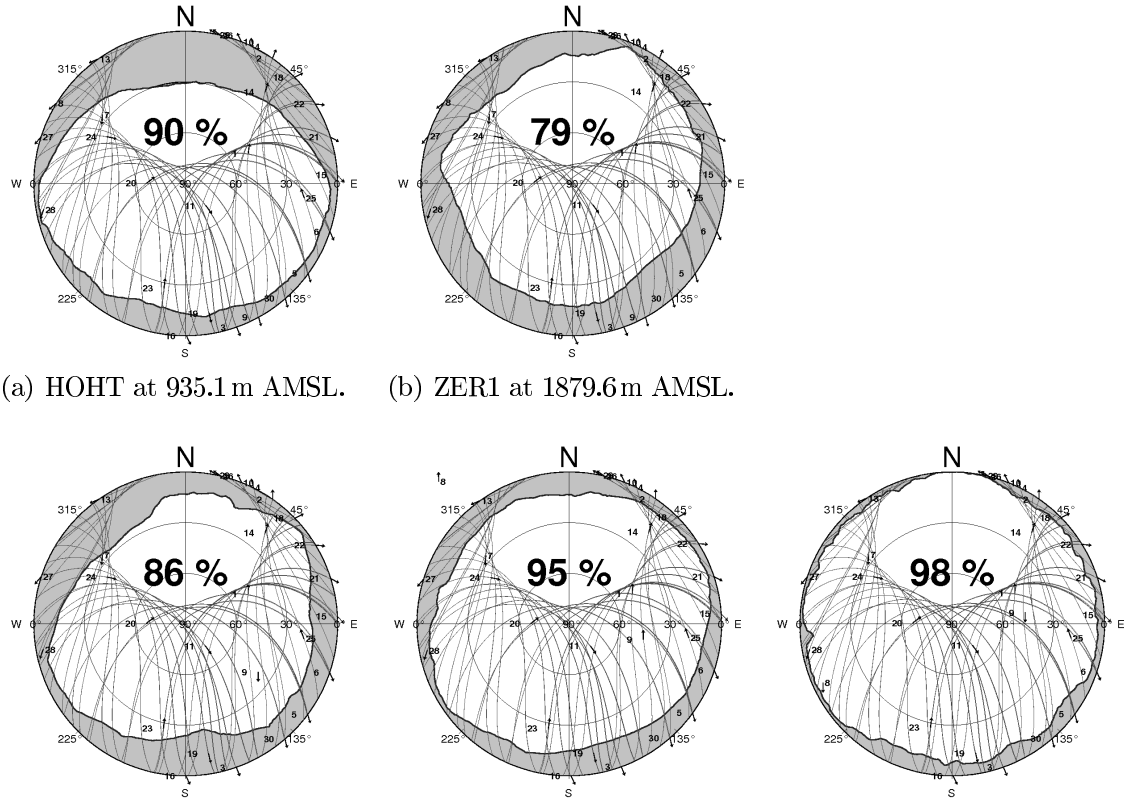

(a) HOHT at 935.1 m AMSL. (b) ZER1 at 1879.6 m AMSL.

(c) BRIG at 701.9 m AMSL. (d) SION at 527.3 m AMSL. (e) ZER2 at 3119.5 m AMSL.

Fig. B.5: Skyplots from the national permanent network stations within the project area. HOHT and ZER1 are two stations of the network AGNES by swisstopo (Subfigs. (a) and (b)), BRIG, SION and ZER2 belong to the Virtual Reference Stations network VRS of the company Swissat (Subfigs. (c), (d) and (e)).

Appendix C

Orbit products from IGS

The International GNSS Service (IGS) collects, archives and distributes GPS and GLONASS observation data sets of sufficient accuracy to meet the requirements of a wide range of scientific and engineering applications and studies. These data sets are analyzed and combined to form the IGS products listed in Tab. C.1 (published by IGS Central Bureau, 2005).

IGS Product	Accuracy orbits	Accuracy clocks	Latency	Updates	Sample Interval
Broadcast	$\approx 160\,\mathrm{cm}$	$\approx 7\,\mathrm{ns}$	real time		daily
Ultra-rapid (predicted half)	$\approx 10\,\mathrm{cm}$	$\approx 5\,\mathrm{ns}$	real time	four times daily	00,06,12,18 UTC
Ultra-rapid (observed half)	$< 5\,\mathrm{cm}$	$\approx 0.2\,\mathrm{ns}$	3 h	four times daily	00,06,12,18 UTC
Rapid	$< 5\,\mathrm{cm}$	$0.1\,\mathrm{ns}$	17 h	daily	daily (12 UTC)
Final	$< 5\,\mathrm{cm}$	$< 0.1\,\mathrm{ns}$	≈ 13 days	weekly	daily (12 UTC)

Tab. C.1: Availability of IGS products and approximate accuracy of orbits and clocks. Note that IGS accuracy limits, except for predicted orbits, are based on comparisons with independent laser ranging results. The precision is better. Furthermore, the accuracy of all clocks is expressed relative to the IGS timescale, which is linearly aligned to GPS time in one-day segments.

Appendix D

Zenith total delay time series of COSMO and GPS

This chapter complements Sec. 6.4.3, pp. 86f. Some examples of ZTD time series of interpolated COSMO model profile data and the corresponding (i.e. the nearest) GPS stations during the field campaign in July and October 2005 are shown. Further, the converted time series within the frequency domain are presented by means of normalized power spectra based on Fast Fourier Transformation.

The six selected sites Emshorn (EMSH), Saas Fee (SFEE), Stalden (STAL), Susten (SUST), Visp (VISP) and Zinal (ZINA) are distributed over the whole project area (see Fig. D.1) and depict the significantly wide range of different station altitudes between 600 m and over 2000 m.

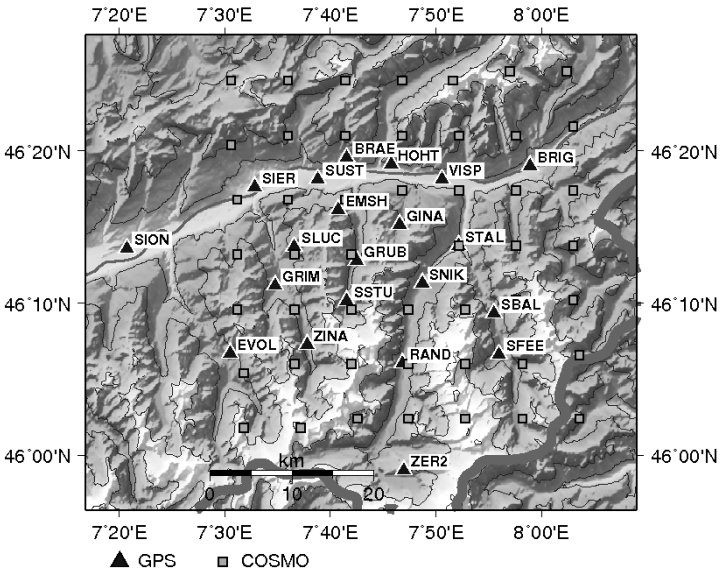

Fig. D.1: Plan view of the project area in the canton of Valais. The local, densified GPS network during the field campaign in July 2005 and the base points of the COSMO profiles are marked.

The correlation coefficient R is calculated based on the section of the time series which is common for both data sets. The weather situation for the duration of the campaigns is given in Appendix A. Especially, the different distribution of rainfall at the two stations shown, is characteristic for the period of the July campaign. During the October 2005 campaign, the cold front passage on the forth day, which provoked precipitation in the whole project area, is the most pronounced meteorological event.

D.1 Examples from the July 2005 campaign

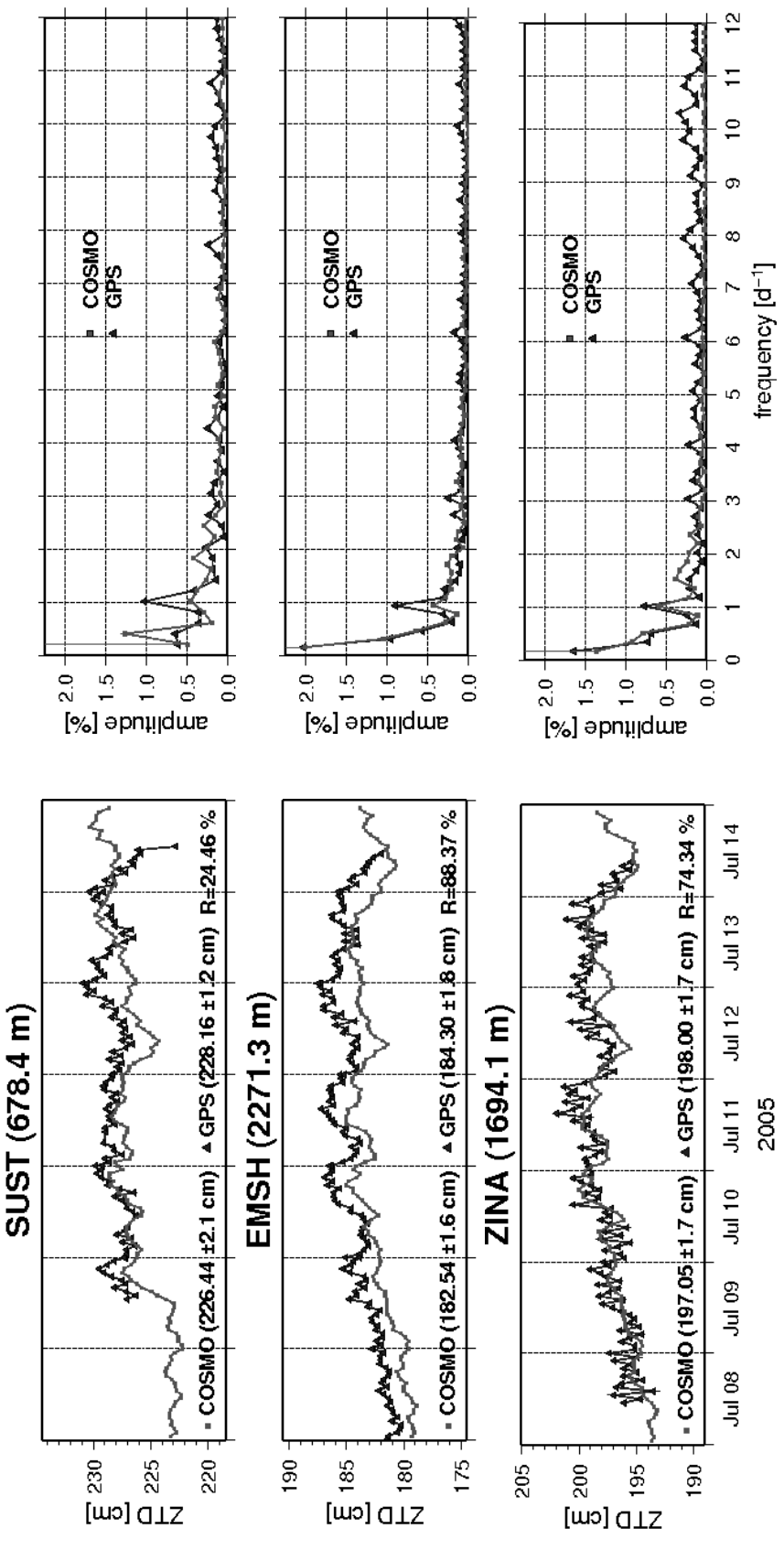

Fig. D.2: ZTD time series and power spectra of interpolated COSMO model data and the corresponding GPS stations SUST, EMSH and ZINA during the field campaign in July 2005. The mean values, their standard deviation and the correlation coefficient R are shown.

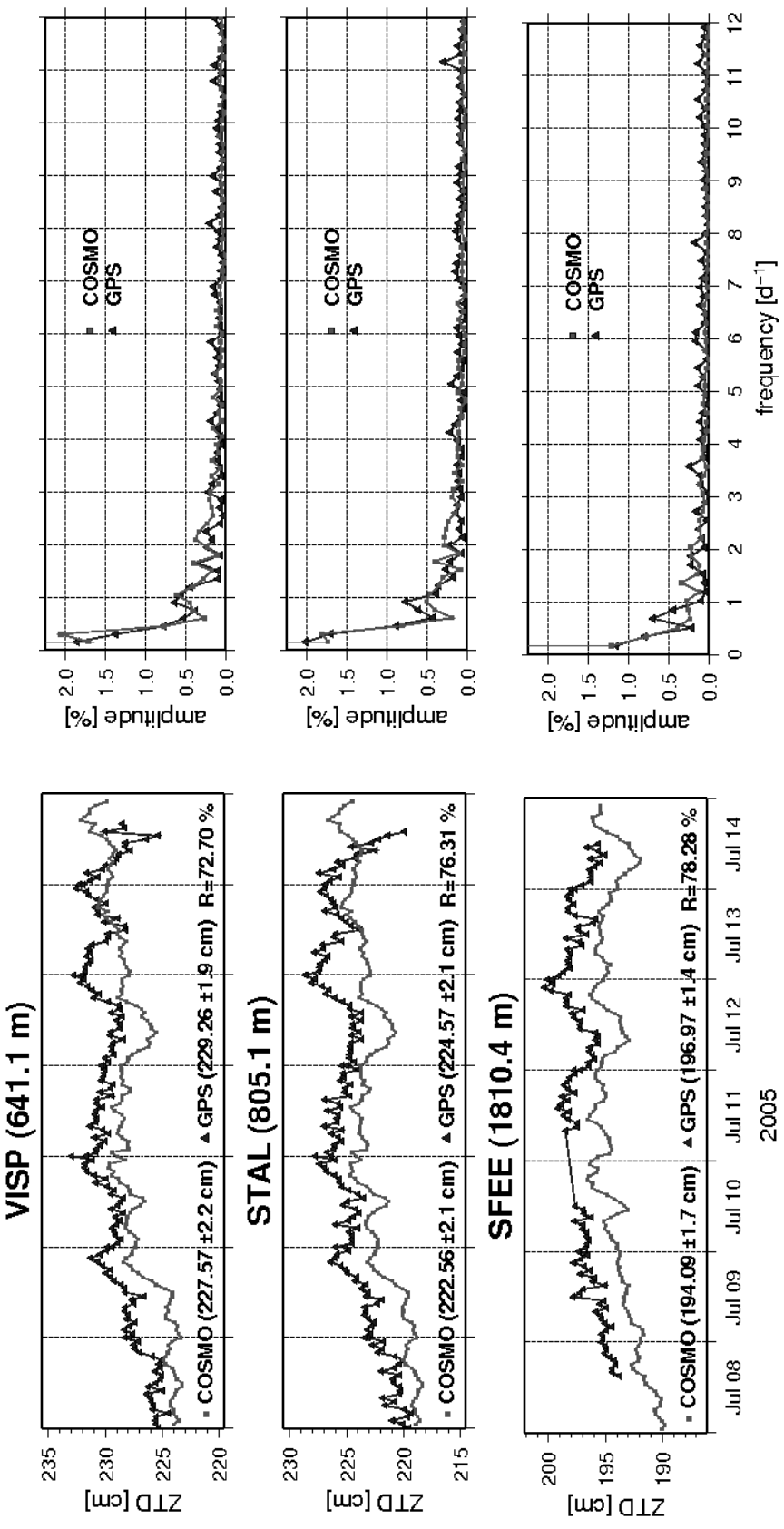

Fig. D.3: ZTD time series and power spectra of interpolated COSMO model data and the corresponding GPS stations VISP, STAL and SFEE during the field campaign in July 2005.

D.2 Examples from the October 2005 campaign

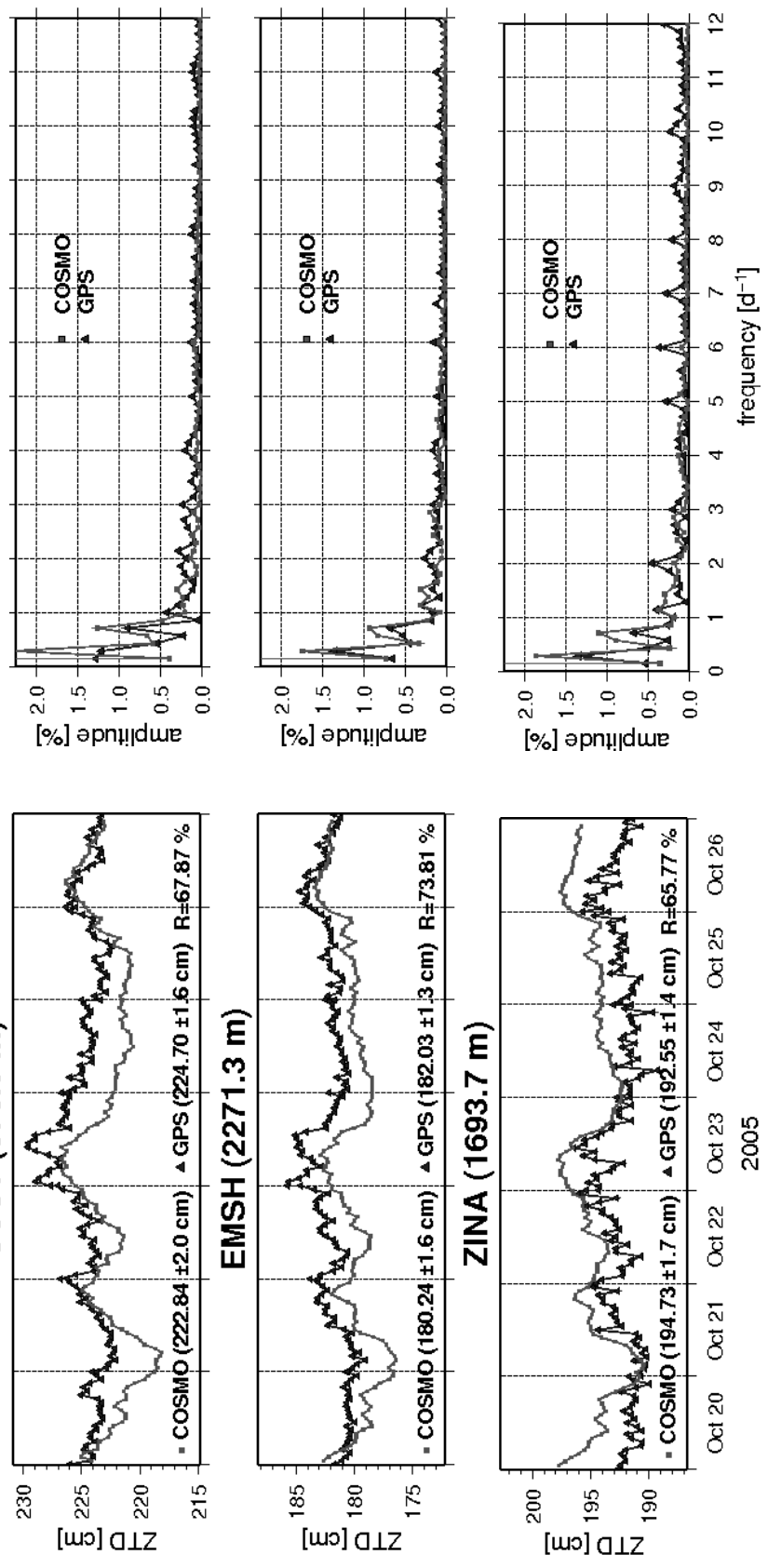

Fig. D.4: ZTD time series of interpolated COSMO model data and the corresponding GPS stations SUST, EMSH and ZINA during the field campaign in October 2005. The mean values and their standard deviation are shown together with the correlation coefficient R.

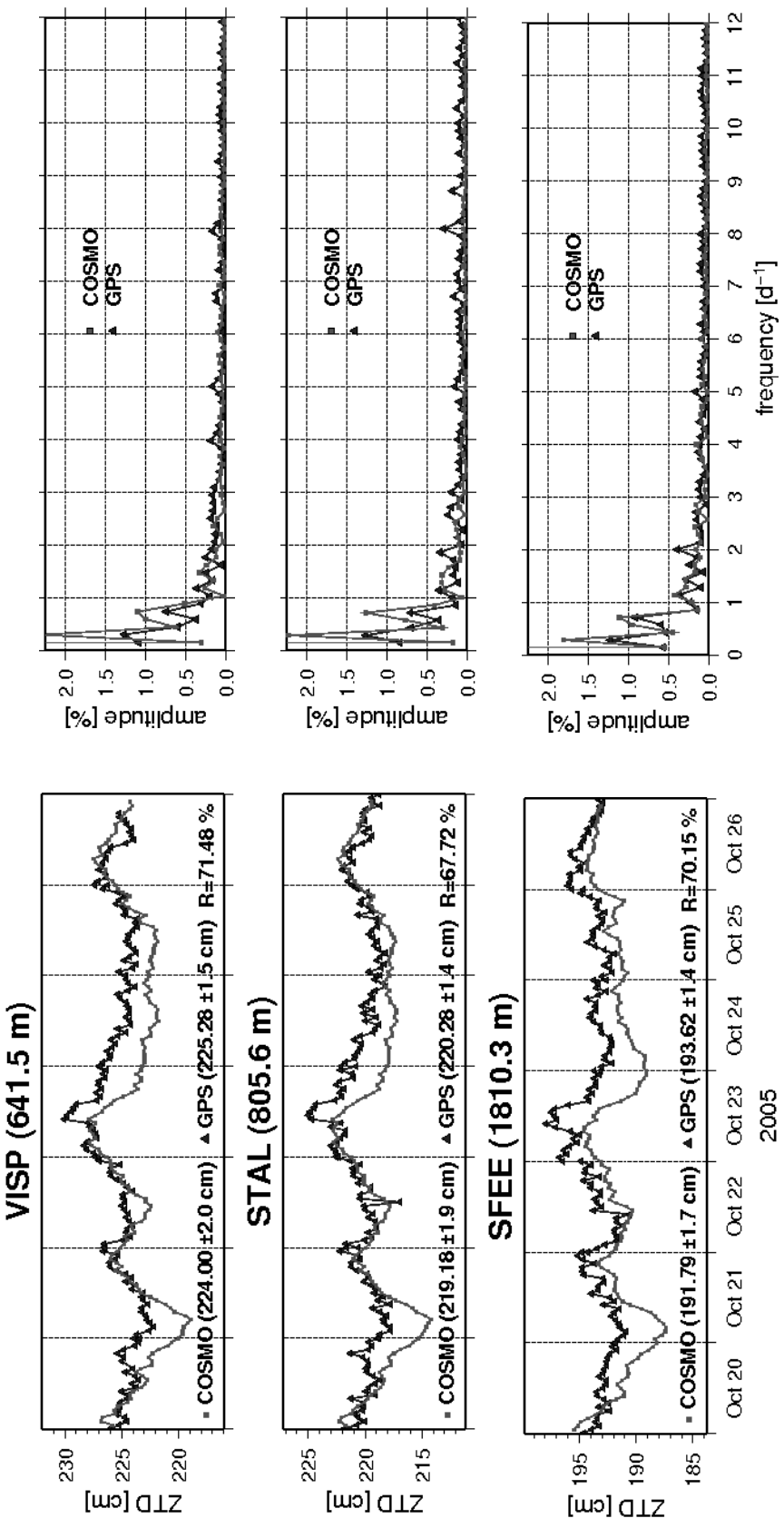

Fig. D.5: ZTD time series of interpolated COSMO model data and the corresponding GPS stations VISP, STAL and SFEE during the field campaign in October 2005.

Appendix E

Wet refractivity and ZWD variation in October 2005

This chapter supplements the examples presented in Sec. 8.1.5, pp. 129f. Four results of wet refractivity variation derived from the tomographic analysis of a voxel model with 3.75 km horizontal grid spacing (see map in Fig. E.1(a)) and 43 layers are shown in Fig. E.2.

The profiles are taken from the stations at Sierre (SIER) and Brig (BRIG) in the main valley in the north of the project area and at Zinal (ZINA) in the Val d'Anniviers and Randa (RAND) in the Mattertal (see also the labeled symbols in Fig. E.1(a) for the geographical location of the sites).

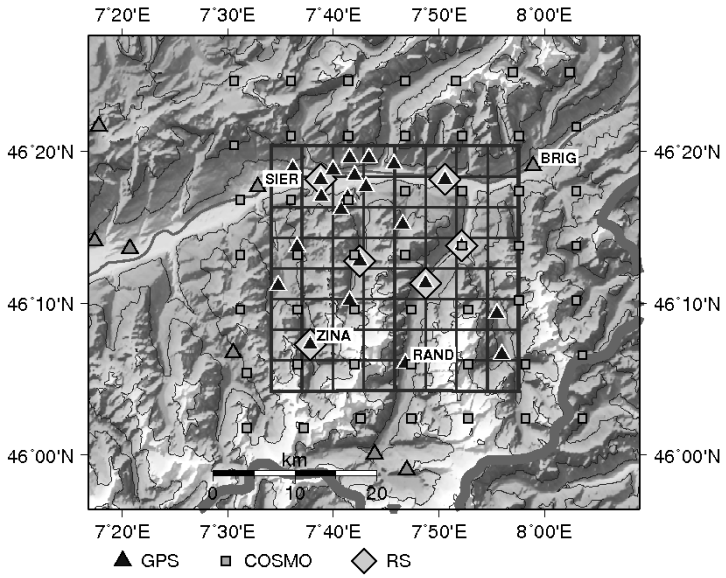

(a) Plan view of the project area in the canton of Valais, Switzerland. The local, densified GPS network during the field campaign in October 2005 and the stations of the examples in Fig. E.2 are marked.

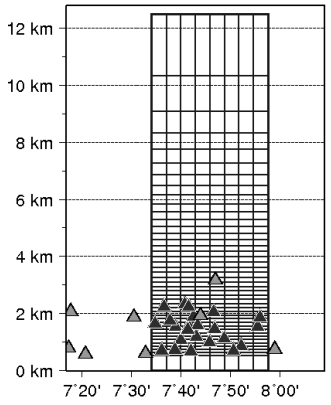

(b) Voxel model cross section with 43 layers and 3.75 km horizontal grid spacing.

Fig. E.1: Plan view and cross section of the voxel model for the examples in Fig. E.2.

The time series of integrated zenith wet delays (ZWD) determined by the tomographic software AWATOS are compared to the interpolated results from the numerical weather model COSMO-7 of MeteoSwiss with respect to the GPS station coordinates. For station ZINA (lower left panel in Fig. E.2) also values from reference radiosondes are available. A detailed description of the graphics is given in Sec. 7.2.1, particularly on p. 95.

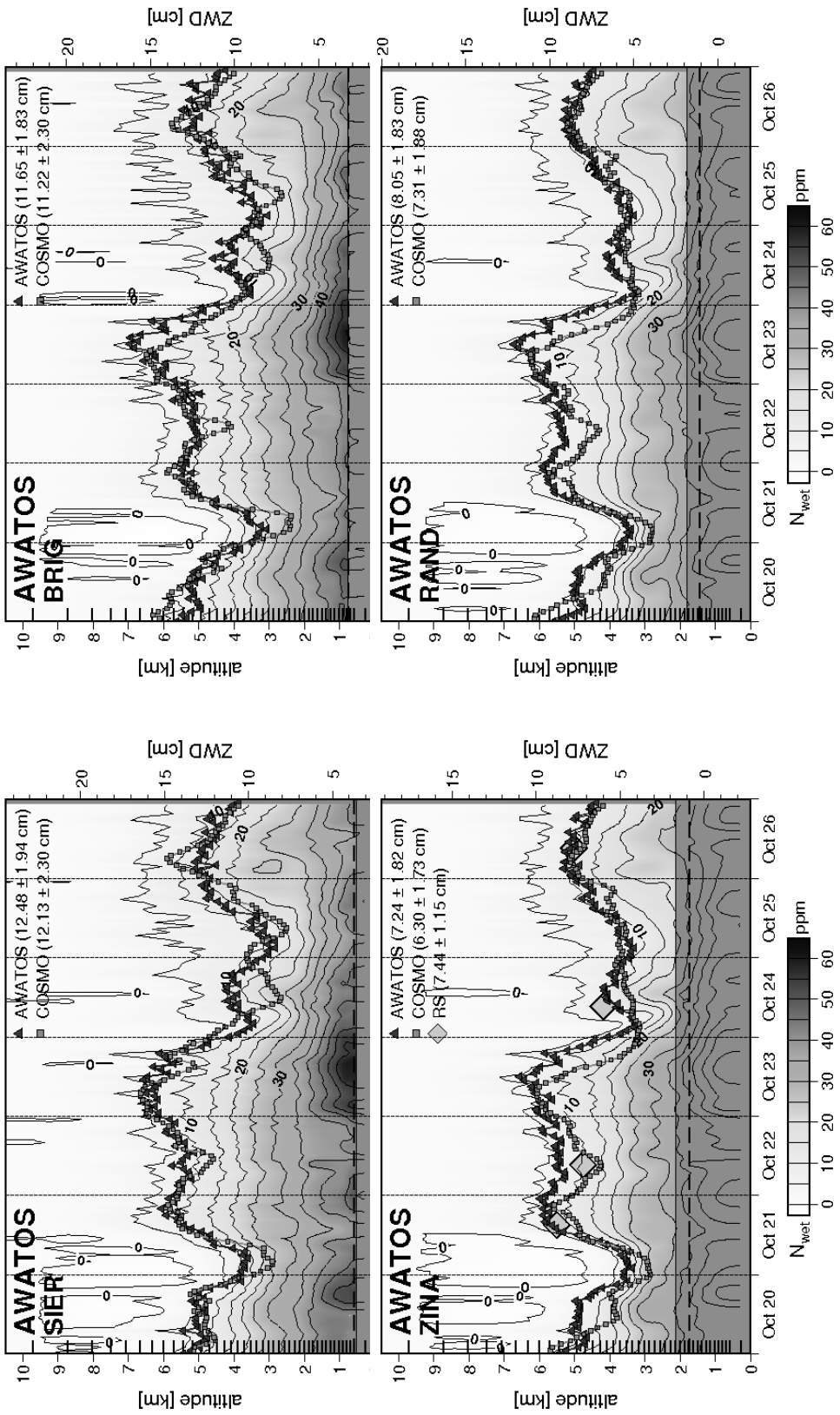

Fig. E.2: Time series of N_{wet} profiles (in ppm) and integrated ZWD at the stations SIER (at 551 m), BRIG (at 702 m), ZINA (at 1694 m) and RAND (at 1407 m) during the October campaign. The data is derived from a tomographic voxel model with 3.75 km horizontal resolution and 43 layers. ZWD time series from COSMO-7 and reference radiosondes are shown for comparison purpose.